Study of the thermo-mechanical behavior of granular media and interactions medium-tank

Nahia Sassine

Communauté
UNIVERSITÉ Grenoble Alpes

THÈSE

Pour obtenir le grade de

DOCTEUR DE LA COMMUNAUTE UNIVERSITE GRENOBLE ALPES

Spécialité : **Matériaux, Mécanique, Génie civil, Electrochimie**

Arrêté ministériel : 25 mai 2016

Présentée par

« Nahia / SASSINE »

Thèse dirigée par **Frédéric-Victor DONZE, Professeur, ISTERRE**

préparée au sein du **Laboratoire 3SR-Grenoble**
dans **l'École Doctorale I-MEP2 - Ingénierie - Matériaux, Mécanique, Environnement, Energétique, Procédés, Production**

Etude du comportement thermo-mécanique d'un milieu granulaire et interactions milieu-réservoir

Thèse soutenue publiquement le **« 16/11/2018 »**,
devant le jury composé de :

M. Philippe NARDIN
Professeur, Université de Franche-Comté, Président
M. Jean-Noël ROUX
Ingénieur de recherche, Laboratoire Navier, Rapporteur
M. Moulay Saïd El YOUSSOUFI
Professeur, Université Montpellier, Rapporteur
M. Frédéric-Victor DONZE
Professeur, Université Grenoble-Alpes, Directeur de thèse
M. Barthélémy HARTHONG
Maître de conférences, Université Grenoble-Alpes, Co-encadrant de thèse
M. Arnaud BRUCH
Ingénieur de recherche, CEA, Co-encadrant de thèse
M. Olivier GILLIA
Ingénieur de recherche, CEA, Invité

Abstract

Thermal Energy Storage (TES) systems are central elements of various types of power plants operated using renewable energy sources. Packed bed TES can be considered as a cost-effective solution in concentrated solar power plants (CSP). Such a device is made of a tank filled with a granular bed through which a heat-transfer fluid circulates. However, in such devices, the tank might be subjected to an accumulation of thermal stresses during cycles of loading and unloading due to the differential thermal expansion between the filler and the tank wall. This research was devoted to investigate the thermo-mechanical behavior of the granular bed inside a packed bed TES tank. To achieve this objective, two approaches were undertaken in this work, i.e. numerical and experimental. A numerical model was defined to describe the tank's behavior under thermal cycling based on the discrete element method (DEM). The evolution of tank wall stresses over thermal cycles, taking into account both thermal and mechanical loads, as well as the kinematics of the granular material at the particles scale (i.e. discrete elements), are studied here. The deformability of the tank itself under thermo-mechanical loads is also included in the numerical model. Simulations were performed for different thermal configurations (i.e. the tank is heated homogeneously along its height or with a moving vertical gradient of temperature) and different boundary condition cases (i.e. rigid wall, tank wall with a higher thermal expansion coefficient than the bed or inversely). The behavior of the tank is dependent on the imposed thermal and boundary conditions. In addition to this, a thermocline prototype was designed and constructed at the CEA laboratory, aiming at studying the stress accumulation over the thermal cycles. The experimental setup, called ESPERA, is equipped with force measurement devices, installed at different height positions on the wall. The force measurement devices were developed and calibrated at the CEA. Their sensitivity was also tested using a different developed setup, P'tit-Pousse. Experimental tests were carried out proving the stress accumulation over the cycles. Eventually, a comparison between the numerical results and the lately-obtained preliminary experimental measurements is proposed.

keywords: Thermal energy storage (TES), Discrete Element Method (DEM), thermal stresses, granular material, experimental tests.

Résumé

Les systèmes de stockage d'énergie thermique sont des éléments centraux de divers types de centrales de production d'énergie fonctionnant à l'aide de sources d'énergie renouvelables. Ces systèmes de stockage thermique de type solide/fluide peuvent être considérés comme une solution rentable dans les centrales solaires à concentration. Un tel dispositif est constitué d'un réservoir rempli d'un lit granulaire à travers lequel circule un fluide caloporteur. Cependant, dans de tels dispositifs, le réservoir pourrait être soumis à une accumulation de contraintes thermiques au cours des cycles de chargement et de déchargement en raison de la dilatation thermique différentielle entre le milieu granulaire et la paroi du réservoir. Cette thèse a été consacrée à l'étude du comportement thermomécanique du lit granulaire à l'intérieur d'un réservoir de stockage thermique de type régénérateur solide/fluide. Pour atteindre cet objectif, deux approches ont été suivies : les approches numériques et expérimentales. Un modèle numérique basé sur la méthode des éléments discrets a été développé pour décrire le comportement du réservoir sous cyclage thermique. L'évolution des contraintes appliquées aux parois de la cuve au cours des cycles thermiques, est étudiée en tenant compte à la fois des charges thermiques et mécaniques, ainsi que de la cinématique du milieu granulaire à l'échelle des particules (c'est-à-dire des éléments discrets) et de la déformation thermo-mécanqiue du réservoir. Des simulations ont été effectuées pour différentes configurations thermiques (chauffage/refroidissement homogène du réservoir sur sa hauteur ou gradient vertical de température) et différents cas de condition limite (paroi rigide, paroi du réservoir avec un coefficient de dilatation thermique supérieur au lit de roche ou inversement). Le comportement du réservoir dépend des conditions thermiques et conditions aux limites imposées. De plus, un prototype de thermocline a été conçu et construit au sein du laboratoire au CEA, visant à étudier l'accumulation de contraintes sur les cycles thermiques. Le dispositif expérimental, appelé ESPERA, est équipé de dispositifs de mesure de force installés à différentes hauteurs sur la paroi du réservoir. Les dispositifs de mesure de force ont été développés et calibrés au CEA. Leur sensibilité a également été testée en développant un autre banc expérimental, P'tit-Pousse. Des essais expérimentaux ont été réalisés permettant de prouver l'accumulation des contraintes au cours des cycles. Finalement, une comparaison entre les résultats numériques et les premiers résultats expérimentaux obtenus en fin de thèse est proposée.

Mots Clés: Energie de stockage thermique, Méthode des éléments discrets, contraintes theriques, milieu granulaire, tests expérimentaux.

Contents

Abstract i

Résumé ii

Contents iii

List of Figures vi

List of Tables xii

1 General introduction 1

2 State of the art 4

2.1 Overview on thermal energy storage systems . . . 4

2.1.1 General introduction . . . 4

2.1.2 Single-tank packed bed heat storage system . . . 6

2.1.2.1 Operating principle and efficiency . . . 6

2.1.2.2 Tank design: thermal ratcheting phenomenon . . . 9

2.1.2.3 Packed-bed storage installations at the industrial/laboratory scale . . . 12

2.2 Numerical and experimental analysis of thermal ratcheting phenomenon in thermocline storage tanks . . . 14

2.2.1 Installation of Solar One (1986) . . . 14

2.2.2 Experimental set up developed by Dreiβigacker et al. . . . 19

2.2.3 Thermo-mechanical study of an industrial thermocline proposed by Sandia National Laboratories . . . 23

2.2.4 Conclusion . . . 27

2.3 Mechanical behavior of a particulate medium subjected to cyclic swelling and shrinking conditions . . . 28

2.3.1 Effect of swelling and shrinking cycles on the densification of a particulate medium . . . 29

2.3.2 Induced pressures on the container walls due to cyclic swelling/shrinking conditions . . . 31

2.3.2.0.1 Diurnal temperature variations: . . . 32

2.3.2.0.2 Moisture content changes: . . . 32

2.3.2.0.3 Hydrogen absorption/desorption reactions: . . . 34

2.3.3 Conclusion . . . 36

2.4 Limiting and avoiding the thermal ratcheting phenomenon . . . 36
2.4.1 Development of a structured thermocline thermal energy storage system 37
2.4.2 Unconstrained packed rock bed thermal energy storage facility . . . 39
2.4.3 Limiting the ratcheting by increasing the internal insulation . . . 39
2.4.4 Dividing the tank into subsections . . . 41
2.4.5 Adopt a truncated conical shape for the thermocline tank . . . 41
2.4.6 Conclusion . . . 43
2.5 Conclusion . . . 43

3 Discrete Numerical Model **45**
3.1 A brief review on the discrete element method (DEM) . . . 45
3.1.1 DEM calculation process . . . 46
3.1.2 Interaction laws . . . 46
3.1.3 Stability condition . . . 49
3.1.4 Sample generation . . . 50
3.2 Thermo-mechanical numerical model . . . 51
3.2.1 Thermal and mechanical coupling for the particulate medium . . . 51
3.2.1.1 Stress Calculation . . . 52
3.2.1.2 Verification and validation of the implementation . . . 53
3.2.2 Thermo-mechanical model used for tank walls . . . 54
3.2.2.1 Cylinder element . . . 56
3.2.2.2 PFacet element . . . 58
3.2.2.3 Recapitulation of all possible interactions . . . 58
3.2.2.4 Definition of physical membrane's properties . . . 59
3.2.2.5 Coupling of thermal and mechanical loadings . . . 62
3.2.2.6 Verification of the implementation . . . 62
3.3 Adopted numerical procedure in this study . . . 63

4 Numerical results **64**
4.1 Rigid boundary Case . . . 64
4.1.1 Thermal cyclic conditions . . . 66
4.1.1.1 Induced normal stresses due to thermal cyclic conditions . . . 68
4.1.1.2 Vertical displacement of particles . . . 70
4.1.2 Analysis of the numerical results . . . 71
4.1.2.1 Kinematical response of the bed . . . 71
4.1.2.2 Evolution of tangential stresses along the tank's height . . . 73
4.1.3 Influence of long term thermal cycles . . . 73
4.1.4 Influence of the mechanical properties: friction angle . . . 75
4.2 Deformable wall . . . 76
4.2.1 Thermal cyclic conditions . . . 78
4.2.1.1 Normal stress and tank wall deformation for the first thermal cycle . . . 78
4.2.1.2 Influence of repeated cycles . . . 80
4.2.1.2.1 Normal induced stresses . . . 80
4.2.1.2.2 Tank wall deformation . . . 81
4.2.1.2.3 Averaged vertical displacements . . . 82

4.2.2 Analysis of the numerical results . . . 84
4.2.2.1 Kinematical behavior of the granular bed . . . 84
4.2.2.2 Comparison with rigid boundaries Case . . . 92
4.2.3 Influence of the differential of TEC between filler/walls . . . 93
4.2.4 Pluri-disperse particle size distribution . . . 94
4.3 Conclusion . . . 96

5 Experimental setup aiming at studying the thermal ratcheting 99
5.1 Experimental setup development . . . 99
5.1.1 Objectives . . . 99
5.1.2 Description of the setup . . . 100
5.1.3 Force measurement device . . . 103
5.1.4 Force sensor calibration . . . 106
5.1.4.1 Calibration process . . . 106
5.1.4.2 Calibration results . . . 107
5.2 Numerical and experimental validation of force measurement device through P'tit-Pousse setup . . . 108
5.2.1 P'tit-Pousse setup . . . 108
5.2.2 Experimental results on P'tit-Pousse . . . 109
5.2.3 Numerical validation . . . 110
5.3 Preliminary results on ESPERA . . . 115
5.3.1 Temperature evolution in ESPERA . . . 115
5.3.2 Resulted stresses on ESPERA . . . 117
5.4 Conclusion . . . 121

6 Conclusions and perspectives 123

A Potential tank's geometries and properties 128
A.1 Aluminum tank walls . . . 128
A.2 Truncated conical tank . . . 129

B Execution plans of ESPERA 132

Bibliography 140

List of Figures

2.1 Schematic diagram of a CSP tower power plant with integrated two tanks molten salt TES system, from Libby (2010) 6
2.2 Schematic diagram of a CSP tower power plant with integrated a dual-media thermocline TES system, from Libby (2010) 7
2.3 Different degrees of stratification with the same amount of stored heat; left, highly stratified and right, moderately stratified (Haller et al. (2009)) 7
2.4 Evolution of temperature profiles of STONE (a 2.4-m^3 packed bed of rocks and sand with thermal oil as HTF): (a) During charge; (b) During discharge. The "dot" results correspond to measured data, while the dashed or continuous lines refer to numerical results obtained using different model assumptions, from Esence (2017) 8
2.5 End-cycle dimensionless temperature profiles at the long-term configuration: (a) With little extraction of the thermocline region at the end of each charge and discharge, (b) With large extraction of the thermocline region at the end of each charge and discharge (Bruch et al. (2014)) 9
2.6 Illustration of the thermal ratcheting phenomenon when the tank expands more than the filler material 10
2.7 Silo failure due to thermal ratcheting: (a) Before failure; (b) After collapse (Carson (2001)) 11
2.8 Dimensions of most packed-bed storage systems existent in the literature (Esence et al. (2017b)) 12
2.9 Thermal storage unit of Solar One: (a) Construction details, (b) Tank cross-section (Faas (1983b)) 14
2.10 Hoop stresses on Solar One thermocline tank. Transient simulation results by Gonzalez et al. (green stands for flexible filler, red stands for rigid filler), simulation results of Flueckiger et. al (rigid filler), and measured data. Experimental readings are figured at three different times, from left to right: April 1982, December 1982 and June 1984; from González et al. (2015) 18
2.11 Thermal storage test device (left) and the interior view towards the flushed closing force measurement devices (right), from Dreißigacker et al. (2013) . . 20
2.12 (a) Force measurement device developed by Dreiβigacker et al., (b) Simulated and measured particle-wall contact force and temperature evolution at a packed bed depth of 0.3 m, from Dreißigacker et al. (2013) 21
2.13 Maximal forces acting on the container wall (left); Force progression over multiple thermal cycles at 0.6 m bed height (right), from Knödler et al. (2016) . . 23

2.14 (a) Operating temperature over four cycles at 7 equally spaced tank elevations, (b) Temperature-dependency of of SST 347 Young's Modulus, from (Kolb et al. (2011)) . . . 24
2.15 (a) Bed Young's modulus values (psi) vs. Temperature (°C), (b) Mean TEC of granite rock (green), sandstone (blue) and 347 Stainless steel (red) as a function of temperature (°C), from (Kolb et al. (2011)) . . . 25
2.16 Equivalent plastic strain: (a) Nominal Young's modulus with high bed's TEC, (b) High Young's modulus with low bed's TEC, from Kolb et al. (2011) . . . 26
2.17 Packing's height variation during thermal cycling: (a) Experimental setup considered in (Divoux et al. (2008)), (b) Height variation h_n ($h_{current}$-h_0) with cycles n, H=140 cm; from Divoux et al. (2008) . . . 30
2.18 (a) Experimental setup considered in (Chen et al. (2006); Chen (2008); Chen et al. (2009)), (b) The change of the packing fraction as a function of number of thermal cycles (case of polystyrene grains in glass container); from Chen et al. (2009) . . . 31
2.19 Change in packing fraction with thermal cycling for a temperature difference of 10°C, 50°C and 100°C . . . 32
2.20 Lateral thermal pressure and wall temperature in the Westeel Model 198 measured at by the sensor located at S 60° E; from Zhang et al. (1993) . . . 33
2.21 (a) Experimental set-up, (b) Average changes in lateral pressures at three measuring levels; from Kebeli et al. (2000) . . . 33
2.22 Influence of the slenderness ratio H/L, (a) Forces acting on the wall as a function of H/L initial ratio (B. Charlas), (b) Average radial stresses for cycle 5 in hydrided (σ_H, highest levels of stresses) and unhydrided (σ_U, lowest level of stresses) states depending on the slenderness ratio (Charlas et al. (2015)) . . . 35
2.23 2 × 4 bricks structure (fluid is represented in light grey) as proposed by (Motte et al. (2014)); Description of geometric parameters . . . 37
2.24 Concrete arrangements in thermocline tank: (a) Axisymmetric configuration, (b) Parallel-plate configuration; from Brown et al. (2012) . . . 38
2.25 The cross-section elevation and the longitudinal sectional elevation of the invention, from Kröger (2014) . . . 40
2.26 (a) Schematic illustration of the thermocline tank with a composite wall consisting of (1) firebrick, (2) steel, and (3) ceramic, (b) hoop stress profile along the filler bed height for all cases (see Table 2.7); from Flueckiger et al. (2013) 41
2.27 STONE experimental set-up; left: picture of the storage tank before insulation, right: scheme of its construction plane with baskets; from Esence et al. (2017a) 42
2.28 Scheme and photograph of the TES unit in Ait Baha, Morocco during construction; (Zanganeh et al. (2014)) . . . 43

3.1 DEM concept . . . 46
3.2 Interaction law at the contact used by Cundall and Strack (Cundall and Strack (1979)) . . . 47
3.3 DEM method: (a) Illustration of the DEM concept for spherical 2D particles (b) Normal and tangential contact models . . . 48
3.4 Schematic representation of the mechanical/thermal coupling procedure . . . 52
3.5 Stress calculation, force distribution on one element nodes . . . 52
3.6 One dimensional simplified problem, force validation . . . 53

3.7 Influence of the slenderness ratio at rest: (a) on the vertical stresses (b) on the horizontal stresses . . . 55
3.8 Cylindrical container membrane formed by a set of spheres, cylinders and PFacets 55
3.9 Sphere/Cylinder interaction, from Effeindzourou et al. (2016) . . . 56
3.10 Coupling between bending moment and shear force in a cylinder element . . . 57
3.11 PFacet/Sphere interaction, from Effeindzourou et al. (2016) . . . 58
3.12 Recapitulating all possible interactions . . . 59
3.13 Rectangular plate subjected to vertical loadings . . . 60
3.14 Rectangular plate subjected to horizontal loadings . . . 61
3.15 Steel cylindrical tank subjected to thermal gradient loadings: (a) Temperature profile along the tank's height for a charge/discharge cycle (b) evolution of radial deformation of the tank along its height . . . 63

4.1 Influence of the mean radius particle on the resulted stresses on the wall, samples with r_{Mean}=0.025, 0.029 or 0.033 m are tested . . . 65
4.2 (a) homogeneous thermal cycling along tank's height, (b) Influence of the slenderness ratio within one thermal cycle . . . 66
4.3 Cylindrical tank filled with about 8000 spherical particles with a mean radius of 0.029 m . . . 67
4.4 Thermal gradient cycling (MTG) . . . 67
4.5 Normalized radial stresses evolution along the tank height within one cycle: (a) Homogeneous cycling, (b) MTG cycling, recalling that the resulting stresses are normalized by the hydrostatic pressure $(1-n)\times\rho gH$ where H is the height of the packed bed and ρ is the particle density and n is the porosity of the filler medium. The thinner dashed lines refer to the minimum and maximum values obtained in the three simulations . . . 68
4.6 The maximum applied radial stress evolution along the tank height over 29 sequenced cycles for both configurations: homogeneous vs. the MTG configuration (the error bars represent the standard deviation calculated based on three initial samples with similar properties) . . . 69
4.7 Vertical displacements of particles at different depths for: (a) homogeneous configuration, (b) MTG configuration . . . 70
4.8 Vertical displacements of particles, normalized by the bed's height, at the deepest layer for: (a) homogeneous configuration, (b) MTG configuration . . . 72
4.9 Evolution of the mobilized friction angle (the ratio ratio of tangential stresses σ_{rz} over normal stresses σ_{rr}) along the tank's height within one cycle: (a) homogeneous cycling, (b) MTG cycling . . . 74
4.10 Influence of cycling on: (a) Applied normal stresses (normalized by the hydrostatic pressure at the bottom) (b) Rearrangement of particles . . . 75
4.11 Influence of friction on: (a) Applied normal stresses (normalized by the hydrostatic pressure at the bottom), (b) Averaged vertical displacement of particles (normalized by the bed's height) . . . 76
4.12 Steep thermal gradient configuration (STMG configuration) . . . 77
4.13 Case 1 (α_w>α_b), first thermal cycle within an homogeneous configuration: (a) Normalized radial stresses evolution along the tank height, (b) Evolution of the tank wall deformation . . . 78

4.14 Case 2 (α_w<α_b), first thermal cycle within an homogeneous configuration: (a) Normalized radial stresses evolution along the tank height, (b) Evolution of the tank wall deformation . . . 79
4.15 Case 1 (α_w>α_b), first thermal cycle within a SMTG configuration: (a) Normalized radial stresses evolution along the tank height, (b) Evolution of the tank wall deformation . . . 79
4.16 Case 2 (α_w<α_b), first thermal cycle within a SMTG configuration: (a) Normalized radial stresses evolution along the tank height, (b) Evolution of the tank wall deformation . . . 80
4.17 Evolution of applied radial stresses on the tank over 30 thermal cycles, within different cyclic configurations: (a) Case 1 (α_w>α_b), (b) Case 2 (α_w<α_b) . . . 80
4.18 Accumulation of tank wall deformation over 30 thermal cycles within an homogeneous configuration: (a) Case 1 (α_w>α_b), end of discharging cycle, (b) Case 2 (α_w<α_b), end of charging cycle . . . 82
4.19 Accumulation of tank wall deformation over 30 thermal cycles within a SMTG configuration: (a) Case 1, end of discharging cycle, (b) Case 2, end of charging cycle . . . 83
4.20 Vertical displacements of particles at different depths within an homogeneous configuration for: (a) Case 1 (α_w>α_b), (b) Case 2 (α_w<α_b) . . . 84
4.21 Vertical displacements of particles at different depths within a SMTG configuration for: (a) Case 1 (α_w>α_b), (b) Case 2 (α_w<α_b) . . . 85
4.22 Case 1 (α_w>α_b): Evolution of the kinematic response of particles at deep within an homogeneous configuration for: (a) first three performed cycles, (b) last three performed cycles (the 28^{th}, 29^{th} and 30^{th} cycles), dashed lines correspond to the temperature evolution for all layers . . . 86
4.23 Case 1 (α_w>α_b): Evolution of the kinematic response of particles at deep within a SMTG configuration for: (a) First three performed cycles, (b) Last three performed cycles (the 28^{th}, 29^{th} and 30^{th} cycles), dashed lines correspond to the temperature evolution for each layer . . . 88
4.24 Schematic diagram explaining the opposite behaviors of bottom and top layers: (a) During the charging cycle , (b) During the discharge cycle . . . 89
4.25 Case 1 (α_w>α_b): Evolution of the kinematic response of particles at deep for: (a) homogeneous configuration, (b) SMTG configuration . . . 90
4.26 Case 2 (α_w<α_b): Evolution of the kinematic response of particles at deep within an homogeneous configuration for: (a) first three performed cycles, (b) last three performed cycles (the 28^{th}, 29^{th} and 30^{th} cycles), dashed lines correspond to the temperature evolution for all layers . . . 91
4.27 Case 2 (α_w<α_b): Evolution of the kinematic response of particles at deep within a SMTG configuration for: (a) First three performed cycles, (b) Last three performed cycles (the 28^{th}, 29^{th} and 30^{th} cycles), dashed lines correspond to the temperature evolution for each layer . . . 92
4.28 Case 2 (α_w<α_b): Evolution of the kinematic response of particles at deep for: (a) homogeneous configuration, (b) SMTG configuration . . . 93
4.29 Radial stresses evolution: Comparison with rigid boundary Case . . . 93
4.30 Influence of the thermal differential coefficient $|\Delta\alpha|$ on the induced stresses . 94
4.31 Influence of the pluri-disperse particle size distribution: radial stress evolution in Case 1 (α_w>α_b): (a) Homogeneous configuration, (b) SMTG configuration 95

4.32 Influence of the pluri-disperse particle size distribution: radial stress evolution in Case 2 (α_w<α_b): (a) Homogeneous configuration, (b) SMTG configuration 95

5.1 Schematic of the CLAIRETTE installation, ESPERA included 101
5.2 ESPERA setup with all its constituting elements 102
5.3 ESPERA setup with all its constituting elements 103
5.4 (a) ESPERA setup; the external cover is removed, (b) ESPERA with the external heat insulator 104
5.5 Concept of the force measurement device placed on the tank's wall 105
5.6 Full bridge configuration 105
5.7 Dimensions of the force measurement device 106
5.8 (a) Positions of windows along the tank's height, including a section at each level (all dimensions are in mm), (b) Different sections through the tank, showing the orientation and number of the existing windows 107
5.9 Positions of the thermocouples in or outside the tank (dimensions in mm) . . 108
5.10 Top view of both cylinders showing the thermocouples inside the tank) 108
5.11 (a) The assembly of 4 sensors, (b) The assembly in the oven used for the calibration process at high temperature 109
5.12 Calibration results for the first assembly: Force/Tension curves: (a) At ambient temperature, (b) At high temperatures (100 and 200° C) 110
5.13 Calibration results for the first sensor: Force/Tension curves for sensor 1 at ambient and high temperatures 111
5.14 Calibration results for the second assembly: Force/Tension curves: (a) At ambient temperature, (b) At high temperatures (100 and 200°) 112
5.15 Schematic view of P'tit-Pousse installation 113
5.16 P'tit-Pousse installation 113
5.17 (a) Force measurement device installed on the fixed wall of P'tit-Pousse, (b) P'tit-Pousse filled with glass beads 114
5.18 Stress variation over 2 cycles of charging/discharging (±3 mm of displacement), responses of 8 experimental tests (dashed lines) and their average (continuous line) 114
5.19 Stress vs. imposed displacement curves for: (a) ±3 mm of displacement, (b) ±10 mm of displacement 115
5.20 Stress variation over 2 cycles of charging/discharging for both ±3 mm and ±10 mm displacements 116
5.21 Simulation 1: Stress/displacement numerical curves over 2 cycles of charging/discharging compared to the experimental curves, with $\varphi = \varphi_s = 5°$ throughout the whole process 117
5.22 Simulation 2: Stress/displacement numerical curves over 2 cycles of charging/discharging compared to the experimental curves, at the sample generation: $\varphi = \varphi_s = 5°$, then before cycling: $\varphi = \varphi_s = 45°$ 117
5.23 Simulation 3: Stress/displacement numerical curves over 2 cycles of charging/discharging compared to the experimental curves, with $\varphi = \varphi_s = 45°$ throughout the whole process 118
5.24 Temperature evolution over one thermal cycle for the average of thermocouple 1,2 (at bottom) and for thermocouple 8 (at top), cycling between ambient temperature and 185°C 118

5.25 Temperature evolution over one thermal cycle for the average of thermocouple 1,2 (at bottom) and for thermocouple 8 (at top), cycling between 50 and 185°C 119
5.26 Applied stresses on ESPERA within 7 performed thermal cycles, normalized with the hydrostatic pressure at the bottom of the tank 119
5.27 Applied stresses on the ESPERA within 7 performed thermal cycles and compared with the numerical results, referring to Table 5.3 121

A.1 Aluminum tank walls: radial stress evolution in Case 1 ($\alpha_w > \alpha_b$): (a) Homogeneous configuration, (b) SMTG configuration 129
A.2 Aluminum tank walls: radial stress evolution in Case 2 ($\alpha_w < \alpha_b$): (a) Homogeneous configuration, (b) SMTG configuration 129
A.3 Aluminum tank walls: evolution of tank walls deformation in: (a) Case 1 ($\alpha_w > \alpha_b$), (b) Case 2 ($\alpha_w < \alpha_b$) 130
A.4 Thermal stresses applied on truncated conical walls at different levels of friction 131

B.1 Schematic plan for the whole setup 133
B.2 schematic cross-sectional elevations of the cylindrical tank letting appear the windows 134
B.3 Top vein 135
B.4 Bottom vein 136
B.5 Perforated plate at the bottom of the tank 137
B.6 Diaphragm system at the bottom of the tank 138
B.7 Schematic plan of the force measurement device 139

List of Tables

2.1 Main characteristics of some packed-bed storage applications from the literature 13
2.2 Characteristic parameters of a thermal cycle of the thermocline of Solar One . 15
2.3 Measured hoop stresses on Solar One thermocline (Faas (1983b)); numbers with * are not used in forming the average 16
2.4 Tank dimensions and material properties of ceramic beads (Dreißigacker et al. (2013)) 19
2.5 Characteristic parameters of a thermal cycle of the thermocline studied by Kolb et al. (Kolb et al. (2011)) 24
2.6 Studied beds with different initial packing fraction ratios; from Ao et al. (2005) 34
2.7 Summary of the cases considered with different wall structural parameters; from Flueckiger et al. (2013) 41

3.1 Mechanical properties used in the simulations 54

4.1 Mechanical properties used in the simulations 66
4.2 Thermo-mechanical properties used in the simulations 67
4.3 Different cases of boundary conditions considered in the study 77
4.4 Mechanical properties for: (a) Granular bed, (b) Cylinders forming the steel membrane, see Chapter 3, Section 3.2.2.4 77
4.5 Summary of all studied cases, numerically 98

5.1 Different numerical studied cases: the corresponding microscopic friction angles and the calculated porosity of the samples 104
5.2 Different numerical studied cases: the corresponding microscopic friction angles and the calculated porosity of the samples, φ is the internal friction angle between particles and φ_s is the static friction angle at the contact with the wall 116
5.3 Input data: Experimental and numerical material properties and thermal conditions 120

Chapter 1

General introduction

Thermal Energy Storage (TES) systems are central elements in CSP plants as they can mitigate the variability and intermittency of solar radiation and provide a continuous operation. The thermocline facility, where hot and cold heat transfer fluid (HTF) are stored in a single tank, is considered as a cheaper alternative to the standard two-tank molten salt facility. To leverage further cost reductions, an inexpensive solid filler material, such as sand and gravel, can be used: the packed bed compensates for the higher-cost of the HTF and the capital cost can be reduced to 33% for an equivalent amount of storage using traditional approach. The granular packed bed can be considered as a suitable primary thermal storage material since it offers a large heat transfer area and thus a high heat transfer rate.

During the heating cycle, hot fluid enters the tank from the top while cold fluid is extracted from the bottom of the tank. The bed is gradually heated, storing the thermal energy. During the cooling cycle, the thermal energy is extracted by injecting the cold fluid from the bottom while the hot fluid is drawing off the top of the tank. The separation between the hot and cold zones of the HTF is naturally enabled by buoyancy forces leading to a region with high temperature gradient, known as the heat exchange region.

However, such devices could face the thermal ratcheting phenomenon, which is mainly due the differential of thermal expansion between the filler and the tank materials. The difference between the thermal expansion coefficients of both storage materials enhance the settlement of the granular particles inside the thermocline tank. Thus, the granular medium is densified over the cycles of charging and discharging, causing a stress accumulation on the tank wall. The resulted thermal stresses may exceed the wall tank yield stress leading to plastic deformation and the tank will be slowly ratcheted outward over the thermal cycles which may cause its failure.

The thermal ratcheting phenomenon has gained the interest of many research studies as it strongly impacts the tank design and its life-time. However, only few data considering the

thermo-mechanical behavior of a granular bed in thermoclines are existent in literature. Most of the results are based on the experimental structural response of a 170 MWh oil-rock thermocline tank integrated in the Solar One CSP pilot plant. However, these experimental data suffer from large uncertainty and the tank became malfunctioning after only few cycles, reducing the possible long-time effects of thermal ratcheting on the tank. On the other hand, two numerical approaches are usually considered to model the thermo-mechanical behavior of a packed bed in storage tanks, aiming at understanding the structural response of thermoclines over thermal cycles. The first approach lies in considering the packed bed as a continuum by assuming that its micro-structure is small compared to the container size (based on the finite element method). Nevertheless, rearrangement of particles submitted to thermal breathing involves local mechanisms which result in a highly nonlinear thermo-mechanical behavior at the continuum scale and this complex behavior is poorly constrained. In contrast, another modeling approach, based on the "Discrete Element Method" (DEM) which reproduces explicitly the granular nature of the filler can be considered, representing the granular materials by a set of discrete elements. The DEM naturally accounts for particle rearrangement without the need for significant modeling efforts. Using DEM, the modeling complexity of such a problem involving thermal dilation of a granular system reduces to the problem of thermal dilation of elastic particles.

Research objectives

The aim of this thesis is to study the thermo-mechanical behavior of a granular bed inside a thermocline storage tank. To fulfill this objective, numerical and experimental approaches will be considered.

- A DEM numerical model is developed, using YADE, to model a thermocline storage tank;
- As a first approximation, the numerical model is realized based on rigid boundaries unaffected by temperature variations;
- A more realistic model, which accounts for the tank wall deformation under temperature variations, is investigated as a second approach;
- Both models are compared and the errors produced using the first approximation is thus evaluated.
- An experimental set-up is constructed and exploited at the French Alternative Energies and Atomic Energy Commission (Commissariat à l'Energie Atomique et aux Énergies

alternatives, CEA). In a near future, the experimental results would allow for a numerical validation of the developed model.

Thesis Outline

This thesis manuscript presents the different scientific approaches followed during the three years of thesis, describes the methods developed and highlights the main results obtained. After this introductory chapter, the manuscript is organized in four chapters.

- **Chapter 2** is a presentation of the state of art on different existing methods aiming to study the problematic raised before.
- **Chapter 3** is dedicated to the definition of the numerical tools used in this study.
- **Chapter 4** deals with the numerical results, considering both assumptions: rigid and deformable boundaries.
- **Chapter 5** introduces the experimental approach leading to the use of a thermocline prototype in order to investigate its structural response over thermal cycles. The set up was at the CEA, Grenoble.

Finally, a general conclusion summarizes the main outcomes of this thesis and provides recommendations for future research works.

Chapter 2

State of the art

This Chapter presents elements from the literature concerning the mechanical response of thermal energy storage systems (or similar systems). It is divided into four main sections. The first section gives an overview of the two-media thermocline thermal energy storage, its operating principle and the encountered mechanical problems. The second section is dedicated to the literature review of the thermo-mechanical behavior of granular materials inside a thermal energy packed-bed storage tank. Both experimental and numerical works that address the thermal ratcheting phenomenon are presented in this section. In the third section, results on the behavior of other systems involving cyclic swelling/shrinking of a granular material in a confined tank are presented. The last section discusses some potential solutions in order to reduce the impact of thermal cycles on the tank wall.

2.1 Overview on thermal energy storage systems

2.1.1 General introduction

Variable renewable energy sources, like wind and solar power, are expected to play a central role in the coming years, especially with confronted climate change problems and natural fuel oils depletion. Thermal energy storage or buffer are critical components of intermittent power plants (Akinyele and Rayudu (2014); Hohmeyer and Bohm (2015); Pudjianto et al. (2014); Esence et al. (2017b)). They can mitigate the variability and intermittency of solar radiation, for example, and provide a continuous operation by avoiding frequent start up and shut down of electrical devices used to convert heat into electricity (i.e. mainly Rankine cycle or Organic rankine cycle), and dispatching production according to demand. This is therefore a way to reduce the levelized cost of energy (LCOE), thus leading to more competitive costs for

renewable energy (Xu et al. (2012)).

Concentrated solar power (CSP) systems generate solar power by concentrating the sunlight (or the solar thermal energy) onto a small area using mirrors and lenses. The concentrated light, converted to heat, is used to generate electricity, via either a heat engine (usually a steam turbine) connected to an electrical power generator (Boerema et al. (2013); Law et al. (2014, 2016)) or a thermochemical reaction (Power; Wald (2013)). CSP is being spread worldwide, with a grown capacity from 354 MW in 2005 to 4,815 MW in 2016. As of 2017, Spain is the world leader in CSP (with a total capacity of 2,300 MW). The United States comes second with a capacity of 1,740 MW.Nevertheless, the CSP do not represent more than 2% of the nowadays installed capacity of solar electricity plants in the world (referring to Wikipedia), where the concentrator photovoltaic (CPV) solar energy plants dominate due to falling prices and low operating costs.

The integration of heat storage systems in CSP plants allows not only for a continuous power generation after sunset or during cloudy days, but also it adds more value to such systems comparing to CPV. The stored heat is converted into electricity which is a key advantage for CSP compared to photovoltaic power plants where electricity is directly generated. The electric storage systems remain quite expensive and less efficient solutions compared to TES systems (Philibert (2011); Sabihuddin et al. (2014)). Hence, thermal energy storage (TES) are currently integrated in about the half of concentrated solar power (CSP) plants throughout the world (Tian and Zhao (2013)) and its spread is expected to grow in the next future (Philibert et al. (2014)).

Three different types of thermal storage systems are mainly identified: sensible-heat storage (based on the temperature elevation of a given material), latent-heat storage (where energy of phase change is used), and thermochemical heat storage (where energy of chemical reversible reaction is considered) (Gil et al. (2010)). Of these, only the sensible-heat systems are so far commercialized since they present the least technical and development risks. Although promising in terms of efficiency, both latent-heat and thermochemical storage still require considerable additional development efforts before their commercial implementation in CSP plants. Latent heat storage systems are still at the prototype stage at the industrial scale (Xu et al. (2015)), while thermochemical storage concept is still needed to be considerably tested at the laboratory scale (Pardo et al. (2014)).

The most widespread sensible TES technology is the two-tank molten salt storage device where the molten nitrate salts are used as storage medium since they offer high volumetric heat capacity and high operating temperature (see Figure 2.1). During loading phases, cold molten salt is heated in solar receptors and then transferred to hot tank. During the unloading phases, the process is inverted and the heat is recovered and ready to be used for thermal or electrical needs. The separation of cold and hot fluids in two different tanks facilitates

the handle of this technology (Gil et al. (2010)). However a huge amount of the high-cost nitrate salts is required making this solution relatively expensive to afford. Moreover, the world's capacity production of natural nitrate is limited and won't be able to supply a soaring demand (García-Olivares et al. (2012)). A cheaper alternative for sensible TES is single-tank packed-bed storage which consists in using an inexpensive solid filler material as heat storage medium and a heat transfer fluid (HTF) in direct contact with the solids (Brosseau et al. (2005); Libby (2010)). Only the concept of the single-tank packed bed heat storage will be developed in the current state-of the art.

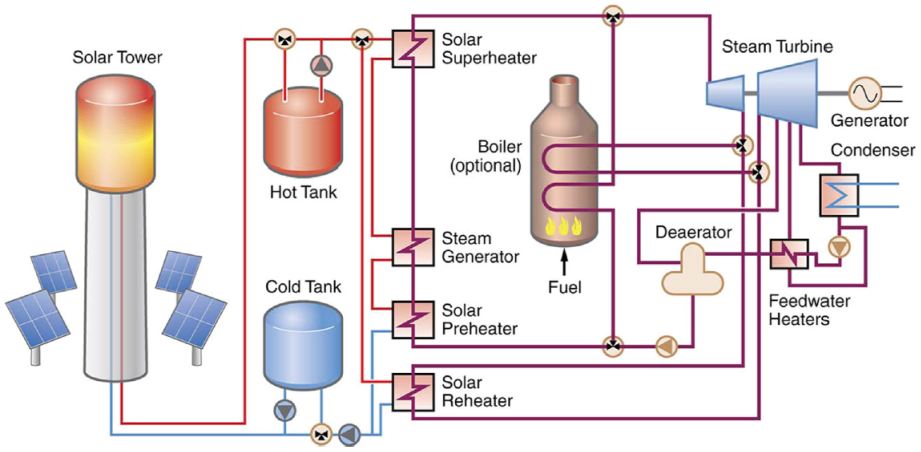

FIGURE 2.1: Schematic diagram of a CSP tower power plant with integrated two tanks molten salt TES system, from Libby (2010)

2.1.2 Single-tank packed bed heat storage system

2.1.2.1 Operating principle and efficiency

In a packed-bed storage facility, an example of which is depicted in Figure 2.2, the hot and cold heat transfer fluid circulate in a single tank and are separated, by the principle of the buoyancy stratification, by a transition zone with a thermal gradient called "thermocline". Thereafter, this kind of storage facility is called by the name of its transition zone as "thermocline storage tank". The use of an inexpensive solid filler material, such as sand and gravel, compensates for the higher-cost of the HTF and the capital cost can be reduced by 33 % for an equivalent amount of storage using traditional two-tank storage approach (Kolb et al. (2011); Pacheco et al. (2002); Libby et al. (2010)). Gravel materials can be considered as suitable primary thermal storage materials since they offer a large heat transfer surface area, thus a high heat transfer rate. Using packed-bed storage instead of two-tank storage thus enables to reduce LCOE of CSP plants (Cocco and Serra (2015)). Besides, the choice of the fluid is more flexible

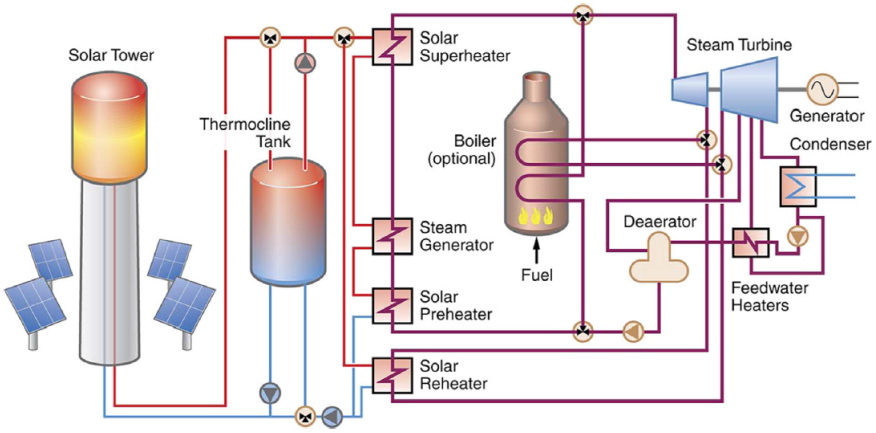

FIGURE 2.2: Schematic diagram of a CSP tower power plant with integrated a dual-media thermocline TES system, from Libby (2010)

and it is therefore possible to use a greater diversity of fluids, either liquid or gaseous. For the sake of limiting the thermal losses with the outside environment, almost all packed-bed storage applications are insulated.

For high exergy and process efficiency levels, and as it is depicted in Figure 2.3, a good stratification between hot and cold regions has to be ensured by a thin thermocline with steep thermal gradient (Haller et al. (2009); Qin et al. (2012)). In order to preserve a good

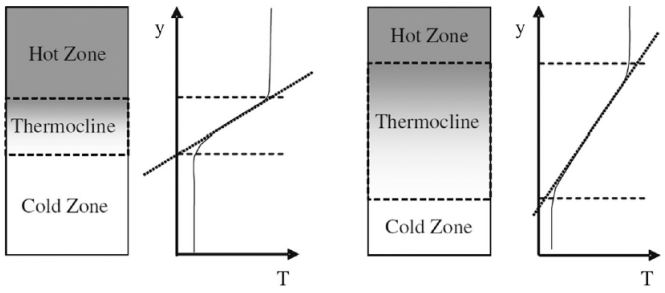

FIGURE 2.3: Different degrees of stratification with the same amount of stored heat; left, highly stratified and right, moderately stratified (Haller et al. (2009))

thermal stratification, the hot fluid is injected through the top of the tank while the cold fluid is extracted from bottom during the heating process, and then during the discharge cycle, the hot fluid is drawn off the top of the tank and the cold fluid is returned to the tank from the bottom (Close (1965)). The piston flow remain the ideal way of injecting the HTF and assuring a good stratification in the tank with an uniform distribution of fluid (Hollands and Sullivan (1984)). Limiting the fluid velocity to some extent prevents the mixing of the thermocline as well (Esence et al. (2017b)). Typical results of numerically or experimentally obtained temperature during the charging and discharging processes, inside STONE set-up, a 2.4 m^3 packed-bed of rocks and sand, are presented in Figure 2.4. The evolution of the

temperature along its 3m-height, at different stages of the charge/discharge stages are plotted in this figure. The thermal oil is used as HTF in this facility and the fluid velocity is set to 1mm/s.

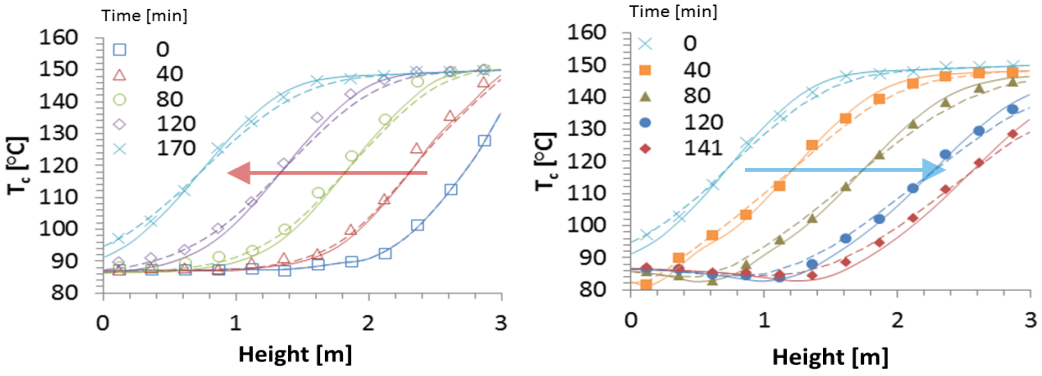

(a) (b)

FIGURE 2.4: Evolution of temperature profiles of STONE (a 2.4-m^3 packed bed of rocks and sand with thermal oil as HTF): (a) During charge; (b) During discharge. The "dot" results correspond to measured data, while the dashed or continuous lines refer to numerical results obtained using different model assumptions, from Esence (2017)

During the charging process, the thermocline moves downward inside the storage. As long as thermocline remains inside the tank, the outlet temperature is constant, then it gradually increases at the end of the charging process, when the thermocline reaches the bottom of the tank. An inverted behavior is shown during the discharge process. During typical operation and for commercial interests, the thermocline has to remain inside the tank so that the outlet temperature remains constant. Otherwise, the efficiency of thermal processes and heat production would decrease with varied outlet temperatures. In contrast, leaving all the thermocline zone inside the tank and under cyclic operational conditions, results in diffusing the thermocline and then occupying the whole tank's volume after several cycles (Bayón et al., 2013), without forgetting that the non-extracted thermocline is thermally unexploited and reduces the storage capacity. Thus, a compromise should be considered when dealing with the extraction or not of the thermocline zone. At long term operations, the behavior of the packed-bed storage ends up by stabilizing with constant performances. The operational conditions, i.e. the extraction of the thermocline zone at the end of the cycles, influences the stabilization process, thus the long-term performances of a thermocline storage tank. Figure 2.5 shows the steady-state reached with two different levels of thermocline extraction, represented by ΔT_1^* and ΔT_2^*. The plotted results are normalized: the dimensionless temperature T^* is calculated through $T^* = \frac{T - T_{ref}}{T_{max} - T_{ref}}$ and the dimensionless height z^* represents $z^* = \frac{z}{H}$. The more the extraction of the thermocline is assured, the faster the steady-state is reached and the greater is the effective storage capacity (represented by the grayed area). Similar results are obtained in (Zanganeh et al. (2012); Cascetta et al. (2015)).

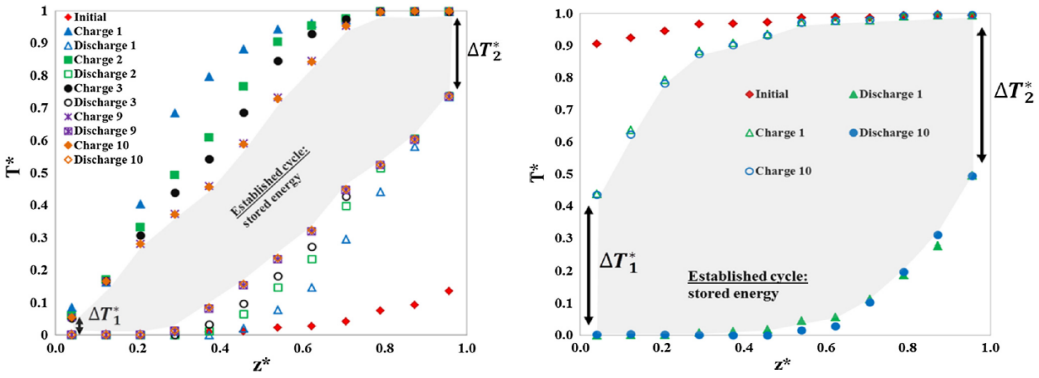

(a) (b)

FIGURE 2.5: End-cycle dimensionless temperature profiles at the long-term configuration: (a) With little extraction of the thermocline region at the end of each charge and discharge, (b) With large extraction of the thermocline region at the end of each charge and discharge (Bruch et al. (2014))

Moreover, the packed-bed storage systems provide high thermal energy efficiency levels (the ratio of the energy recovered above an arbitrary fixed temperature level to the previous stored energy). Bruch et al. (Bruch et al. (2017)) obtained energy efficiencies between 88% and 92% on the experimental oil-rock packed-bed STONE set-up. Zavattoni et al. (Zavattoni et al. (2014)) showed numerically that the energy efficiency of an industrial-scale air-rock packed-bed storage reaches 92%. Similar numerical and experimental values had been obtained by several authors as in (Xu et al. (2012); Libby (2010); Faas (1986); Yang and Garimella (2010); Van Lew et al. (2011)).

2.1.2.2 Tank design: thermal ratcheting phenomenon

Despite the well-understanding and the large documentation of thermal and hydraulic behavior of packed-bed storage tank, its mechanical behavior is still a problematic that limits its spread at large industrial scale. In particular, it is feared that the tank could suffer from premature damage, if not from catastrophic collapse, due to a thermal ratcheting phenomenon. The ratcheting phenomenon is commonly encountered in granular materials and consists in a tiny but irreversible phenomenon which accumulates over cycles until it eventually becomes significant. Thermally-induced ratcheting phenomena (thermal ratcheting in short) have to be carefully taken into account in the design of thermocline storage tanks since they need to live through a very large number of thermal cycles in their lifetime. However, the exact mechanisms and consequences of thermal ratcheting are not yet really understood. It is usually explained as follows, although this scenario is not yet proven. Besides the hydrostatic pressures of the solid filler and the HTF, thermal stresses may accumulate from one cycle to another due to differential thermal dilatation between filler and tank wall, leading to plastic

deformations in the tank shell which could accumulate over cycles until failure.
When rocks and steel are used as the storage medium and tank material respectively, and since the steel usually has a higher thermal expansion coefficient (TEC) than rocks and gravels, the tank wall expands more than the solid medium during the charging process, allowing the settlement of the filler material. During the discharge stage, the tank contracts against the bed, resulting in thermal stresses. This case is reproduced in Figure 2.6. Conversely, when the

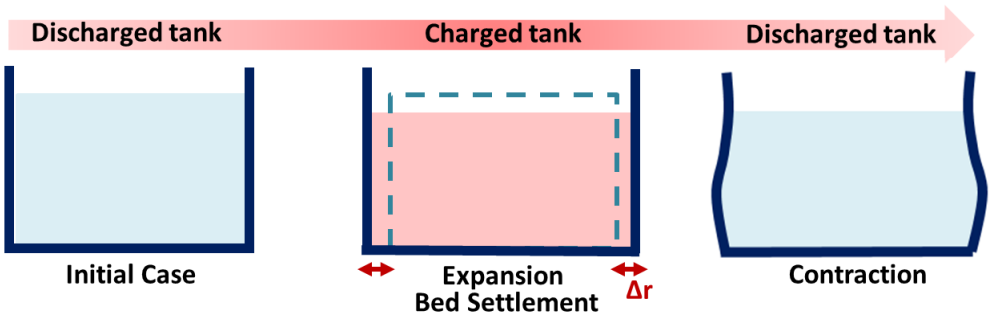

FIGURE 2.6: Illustration of the thermal ratcheting phenomenon when the tank expands more than the filler material

solid filler has a higher thermal expansion coefficient with respect to the tank wall, the bed expands more than the tank wall during the charging process resulting in thermally-induced stresses. Then, upon cooling, the bed shrinks more than the walls allowing the slump of grains, and so on. This phenomenon is repeated over many and many cycles, the particulate medium inside the tank reorganizes with time leading to its densification. It is feared that in such a process, ratcheting would result in a progressive increase of the thermal stresses over the cycles, eventually leading to damage or plastic strain within the tank wall, ultimately leading to failure of the tank.
The thermal ratcheting phenomenon occurs not only due to thermal cyclic conditions, but also due to any cyclic swelling and shrinking conditions (humidity or absorption/desorption reactions...) applied to a particulate medium stored in a container. It could be a real threatening problem:

- The 24 m-diameter bolted steel silo, shown in Figure 2.7, collapsed in 1996 in southwestern United States, after about two weeks of its first filling to capacity. Around 10000 tons of fly ash were ejected in the accident. The accident occurred at night when the silo was neither filled or discharged. The investigation assumed that the silo was under designed to account for the thermal ratcheting phenomenon, driven from the diurnal temperature variations (Carson (2001)).

- A silo of 7.3 m of diameter, storing 700 tons of wet grains mixture (corn, spent brewer's grains and other ingredients), collapsed during a standby holiday period (several days

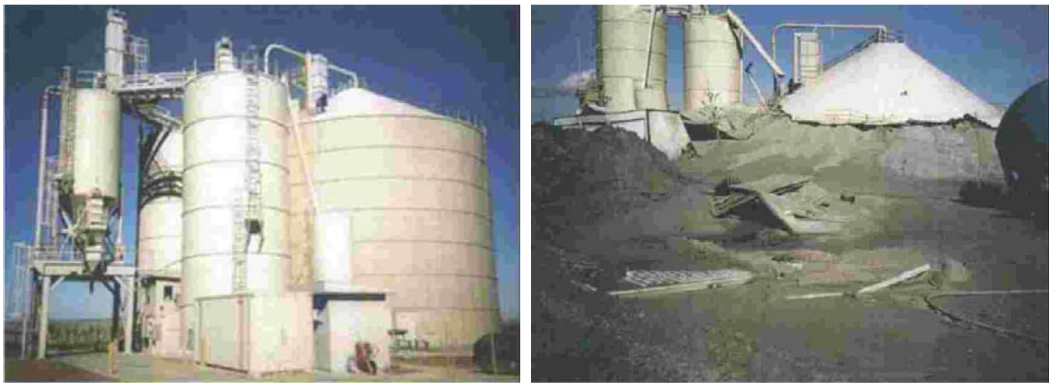

(a) (b)

FIGURE 2.7: Silo failure due to thermal ratcheting: (a) Before failure; (b) After collapse (Carson (2001))

without any discharge). The main potential reason behind this failure is the thermal ratcheting phenomenon caused by the swelling of corn grains with increasing moisture contents. Higher pressures are thus induced on the silo wall causing its fracture (Carson (2001)).

The thermal ratcheting phenomenon strongly influences the tank design, and one of the main researchers' interests is to limit its impact on the packed-bed tank wall.

Thereafter, it is believed that the slenderness ratio (the height-to-diameter ratio) of the tank has a great influence on the resulted applied thermal stresses. Numerical simulations recommend a low value of slenderness ratio to reduce wall stresses (B. Charlas; Charlas et al. (2015)). This idea is evoked later in details in Section 2.3.2.

Practically and at industrial scale, the maximum height of packed-bed thermal storage tanks should not exceed 16 m for mechanical reasons (Libby (2010); Pacheco et al. (2002)). As well, low values of slenderness ratio reduce the heat losses allowing a slow circulation of the fluid inside the tank (Mertens et al. (2014)). Nevertheless, a low slenderness ratio value can spoil the thermal performance of the packed-bed thermocline tank; a large slenderness ratio improves thermal stratification and efficiency of the system (Pacheco et al. (2002); Cascetta et al. (2015); Mertens et al. (2014)). It also reduces the flow heterogeneities with a larger volume of filled packed-bed (Szekely and Poveromo (1975)). In the end, a trade-off between mechanical, flow distribution, pressure drop, thermal loss and stratification issues have to be considered when dimensioning a thermal energy packed-bed storage tank.

In this manuscript, a numerical and an experimental approaches were developed to study the evolution of wall stresses in a storage tank with the idea of bringing evidence and further understanding of the thermal ratcheting phenomenon. But before, a glimpse of the most

relevant existent thermocline storage tanks in the world, at the laboratory or industrial scale, is briefly presented in the next Section 2.1.2.3.

2.1.2.3 Packed-bed storage installations at the industrial/laboratory scale

Some of the most relevant packed-bed storage installations with liquid or gaseous HTF are listed in Table 2.1. In addition to this, Figure 2.8 recapitulates the dimensions of most of liquid-solid or gaz-solid packed-bed facilities found in the literature, showing their height-to-diameter ratio.
As shown in Table 2.1, most of packed-bed storage facilities have a cylindrical shape with the aim of reducing mechanical problems (Melanson and Dixon (1985)) and assuring an uniform fluid flow by avoiding corner effects. Other potential shapes are rectangular or truncated conical (with largest cross section at the top).

Not all of the listed packed-bed storage installations were "mechanically" exploited to study the thermal ratcheting phenomenon. Only the mechanically studied installations are the subject of the following Section 2.2.

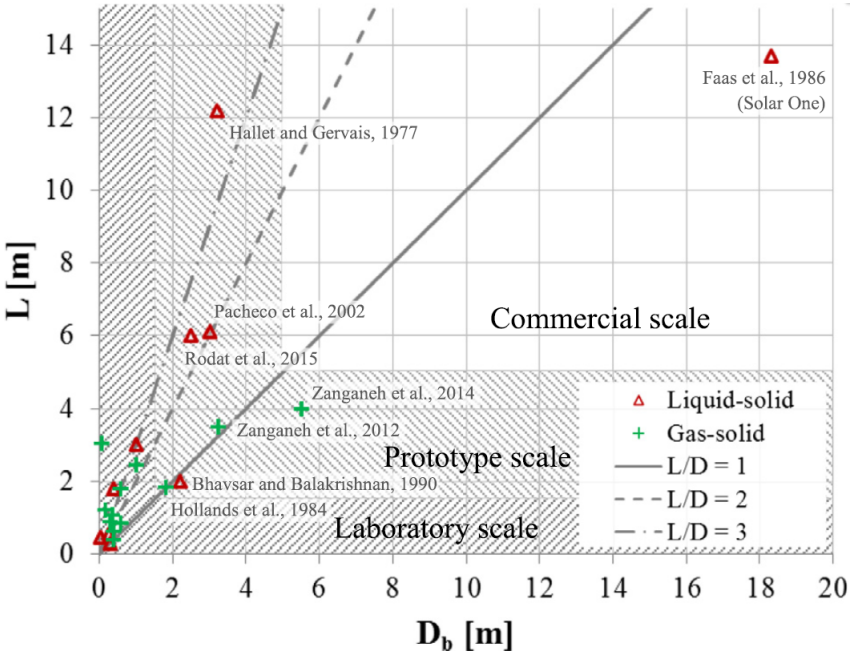

FIGURE 2.8: Dimensions of most packed-bed storage systems existent in the literature (Essence et al. (2017b))

TABLE 2.1: Main characteristics of some packed-bed storage applications from the literature

Publications	Shape	Solid	HTF	Dimensions	Slenderness ratio	Particles diameter (mm)	Temperature	Country
Hallet Jr and Gervais (1977)	Cylindrical	River gravels (granite) and silica sand	Caloria HT 43 (oil)	Hb=12.2 m; D=3.2 m	3.81	25/1.5	218-302	United States
Faas (1983a)	Cylindrical	Rocks and sand	Caloria HT 43 (oil)	Hb=14 m; D=18.3 m	0.765	25/-	204-304	United States
Pacheco et al. (2002)	Cylindrical	Quartzite rocks and silica sand	Hitec XL	Hb=6.1 m; D=3 m	2.033	19/-	290-390	
Rodat et al. (2015)	Cylindrical	Silica gravels and silica sand	Therminol 66 (oil)	Hb=6 m; D=2.5 m	2.4	30/3	100-250	
Bruch et al. (2014)	Cylindrical	Silica gravels and silica sand	Therminol 66 (oil)	Hb=3 m; D=1 m	3	30/3	50-250	France
Zanganeh et al. (2012)	Truncated conical	Sedimentary rocks	Air	Hb=2.9 m; Dbot=2.5m; Dtop=4 m	0.725-1.16	20–30	280–640	Morocco
Cascetta et al. (2015)	Cylindrical	Sintered alumina beads	Air	Hb=1.8 m; D=0.58 m	3.24	7-9	38-239	
Zanganeh et al. (2014)	Truncated conical	Rocks	Air	Hb=4 m; Dbot=5 m; Dtop=6 m	0.66-0.8	-	200-650	
Dreißigacker et al. (2013)	Rectangular	Spherical ceramical beads	Air	Hb=1.7 m; area=0.6 x 0.8 m2	2.125-2.833	17	20-550	Germany

2.2 Numerical and experimental analysis of thermal ratcheting phenomenon in thermocline storage tanks

2.2.1 Installation of Solar One (1986)

Solar One was a concentrated solar power plant of 10 MW_e using steam as a heat transfer fluid in the solar field and possessed a oil/solid filler storage tank of 182 MWh_t (Hallet Jr and Gervais (1977); Faas (1983a)). The storage installation was mainly intended for validation of its design and experiments. However it was only functional from 1982 till 1986 when a steam explosion occurred and put the system out of service.

The cylindrical steel tank (ASTM A533 Class 2 grade A) is filled with a compacted bed of rock and sand impregnated with thermal oil (Caloria HT43, $\rho = 692.4 Kg/m^3$). The granulometry of the mixture is not specified. The tank is bedded on a 25 mm-thick layer of sand over 0.61 m of insulating concrete and 1.52 m of structural concrete (see Figure 2.9a). It is thermally insulated from its environment with a 0.229 m thickness glass wool. The thickness of the wall tank varies from 0.0079 m at the top to 0.0286 m at the base. Figure 2.9b is a cutaway view of the thermal storage unit.

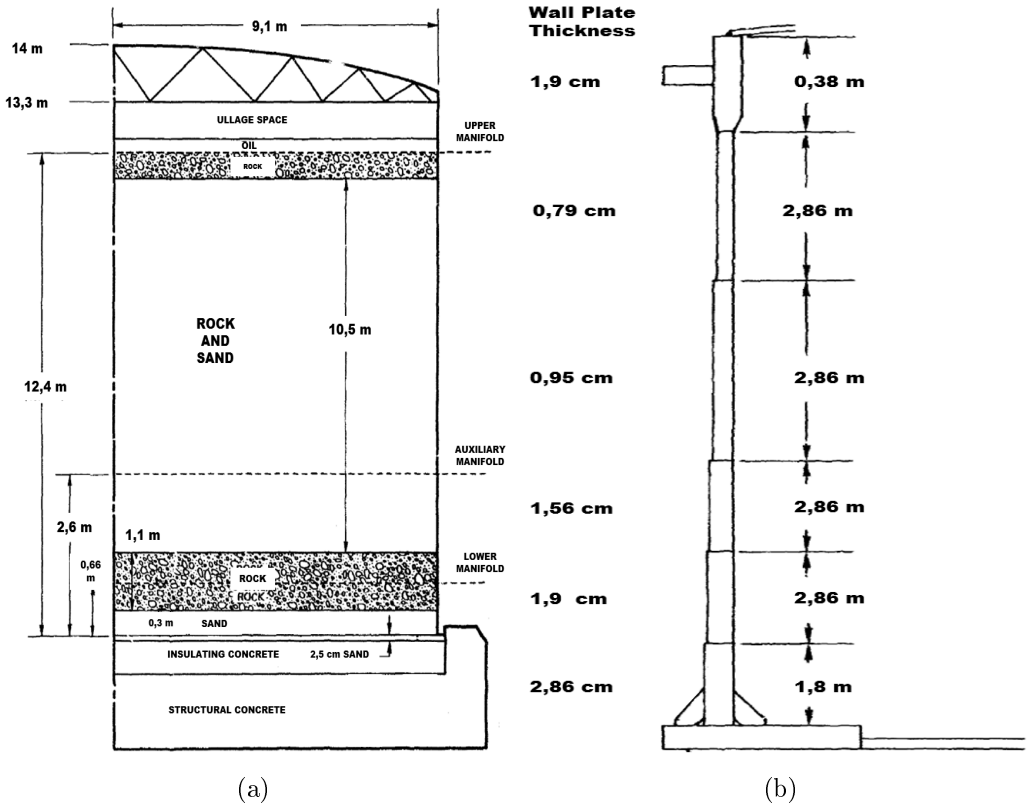

FIGURE 2.9: Thermal storage unit of Solar One: (a) Construction details, (b) Tank cross-section (Faas (1983b))

The ullage above the oil and the granular material is slightly pressurized with nitrogen gas to prevent oxygen infiltration, and thus to prevent any oil oxidation. The tank's dimensions as well as the characteristic parameters of the thermal cycling tests are presented in the Table 2.2.

TABLE 2.2: Characteristic parameters of a thermal cycle of the thermocline of Solar One

Tank's dimensions	**Solid filler**	**Heat transfer fluid**	**Cycle temperatures**	**Cycle duration**
D_{in}= 18.2 m H=14 m H/D =0.77	Mix of gravel and sand (n=0.22)	Oil: Caloria HT43 (908 m^3)	T_{ch}=304°C T_{dich}=204°C	1 day

The thermocline of Solar One was investigated to obtain some experimental data on the induced thermal stresses in the tank shell. Horizontal and vertical stresses were determined experimentally by placing 30 cm-uniformly spaced strain gauges along the height of the tank at different azimuth angles. Table 2.3 shows the recorded hoop and vertical stresses at three different times: just before the charging of the tank (April 1982), after executing a certain number of cycles (December 1982) and finally after two years of service (June 1984).
The authors confirmed that the experimental data suffer of large uncertainty when analyzing the strain gauge measurements errors. These data cannot be referred as a good indication of the actual stresses in the tank wall and cannot predict any trends of the stress evolution over time. The thermal ratcheting effects cannot be evaluated on the basis of the analysis of these measurements.
Although these experimental data suffer from large uncertainty, they were the input data of many other studies in order to validate their numerical models.

Flueckieger et al. and Gonzalez et. al modeled the thermocline of Solar One based on the finite-element method (Flueckiger et al. (2011); González et al. (2015)). They studied the transient evolution of thermocline tank wall stresses, taking into account both thermal and mechanical loads for validation purposes and getting better understanding of the stress-strain response of the structure. For problem simplifications, the steel tank wall is considered as cylindrical with a circumferential symmetry and have a constant thickness of 0.02 m.
Two extreme filler reactions are considered, knowing that a realistic behavior for the filler material lies in between. The first case considers the filler material as a flexible filler ($\alpha_{filler} = \alpha_{steel}$), which means that the filler behaves like a fluid inside the tank. The tank is allowed to shrink and expand freely except for the stress originating from the hydrostatic pressure of the fluid, the nitrogen gas in the ullage space and the weight of the filler itself. No additional thermal stresses should be generated in the tank wall. Friction between the filler material and wall is neglected. The second case assumes that the filler has a $\alpha_{filler} = 0$ and does not allow for the contraction of the tank upon cooling process due to the gravity and its internal friction. Its own weight will not have any influence on the induced loads in the tank. This

TABLE 2.3: Measured hoop stresses on Solar One thermocline (Faas (1983b)); numbers with * are not used in forming the average

Elevation (m)	**Azimuth angle (◦)**	**April 1982**	**December 1982**	**June 1984**
0.3084	45	-83	-41	41
0.3084	193	-48	7	NA
0.3084	347	-41	14	280
Average		**-55**	**-7**	**120**
0.6096	45	21	-7	200
0.6096	193	0	21	180
0.6096	347	7	55	170
Average		**7**	**21**	**170**
0.9144	45	41	69	1900*
0.9144	193	21	100	170
0.9144	347	48	76	200
Average		**34**	**83**	**190**
1.2192	193	41	28	150
1.2912	347	48	69	230
Average		**48**	**48**	**190**
1.524	193	130	62	NA
1.524	347	55	48	370
Average		**97**	**55**	**370**
5.486	193	28	62	28
5.486	347	62	120	120
Average		**48**	**97**	**76**
12.5	193	-14	34	7
12.5	347	-21	-120	-55
Average		**-18**	**-43**	**-24**
13.11	193	370	NA	NA
13.11	347	41	-28	-390
Average		**200**	**-28**	**-390**

case will be referred to the "rigid filler" case. Thermal loads are maximized since the larger potential thermal expansion differential, between both filler and tank mediums, is considered. Both filler reaction cases are considered in Gonzalez et al study, while Flueckieger's model considered only the rigid filler case.
A linear thermo-elastic solid model is applied for the steel walls of the tank. A linear model is considered because the tank is subjected to small strains and it is elastic since it is enough to predict if the yield strength is reached or not.

The resulting hoop stresses obtained by Flueckiger et al. and Gonzalez et al. (for both flexible and rigid filler material cases) are plotted in Figure 2.10 and are compared to the recorded hoop stresses measured by Solar One. The results obtained by Gonzalez et al. in both extreme cases (green curves referring to the fluid-like case and red curves referring to the rigid filler case) present the evolution of hoop stresses during the discharge cycle.
As it was detailed earlier, and according to the original authors, the recorded data are not very reliable measurements: the error bar of the measurements at each position are huge, reducing the ability to rely on them. In addition to this, there is no information about the specific time of the charge or discharge cycle at which the data was recorded.
Moreover, the thermocline of Solar One was instrumented with strain gauges installed uniformly along the tank's height (each 30 cm). However, there are a lot of missing/not published data (between the height 1.524 m and the top of the tank), most probably due to their inaccurateness.
For a rigid filler, referring to the results of Flueckiger et al. and the end-of-discharge stresses obtained by Gonzales et al., the resulted hoop stresses are maximal and uniform at a middle zone of the tank's height. Thermal hoop stresses are generated due to shrinking restriction during the discharging cycle. These thermal loads are proportional to the differential temperature ΔT between charging and discharging. The constant value of hoop stress observed in this zone is owed to a constant $\Delta T = 100°C$. These thermal loads are added to the hydrostatic pressure of the fluid.
Although the global qualitative shape agreement of the results obtained by both studies for a rigid filler material, a significant difference coming from using different values of the Young's modulus, is seen. A lower value of Young's modulus (140 GPa) is used by Flueckiger et al. (versus a value of 186 GPa used in Gonzalez et al. study) leads to a lower range of stresses, knowing that value of 140 GPa is relatively low for a steel. Moreover, the differences in the shell temperature profiles (probably affected by sensibly different CFD simulations) lead to the difference shown in the location of maximum stresses. In the results of Flueckiger et al., the location of maximum hoop stresses is shifted toward the bottom of the tank when compared to Gonzalez et al.'s results.
For a flexible filler material configuration, hoop stresses increase linearly from top to bottom of the tank height. They are proportional to the hydrostatic pressure of both fluid and filler bed.

Comparing the results with the reading taken from Solar One strain gauges, it is noticeable that the linear decrease of stresses in the flexible case does not agree with the measured data variability along the tank height especially in the zone extended between 0.6 and 1.2 m where the hoop stresses tend to increase along the height. Therefore, the filler material behavior is likely closer to a rigid nature than to a flexible one.
Comparing the results with the yield strength of the tank shell (414 MPa), the measured and calculated hoop stresses are lower than the yield strength except for the recorded data on June 1984 at 1.524 m of the tank's height. Finally, all the numerical results show that the tank wall does not exhibit any residual plastic deformation at the end of the discharge cycle (the resulting stresses remain lower that the steel yield strength), allowing the full recovery of the tank deformations. Thereafter, the hoop stresses will not increase with further thermal cycles, eliminating the potential occurrence of the thermal ratcheting effects.

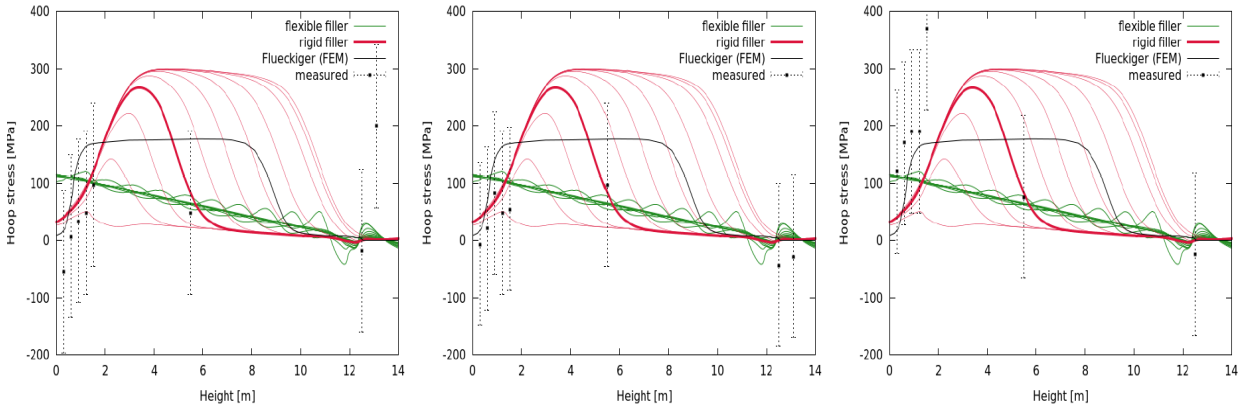

FIGURE 2.10: Hoop stresses on Solar One thermocline tank. Transient simulation results by Gonzalez et al. (green stands for flexible filler, red stands for rigid filler), simulation results of Flueckiger et. al (rigid filler), and measured data. Experimental readings are figured at three different times, from left to right: April 1982, December 1982 and June 1984; from González et al. (2015)

Conclusion/Discussion: Unfortunately, and according to the original authors, there was significant uncertainty in the measurements of strain recorded on the thermocline storage tank of Solar One, even though they are the only existing experimental results on an industrial installation. Some recorded values of stresses were inconsistent with the problem physics which makes harder the validation of numerical results and the interpretation of the behavior of the thermocline under thermal cyclic operations. Moreover, the thermocline started malfunctioning after only a few cycles of operations due to a problem that is not related to any excessive plastic deformations in the tank shell, reducing the potential impact of thermal ratcheting on the tank.
The existent studies on the thermocline of Solar One consider extreme cases for bed's behavior. Nevertheless, an intermediate model for the filler material, that considers its own thermal expansion must be considered for future works. Based on Gonzalez et al. and Flueckiger et. al numerical FE approaches, and since the tank has not been plastified from the first thermal

cycle, it will always behave elastically over all the other cycles. The stress accumulation occurs only through the accumulation of residual strains in the tank wall, otherwise the behavior remains elastic regardless the number of performed cycles.
Understanding the thermo-mechanical behavior of a thermocline storage tank using the finite element method (FEM) might not be the best solution, especially when neglecting all physical natural responses of a granular material subjected to thermal cyclic operations, such as particle rearrangements and packing densification, as it is the case in the afore presented studies. The behavior of the granular medium inside the tank is complex and thus requires the integration of complex constitutive laws when using the FE methods in the aim at reproducing its physical natural responses. Otherwise, the accumulation of stresses and tank wall deformations over thermal cycles due to particles rearrangements, bed densification and thermal ratcheting effects will not be detected.
The recourse to the discrete element method may facilitate the understanding of the thermo-mechanical behavior of a granular medium inside a thermocline storage tank, since it reproduces naturally, and based on simple constitutive laws, the natural behavior of a particulate medium. However, high computational capabilities are required.

2.2.2 Experimental set up developed by Dreiβigacker et al.

A test rig was developed and erected by Dreiβigacker et al. (Dreißigacker et al. (2013, 2010); Knödler et al. (2016)) in order to study the behavior of thermocline tanks under thermal cyclic operations and validate a numerical model. The storage tank is a container operating at high temperature (up to 550°C) using air as a heat transfer fluid. The tank has a filling volume of 0.9 m^3 with a square cross-sectional area of 0.6 × 0.8 m^2. Spherical ceramic beads with an average diameter of 17 mm fill the tank up to a height of 1.7 m. The outer surface of the 5-mm-thick stainless steel tank wall is insulated as it can be seen in the Figure 2.11. Table 2.4 summarizes the dimensions of the container as well as the material properties of the packed bed.

TABLE 2.4: Tank dimensions and material properties of ceramic beads (Dreißigacker et al. (2013))

Tank dimension			**Solid filler material**		
Cross sectional area (m^2)	**Tank height (m)**	**Bed height (m)**	**Diameter (mm)**	**Density (Kg/m^3)**	**Coefficient of thermal expansion (K^{-1})**
0.6 × 0.8	1.87	1.7	17	2400	5 $\times 10^{-6}$

The device was cycled between 20 and 550°C as cold and hot temperatures respectively. Strain gauges are used to measure wall forces, but in order to handle such high temperatures, an additional cooling system was integrated into the measurement devices: ambient air is used to

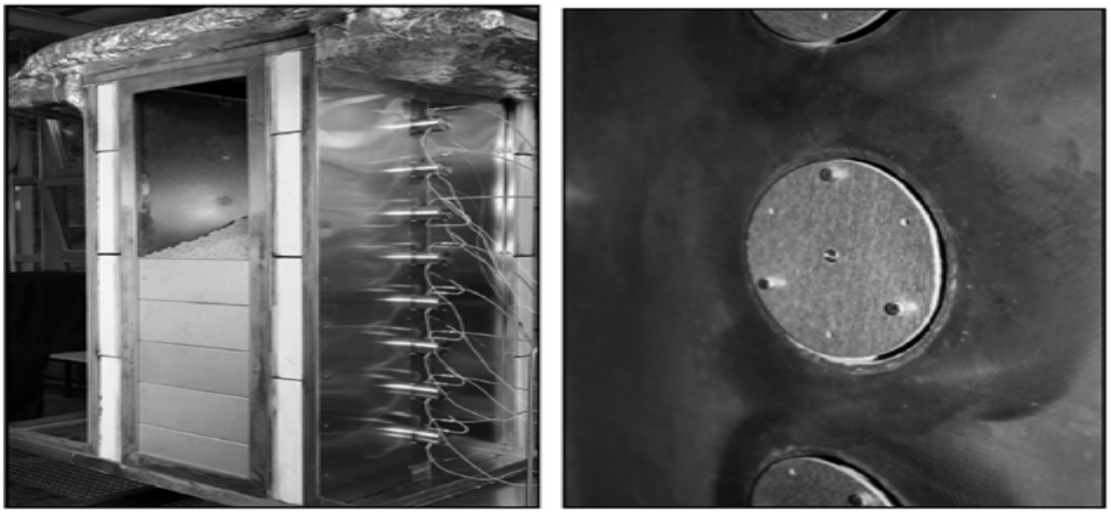

FIGURE 2.11: Thermal storage test device (left) and the interior view towards the flushed closing force measurement devices (right), from Dreißigacker et al. (2013)

keep the device at low temperatures. Six devices are attached at one of the containment walls at bed depths between 0.3 and 1.3 m (see Figure 2.11) and are able to detect the particle-wall contact forces. The acting forces on the measurement disc are transferred via the rod to the strain gauge sensor. Bearings are used so that the measurement of axial loads is not influenced by any component of torque. The developed design is shown in Figure 2.12a. Apart from the force measurement devices, 25 thermocouples were placed inside the packed bed at different locations to measure the temperature variations in time and space.
The tank is experimentally exploited under ambient and cyclic conditions. At ambient conditions, the tank is filled and emptied for three sequenced cycles to estimate the influence of the stochastic nature of the generation process. At the end of each filling cycle, the particle-wall contact force is recorded. Then a sequence of seven cycles and 2 still stand periods (where the tank is maintained at cold temperature) are realized. For these tests, the bed is heated from the top with a temperature of 550°C and cooled from the bottom with an inlet temperature of 20°C. A maximum outlet temperature at the bottom of 270°C during the charging process is allowed.
The packed bed inside the thermocline is modeled using the discrete element method (DEM). Further details about DEM concept, the method chosen for our modeling, are provided in Chapter 2- The Numerical Modeling.

The mechanical model is coupled to the thermal expansion of particles by growing/shrinking the particles radii proportionally to the imposed differential temperature.
Thermo-cyclic tests are conducted and thermal loads are induced in the tank wall. Figure 2.12b shows the average of the three simulations force values as well as the temperature variation for a packed bed depth of 0.3 m. Both experimental and numerical results show that the forces are increased during the charging process due to the thermal expansion of

particles, while they are decreased during the discharge. This result is somehow contradicting with expected results: the stainless tank wall should have a higher TEC than ceramic beads, leading to a higher expansion of the walls with respect to the beads during the charge, reducing the resulted stresses on the walls when heating. These stresses should be increased upon the discharge cycle during the shrinking of the walls, prevented by the settled beads. This idea was not evoked or justified by the original authors.
Referring to 2.12b, with increasing number of cycles, the results tend to be similar due to the bed densification. The experimental and numerical results show a satisfying agreement and the differences between them might be referred, up to the authors opinions, to different initial bed arrangements of particles. The reason of the brutal drops of the forces even before the beginning of the discharge process is unexplained.

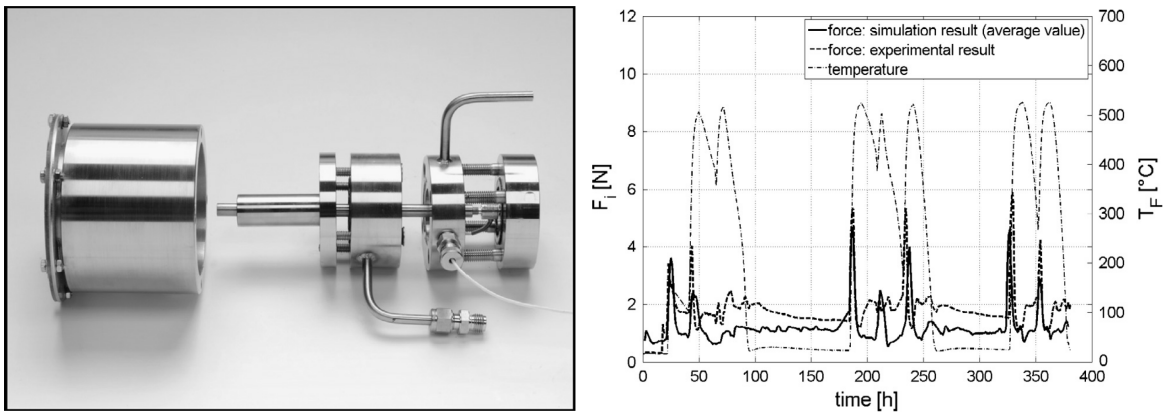

(a) (b)

FIGURE 2.12: (a) Force measurement device developed by Dreiβigacker et al., (b) Simulated and measured particle-wall contact force and temperature evolution at a packed bed depth of 0.3 m, from Dreißigacker et al. (2013)

The authors marked that the particle-wall contact force is increased by a factor of 5 at a bed depth of 1.3 m due to thermal effects compared to the force value obtained at rest.
It is important to mention that the three simulation runs have a relatively high standard deviation of 0.35 relating to the average values and a higher number of simulations and experimental test is required to reduce the effects of the stochastic character of such randomly arranged particulate mediums.

Knödler et al. (Knödler et al. (2016)) studied the same experimental set up but this time, the DEM model is only used to get the effective mechanical parameters of the packing and then implement these parameters in a simplified FEM model.
A discrete element model is able to better reproduce the natural behavior of such particulate mediums comparing to continuum model, but it requires a high computing time. To save time, the finite element method, where a macroscopic perception of the packed bed is considered, can be used but the accuracy of such continuum models highly depends on the mechanical parameters used to describe the medium.

Based on this, an effective Young modulus, dependent from the temperature and subjected stress is used in the FE simulations realized by Knödler et al. Three methods are investigated to calculate the effective Young's modulus at 20 and 600°C: analytically using the Reimann's equation (Reimann et al. (2000)), by conducting uniaxial compression test (UCT) or by reproducing this test using a DEM model. All methods give satisfying agreements.
The effective Young's modulus E_{eff} is about two orders of magnitude smaller than the Young's modulus of the bulk material (at 20°C, $E_{ceramic}$=71.9 GPa), which agrees with the results shown in Ying (Ying et al. (1998)). These obtained results of the effective Young's modulus are used to conduct numerical tests using the thermo-mechanical continuum model.
Experimental tests are performed using the same set up, where the packed bed is cycled between 20°C and 600°C and 10 repeated cycles are realized. After the completion of one measurement procedure, the tank is emptied and refilled again for another sequence of cycles. A total of three test runs are realized and the obtained results, are presented in Figure 2.13 (left side). Here, the maximal applied loads during charging/discharging processes are shown. In Figure 2.13 (right side), the evolution of the recorded forces on the container wall over 8 thermal cycles is presented at a bed height of 0.6 m. At this height, the bed temperature reaches 500°C. It can be seen that the continuum model is able to predict the forces acting on the tank wall.
Up to the authors opinion, in spite of the difference observed between the experimental data at 600°C, that are might be caused by the stochastic behavior of the medium, the numerical and experimental results show a satisfying agreement. For both experimental and simulated results, the loads acting on the containment walls are increasing with increasing bed depth. Comparing the results before and after heating, the contact forces are increased by about a factor of 5-6.
Figure 2.13 (right side) shows that the contact forces increase during the charging process due to the thermal expansion of particles and decrease during the discharging. With increasing number of cycles, the loads start to be similar, representing a higher densification of the medium and a reduction of the initial irregularities. The results are quantitatively similar to the obtained ones with the DEM model.

Conclusion/Discussion: The numerical models are able to somehow predict the induced loads during thermal cyclic operations since they were validated by recorded data. But it is important to note that these recorded data suffer from some inconsistencies such as the brutal relaxation observed in the tank wall even before the beginning of the unloading cycle. As well, the evolution of contact forces does not follow the evolution of temperature over the cycles, which remains unexplained. In addition to this, there is no published data that show the validation of the developed force sensors response based on any predictable or analytical behavior of a particulate filler, before conducting tests on the packed-bed storage unit. The increase of applied loads during the charging process and their decrease during the discharge phase is in contrast with the previously presented results in Section 2.2.1, where a higher TEC

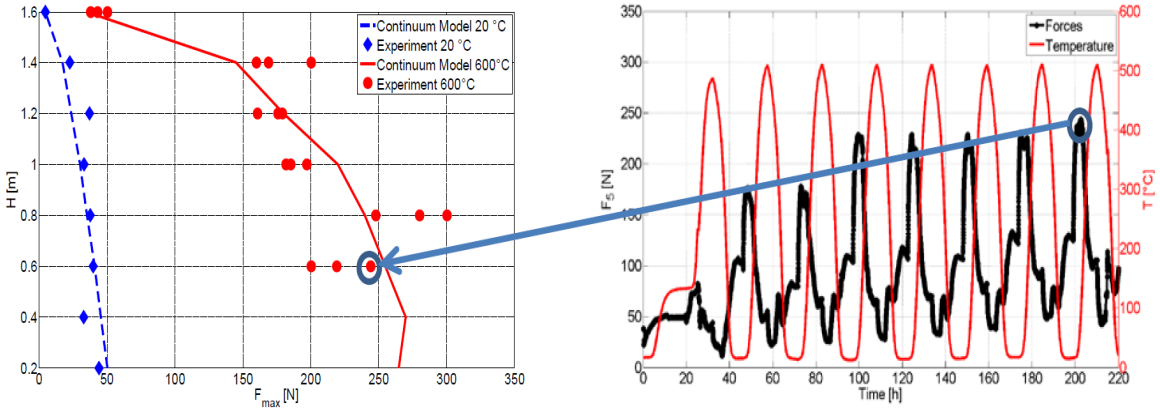

FIGURE 2.13: Maximal forces acting on the container wall (left); Force progression over multiple thermal cycles at 0.6 m bed height (right), from Knödler et al. (2016)

for the tank wall than for the bed is adopted. The difference might be related to different boundary conditions. A larger number of tests is needed as well to reduce the dispersion of the results, enabling a more significant comparison.
Eventually, a thermocline storage tank with a square-cross-section might not be the best geometry to study the thermo-mechanical behavior of the granular bed inside. This geometry might involve lots of perturbations caused by corners effects, such as high friction levels. Moreover, high stress concentration may be driven at the corners, leading to high deformation in the wall (Pilkey and Pilkey (2008)).

2.2.3 Thermo-mechanical study of an industrial thermocline proposed by Sandia National Laboratories

Sandia National Laboratories and the Electric Power Research Institute (EPRI) are interested in the development of larger thermoclines operating at higher temperature than the one developed in Solar One power plant. Hence, they conducted numerical simulations on the hypothetical thermocline in order to test in thermo-mechanical behavior upon thermal cycles (Kolb et al. (2011)). The advanced thermocline of current interest will store up to 3000 MWht and it is cycled between 300°C as cold temperature and 600°C as hot temperature. It has an inner diameter of 47 m and a height of 14.3 m. The tank is filled with gravels and sand and the molten salt is used as heat transfer fluid. The stainless steel walls have a variable thickness: max 8.9 cm at the bottom and min 2.2 cm at the top. Table 2.5 summarizes the dimensions and the characteristic parameters of the thermal cycle.
In addition to the daily heat up and cooldowns, the thermocline is subjected to periodic cooldowns where the tank is at uniform temperature over its height. These cooldowns are usually repeated once every three to five years. Since the molten salt crystallizes at 240°C, the standby temperature is assumed to be 290°C to maintain the HTF in its liquid state. Figure 2.14a illustrates the variation of the temperature over four days of heating and cooling

cycles. Colored curves correspond to the evolution of the temperature at 7 equally spaced tank elevations. By the third or fourth cycle, the temperature variation reaches the steady state. Radial gradient temperature is not assumed to exist neither in the tank nor in the bed.

TABLE 2.5: Characteristic parameters of a thermal cycle of the thermocline studied by Kolb et al. (Kolb et al. (2011))

Tank's dimensions	Solid filler	Heat transfer fluid	Cycle temperatures	Cycle duration
D_{in}= 47 m H=14.3 m H/D =0.312	Mix of quartzite gravel and silica sand	Molten salt	T_{ch}=600°C T_{dich}=300°C Standby temperature=290°C	1 day

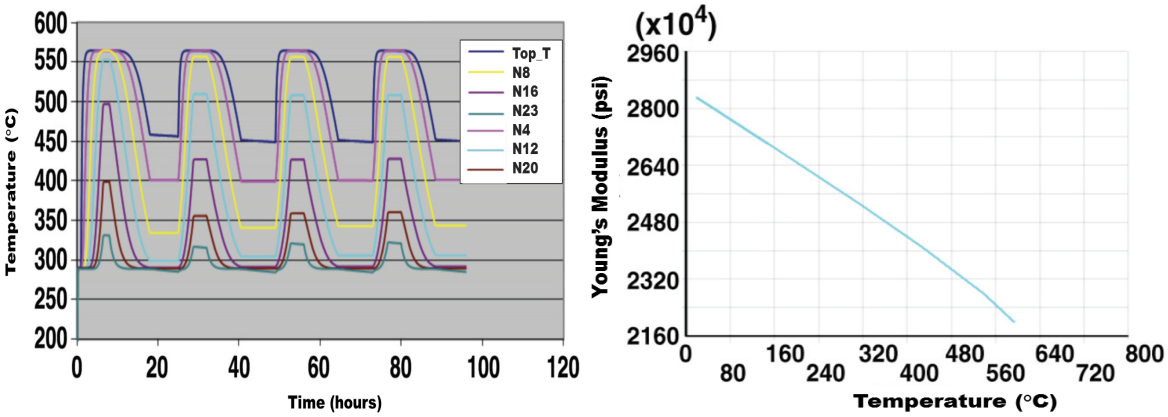

(a) (b)

FIGURE 2.14: (a) Operating temperature over four cycles at 7 equally spaced tank elevations, (b) Temperature-dependency of of SST 347 Young's Modulus, from (Kolb et al. (2011))

The thermocline is modeled using ANSYS. Elasto-plastic constitutive laws, Multilinear Kinematic Hardening (ANSYS designation KINH) and Durcker-Prager (DP) plasticity, are used respectively for the tank and the bed. The mechanical properties of the stainless steel of the tank wall are taken from Section II, Part D of the ASME Code (Boiler and Code (1998)). The temperature-dependency of its Young's modulus is given in Figure 2.14b.

The material properties of the bed and the tank are assumed to be isotropic, thus an axisymmetric approach is considered. The bed is discretized using solid continuum elements (ANSYS quadratic PLANE183). The bed's Poisson's ratio is fixed to 0.25, its cohesion is fixed to 5 psi (34 KPa).
Several cases are considered aiming at studying the influence of the variation of the mechanical properties of the bed, as the variation of its Young's modulus or its internal angle of friction, and the variation of its thermal expansion coefficient. Temperature-dependent values of the bed's Young's modulus and bed's TEC are considered.

High, medium and low values for the Young's modulus of the bed are considered, as it is depicted in Figure 2.15a. As well, the variation of the coefficient of thermal expansion (TEC) of the bed is given in Figure 2.15b: the TEC of the bed is either similar to that of the Sandstone (also Quartzite) or to TEC of the Granite. In the first case, the bed's temperature-dependent TEC is relatively close to the 347SS-steel, while more differences in the temperature-dependent TECs are observable between Granite and Steel. Moreover, two values for the internal friction angle 15° or 40° are considered.

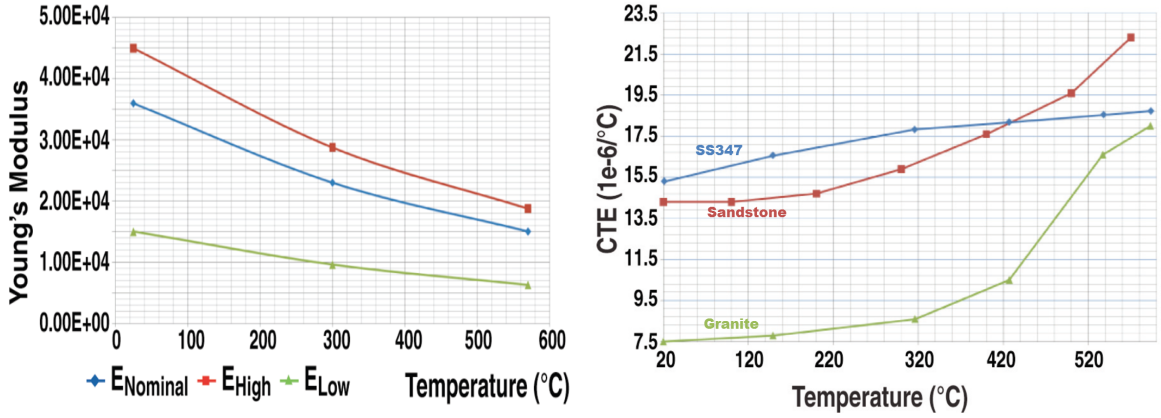

(a) (b)

FIGURE 2.15: (a) Bed Young's modulus values (psi) vs. Temperature (°C), (b) Mean TEC of granite rock (green), sandstone (blue) and 347 Stainless steel (red) as a function of temperature (°C), from (Kolb et al. (2011))

Only the results of two cases are detailed here. More results of the study can be found in (Kolb et al. (2011)). Figure 2.16a shows the equivalent plastic strain at six tank wall elevations for the case where a nominal value of the bed's Young's modulus and high values of TEC (equal to Sandstone) are used. In this case, 13 charging/discharging cycles are performed, followed by a cooldown period to 290°C before performing 10 additional thermal cycles. Note that the time label on abscissa of ANSYS plots refers to load step number, not physical time. The high values of strain are found at the wall-to-base transition knuckle (eppl_base) or next to the transition at the ring 1 (eppl_r1). Up to the authors opinions, these strains in the transitional zones can be ignored since they are derived from design problems. A redesign of the knuckle and/or an introduction of a stiffening gusset between the base and the tank wall can reduce the obtained high plastic strains. Only the strains far from the transition zone are then evaluated.

Lower values of plastic strains are obtained in the areas away from the transition- i.e. at the end, the accumulated strain is below 0.25%, which is acceptable. In these areas, the plastic strain increases with time but at a decreasing rate at each cycle. The cooldown period after 13 hot/cold cycles causes the increase of plastic strain (at that instance) but to a magnitude smaller than the obtained one after the first performed cycle. The plastic strains then continue to increase at a similar rate as before the cooldown cycle. The authors suggest that in this

case, plastic strain will occur in the walls but will be limited over cycles. In any way, a larger number of operating cycles and cooldowns have to be performed to confirm that the accumulated plastic strain remain below damaging levels.

Another studied case, where the high Young's modulus and the lower TEC are attributed to the packed bed, is given in Figure 2.16b. It shows the evolution of equivalent plastic strain during a sequence of 18 cycles without considering the cooldown to 290°C. As before, eppl_base and eppl_r1 are ignored. The plastic strain is progressively and rapidly increasing from one cycle to another. Such an evolution stands for the effects of thermal ratcheting that are more important when a larger difference exists between the TECs of the bed and the tank. Therefore, it is advisable to match the storage materials such as their TECs are as close as possible. The other studied cases, where lower values of Young's modulus or higher values of TEC are considered, do not show higher strain values from the case (high Young's modulus-Low TEC). The safest case stands for the case using the combination of lowest Young's modulus and highest TEC for bed, where no plastic strain is observed during the cycles.

Eventually, some cases studied the influence of increasing the internal angle of friction of the particulate medium. Increasing the internal friction angle increases the bed shear strength and thus increases the resistance of particles to slump, resulting in lower ranges of plastic strain compared to lower angles of friction.

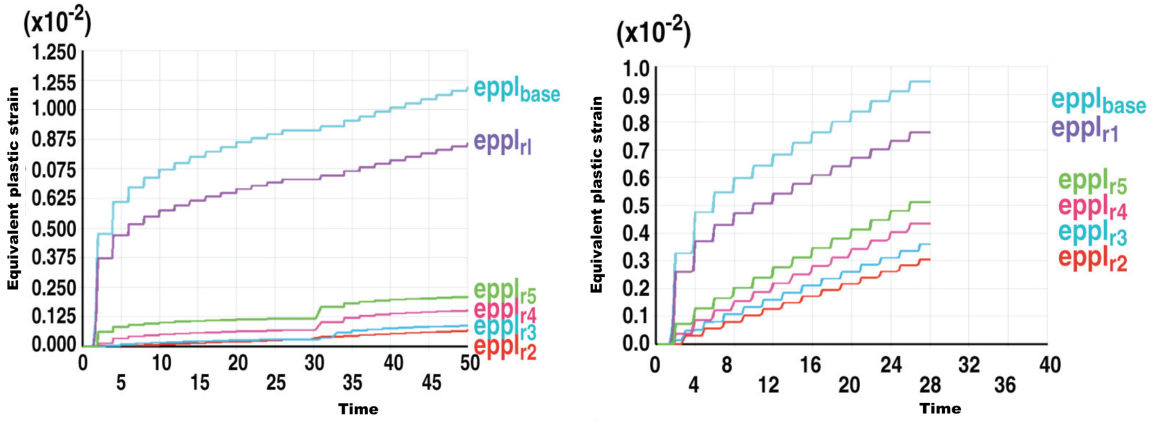

(a) (b)

FIGURE 2.16: Equivalent plastic strain: (a) Nominal Young's modulus with high bed's TEC, (b) High Young's modulus with low bed's TEC, from Kolb et al. (2011)

Conclusion/Discussion: The studied thermocline is a large industrial one proposed by Sandia National laboratories. The current study shows the influence of the Young's modulus and the internal angle of friction of the filler bed as well as the influence of the difference of TECs of the storage materials on the resulting plastic strains. The results show that a stiffer bed may increase the plastic deformations in the tank wall.

Moreover, the impact of increasing the difference between the TECs of the used material is the increase of plastic strains. This may suggest the benefit of matching the TEC of the bed with that of the tank as closely as possible.
Increasing the internal angle of friction of the particles makes the filler more resistant to settlements that may occur during thermal cycles, thus the thermally-induced plastic strain is reduced. The introduction of cooldown cycle to uniform 290°C causes higher plastic strain rate over number of cycles following it.

However, a larger number of cycles (including the cooldown periods) is recommended to better track the tank's plastic strains over the cyclic operations.
Furthermore, the Young's modulus is considered uniform over the bed's height while in reality, it is dependent on the hydrostatic pressure of the packed bed. The bottom part of the filler is stiffer than the upper part due to a higher densification. Better predictions of strains may be obtained if an equivalent Young's modulus for the bed is attributed at different levels of the packed bed height.

2.2.4 Conclusion

As presented previously, only few studies are carried out to study the phenomenon of thermal ratcheting in thermocline storage tanks. The lack of experimental data in this domain, which makes the validation of numerical results and the evaluation of the significance of the problem harder when constructing these kinds of tanks.
The data recorded on the only existent thermocline storage tank at the industrial scale, Solar One, were not reliable data, since they show large uncertainties. Hence, the time history at which they were recorded, i.e. at which cycle or at which instant of the charging/dicharging process, is unknown. Another experimental set-up, at the laboratory scale, was mechanically instrumented in order to test the stress evolution over thermal cycles. The square section of the test rig may generate higher stress concentrations at the corners, limiting the reliability of the obtained results.

Furthermore, for the bed modeling, two approaches were used to study the thermo-mechanical behavior of the packed bed inside a thermocline storage tank. The first approach lies on considering the packed bed as a continuum medium, using the finite element method. Most of the studies using the FE method, considered simplified conditions, as modeling only extreme cases, i.e. infinitely rigid or fluid-like configurations, and do not account for the particulate nature of the packed bed neglecting the effects of the densifiction of the medium during cycles. These simplified hypothesis and boundary conditions may largely affect the resulting stresses in the tank shell. The studies that reproduced the Solar One thermocline, show that the tank behaves elastically under the subjected thermal loads; the tank is not supposed to fail.
Another approach is based on the discrete element methods. Considering this approach, the

granular nature of the bed is easily taken into account, but this representation is time costly, limiting the number of performed thermal cycles. The studies conducted on the squared set up show some inconsistencies in terms of following the thermal loads: the numerical or/and experimental stress evolution does not follow the temperature profile. The highest stresses are measured while the charging process is still going on.

Thus the necessity of the study of the thermal ratcheting phenomenon is clear on both numerical and experimental levels, especially that it largely impacts the design and life-time of the thermal energy packed-bed storage tanks.
As well, the stress and strain accumulations in the tank wall and bed densification are also common in containers where a particulate medium exhibits swelling and shrinking behaviors. These behaviors can be caused by temperature and humidity variations, absorption/desorption reactions, etc... The effects of these swelling/shrinking conditions on the filler bed and on the resulted stresses are addressed in the upcoming Section 2.3.

2.3 Mechanical behavior of a particulate medium subjected to cyclic swelling and shrinking conditions

Cyclic swelling and shrinking conditions that a particulate medium may undergo, lead to internal perturbations that can have significant effects on the bulk properties of granular materials after many cycles. The sensitivity of granular materials to such perturbations has been referred to as granular fragility (Cates et al. (1998); Roux and Combe (2002)) and has showed so far considerable attention in literature. As an example, it was demonstrated that temperature changes within granular materials affect the "apparent" weight of a granular pile (Clément et al. (1997); Claudin and Bouchaud (1997)), the thermal conductivity of a granular packing (Vargas and McCarthy (2007); El Shamy et al. (2011)) and the path of sound transmission in granular media (Liu and Nagel (1994)). Moreover, even small thermal variations can densify a granular packing (Vargas and McCarthy (2007); Chen et al. (2006); Chen (2008); Chen et al. (2009); Divoux et al. (2008)), cause pressure accumulation (Blight (1985); Zhang et al. (1993); Lapko and Prusiel (2006)) or even the failure of industrial scale storage silos subjected to diurnal temperature changes (Carson (2001); Dogangun et al. (2009)). Besides temperature variations, other conditions can lead to such kind of internal perturbations such as the wetting/dewetting conditions due to humidity variations in grain bins (Lindley et al. (1996)) or the hydrogenation/dehydrogenation phenomenon of metallic powders in hydrogen storage tanks (Charlas et al. (2015); Wang et al. (1987)).

Therefore, some existent experimental or numerical tests on particulate mediums subjected to swelling and shrinking conditions are reported hereafter. The focus is set on either the effect of these cyclic conditions on the compaction dynamics of a granular bed or on the induced

applied pressures on the container walls. These tests are believed to provide much information on the behavior of such particulate beds in order to better understand the behavior of the granular filler in thermocline storage tanks.

2.3.1 Effect of swelling and shrinking cycles on the densification of a particulate medium

Upon heating and cooling cycles, the grains and their containers both undergo thermal expansions and contractions, leading to particles rearrangements due to the metastable nature of a particulate medium. These rearrangements are not reversible along with thermal cycles. The effect of the temperature changes on the grain dynamics has been largely explored (Vargas and McCarthy (2007); Chen et al. (2006); Chen (2008); Chen et al. (2009); Divoux et al. (2008)) and many experimental setups are constructed in order to study the compaction of granular materials subjected to thermal cycles.

One way to study the grain compaction is to measure the height variation of the packing during the thermal cycles. Therefore, an experimental setup allowing the tracking of the height variation is considered in (Divoux et al. (2008)). It consists of a 1.7 m high-glass tube (inner diameter of 13 mm) firmly fixed to the wall in order not to allow any external mechanical vibrations causing the rearrangement of the bed (Figure 2.17a). The tube is filled with spherical glass beads (with a diameter d=510±90 μm) to a height H. The temperature cycles are imposed by means of heating cables bonded to the outer surface of the tube allowing to homogeneous temperature along the tube's height. The resulting temperature is measured by a sensor located close to the free surface of the granular sample (see Figure 2.17a). A video camera allows to image the free surface and thus to measure the height H over the cycles of heating and cooling. 20 measures are performed during a temperature cycle. The cycling period is fixed to 10 minutes. Prior to each test, an upward flow of dry nitrogen can be injected from the bottom making the sample looser, preparing it at a low-density state.
Results show that even for low temperature changes (an overall temperature variation between the heating/cooling processes of ΔT=10.8°C), the column's height decreases over cycles, despite that the filler and the container are both made of the same material. Moreover, the oscillations of the height H associated to temperature variations of the heating and cooling cycles are also observed (Figure 2.17b). Note that within 1000 thermal cycles, the bed continues to settle without reaching the stable state. The porosity of the bed decreases by about 0.1%.
Nevertheless, it is crucial to mention that the induced thermal loads are not homogeneously generated in the radial direction, by heating the outer surface of the tube through heating cables. These temperature variations between the bed and the tube, due to the non-homogeneous lateral heat spread, cause temperature differentials and lead to further particles rearrangements.

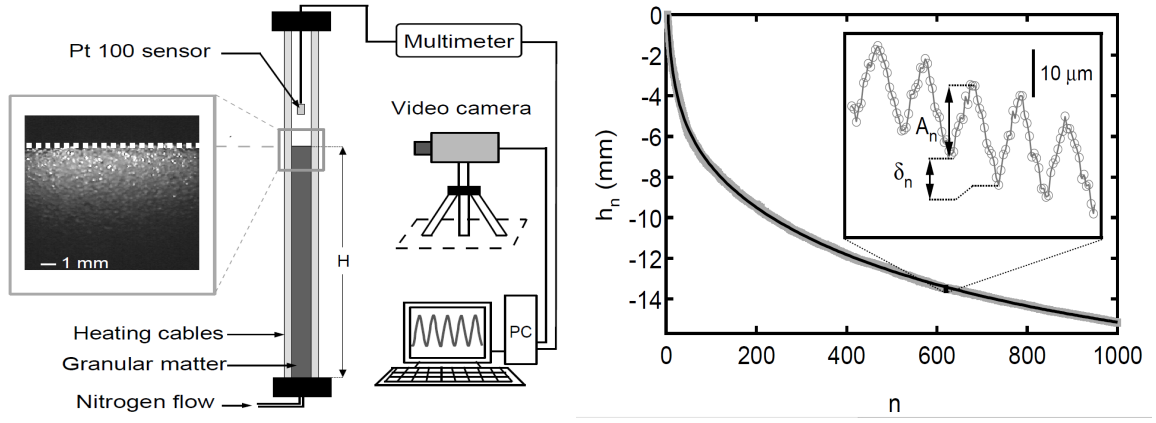

(a) (b)

FIGURE 2.17: Packing's height variation during thermal cycling: (a) Experimental setup considered in (Divoux et al. (2008)), (b) Height variation h_n ($h_{current}$-h_0) with cycles n, H=140 cm; from Divoux et al. (2008)

Another way to study the compaction of the granular system is to track the variation of the packing fraction during thermal cycles. The packing fraction of a granular material is defined as the fraction of the sample volume filled by grains rather than by empty space. An experimental setup (Figure 2.18a) dedicated to the measurement of the packing fraction variations is considered in (Chen et al. (2006); Chen (2008); Chen et al. (2009)). Graduated cylindrical containers are filled with spherical granular materials with a constant initial packing fraction through a funnel raised by a stepper motor at a constant rate. An initial packing fraction of $58.9 \pm 0.2\%$ is obtained. The heating process is realized inside an oven until a pre-set temperature is reached and then the sample are allowed to cool slowly at ambient temperature (22 $\pm 2°C$) before measurements. About 20 hours are required for each cycle limiting the number of performed cycles. Great precautions are taken to prevent any mechanical agitations of the samples that can affect the measurements. At the end of each thermal cycle, the packing fraction is determined by referring to the container's graduation. The influence of the differential expansion between both materials is investigated by using different combinations of granular and container materials.

Results show that the differential expansions between both materials can have a great influence on increasing the packing fraction of a sample: the packing fraction relaxation observed in glass grains ($\alpha_{glass} = 9 \times 10^{-6}$) in a plastic container ($\alpha_{HDPEplastic} = 110 \times 10^{-6}$) is much more than that from glass grains in glass containers (Chen (2008)). However, the fractional changes under thermal cycles may be affected by other factors than differential expansions between both materials, such as the inter-grain friction and grain/wall friction (Vandewalle et al. (2007); Jerkins et al. (2008)). The packing fraction does not depend only on the magnitude of the size changes induced by temperature and therefore, in the authors point of view, a direct scaling that relate the fractional packing to the differential expansion coefficients may not be intuitive. In addition to this, it has been seen that the packing fraction continues to

increase under multiple successive thermal cycles but with a decreasing relaxation rate (see Figure 2.18b).

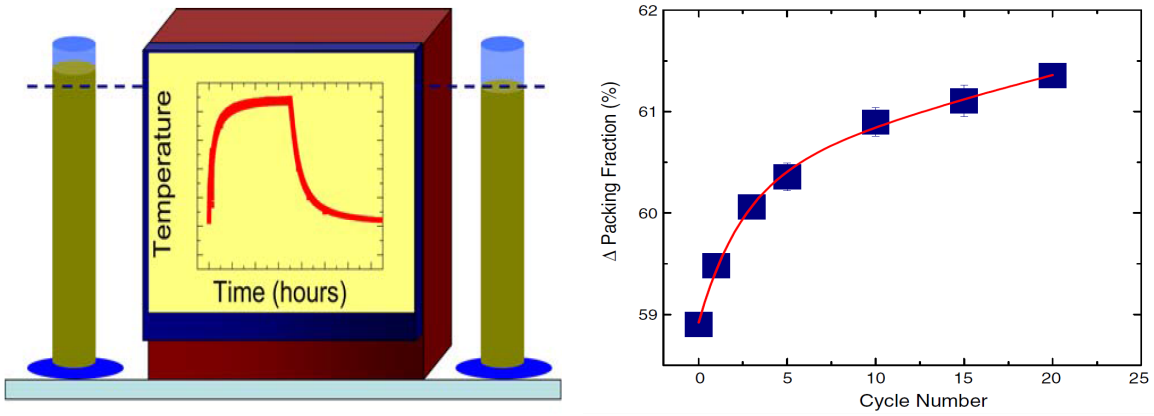

(a) (b)

FIGURE 2.18: (a) Experimental setup considered in (Chen et al. (2006); Chen (2008); Chen et al. (2009)), (b) The change of the packing fraction as a function of number of thermal cycles (case of polystyrene grains in glass container); from Chen et al. (2009)

,

Vargas et al. (Vargas and McCarthy (2007)) examined numerically the packing fraction for spherical glass particles in a vertical plastic container subjected to repeated thermal cycling from a reference temperature, much in the same way as the experiments conducted by Chen et al. (Chen et al. (2006)). Many cycles of heating and cooling are performed with overall different temperature variations (ΔT=10°C, 50°C and 100°C). Good agreements are shown by comparing both the current simulation results with the experimental observations reported by Chen et al. In fact, the simulated results show a clear increase in packing fraction even for a single cycle (Figure 2.19). A continuous increase of the packing fraction is shown over cycles before reaching a plateau at a high number of executed thermal cycles. A higher ΔT leads to a higher rearrangements and thus higher packing fraction. Moreover, consistent conclusions with Chen et al. are obtained regarding the influence of the differential thermal expansion between the grains and the container on the changes of the packing fraction. Although the current simulations do not account for thermal expansion of the wall, the compaction of the bed is achieved due to the expansion/compaction of grains only, knowing that a higher degree of compaction may be attained when the expansion of the wall in considered.

2.3.2 Induced pressures on the container walls due to cyclic swelling/shrinking conditions

Unusual loading conditions can occur as a result of temperature and/or moisture effects. Temperature fluctuations, such as would occur from daytime to nighttime, can lead to much higher hoop stresses than would otherwise be expected. A similar phenomenon can occur if

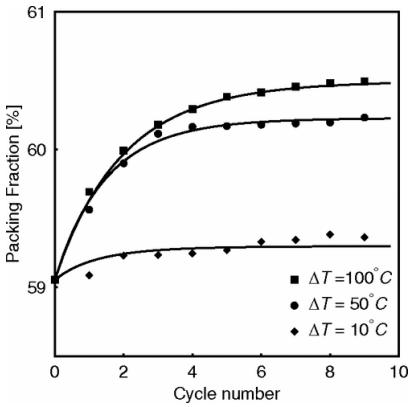

FIGURE 2.19: Change in packing fraction with thermal cycling for a temperature difference of 10°C, 50°C and 100°C

the bulk solid being stored is moist and has a tendency to expand with increased moisture content.

2.3.2.0.1 Diurnal temperature variations: An increase of lateral pressures applied on the walls of filled metal grain storage bins is shown when bins are subjected to a declining ambient temperature (Blight (1985); Puri et al. (1986)). When a metal bin is subjected to a rapidly declining ambient temperature, the wall bins are more rapidly affected by the temperature modifications; the bin walls are restrained to contract by the stored grains causing an increase in lateral pressures on the bin walls (Zhang et al. (1987)). An experiment was conducted using a commercial grain storage bin (Westeel Model 198, Westeel, Winnipeg, MB) in order to explore the influence of diurnal variation on thermally-induced loads (Zhang et al. (1993)). The corrugated galvanized steel tank had a diameter of 5.8 m and an eave height of 6.2 m. It was filled with hard red spring wheat to a depth of 5 m. The bin was instrumented with six diaphragm pressure sensors fixed at the internal surface of the bin wall at 0.9 m from the bottom. They were placed 60° apart around the bin circumference. For each sensor, four strain gauges connected to a full-Wheatstone bridge are mounted. Temperature calibrations for the sensors were performed assuring the compensation of temperature effects. Thermocouples are used to measure the wall temperatures near the pressure sensors. Lateral bin-wall pressures and wall temperatures were measured continuously for 23 days in February 1990. Both wall temperature and thermal induced pressures fluctuated diurnally (Figure 2.20). The minimum pressure occurred during the daytime while the maximum pressure occurred during the nighttime. The average thermal pressure increment was of 114 Pa/°C for a wall temperature varying from -11 °C to -29°C.

2.3.2.0.2 Moisture content changes: The change of the moisture content of the stored material may produce additional loads on structures. The expansion of wet grains is restricted by the bin walls and consequently additional "hygroscopic" pressures are induced on the bin

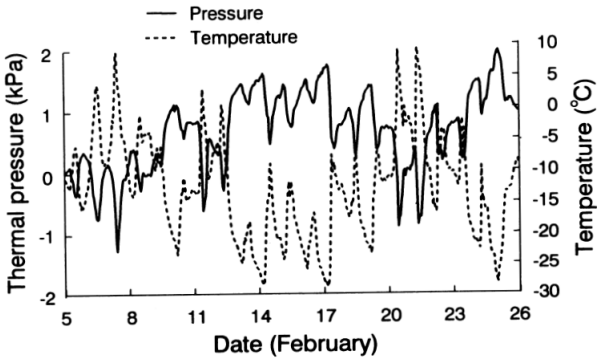

FIGURE 2.20: Lateral thermal pressure and wall temperature in the Westeel Model 198 measured at by the sensor located at S 60° E; from Zhang et al. (1993)

walls (Lindley et al. (1996)).

Kebeli et. al measured the lateral pressures and hoop stresses on a 0.4-mm-thick grain bin using strain gauges (Kebeli et al. (2000)). The bin walls were made of galvanized steel and the model bin had a diameter of 0.6 m and a height of 1 m (Figure 2.21a). The bin was equipped with a humidification system permitting the increase of the moisture content of soft spring wheat in the bin. Six two-elements 90° rosette strain gauges were placed at three different levels of the bin: at 15 cm, 45 and 75 cm starting from the bottom. At each level, two rosettes were placed 180° apart from each other. The measured pressures were dramatically increased with increasing grain moisture content (Figure 2.21b). Results showed that the lateral pressures were multiplied by nine at the bottom level with an increase of 12 % d.b. in grain moisture content (moisture content expressed on the dry basis: mass of water with respect to the material dry mass). As a consequence, the hoop stresses in the wall bins were nine times greater than the initial average stress at the deepest levels. Lower stresses are obtained at the middle an at top levels of the container.

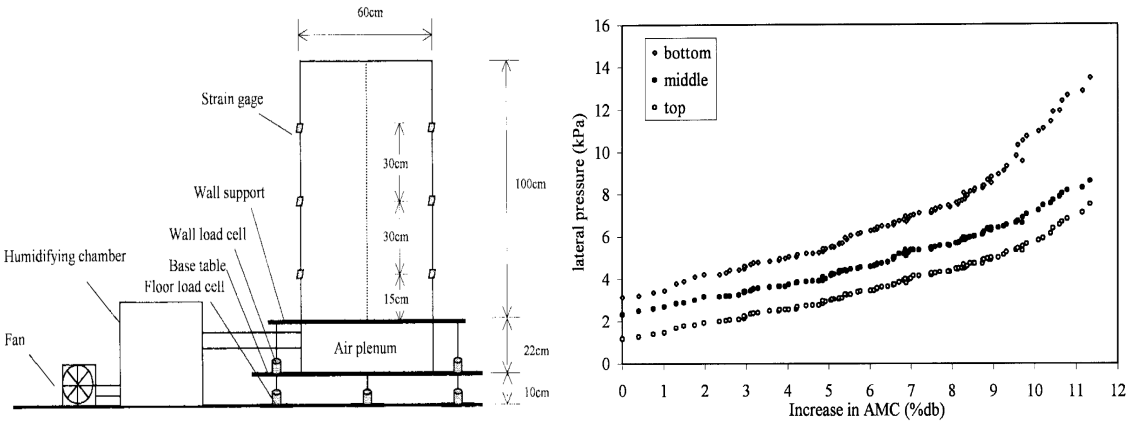

(a) (b)

FIGURE 2.21: (a) Experimental set-up, (b) Average changes in lateral pressures at three measuring levels; from Kebeli et al. (2000)

2.3.2.0.3 Hydrogen absorption/desorption reactions: The wall stress accumulation is also shown during hydrogen absorption/desorption cycles (Charlas et al. (2015); Ao et al. (2005); Lin and Chen (2012); Okumura et al. (2012)). Hydrogen storage has become a very interesting way to store energy relying on the exothermic and endothermic aspects of the hydriding and dehydriding reactions respectively (Latroche (2004)). But the hydrogenation (absorption of hydrogen) goes with volume increase (Latroche (2004)) and the medium is thus subjected to a cyclic procedure of swelling and shrinking accompanied with the absorption and desorption of hydrogen. The settlement of the powder bed due to both the decrepitation and hydride breathing, leads to a progressive increase of strain and stresses on the container walls.

It is crucial to note that the volume expansion ratio after absorbing hydrogen is larger than 20%, depending on the storage material. This volume change is much greater than the ones that occurred due to thermal variations as in thermocline storage tanks, where the volume change is less than 1%. Therefore, the upcoming results are presented briefly and their analysis is restricted to the qualitative response of the granular bed only.

As an example, Lin et al. studied the increase of wall stresses of $LaNi_5$ hydrogen storage beds regarding the number of cycles of hydrogen absorption/desorption, packing fraction and thickness of the beds walls (Ao et al. (2005)). The $LaNi_5$ alloy's volume expansion ratio is up to 24% after absorbing hydrogen. The stresses of three different beds filled with commercial $LaNi_5$ alloys are measured using a strain gauge-type pressure sensor. The basic parameters of the three beds are presented in Table 2.6. Strain gauges are attached to the external surface at different locations (3/10, 5/10 and 7/10 from bottom to top along the bed). The experimental temperatures are kept at 25 ± 1 °C. The experimental results indicate that the wall stresses increase with hydrogen absorption/desorption cycles, and decrease with wall thickness.

Furthermore, different locations exhibit greatly different levels of maximal strain: the largest strain value appears at the location of 3/10 and the smallest strain value appears at the location of 7/10. The concentration of stresses at bottom is related to the higher $LaNi_5$ alloy density at bottom comparing to the top. In addition, even for the Bed 1 having lowest packing fraction, plastic deformation can quickly occur on the wall as the hydrogen absorption/desorption cycles progress. Eventually, the continually changed densities of the bed is responsible for the stress accumulation. Similar results are found in (McKillip et al. (1992); Nasako et al. (1998)).

TABLE 2.6: Studied beds with different initial packing fraction ratios; from Ao et al. (2005)

Bed code	Wall thickness (mm))	Bed volume (cm^3)	Packing fraction (%)
1	2.5	50	60
2	1.5	50	70
3	1.5	50	80

Mechanical stresses tend to be more important when dealing with slender containers in which cyclic shrinking and swelling conditions occur. This is sometimes attributed to a larger volume fraction of the bed at the bottom of a high vertical tube compared to a shallower container. Charlas et al. (B. Charlas) investigated the dependency of the size of the container on the resulting loads under uniaxial lateral compaction or swelling. A parallelipedic container filled with a mono-disperse spherical powder bed was modeled using DEM. Different ratios of H/L, where H and L are respectively the height and the width of the container were considered. The compaction of the medium was assured by imposing a wall displacement corresponding to a volume reduction of 20% while the swelling case was assured by a volume increase of 20% of the spherical particles. The results showed a great influence of the H/L ratio on the maximal force applied of the wall (Figure 2.22a). The resulting forces acting on the wall, for both compaction and swelling cases, are similarly increasing exponentially with an increasing H/L ratio.

Further numerical DEM studies have reported the importance of the slenderness ratio on the induced stresses under cyclic swelling and shrinking conditions during the hydriding/dehydriding reactions (referred as the hydride breathing phenomenon) (Charlas et al. (2015); Qin et al. (2008)). The stresses increase if the height of the sample increase for a given width. A more constrained powder bed is obtained when dealing with high slenderness ratios, especially at the deepest levels, restraining the breathing of the hydride bed and leading to higher applied stresses on the container walls. Charlas et al. (2015) suggested a slenderness ratio lower than one in order to prevent high values of induced stresses on the wall (Figure 2.22b).

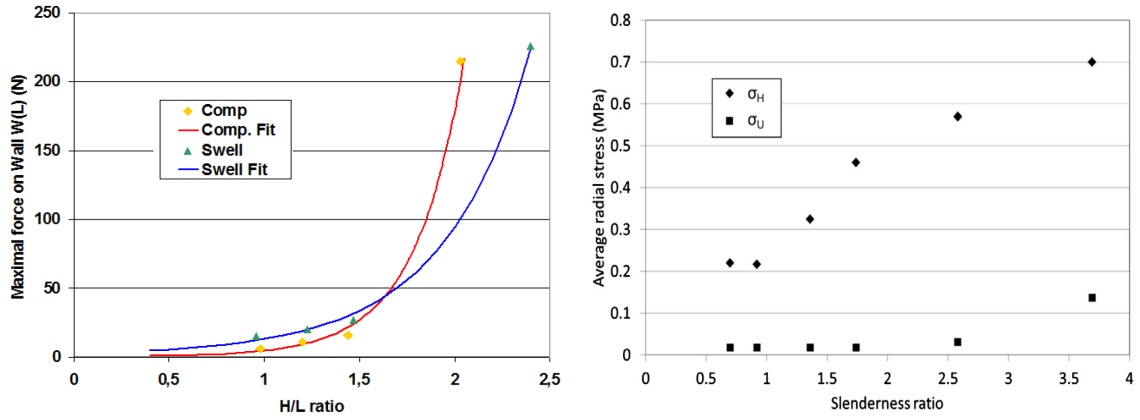

(a) (b)

FIGURE 2.22: Influence of the slenderness ratio H/L, (a) Forces acting on the wall as a function of H/L initial ratio (B. Charlas), (b) Average radial stresses for cycle 5 in hydrided (σ_H, highest levels of stresses) and unhydrided (σ_U, lowest level of stresses) states depending on the slenderness ratio (Charlas et al. (2015))

2.3.3 Conclusion

A particulate medium can be very sensitive to cyclic swelling and contracting conditions. The internal perturbations caused by cyclic conditions, whether it comes from humidity and thermal variations or hydrogenation/dehydrogenation reactions, always lead to common behaviors: particles rearrangements, packing densification and thus increase of induced stresses in the tank shell.
The packing fraction of the particulate medium continue to increase under these cyclic conditions, but with an decreasing rate over cycles. When thermal cyclic loads are applied, the densification of the medium is accentuated with higher temperature variations ΔT between charging/discharging processes. and with greater TECs differences between the medium and the container. However, results showed that there is no direct scaling relating the densification of the medium to higher TECs differences between the medium and the container. The densification depends also on different mechanical properties of the bed, such its internal friction angle and the friction coefficient at the container boundaries.
The wall stress accumulation under swelling/shrinking conditions was also investigated. The induced stresses are always more important at depth, and they depends on the initial packing fraction of the medium. The denser the particulate medium is, the higher stresses are induced in the walls. The presented studies offer an insight into the comprehension of the global behavior of a packed bed in thermocline storage tanks. But, it is believed that this behavior is largely dependent on the problem conditions: initial state conditions of the packed bed (its initial packing fraction), its mechanical (friction coefficients) and thermal (TECs differences and applied ΔT) properties, the cyclic (percentage of volume changes) and boundary conditions...
The dependency of the results on all these factors makes harder the comparison between all the presented studies. Nevertheless, all of them show similar behaviors for the particulate medium and higher wall stress generation, evoking the complexity of the problem and the necessity of a well understanding of all included phenomena.
Eventually, The thermo-mechanical behavior of a particulate bed is very complex and not has not been completely understood yet. So far, some applications, studies or inventions aiming at limiting or preventing the danger resulted from this complicated behavior, have been thought of and are presented in the next Section 2.4.

2.4 Limiting and avoiding the thermal ratcheting phenomenon

Thermal ratcheting phenomenon could be one of the major mechanical problems we might encounter when dealing with a dual-media storage tank. Hereafter are presented some ways of limiting or avoiding this phenomenon proposed by the literature.

2.4.1 Development of a structured thermocline thermal energy storage system

The development of innovative structured thermocline storage tanks, permitting to avoid the issue of thermal ratcheting, starts to attract the concern of many researchers. Within this technology, the packed bed filler material is replaced by a cheap structured bed configuration, always allowing the overall cost reduction compared to the two tank configuration. Significant

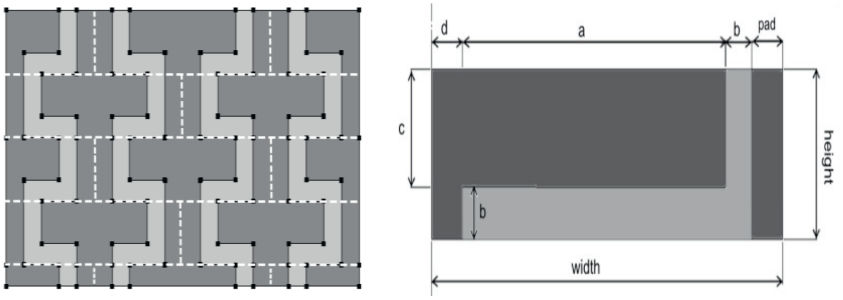

FIGURE 2.23: 2 × 4 bricks structure (fluid is represented in light grey) as proposed by (Motte et al. (2014)); Description of geometric parameters

efforts have been exerted to develop this kind of storage tank while maintaining a good storage efficiency of the system, low filler material costs with chemical characteristics compatible with the heat transfer fluid at high temperatures. Emerson and al. (John et al. (2011)) propose a structured thermocline storage where simple rectangular bricks made of a mixture of concrete and fly ash are integrated. Some of these mixtures were found to be compatible with molten solar salt up to 585°C and are potentially suitable for structured thermocline storage. As a major advance towards such a sustainable TES, recent achievements have been done in the production of 100% recycled ceramics from industrial wastes (Py et al. (2009); Meffre et al. (2011); Py et al. (2011)). Those refractory ceramics present good compatibility with nitrate molten salts (Calvet et al. (2013)) and high thermo-mechanical strength. Motte et al. presents in (Motte et al. (2014); G. Papakokkinos and Py (2012)) a numerical model to study the feasibility of building a structure from a simple brick made of a ceramic derived from asbestos containing waste (Cofalit Py et al. (2011)). This material is easy to manipulate and does not require any special know-how to build the brick wall. A nitrate mixture solar salt is used as a heat transfer fluid. The geometry of the used brick is illustrated in Figure 2.23. Various geometrical parameters and physical variations are tested in the aim of optimization of such a structured bed thermocline storage tank. The simulated structured thermocline show interesting results regarding its feasibility and its capacity of storing heat. However, the convective transfers between the HTF and the structured filler material are lower compared to the basic packed bed configuration, which shows the necessity of improving the structured geometrical configurations or testing other brick designs.

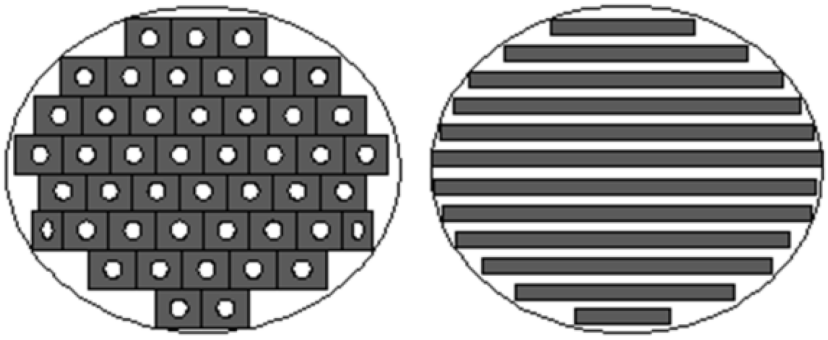

(a) (b)

FIGURE 2.24: Concrete arrangements in thermocline tank: (a) Axisymmetric configuration, (b) Parallel-plate configuration; from Brown et al. (2012)

Moreover, concrete could be a promising sensible heat storage medium in structured thermocline systems. Concrete, which has an approximate media cost of 1$ per kilowatt-hour thermal (Herrmann et al. (2002)), has shown a great compatibility with molten solar salt operating at temperatures exceeding 500°C (Coa (2011)). Preliminary testing, where concrete was incorporated with an embedded stainless-steel-tube heat exchanger, allowed for temperatures in the concrete storage media to reach temperatures of up to 450°C (Skinner et al. (2014)) but the costs of this method of design rendered the thermocline storage tank too expensive. Brown et al. (Brown et al. (2012)) proposed and developed a structured thermocline system where concrete and molten salt are incorporated. A numerical modeling based on the finite-difference method was implemented to optimize a structured concrete filler material. Two unique arrangements of filler material were modeled: concrete prisms with an internal, circular holes running vertically along the height of the prism (axisymmetric configuration, Figure 2.24a and parallel concrete plates standing vertically inside the thermocline tank (Figure 2.24b). The exact geometries of these two system configurations were optimized to provide the optimum energy storage to energy retrieval ratio. Eventually, of the two filler material configurations, it was found that the parallel-plate model provided the highest discharge efficiency and allowed for the most energy retrieval per unit cross section of the thermocline tank.

The structured thermocline storage tanks are promising in the future. However, the challenge is to find convenient combinations between the storage materials and the heat transfer fluid allowing for the operation of the TES at high temperatures and preventing any chemical reactions or solid crushing. The reduction of the overall cost of the tank as well as the provision of a high system efficiency are compulsory if the competition with the basic packed bed thermocline facility is required.

2.4.2 Unconstrained packed rock bed thermal energy storage facility

The invention of an unconstrained packed rock bed energy storage facility associated with concentrating solar power plant is proposed in the patent (Kröger (2014)). The storage facility mainly consists of an unconstrained pile of rocks that is free to dilate and contract with temperature variations without generating significant stresses on the tank wall. The cross-section elevation and the longitudinal sectional elevation of the proposed invention are schematically illustrated in Figure 2.25. The hot air is provided into or extracted from the tank through ducts that communicate with the space 1 above the bed (Figure 2.25) whereas the cold fluid communicates with the tank through communication ducts associated to the space 2, below the packed bed. During the charging/discharging phases, the fluid may flow between the first and the second spaces by way of interstices between rocks in order to assure the transfer of heat. The bed is completely covered by an insulated arched roof. The entire top surface of the pile is exposed to the free space 1 without any connection with the tank wall, preventing the thermal ratcheting phenomenon. The rock pile has a flat top and then it reposes naturally on a central flat region and side regions that are inclined upwardly by a gentle slope. The larger rocks shown in the Figure retain the smaller rocks of the packed bed and allow the maintenance of the space 2. Numerous arrangements may be deducted from the proposed invention in order to be used for larger thermal energy storage facility and are proposed in (Kröger (2014)). The described invention might be a future feasible application except that it still needs lot of efforts in order to study the thermal flows inside the tank and ensure a good distribution of temperature. The overall efficiency of the system has to be tested and quantified, heading for the comparison to the efficiency of the simple packed bed thermocline systems, keeping in mind that the heat losses from ductwork (even if insulated) and packed bed corners may be significant which can limit the efficiency of the system.

2.4.3 Limiting the ratcheting by increasing the internal insulation

Based on the thermo-mechanical model previously described in Section 2.2.1, Flueckiger et al. concluded from a numerical parametric study, that the hoop stress levels in tank wall are reduced by increasing the internal insulation layer thickness (Flueckiger et al. (2011, 2013)). In this work, a thermocline tank with internal diameter of 12 m is filled with a porous bed of quartzite rock to a height of 12 m. A molten-salt is used as a heat transfer fluid operating at 450°C and 293°C respectively as hot and cold temperature limits. The tank considered here has a complex wall consisting of multiple layers: an inner firebrick layer for thermal isolation, a steel shell layer and an outer layer of ceramic fiber for corrosion protection and thermal insulation. A schematic illustration of the modeled thermocline is presented in Figure 2.26a The maximum and minimum temperatures in the steel shell at each discretized location level, obtained throughout the charge and discharge processes, are determined through

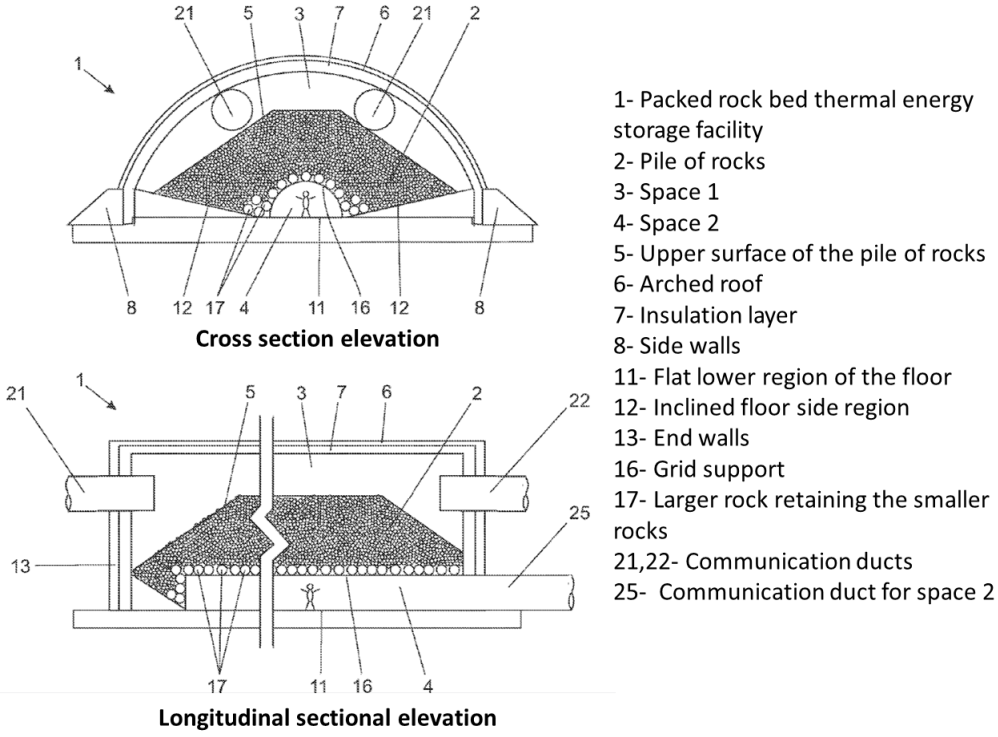

FIGURE 2.25: The cross-section elevation and the longitudinal sectional elevation of the invention, from Kröger (2014)

solving thermal analysis model using the commercial computational fluid dynamics (CFD) software, FLUENT (FLUENT). The tank behavior for various composite wall thicknesses is investigated. The composite wall characteristics for each case are summarized in Table 2.7. The hoop stresses generated in the steel shell are normalized with respect to the yield strength and are plotted in Figure 2.26b. The results show that by adding insulation between the filler region and the steel, the induced hoop stresses decreases by diminishing the sensitivity of the steel shell to the fluctuating molten-salt temperatures (Case 2). Case 3 also exhibits lower stress levels; a thicker steel layer increases axial conduction which reduces the temperature gradients along the shell. In contrast, a thicker layer of external insulation decreases the external losses which increases the sensitivity of the steel shell to the cyclic heat transfer fluid behavior and thus to temperature fluctuations (Case 4).

Even though that this recommended solution could be adequate to minimize the potential for thermal ratcheting phenomenon, but the results still need to be experimentally verified and validated. Moreover, great precautions on the feasibility of adding internal insulation in thermolcine storage tank should be considered to avoid any leakage of the fluid through the insulation. Furthermore, thermal ratcheting might result in excessive pressure on the firebrick causing them to be crushed and limiting their function of insulation. These major problems have to be solved and verified before applying the proposed solution.

TABLE 2.7: Summary of the cases considered with different wall structural parameters; from Flueckiger et al. (2013)

Cases	$\delta_{firebrick}(m)$ (Pa)	$\delta_{steel}(m)$	$\delta_{ceramic}(m)$
1	0.1	0.02	0.05
2	0.2	0.02	0.05
3	0.1	0.04	0.05
4	0.1	0.02	0.025

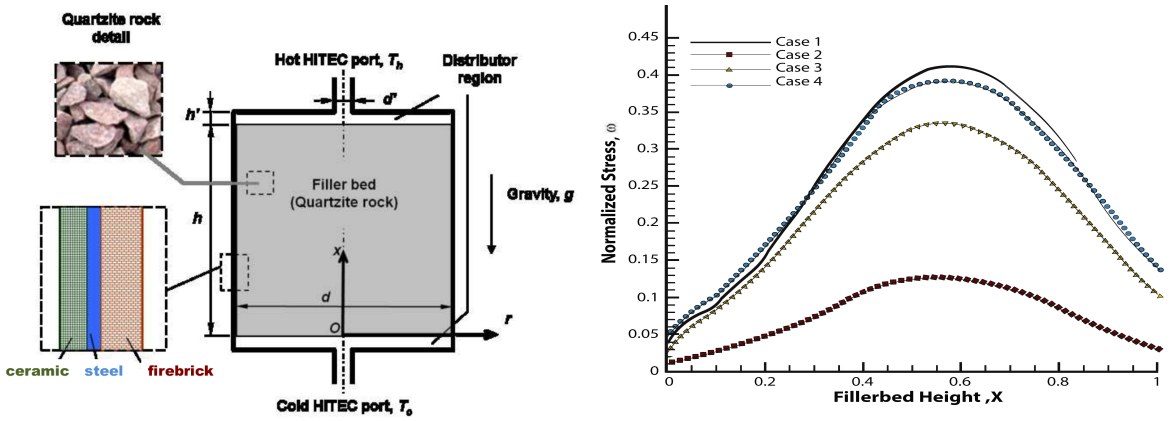

(a) (b)

FIGURE 2.26: (a) Schematic illustration of the thermocline tank with a composite wall consisting of (1) firebrick, (2) steel, and (3) ceramic, (b) hoop stress profile along the filler bed height for all cases (see Table 2.7); from Flueckiger et al. (2013)

2.4.4 Dividing the tank into subsections

As it was seen in Section 2.3.2, the applied wall stresses are more important when dealing with slender storage tanks. One way to reduce the resulted stresses is to divide the internal space of the packed-bed storage tank into several subsections using basket-like concept, reducing the height-to-diameter ratio though. This method is applicable only for thermoclines at laboratory scale. Figure 2.27 shows the STONE thermocline, constructed on the basis of the proposed solution (Esence et al. (2017a)). With large thermocline tanks, the built-in baskets will not be able to handle the applied weight of the bed and the use of pile is necessary to hold the baskets and transmit the weight. However, such a design is expensive and even it adds internal boundaries in contact with the packed bed, leading to the same encountered problems with the original boundaries.

2.4.5 Adopt a truncated conical shape for the thermocline tank

An industrial-scale thermal energy storage system, based on a packed bed of rocks as storing material and air as heat transfer, is constructed in Ait Baha, Morocco (Zanganeh et al. (2012,

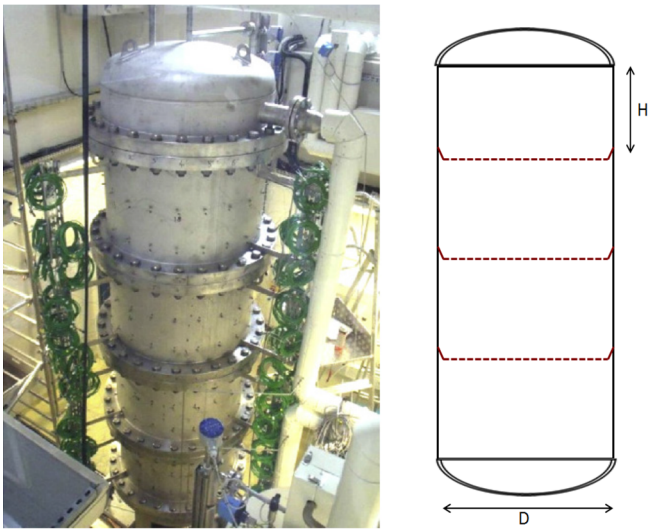

FIGURE 2.27: STONE experimental set-up; left: picture of the storage tank before insulation, right: scheme of its construction plane with baskets; from Esence et al. (2017a)

2014)). Its schematic design is presented in Figure 2.28. The tank has a truncated cone shape, with an increasing inscribed circle radius going from 1.25 m at the bottom to 2 m at the top, at a wall inclination of 12°. The tank, which is immersed in the ground, has a dodecagonal cross section and a total height of 4 m. The truncated cone shape exploits the effect of lateral earth pressure at higher load bearing and reduces the normal force on the walls during thermal expansion of the rocks by guiding them upwards (Lang et al. (1990)). The tank wall is made of concrete for avoiding deformation caused by thermal expansion of the heat-storing material, since it provides a low TEC comparing to metallic structures. The 12 lateral wall segments consist of a 15-mm layer of ultra-high performance concrete on the packed bed side with high mechanical stability and thermal conductivity and a 235-mm layer of low density concrete with low thermal conductivity in order to reduce the thermal losses. The tank is filled to the height of 2.9 m with pebbles with an equivalent sphere diameter of 2-3 cm. The charging process is executed from the top while the discharge process is executed from the bottom. The cycling temperature limits are 280°C during the discharging phase and 640°C during the charging phase.

Although the overall thermal efficiency of the constructed thermocline storage tank was tested numerically using a dynamic numerical heat transfer model, the experimental results are still needed to verify the performance of such a thermocline with a truncated conical shape. Especially that some studies present contradictory results about the performance of a truncated conical tank, where it is shown that a conical shape can significantly reduce the overall storage efficiency compared to a cylindrical tank (Ortega-Fernández et al. (2016)).

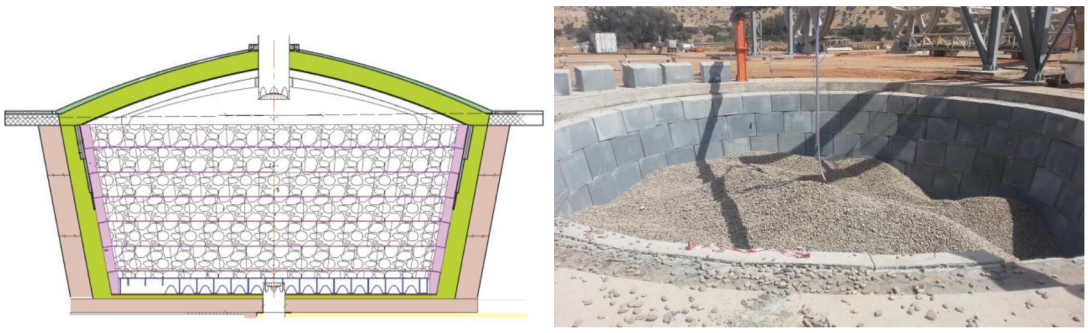

FIGURE 2.28: Scheme and photograph of the TES unit in Ait Baha, Morocco during construction; (Zanganeh et al. (2014))

2.4.6 Conclusion

Despite that all the proposed ways of prevention to the thermal ratcheting might be effective solutions, but they are still somehow far to be executed, either because they still need lot of research efforts to find the compatible combinations of storage and tank materials and to verify the overall efficiency of the system (numerically and experimentally), or because they are simply limited by the on-site realization (internal insulation with oil or molten salt thermocline systems) or the high-cost of the proposed system.

2.5 Conclusion

A review on most of the mechanically-studied thermocline storage tanks is presented in this chapter. Numerical models and experimental works are presented. Most of the existent experimental data in this domain suffer from large uncertainties and can not be considered as reliable data. Thereby, these experimental data cannot be used for numerical modeling validations.

Some studies modeled the Solar One thermal storage unit, based on FE methods. For their modeling, they considered extreme behaviors for the packed bed, ignoring its granular nature that enables it to rearrange under cyclic thermal loads. The obtained stresses remain lower than the wall yield strength after the first thermal cycle. Since the tank is not plastified after the first cycle, no residual strains in the walls and the tank will always behave elastically no matter the number of applied thermal cycles. In other words, their continuum approach was unable to reproduce the accumulation of stresses over cycles due to bed's densification.

Other studies considered the DEM in their numerical modeling. A wall stress accumulation, related to a higher densification of the packed bed, is observed. Their numerical results were compared to some measured data, based on a square-section-thermocline tank. Some incoherence are shown in both experimental and numerical data. In any way, a parallelipedic storage

tank may generate higher stress levels driven by the geometric discontinuities at the corners causing its deformation and might lead to inaccurate results.
Given the lack of numerical and experimental data referring to the thermal ratcheting phenomenon in thermocline storage tanks, the works that have been carried out in similar applications where the global behavior of the packed bed medium is conserved, are then reported. The densification and stress accumulation over the cycles of swelling and shrinking are observed and are dependent on the cyclic conditions imposed.
the interplay of many phenomena makes difficult the understanding of the packed bed behavior. The densification of the packed bed under swelling/shrinking conditions largely depends on the resulted volume changes (due to thermal variations, variation of the moisture content,...), the TECs differences between the filler and the container (in the case of thermal loads), on the internal angle of friction between particles and the particle/wall friction angle as well (depending also on the particles shape, poly-dispersity of particles size distribution...). It also depends on the initial packing fraction of the packed bed.
For a better understanding, the influence of each of these parameters will be studied apart in this manuscript. The discrete element method is chosen as the modeling approach, since it simply reproduce the nature behavior of a granular material using simple constitutive laws. The details of the numerical modeling as well as the obtained results will be provided in the subsequent chapters.
Finally, the potential ways to limit the thermal ratcheting problem are described in the latest section of the chapter. Not all the proposed solutions are feasible for the moment and some of them remain innovative ideas far from being directly applicable at the industrial scale and still need a lot of research to assure the best combinations of insulation/filler/tank materials at the best cost deals.

Chapter 3

Discrete Numerical Model

This chapter introduces the discrete numerical model used in our study. In the discrete element method (DEM), the granular assembly is modeled as a set of independent entities, which interact with each others. This method can model the complex behavior of a granular medium with few physical parameters, unlike phenomenological models (requiring more parameters), and give access to the properties of the micro-structure of the granular assembly. Therefore, for studying the thermo-mechanical behavior of the granular material inside thermocline storage tanks, the DEM is chosen as the numerical tool in our simulations.
In what follows, a brief literature review of the discrete element method is first presented in Section 3.1. Thereafter, the discrete numerical model used in this study is introduced in Section 3.2.1 in which the thermo-mechanical model used for spherical interacting particles is detailed, and Section 3.2.2 is dedicated to present the numerical tools used to implement thermal conditions for the tank walls. Finally, the validation of the numerical tools used for both particulate medium and tank walls are presented in Sections 3.2.1.2 and 3.2.2.6.

3.1 A brief review on the discrete element method (DEM)

DEM meets a growing success as a tool to study the behavior of particulate assemblies. It was initially proposed by Cundall and Strack (1979) Cundall and Strack (1979) to solve problems in rock mechanics. The discontinuous nature of granular materials is represented by a set of discrete rigid elements and the forces between the interacting elements are computed based on linear springs and sliders defined at the contact locations. An explicit numerical scheme monitors the resolution process and the motion of each particle is predicted at each time step.

3.1.1 DEM calculation process

The calculation process of DEM is quite simple. It consists in applying, at each numerical cycle, Newton's second law of motion and a force-displacement law at the contacts. Figure 3.1 shows the DEM calculation cycle. It involves two stages:

- **Detection of the list of interactions and computation of contact forces:** Two spherical particles are in contact if the distance between their centers is smaller than the sum of their radii. Interaction forces (F_i) and moments (M_i) are then computed between interacting particles based on predefined interaction laws.
- **Calculation of the new particles' positions:** Newton's second law is applied for each particle and its resulting acceleration is thus determined. The acceleration is then integrated in order to find the new particle positions.

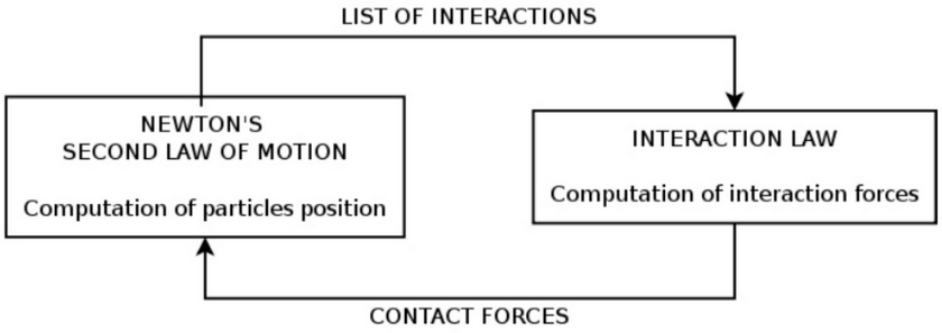

FIGURE 3.1: DEM concept

The new elements positions allow the update of the list of interactions and then the calculation of new interaction forces at contacts. This calculation process is looped until the achievement of the simulation.

3.1.2 Interaction laws

One of the strengths of DEM is its capacity to reproduce complex mechanical behavior using simple interaction laws, that require the determination of few mechanical parameters. These contact laws describe how elements behave when they are in contact with each other. Several types of contact laws are found in the literature. Only the two most common contact models are briefly presented below.

- **Contact model with constant stiffnesses:** It is one of the simplest models, pioneered by Cundall and Strack (Cundall and Strack (1979); Matuttis et al. (2000); Radjaï and

Roux (2003); Donzé et al. (2009)). The contact between two spheres is modeled by normal and tangential springs with constant stiffnesses. In series with the tangential spring is put a slider of friction angle φ_c (see Figure 3.2). This law is similar to an elastic-perfectly plastic behavior. This conventional contact model is used in this study to describe the behavior of two particles in contact.

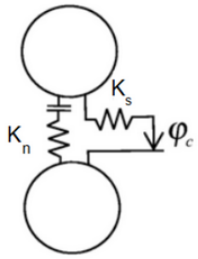

FIGURE 3.2: Interaction law at the contact used by Cundall and Strack (Cundall and Strack (1979))

Each particle is defined by its radius r, position $\overrightarrow{x}$, velocity $\overrightarrow{v}$ and its rotational velocity $\overrightarrow{\omega}$ (Figure 3.3a). When the particles are in contact, the resulting normal and incremental shear forces are determined based on the following linear contact law equations:
When $\delta_n < 0$ (particles overlap):

$$F_n^{ij(t)} = K_n {\delta_n}^{(t)} \tag{3.1}$$

$$dF_t^{ij(t)} = K_t {\dot{\delta}_t}^{(t)} dt \tag{3.2}$$

$$F_t^{ij(t)} = F_t^{ij(t-dt)} + dF_t^{ij(t)} \tag{3.3}$$

Otherwise,

$$F_n^{ij(t)} = F_t^{ij(t)} = 0 \tag{3.4}$$

Where K_n and K_t are respectively the normal and tangential stiffness of the contact between two particles, t is the current time, dt is the time increment between two simulation steps, δ_n represents the normal overlap, $\dot{\delta}_t$ is the relative shear velocity between the two overlapping elements. δ_n and $\dot{\delta}_t$ are calculated in Equations 3.5 and 3.6 respectively.

$$\delta_n = |\vec{x_j} - \vec{x_i}| - r_i - r_j \tag{3.5}$$

$${\dot{\delta}_t}^{(t)} = \vec{v_i} - \vec{v_j} + (\vec{x_i} - \vec{C}) \times \vec{\omega_i} - (\vec{x_j} - \vec{C}) \times \vec{\omega_j} \tag{3.6}$$

where $\vec{C}$ is the contact point located at $\vec{x_i} + (r_i + \|\delta_n\|/2)\vec{n}$. The Coulomb criterion is also introduced for the shear force, and F_t is limited by the following relationship:

$$\|F_t\| \leq \tan(\varphi_c)\|F_n\| \tag{3.7}$$

where φ_c is the critical static friction angle.
The mechanical response of the normal and shear contact models are described in Figure 3.3b.

The normal and tangential components of the force describing the contact between two particles are summed up with other external forces (i.e. gravitational loads) to integrate the second law of motion, in order to obtain the acceleration, velocity and finally update the position of the particles at each time step.

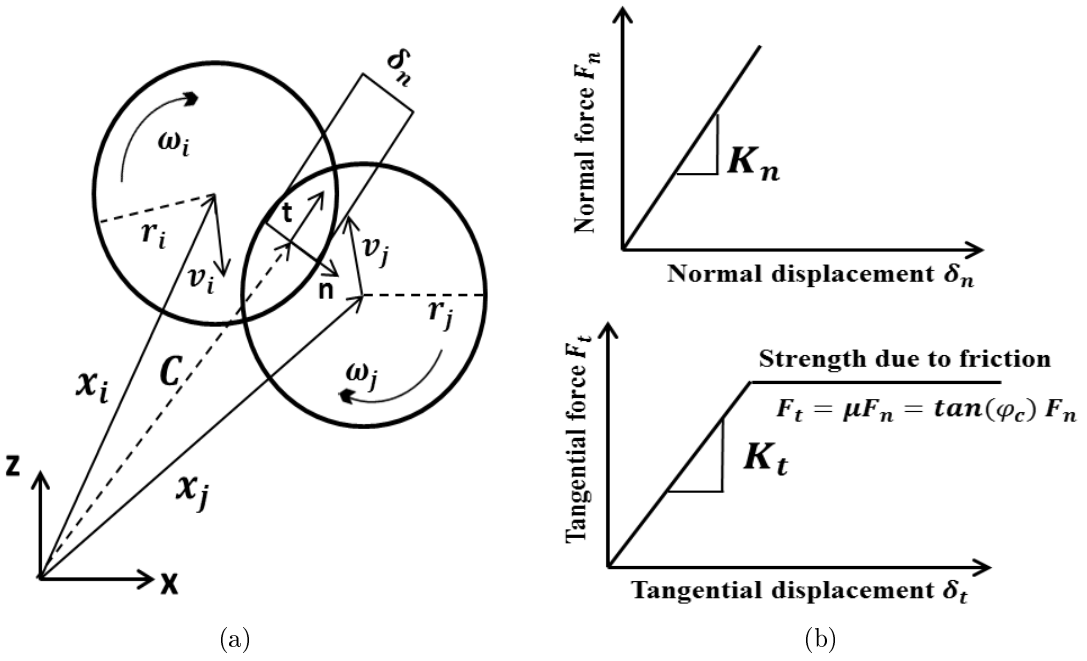

(a) (b)

FIGURE 3.3: DEM method: (a) Illustration of the DEM concept for spherical 2D particles (b) Normal and tangential contact models

- **Hertz-Mindlin contact model:** It is based on the full analytical resolution of the problem of two indenting, linear elastic bodies in frictional contact (Chareyre (2003)). A non-linear elastic relationship between the contact forces and the relative displacements at the contact are defined. The relative displacement between particles depends on the mechanical properties of the material (the shear modulus, G, and Poisson's ratio, ν). The corresponding normal and tangential stiffnesses are expressed as follows:

$$K_n^* = \frac{dF_n}{d\delta_n} = \frac{G\sqrt{2R}}{1-\nu}\sqrt{\delta_n} \tag{3.8}$$

$$K_t^* = \frac{dF_t}{d\delta_t} = \frac{2(G^2 3(1-\nu)R)^{\frac{1}{3}}}{2-\nu} F_n^{\frac{1}{3}} \tag{3.9}$$

where F_n and F_t are the normal and tangential contact forces respectively, R is the particle's radius, δ_t is the tangential relative displacement and δ_n is the normal overlap between two spheres.

These contact stiffnesses are updated at each time step of the simulation. Consequently, this may be computationally expensive, knowing that laws of constant stiffnesses, less expensive, lead to equivalent behaviors at the macroscopic scale (Cundall and Strack (1979)).

3.1.3 Stability condition

The DEM is usually based on an explicit time integration scheme implementing a central finite difference method, used for the integration of the equations of motion. In other words, it is crucial to use a sufficiently fine discretization of time Δt_{crit} in the sake of convergence towards a stable solution. At the beginning of each cycle, the critical time step Δt_{crit} is calculated as the minimum natural vibrational period of all particles. In translation, the natural period of each particle, for all the degrees of freedom, supposed independent to each other is computed as follows:

$$T_i^{trans} = \sqrt{\frac{m}{K_i^{trans}}} \tag{3.10}$$

where m is the mass of the particle, K_i^{trans} is the equivalent translational stiffness of the contacts surrounding the particle for each degree of freedom i. Therefore, the translational critical time step is given by:

$$\Delta t_{crit}^{trans} = min\sqrt{\frac{m}{K_i^{trans}}} \tag{3.11}$$

It is valuable to mention that the instability of the numerical scheme in translational motion is usually easily detected by the user and in most cases is due to the ejection of some particles away from the granular assembly.

During simulations, elastic waves are generated in the medium and propagate throughout the model. Energy should be dissipated for these waves to stop and to assure the stability of the system. However, for low amplitude waves, the medium behaves purely elastic, the friction does not dissipate energy and the waves are trapped indefinitely. Thus, the introduction of a damping may be necessary. Two forms of damping are distinguished: viscous and non-viscous dampings. On one hand, viscous damping may be introduced via normal and shear dashpots added to each contact. On the other hand, Cundall and Strack (Cundall and Strack (1979)) proposed using a non-viscous damping which acts independently to each particle to limit

their oscillation. The equations of motions are damped by adding a damping term, F^a and the dissipation of energy in the whole system is thus assured. F^a is obtained by the relation:

$$F_i^a = -\lambda^a \|F_i\| sign(v_i), \text{with } \lambda^a \in [0,1] \tag{3.12}$$

where λ^a is the damping coefficient and v_i is the translational velocity in direction i.

3.1.4 Sample generation

The generation of the packing is a very important operation since its macroscopic behavior is strongly dependent on its initial characteristics (the initial density, granulometry, homogeneity and isotropy/anisotropy of the microstructure). There are two methods to generate samples: geometric methods and dynamic methods.

- **Geometric methods:** Geometric functions are applied to particles to generate geometric granular packings. Different geometric algorithms were developed, for instance to generate sphere packing in cubical (Jodrey and Tory (1985)) or cylindrical (Mueller (2005)) containers. Using geometric methods enables the generation of dense polydisperse assemblies at a lower computational cost comparing to dynamics methods.
- **Dynamic methods:** Dynamic methods consist in determining the trajectory and the spheres' final positions of particles inside a container using the Newton's second law of motion. Different dynamics techniques exist to generate the sample, for instance particles can be deposited by gravity or by the action of external compaction load. On one hand, the gravitational method implies that particles fall under the effect of gravity. They can be released one by one in a box (Aparicio and Cocks (1995)) or placed following a given mesh (Jerier et al. (2010)). However, an anisotropic distribution of the contact orientations is obtained when using this method: the preferential orientation is about 45 ° along the direction of the gravity (Chen et al. (1988)). Moreover, this method leads to an non-homogeneous granular assembly with a looser layer at the top compared to denser layers in deep. On the other hand, the dynamic method by compaction consists firstly of creating a random cloud of granular assembly then performing a uniaxial compaction (Dutt et al. (2005)), or an isotropic compaction (Combe (2001)) or a compaction by the expansion of particles' radius (Chareyre (2003)). With this approach, the control of the packing properties can be easily assured and isotropic assemblies with a high density can be generated. For instance, changing the value of the inter-granular friction angle during compaction can modify the final density of the assembly (see Chareyre and Villard (2005)). The lower is the inter-granular friction angle, the denser the packing becomes. Nevertheless, the packing preparation is relatively costly.

3.2 Thermo-mechanical numerical model

3.2.1 Thermal and mechanical coupling for the particulate medium

Within the DEM method used in this study, the contact interaction between frictional particles is represented by linear springs in normal and tangential directions with constant stiffnesses. It was previously detailed in Section 3.1.2.

The numerical model considers that the volumetric change of the particles is due at the first order to the temperature imposed by the heated fluid and does not account for the heat transfer equations between the particles. The contribution of the fluid is taken into account by imposing transient temperature profiles as thermal boundary conditions. These temperature profiles derive from experimental data obtained on the rock-bed thermocline set-up STONE developed by the French Atomic Agency (Grenoble). The experimental results obtained on the STONE installation have shown that temperature distribution is essentially uniform radially and that considering an uniform temperature inside the particle is relevant for small particle size (Bruch et al. (2017, 2014)).

So, in order to reproduce the effect of thermal loads, the mechanical model is coupled to the thermal expansion of particles according to linear thermoelasticity. The effect of thermal expansion is introduced as a dimensional change of the particles with respect to the temperature, according to the following relationship:

$$r_i(T) = r_i(T_0)[1 + \alpha_b(T - T_0)] \tag{3.13}$$

where r is the radius of the i^{th} particle at the temperature T, $r_i(T_0)$ its radius at the reference temperature T_0 and α_b is the thermal expansion coefficient of the granular material.
Thus the normal overlap δ_n, dependent on the imposed temperature T, $\vec{x_i}$ and $\vec{x_j}$, can be calculated as follows:

$$\delta_n^{(t)}(T, \vec{x_i}, \vec{x_j}) = |\vec{x_j} - \vec{x_i}| - r_i(T) - r_j(T) \tag{3.14}$$

Where $\vec{x_i}$ is the position of the i^{th} particle.
Eventually, the calculation procedure consists in firstly determining the particle size, then computing the interacting forces once the contact occurs, and then computing the resulting particle displacement by integrating Newton's equations. The thermal loading or unloading is applied by increasing or decreasing the temperature by small increments and the simulation is run until the sample stabilizes after each increment. Then, the temperature is increased/decreased again, and so on. A schematic representation of the procedure is showed in Figure 3.4.

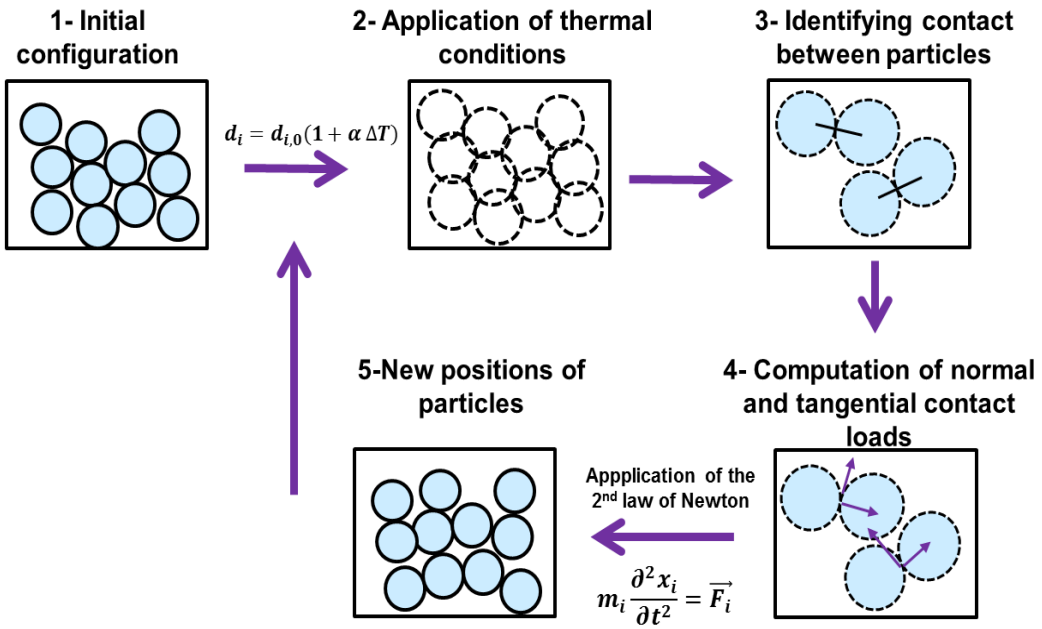

FIGURE 3.4: Schematic representation of the mechanical/thermal coupling procedure

3.2.1.1 Stress Calculation

Wall stresses are estimated using the forces applied on the walls by boundary particles. The cylindrical tank is discretized into rectangular elements defined by Dz and $D\theta$, as it can be seen in Figure 3.5. Each particle/wall force acting inside an element is distributed on its nodes, after affecting it by the opposite node area to the total element area coefficient. In such a way, the equilibrium of the problem is maintained. The forces, driven from several particle/wall contacts are summed at each node. Eventually, the stresses around each node are then computed and averaged on the circumference. For all subsequent stresses calculation, Dz and $D\theta$ are fixed to 0.15 m and 10 degrees respectively. These values provide an appropriate amount of particle/wall contacts for each element.

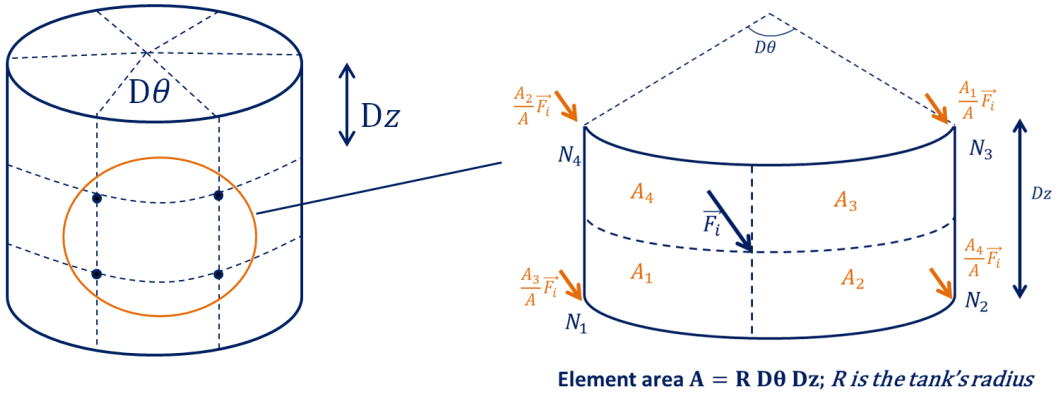

FIGURE 3.5: Stress calculation, force distribution on one element nodes

3.2.1.2 Verification and validation of the implementation

Test case: one dimensional problem

In order to verify the implementation of thermal loads in DEM simulations, a simple configuration was investigated. Five particles with an initial radius of $r_0 = 0.1$ m are considered as shown in Figure 3.6. The particles at the boundaries are fixed and unaffected by temperature variations (referred as striped particles in Figure 3.6). The gravity load is neglected, thus only the induced thermal loads are involved. The thermal expansion coefficient α_b and normal stiffness K_n of particles are respectively equal to 4 x 10^{-6} $°C^{-1}$ (i.e. Granite or Gabbro rocks (Huotari and Kukkonen (2004))) and 1 x 10^8 Pa. A total temperature variation of $\Delta T = 2°$C is applied. The resulted applied loads on the walls (represented by particles 6 and 10) are computed. It is also important to note that the Newton's equations in DEM are solved using an explicit integration scheme (Verlet scheme), so in order to ensure the integration scheme stability, the temperature is varied by applying small temperature increments δT between two temperature increments, the simulation is run until the sample stabilizes.

Hence two temperature variations $\delta\ T_1$=0.1°C and $\delta\ T_2$=0.5°C are considered to reproduce the total variation of temperature ΔT. The computed force values applied on the facets $F_{2\to1}$ and $F_{4\to5}$ (Figure 3.6) are equal in both cases and agree with the analytical solution $F_{induced} = K_n\alpha_b\Delta T r_0^2 = 0.799N$ independently from δT. From now on, the value of δT is fixed to 0.1°C in order to assure a compromise between integration scheme stability and computational cost.

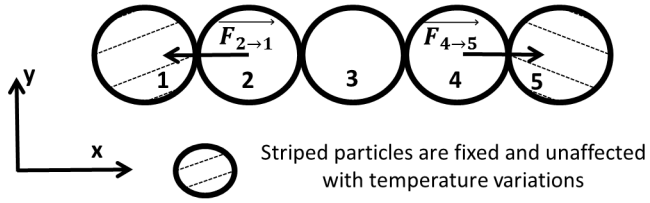

FIGURE 3.6: One dimensional simplified problem, force validation

Test case: comparison to Janssen's model

Besides verifying the implementation of thermal loads in DEM simulations, the model is compared to the statement proposed by Janssen (1895) (Janssen (1895)), in which the vertical pressure at rest measured at the bottom of a vertical cylindrical does not depend upon the height of the filling as it is the case when dealing with Newtonian fluids but it follows instead a different law which accounts for stress saturation (Schulze (2005)). The vertical and horizontal stresses can be expressed such as:

$$\sigma_z = \frac{(1-n)\rho g R}{2\lambda \tan(\varphi_s)}[1 - \exp\frac{-2\lambda \tan(\varphi_s) z}{R}] \tag{3.15}$$

$$\sigma_h = \frac{(1-n)\rho g R}{2\tan(\varphi_s)}[1 - \exp\frac{-2\lambda\tan(\varphi_s)z}{R}] \tag{3.16}$$

Where σ_z and σ_h are respectively the vertical and horizontal pressures, ρ is the bed density, g is the gravity acceleration, n is the porosity of the medium, R is the radius of the cylindrical tank, and z is the height of the column of granular bed above the level of measurement. σ_h is proportional to σ_z by the constant $\lambda = \sigma_h/\sigma_z$. φ_s is the static friction angle at the contact with the wall. The stress increases when the height of granular packed bed increases for a given width until it stabilizes and saturates in the case of slender tanks. In fact, part of the weight of the granular material is transmitted as friction loads to the walls.
Hence, various simulations of sets of mono-disperse spherical particles with a radius of 0.029 m filled by pluviation in a cylindrical tank with a diameter of D=1 m are considered. The height of packed bed H is varied and different initial slenderness ratios $S_r = H/D$ are obtained. The density of the packed bed is 2750 Kg/m^3 and the static friction angle at the wall contact φ_s is set to a value of 5°. The obtained porosity n and stress ratio λ for all sets are 0.40 and 0.75 respectively. The mechanical properties used in this section are provided in Table 4.1.

Bed density (Kg/m^3)	Particles		Wall		$\varphi(°)$	$\varphi_s(°)$	Damping (-)
	K_n (N/m)	K_t (N/m)	K_n (N/m)	K_t (N/m)			
2750	3×10^6	1.05×10^6	6.1×10^9	2.75×10^9	5	5	0.4

TABLE 3.1: Mechanical properties used in the simulations

The initial vertical and radial stresses calculated at depth z=H are presented in Figure 3.7 and are compared to the analytical solution. It has been checked that if the walls are frictionless, the vertical pressure follows the hydrostatic pressure (Schulze (2005)). As soon as the particle/wall friction angle φ_s increases, the vertical stresses diverge from the linear hydrostatic pressure (even for low values of φ_s) and they saturate for high slenderness ratios. It can be seen that the obtained vertical and radial stresses at rest agree well with the analytic solutions proposed by Janssen especially for high values of S_r.

3.2.2 Thermo-mechanical model used for tank walls

Modeling the tank walls required the usage of specific elements developed in the YADE-DEM code and able to model flexible and deformable structures. This way the tank is able to dilate/contract with temperature variations. The tank material is modeled using deformable membrane elements developed by Bourrier et al. (Bourrier et al. (2013)), and Effeindzourou et al. (Effeindzourou et al. (2016)). This model will be used in the next sections. The container walls are formed by a collection of spheres, cylinders and thick facets (called also PFacets) as

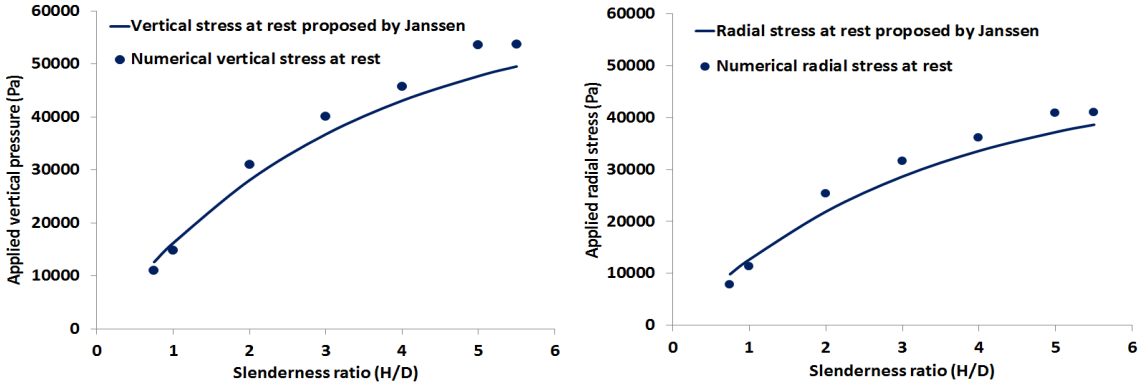

(a) (b)

FIGURE 3.7: Influence of the slenderness ratio at rest: (a) on the vertical stresses (b) on the horizontal stresses

it is depicted in Figure 3.8. An overview of the model is given below.

A cylinder is geometrically constructed by the Minkowski sum of a sphere and a segment, and

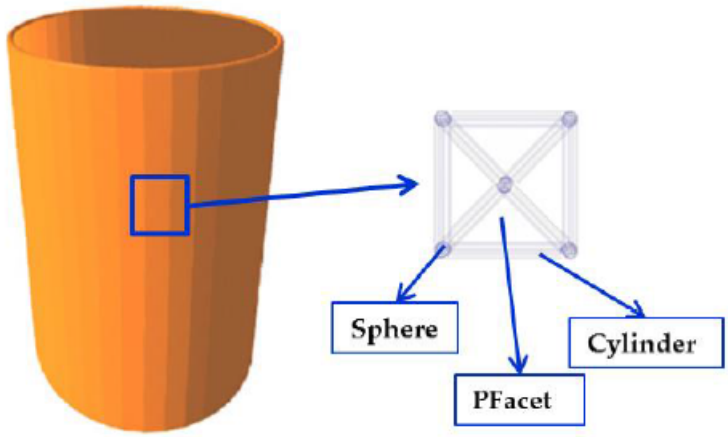

FIGURE 3.8: Cylindrical container membrane formed by a set of spheres, cylinders and PFacets

the facet corresponds to the Minkowski sum of a triangular facet and a sphere and it is formed by three nodes (spheres) and 3 connections (cylinders). The nodes behave as classical rigid discrete elements. The cylinder deformation is defined by the positions and orientations of its two nodes. The segments are massless and the masses are concentrated on the nodes. The PFacets permit the detection of the geometrical position of the contact, thus the corresponding contact overlap and forces, before distributing the forces on their nodes.

3.2.2.1 Cylinder element

The cylinder formulation identifies three types of interactions: Sphere/Sphere (interaction between two adjacent nodes), Sphere/Cylinder and Cylinder/Cylinder.
The Sphere/Sphere contact model, detailed in the previous section 3.1.2, is used to calculate the Sphere/Cylinder interaction. A virtual sphere S_c with the same radius as the cylinder is introduced at the contact (Figure 3.9). The displacement at the surface of the cylinder is

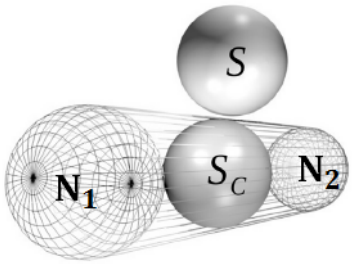

FIGURE 3.9: Sphere/Cylinder interaction, from Effeindzourou et al. (2016)

assumed to vary linearly between its two nodes N_1 and N_2. Thereby, its translational and rotational velocities at the contact, v_c and ω_c respectively, are linearly interpolated between its two nodes as follows:

$$v_c = \Lambda v_{N_1} + (1 - \Lambda) v_{N_2} \tag{3.17}$$

$$\omega_c = \Lambda \omega_{N_1} + (1 - \Lambda) \omega_{N_2} \tag{3.18}$$

$$\Lambda = \frac{\|N_1 - C\|}{\|N_1 - N_2\|} \tag{3.19}$$

Knowing all the kinematic components of the cylinder at the contact with the sphere S, equations 3.1-3.6 are reused to determine the resultant forces between S and S_c and then distributed to the cylinder's nodes. Note that, if the contact comes between a sphere and the convex part of the cylinder N_1 or N_2, the contact is simply solved as a contact between two spheres (by setting Λ to 0 or 1 for a contact between S and N_1 or N_2 respectively).

The interaction between two nodes of interconnected cylinder elements is defined to produce beam-like behavior able to withstand normal, shearing, bending and twisting loading (Kunhappan et al. (2017); Zienkiewicz and Taylor (2005)). In this case, the tensile and torsional stiffnesses of the cylinder behaving as beam element, K_n^b and K_t^b, are computed through equations 3.20 and 3.21:

$$K_n^b = \frac{E^b A^b}{L^b} \tag{3.20}$$

$$K_t^b = \frac{G^b I^b}{L^b} \tag{3.21}$$

With the exponent b refers to the beam element, E^b the tensile modulus of the beam material, and G^b the shear modulus associated with the twisting loading, A^b the surface area of the beam, I^b its polar moment of inertia and L^b its length $\|N_1 - N_2\|$.
Normal force $\vec{F_n^b}$ and twisting moment $\vec{M_t^b}$ between cylinders nodes are thus computed as:

$$\vec{F_n^b} = K_n^b(L^b - L_0^b)\vec{n^b} \tag{3.22}$$

$$\vec{M_t^b} = K_t^b \Omega_{\vec{t_{(N_1,N_2)}}} \tag{3.23}$$

Where L_0^b refers the length of the fiber segment at the stress free configuration, $\Omega_{\vec{t_{(N_1,N_2)}}}$ is the twisting component of the relative rotation between the two nodes N_1 and N_2, $\vec{\Omega}_{t(N_1,N_2)}$=$[(\vec{\Omega}_{N_1} - \vec{\Omega}_{N_2}).\vec{n^b}].\vec{n^b}$.

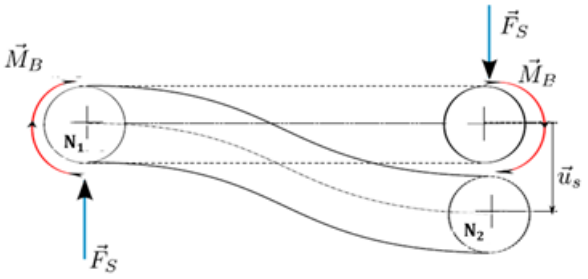

FIGURE 3.10: Coupling between bending moment and shear force in a cylinder element

Since the bending moment $\vec{M_b}$ and shear force $\vec{F_s}$ are mechanically coupled, as shown in 3.10, their rates of change are expressed in terms of the rotational and translational velocities ($\vec{v}$ and $\vec{\omega}$) of the nodes , by introducing a matrix similar to the classical stiffness matrix of a beam element used in Finite element methods (FEM).

$$\begin{bmatrix} \dot{\vec{F}}_{sN_1} \\ \dot{\vec{M}}_{bN_1} \\ \dot{\vec{F}}_{sN_2} \\ \dot{\vec{M}}_{bN_2} \end{bmatrix} = -\frac{E^b I^b}{(L^b)^3} \begin{bmatrix} 12 & 6L^b & -12 & 6L^b \\ 6L^b & 4(L^b)^2 & -6L^b & 2(L^b)^2 \\ -12 & -6L^b & 12 & -6L^b \\ 6L^b & 2(L^b)^2 & -6L^b & 4(L^b)^2 \end{bmatrix} \begin{bmatrix} v_{\vec{N}_1} \\ \omega_{\vec{N}_1} \\ v_{\vec{N}_2} \\ \omega_{\vec{N}_1} \end{bmatrix} \tag{3.24}$$

The Cylinder/Cylinder interaction requires the introduction of two virtual spheres at the contact point. The shortest distance, simultaneously perpendicular to both cylinder elements, allows the determination of the contact point belonging to both cylinders. Contact laws are thus known and the corresponding forces and moments are linearly distributed to the nodes.

3.2.2.2 PFacet element

Similarly, the Pfacets implement the Sphere/PFacet, Cylinder/PFacet and PFacet/PFacet as additional interactions.

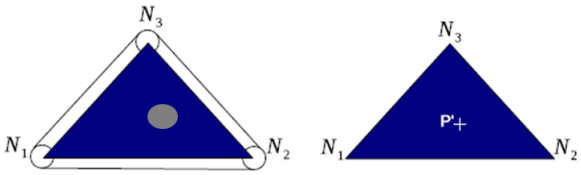

FIGURE 3.11: PFacet/Sphere interaction, from Effeindzourou et al. (2016)

For a Sphere/PFacet interaction (represented in Figure 3.11), the translational and rotational components of the inserted virtual sphere at the contact are computed using the barycentric coordinates of the contact point when the contact is identified inside the PFacet. The contact point projected in the plane formed by the PFacet nodes (N_1,N_2,N_3), P', is expressed in terms of its barycentric coordinates (p_1,p_2,p_3) as follows:

$$p_1 = \frac{\|N_1N_3\|(N_1N_2.N_1P') - (N_1N_2.N_1N_3)(N_1N_3.N_1P')}{\|N_1N_2\|\|N_1N_3\| - (N_1N_2.N_1N_3)(N_1N_2.N_1N_3)} \tag{3.25}$$

$$p_2 = \frac{\|N_1N_2\|(N_1N_3.N_1P') - (N_1N_2.N_1N_3)(N_1N_2.N_1P')}{\|N_1N_2\|\|N_1N_3\| - (N_1N_2.N_1N_3)(N_1N_2.N_1N_3)} \tag{3.26}$$

$$p_3 = 1 - p_1 - p_2 \tag{3.27}$$

The Sphere/PFacet interaction verifies the conditions $p_1 \geq 0$, $p_2 \geq 0$ and $p_3 < 1$ for a contact inside the PFacet. Thereby, the translational and rotational velocities (v and ω respectively) of the contact point P' are linearly interpolated between the three PFacet nodes:

$$v'_P = p_1 v_{N_1} + p_2 v_{N_2} + p_3 v_{N_3} \tag{3.28}$$

$$\omega'_P = p_1 \omega_{N_1} + p_2 \omega_{N_2} + p_3 \omega_{N_3} \tag{3.29}$$

If the contact is not located inside the PFacet, a Sphere/Cylinder interaction is then considered. The last Cylinder/PFacet and PFacet/PFacet interactions are handled using one of the previously mentioned interactions.

3.2.2.3 Recapitulation of all possible interactions

All types of interactions are recapitulated in Figure 3.12.

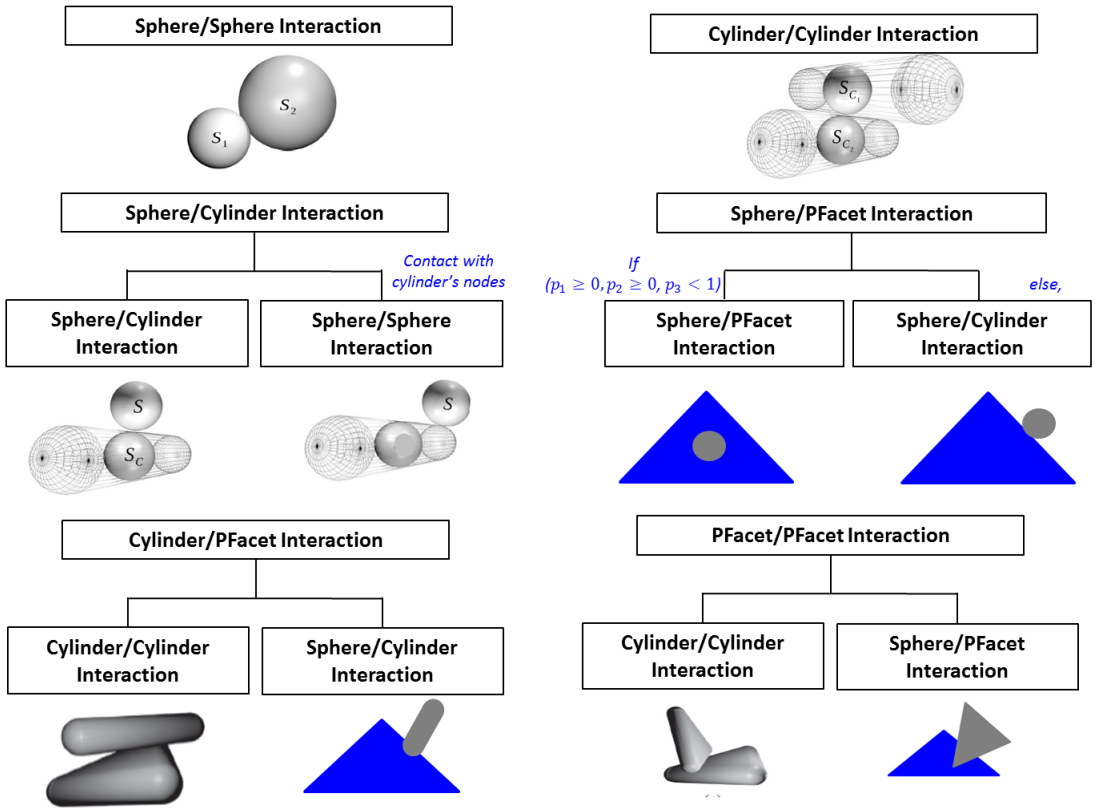

FIGURE 3.12: Recapitulating all possible interactions

3.2.2.4 Definition of physical membrane's properties

Using the aforementioned model, the tank walls are modeled as a truss structure, since only cylinders contribute to the mechanical strength. Thereby, and in order to reproduce an equivalent shell behavior, the geometry and the physical microscopic mechanical parameters of the elementary beams (Young's modulus E and Poisson's coefficient ν) are controlled in such a way that the global macroscopic behavior of the truss follows the behavior of a membrane of the desired modeled material.

The parameters controlling the macroscopic Young's modulus E^{Macro}, Poisson's ratio ν^{Macro} and thickness of the membrane are the Young's modulus E^{Micro}, the radius of the cylinders R_{cyl} and the shape of the truss. To minimize anisotropy, the membrane was designed using equilateral triangular cells. The membrane thickness e was set equal to the cylinders' diameter. The relations between E^{Micro} and E^{Macro} are identified in both vertical and horizontal directions (the directions of the principal stresses and strains due to the axisymmetric problem) and detailed in the following.

Determining E^{Macro} in the vertical direction:

When a rectangular membrane is constrained vertically (cf. to Figure 3.13), the prob-

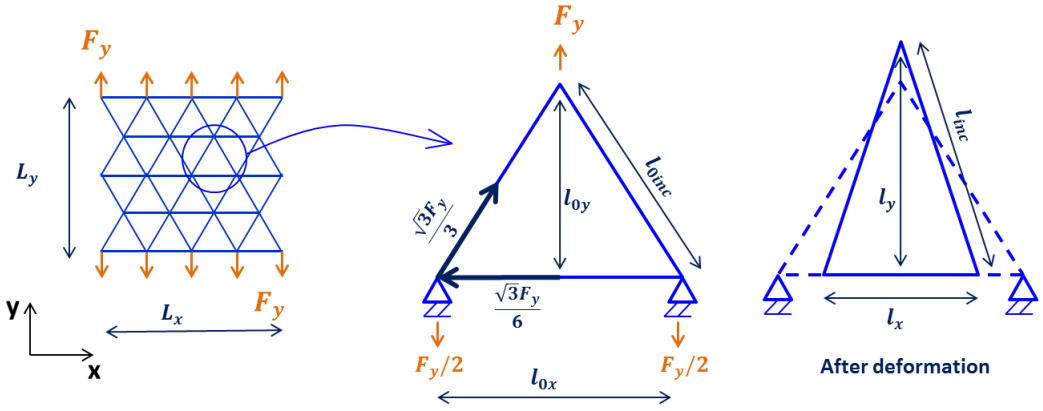

FIGURE 3.13: Rectangular plate subjected to vertical loadings

lem is symmetric with respect to the horizontal middle axis with a null displacement of nodes located at this line. Then, the elementary mesh representing the membrane deformation is reduced to a triangle with two vertically-blocked nodes, as it is seen in Figure 3.13.
The deformation, ε_{xx}, ε_{yy} and ε_{inc}, are calculated as:

$$\varepsilon_{xx} = \frac{l_x - l_{0x}}{l_{0x}} = -\frac{\sqrt{3}}{6}\frac{F_y}{\pi R_c^2 E^{Micro}} \tag{3.30}$$

$$\varepsilon_{yy} = \frac{l_y - l_{0y}}{l_{0y}} = \frac{\sigma_{yy}}{E_y^{Macro}} = \frac{F_y}{E_y^{Macro} e L_x} \tag{3.31}$$

$$\varepsilon_{inc} = \frac{l_{inc} - l_{0inc}}{l_{0inc}} = \frac{\sqrt{3}}{3}\frac{F_y}{\pi R_c^2 E^{Micro}} \tag{3.32}$$

Using the equations 3.30 and 3.32 and referring to the problem's geometry, one can establish the following relation between l_y and (ε_{inc}, ε_{xx}):

$$l_y^2 = l_{0inc}^2(\varepsilon_{inc} + 1)^2 - \frac{1}{4}l_{0x}^2(\varepsilon_{xx} + 1)^2 \tag{3.33}$$

Finally, since we are dealing with small deformations problem and using the aforementioned equations, equation 3.33 is thus written as:

$$l_y = \frac{\sqrt{3}}{2}l_{0inc}\left(1 + \frac{\sqrt{3}F_y}{\pi R_c^2 E^{Micro}}\right)^{\frac{1}{2}} = \frac{\sqrt{3}}{2}l_{0inc}\left(1 + \frac{1}{2}\frac{\sqrt{3}F_y}{\pi R_c^2 E^{Micro}}\right) \tag{3.34}$$

Eventually, the macroscopic vertical Young's modulus of the membrane is identified:

$$E_y^{Macro} = \frac{\sqrt{3}}{2}\frac{\pi R_c E^{Micro}}{L_x} \tag{3.35}$$

The Poisson's ratio in the vertical direction is thus determined as follows:

$$\upsilon_y = -\frac{\varepsilon_{xx}}{\varepsilon_{yy}} = -\frac{-\frac{\sqrt{3}}{6}\frac{F_y}{\pi R_c^2 E^{Micro}}}{\frac{\sqrt{3}}{2}\frac{F_y}{\pi R_c^2 E^{Micro}}} = \frac{1}{3} \tag{3.36}$$

Determining E^{Macro} in the horizontal direction:

Similarly to previous calculations in vertical direction, the E_x^{Macro} is identified in terms

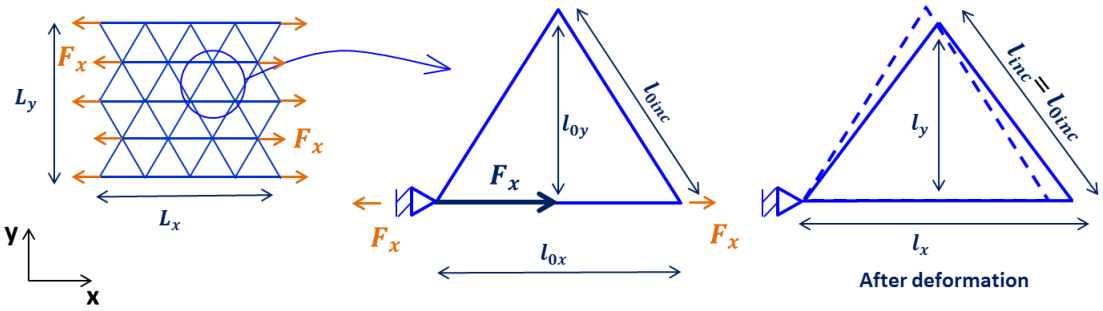

FIGURE 3.14: Rectangular plate subjected to horizontal loadings

of E^{Micro}. Nevertheless, this time the applied horizontal load F_x, as it can be seen in Figure 3.14, is directly transmitted to the horizontal bars causing the horizontal deformations ε_{xx}:

$$\varepsilon_{xx} = \frac{F_x}{\pi R_c^2 E^{Micro}} \tag{3.37}$$

At the same time, one can write:

$$\varepsilon_{xx} = \frac{F_x}{L_y e E_x^{Macro}} \tag{3.38}$$

Eventually,

$$E_x^{Macro} = \frac{1}{2}\frac{\pi R_c E^{Micro}}{L_y} = E_y^{Macro} \tag{3.39}$$

ε_{inc} is null in this case, since the resulted forces in the inclined bars are null too. The inclined bars conserved their initial lengths at the deformed shape. ε_{yy} is calculated in function of ε_{xx} through Equation 3.33, where l_y is replaced by $(\varepsilon_{yy}.l_{0y} + l_{0y})$. As a result, one can obtain:

$$\varepsilon_{yy} = -\frac{1}{3}\varepsilon_{xx} \tag{3.40}$$

And the Poisson's coefficient in the horizontal direction is thus equal to $\frac{1}{3}$.

Considering equilateral triangles to form the deformable membrane permits equal Young's

moduli and Poisson's ratios in both directions and thus the membrane will behave like an isotropic material as long as the principal directions of stress and strain remain aligned with the horizontal and vertical directions (this condition is satisfied if axisymmetry is assumed). The Poisson's ratio υ is constant in both cases and is equal to 0.33 (due to the choice of equilateral triangles).
In the subsequent work, and using these assumptions, E^{Micro} is computed in order to obtain a desired value of E^{Macro} for the membrane. Poisson's ratio is uniquely defined by the truss geometry and cannot be controlled; in the following it is 0.33 whatever the material considered.

3.2.2.5 Coupling of thermal and mechanical loadings

The implementation of thermal loads for the tank is achieved by imposing axial forces on the nodes of each cylinder element equivalent to those created by a temperature variation as follows:

$$F^{th} = \alpha_w E_{cyl} A_{cyl} (T - T_0) \tag{3.41}$$

Where α_w is the thermal expansion coefficient of the wall, E_{cyl} is the microscopic Young's modulus of the cylinder and A_{cyl} is the cross section area of the cylinder.

3.2.2.6 Verification of the implementation

The verification of the thermal implementation in the complete model is realized over two different simplified examples.

- A rectangular membrane with fixed nodes on the boundary subjected to an increase of 1°C of temperature is firstly used to verify the implementation. The resultant numerical stresses on the boundaries agree with the expected analytical solution σ=α_wE^{Macro}/(1-υ).
- An empty steel cylindrical tank with a 1 m diameter and 2 m height, subjected to a vertical thermal gradient loading is used to validate the implementation. The thermal expansion coefficient of the wall is set to $\alpha_w = 16.10^{-6}$/°C. A charging/discharging is performed with a total temperature variation of $\Delta T = 300$°C. The temperature profile along the height of the tank as well as the radial deformation of the cylindrical membrane are plotted in Figure 3.15. The tank's deformation agrees well with the temperature evolution, and the thermal gradient propagates through the height of the tank. The final attained radial deformation at the end of charging process corresponds well with the analytical predicted value $4.8 \times 10^{-3} = \alpha_w \Delta T$.

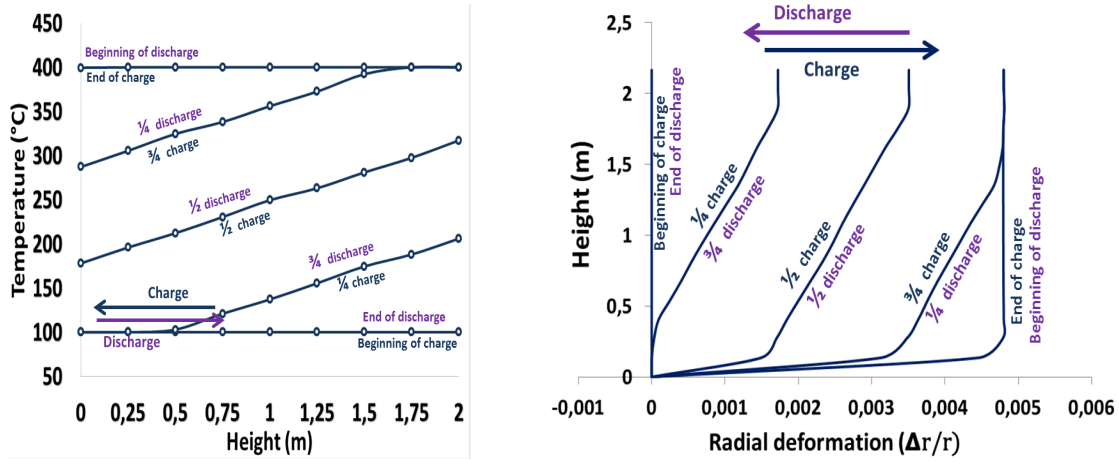

(a) (b)

FIGURE 3.15: Steel cylindrical tank subjected to thermal gradient loadings: (a) Temperature profile along the tank's height for a charge/discharge cycle (b) evolution of radial deformation of the tank along its height

3.3 Adopted numerical procedure in this study

In the next chapters, the described thermo-mechanical models are used to study the behavior of the granular medium inside thermocline storage tanks over cycles of heating and cooling. As a first approximation, the tank is considered as purely rigid and not sensitive to temperature. Thus, only the expansion and contraction of particles filling the tank are considered. Note that this assumption means that an equivalent differential expansion coefficient ($|\Delta\alpha|=|\alpha_w - \alpha_b|$) is considered with α_w null and thus $|\Delta\alpha|=|\alpha_b|$. Chapter 4 presents the numerical results obtained based on this assumption.

Then, the more complete model involving the thermo-mechanical behavior for both, particles and wall, is used. It reflects the wall ability to dilate/contract depending on temperature variations as well as the accumulation of deformations over the thermal cycles. In this case, the thermal loads are imposed on particles and cylinder nodes, by applying small temperature increments, the interacting forces are then computed enabling the determination of the new particles and nodes displacements. The numerical results using this complete model are presented in the second part of Chapter 4.

Chapter 4

Numerical results

The evolution of tank wall stresses over thermal cycles, taking into account both thermal and mechanical loads, is studied here using the numerical model presented in Chapter 3. Simulations are performed for different thermal configurations: (i) the bed is heated and cooled homogeneously along the tank height and (ii) corresponding to a functional configuration where a vertical thermal gradient moving through the storage tank is considered. Besides the different thermal configurations, different boundary conditions are considered as well.
The first section presents the results obtained with the assumption of tank walls that are unaffected with imposed temperature variations. This case will be referenced as the "Rigid boundary Case" in the following. Based on this assumption, different mechanical parameters are studied as well as different potential tank geometries.
The second part of this chapter is dedicated for the results obtained with cylindrical walls able to interact with temperature variations. Subsequently, this case is referred as "Deformable walls". Two cases are emerging: the case where the tank walls have a greater thermal expansion coefficient than the granular filler and inversely. Both cases and their corresponding results are presented in this part.
In all studied cases, the applied stresses resulting from the different loadings and boundary conditions, are compared as well as the kinematic response of the internal granular material. The kinematics of the granular material are analyzed at the particles scale (i.e. discrete elements), with a focus on the effect of particle/particle and wall/particle friction.

4.1 Rigid boundary Case

Numerical simulations are run to investigate the thermo-mechanical behavior of a packed bed in thermal storage containers according to different thermal conditions, based on the

assumption of rigid boundaries. Besides, the sensitivity of friction on the mechanical response of the bed is analyzed.

To begin with and before applying any cyclic thermal condition, the dicretization of the problem (i.e. the choice of the average radius of particle) is verified. Thus, three samples with different mean particle radius (r_{Mean}=0.025, 0.029 or 0.033 m) are generated and subjected to one cycle of charging/discharging. The size distribution for all the samples is close to the mono-disperse distribution with a ratio $r_{0max}/r_{0min} = 1.1$ where r_{0max} and r_{0min} correspond to the maximum and minimum particle's radius respectively. This distribution have been introduce to avoid "crystallization" of the granular media. The stresses applied by the granular bed along the tank's height are normalized with the hydrostatic pressure at the bottom of the tank $(1-n)\times\rho gH$ where H is the height of the packed bed and ρ is the particle density and n is the porosity of the filler medium. Then they are plotted at three different stages, namely at the initial state, and at the end of the charging and discharging processes in Figure 4.1. The temperature evolution is given in Figure 4.2a. One can see that the results are similar within r_{Mean}=0.029 and 0.025 m. For all the upcoming simulations, the mean radius of particles is fixed to 0.029 m, allowing to reduce the computational time needed without affecting the results.

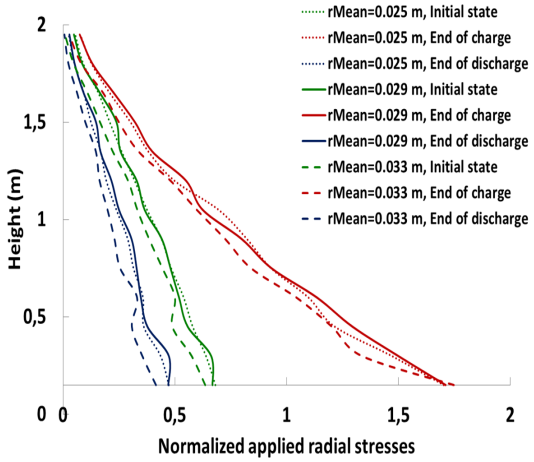

FIGURE 4.1: Influence of the mean radius particle on the resulted stresses on the wall, samples with r_{Mean}=0.025, 0.029 or 0.033 m are tested

In addition to this, the influence of the height of the packed bed inside the tank on the induced thermal stresses is also evaluated. To do so, the same samples used to confront the DEM results to the Janssen's law in the previous Chapter 3-Section 3.2.1.2, are subjected to one cycle of charging/discharging. The used parameters are recalled in Table 4.1. The samples are cycled homogeneously along the tank's height between 100 and 400°C. The bed temperature evolution along the tank's height during cycling is represented in Figure 4.2a. The thermal expansion coefficient of the bed α_b is set to $4\times10^{-6}/°C$.

Particle density (Kg/m^3)	Particles K_n (N/m)	Particles K_t (N/m)	Wall K_n (N/m)	Wall K_t (N/m)	$\varphi(°)$	$\varphi_s(°)$	Damping (-)
2750	3×10^6	1.05×10^6	6.1×10^9	2.75×10^9	5	5	0.4

TABLE 4.1: Mechanical properties used in the simulations

The induced thermal stresses after the first loading are plotted in Figure 4.2b with the initial stresses. The induced stresses increase with an increased slenderness ratio, then similarly to the initial stresses (due to gravity loads only), they saturate with large slenderness ratios. The increase of the applied stresses are related to the fact that the granular medium inside a slender tank are more restrained to displace and to rearrange than a shallower one. The saturation can be related to the fact that increasing the slenderness ratio increases the influence of the container wall friction. Thus, arches are formed inside the granular medium which makes the lower zones relatively unaffected by the upper zones.
For the following calculations, a slenderness ratio equal to 2 is chosen for the purpose of limiting the calculation time, knowing that the slenderness ratio of existed thermocline storage tanks does not exceed the value of 3 (Esence (2017)).

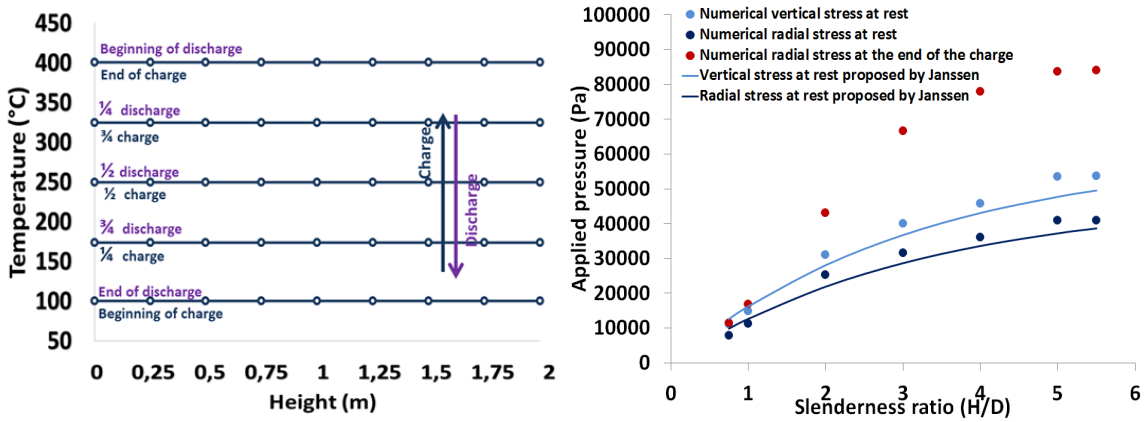

(a) (b)

FIGURE 4.2: (a) homogeneous thermal cycling along tank's height, (b) Influence of the slenderness ratio within one thermal cycle

4.1.1 Thermal cyclic conditions

The simulations consider a set of approximately 8000 spherical particles filled in a cylindrical tank (tank's diameter D=1 m, bed's height H= 2 m) by pluviation (see Figure 4.3).

Both the internal friction angle φ between particles and the static friction angle φ_s at the contact with the wall are set to 45°. A high value of friction coefficients are chosen to take into account the effect of surface roughnesses of real gravels. The initial porosity n of the whole

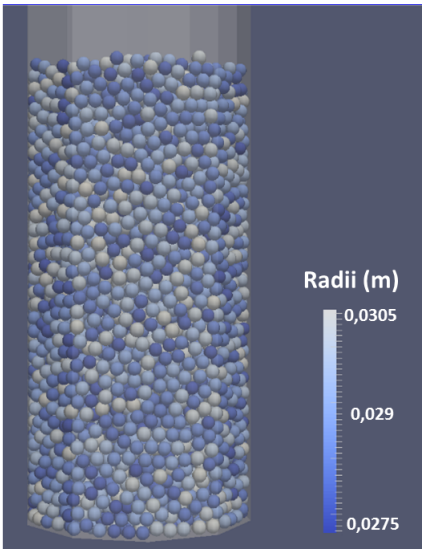

FIGURE 4.3: Cylindrical tank filled with about 8000 spherical particles with a mean radius of 0.029 m

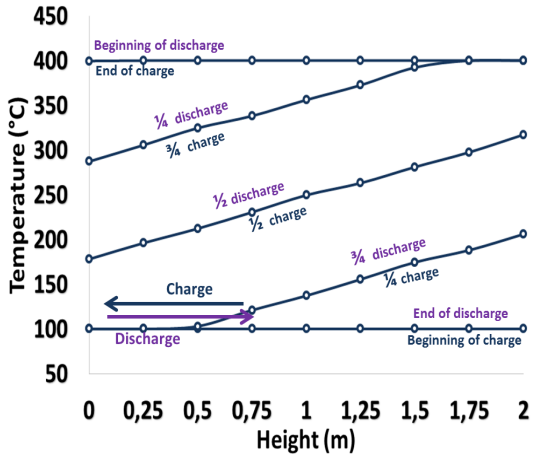

FIGURE 4.4: Thermal gradient cycling (MTG)

Mean particle Radius (m)	Particle density (Kg/m^3)	Particles K_n (N/m)	Particles K_t (N/m)	α_b (/°C)	$\varphi(°)$	$\varphi_s(°)$	Damping (-)
0.029	2750	3×10^6	1.05×10^6	4×10^{-6}	45	45	0.4

TABLE 4.2: Thermo-mechanical properties used in the simulations

packed bed is equal to 0.390. The mechanical properties used in this section are provided in Table 4.2. The tank is cycled between 100 and 400°C in two different ways: either by charging and discharging the tank homogeneously along its height (Figure 4.2a) or by considering a moving thermal gradient (MTG) that simulates either the hot fluid flowing progressively through the tank from the top to the bottom during a loading cycle or the cold fluid injected from the bottom to the top during the unloading phase. The temperature field is applied as an

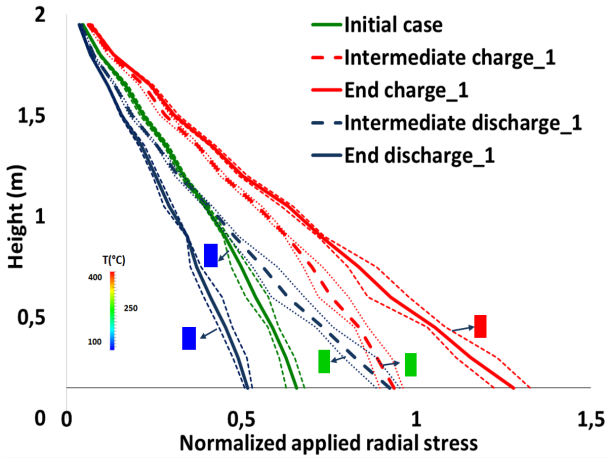

(a)

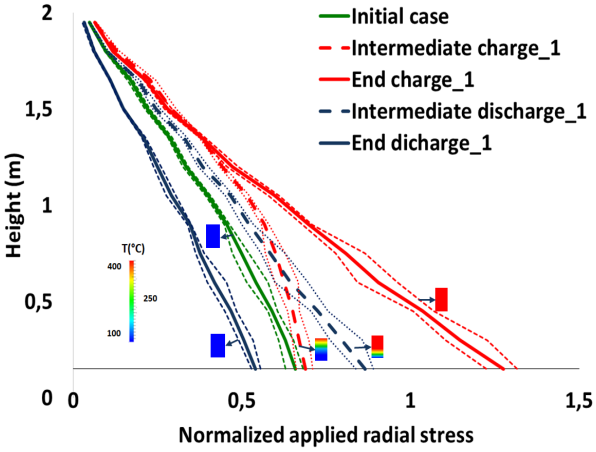

(b)

FIGURE 4.5: Normalized radial stresses evolution along the tank height within one cycle: (a) Homogeneous cycling, (b) MTG cycling, recalling that the resulting stresses are normalized by the hydrostatic pressure $(1-n) \times \rho g H$ where H is the height of the packed bed and ρ is the particle density and n is the porosity of the filler medium. The thinner dashed lines refer to the minimum and maximum values obtained in the three simulations

internal field based on experimental temperature profiles based on the rock-bed thermocline STONE set-up developed by the CEA, Grenoble (Bruch et al. (2014)). The bed temperature evolution of a MTG along the tank's height during cycling is represented in Figure 4.4.

4.1.1.1 Induced normal stresses due to thermal cyclic conditions

Thermo-cyclic tests are conducted to determine the effect of thermally induced forces. Three samples are considered to examine the influence of the stochastic nature of the generation process. Figure 4.5 shows the evolution of the radial normal stress applied to the tank wall at different times within one cycle in both processes of heating and cooling. The resulting normal stresses at each phase are averaged and presented by the thicker lines on Figure 4.5.

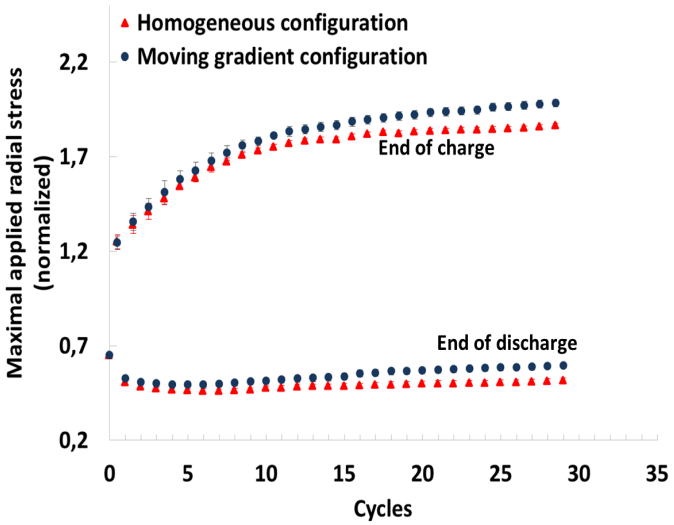

FIGURE 4.6: The maximum applied radial stress evolution along the tank height over 29 sequenced cycles for both configurations: homogeneous vs. the MTG configuration (the error bars represent the standard deviation calculated based on three initial samples with similar properties)

The resulting stresses are normalized by the hydrostatic pressure $(1-n) \times \rho g H$ where H is the height of the packed bed and ρ is the particle density and n is the porosity of the filler medium. Each curve is accompanied by a diagram indicating the temperature state inside the tank and is bounded by its maximum and minimum values of the three simulated cases (presented by the thinner lines on the figure). The blue color of the diagram refers to a cold temperature, the red color corresponds to a hot temperature and the green color stands for transitional temperatures. During loading phases and in both cases, stresses increase due to the thermal expansion of the particles and they decrease during the unloading phases to a stress state lower than the one obtained at rest (initial case). Furthermore, results show increasing stresses during loading with increasing bed depth, revealing the bed's ability to reduce generated thermal stresses through particle rearrangements close to the top free surface. In fact, particles close to the free surface are relatively free to move whereas at the bottom part of the bed, particle displacements are greatly restricted by friction through the increase of contact forces due to the weight of particles above leading to high stresses at the lowest part of the tank.

When the container is homogeneously loaded and unloaded, the applied stresses evolve homogeneously through time along the height of the tank (Figure 4.5a), while in the second case, the evolution of stresses follows the thermal gradient evolution (Figure 4.5b). For instance, at the middle of the loading process, stresses remain constant in the lower part while they increase at the top of the tank, following the temperature field (red dashed curve in Figure 4.5b).

Then a sequence of 29 cycles is run to highlight the influence of repeated cycles on the evolution of normal stresses in the tank. The averaged values of the maximum normalized normal

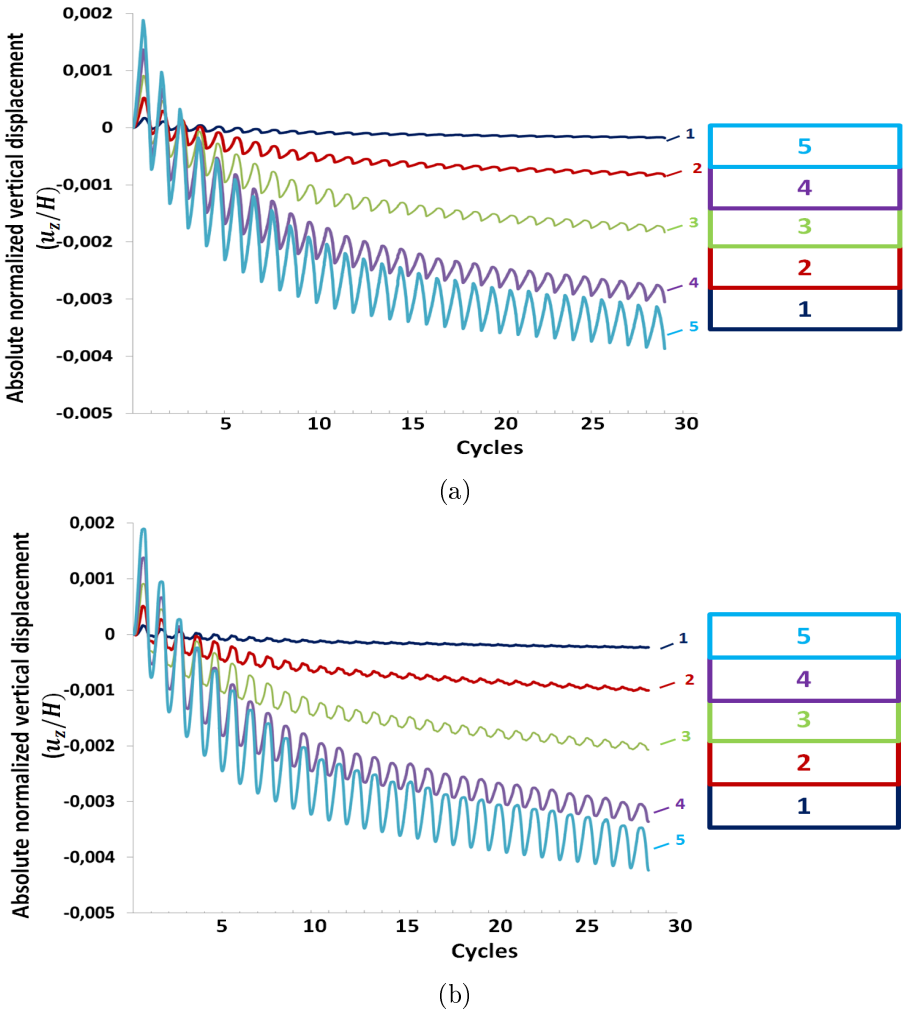

FIGURE 4.7: Vertical displacements of particles at different depths for: (a) homogeneous configuration, (b) MTG configuration

stress applied along the tank height with the corresponding error bars are presented in Figure 4.6. Cycle 0 refers to the initial state, the half cycles refer to the end of the loading cycle and the full cycles correspond to the end of the unloading phase. In both cases, the stresses are increasing from one cycle to another. At the first performed cycles, no much difference is visible between both configurations but when a larger number of cycles is executed, a clear difference appears and the stresses obtained in the MTG case are more important comparing to the homogeneously cycled case.

4.1.1.2 Vertical displacement of particles

In order to better understand the kinematics of the granular material, the tank is divided into five layers, and the corresponding averaged vertical displacement of particles u_z is computed. The ratio u_z/H is plotted in Figure 4.7 for both configurations. One can see that most of the

particles start to move upwardly when they are heated, since the upper surface is a free surface, before settling down during unloading. Furthermore, the deepest elements have almost no displacement (dark blue curves) compared to a higher displacement range for particles close to the free surface (purple and light blue curves). This result can be explained by the restriction in their movement due to a high static pressure correlating with higher stresses in the lower part of the wall tank (Figure 4.5). Also, it can be seen that the average vertical displacement of the particles is more significant when thermal gradient exists and a faster rearrangement of the particles inside the tank is observed comparing to the homogeneous configuration case. Further detailed results will be provided in the next section (Section 4.1.2).

4.1.2 Analysis of the numerical results

Regarding the complexity of the kinematical and mechanical responses of the packed bed inside the thermocline, more detailed results are presented.

4.1.2.1 Kinematical response of the bed

Figure 4.8 , which illustrates the normalized averaged vertical displacement of particles at the deepest layer of the tank for both configurations, reveals that the motion of particles in both configurations is different especially at deep. The inset figures represent a zoom of particles' displacements in deep at the 1^{st} and 25^{th} cycles. In the homogeneous case (Figure 4.8a), the kinematical response of particles is always similar and independent of their positions: particles are expanding during the loading cycle, they move upward and then they settle down in the discharge phase (inset in Figure 4.8a). However, it is not the case when dealing with a moving thermal gradient. The inset in Figure 4.8b (25^{th} cycle) shows that the averaged vertical displacement of a particle depends on its initial position and on the phase of charging/discharging process. During the charging process, the simulated effect of the hot fluid enters the tank from the top, particles at the upper layers start to move upward while particles at the bottom are still waiting for the arrival of hot fluid and show no displacement. When the "hot fluid" reaches a deep layer (but not the deepest one), particles tend to move up, but since they are subjected to a high static pressure associated to friction at the particle/wall interface, instead of moving up they push downward particles of the layer below. The particles at the deepest layer show a downward displacement (when particles above them start expanding) before moving upward (when the layer itself is heated). During the discharge process, the cold fluid starts cooling the packed bed from the bottom. So the deepest layer is the first layer to be affected by the cooling process and their corresponding particles move downward. When the cold fluid reaches the layer above, the corresponding particles start to shrink releasing the particles below and allowing them a small movement upwards due to elastic recovery. Then again, a zero displacement is shown when the discharge process is far from the designated layer.

Note that the more the deepest layer is densified over cycles of thermal loading and unloading (comparing the displacement of particles at the deepest layer at the 1^{th} and the 25^{th} cycles in the Figure 4.8b), the more the particles are confined before showing the kinematical behavior presented previously. This mechanism of elastic compression of deep layers could explain the faster settling of the particles in the presence of a MTG compared to the homogeneous heating/cooling case. Moreover, the behavior of the layer at top of the tank is similar to the usual response because here the particles are close to the free surface, and then they can easily move upward once they are heated instead of influencing on the particles in the layer below. To sum up, a thermal gradient loading provokes a faster rearrangement of particles, thus a faster densification of the medium, especially in deep layers. The more the medium is densified, the more its ability to accommodate the thermal stresses into particles rearrangements is reduced and thus, thermal stresses are generated.

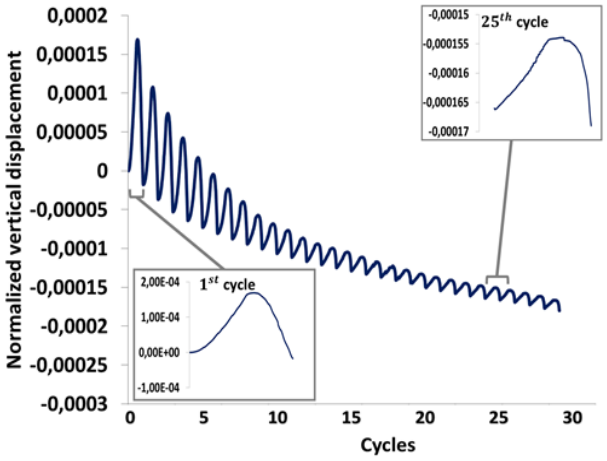

(a)

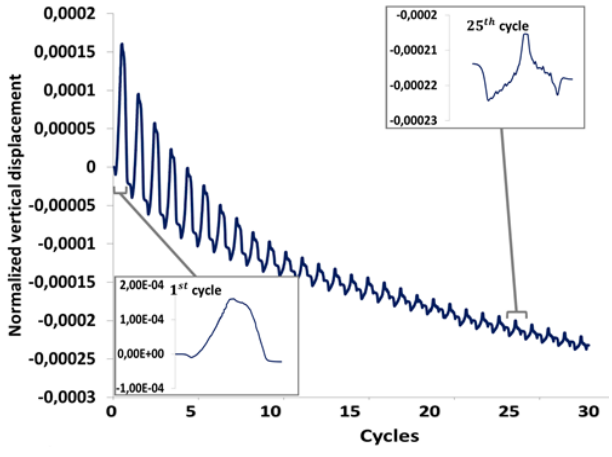

(b)

FIGURE 4.8: Vertical displacements of particles, normalized by the bed's height, at the deepest layer for: (a) homogeneous configuration, (b) MTG configuration

4.1.2.2 Evolution of tangential stresses along the tank's height

The propagation of normal stresses along the tank's height generates tangential stresses moving with the temperature gradient. The ratio of tangential stresses σ_{rz} over normal stresses σ_{rr} (known as the mobilized friction coefficient between the tank wall and the particles) is shown by thick lines in Figure 4.9 for both cases. The thinner lines refer to the maximum and minimum values of the ratio σ_{rz}/σ_{rr} obtained in the three simulated cases at different phases of the thermal cycle. Throughout the charging process, the normal stress σ_{rr} remains compressive (negative). In the initial state, tangent stresses σ_{rz} oppose gravity and therefore are directed upwards (positive). As a result, the ratio σ_{rz}/σ_{rr} is initially negative. In the fully charged configuration, the particles are dilated, which results in a general upward movement of the granular material. As a result, friction forces oppose this movement and change their directions, so that the tangent stresses point downward and become negative. The radial stresses remaining negative, the result observed in Figure 4.9 is that the ratio σ_{rz}/σ_{rr} becomes positive. After one full charge/discharge cycle, the distribution of tangent and normal stresses are close to the initial state. In the homogeneous heating case (Figure 4.9a), the mobilized friction coefficient evolves in a rather continuous manner between the loaded and unloaded states. Besides, the presence of a thermal gradient makes the distribution of tangent stresses more complex. During charging, the hot front is introduced at the top and moving downwards. The behavior visible in Figure 4.9b (red-dashed curve) can be explained by considering that particles located at the top of the tank start moving upward due to thermal dilation, resulting in the change in the sign of σ_{rz}, as explained above. Meanwhile, the particles located at the bottom of the tank remain cold and no movement is observed, which explains that the base of the σ_{rz}/σ_{rr} curve remains unchanged. Moreover, it is important to note that the particles at boundaries adhere to the tank wall: small displacements of particles occur and no sliding is observed. This can be concluded by comparing the mobilized friction coefficient to $\tan(\varphi_s) = tan(45) = 1$, which shows that the mobilized friction coefficient remains lower than $\tan(\varphi_s)$ during the thermal cycle in both configurations and verifies that there is no sliding of particles at the contact with the wall. The magnitude of tangential stresses applied on the walls is relatively small comparing to the normal produced stresses and can be neglected.

4.1.3 Influence of long term thermal cycles

In order to study the influence of repeated cycles and due to the large calculation time needed for cycling (for about 20 hours for each cycle), only one sample (with $\varphi = \varphi_s = 45°$) is cycled for a sequence of 108 loading and unloading cycles (approximately for 3 months as time calculation) in the aim of reaching the stability of the packed bed. Figure 4.10a presents the maximal normal stress applied on the tank wall over the sequence of 108 cycles and the averaged vertical displacement of particles. The accumulation of stresses over the cycles is

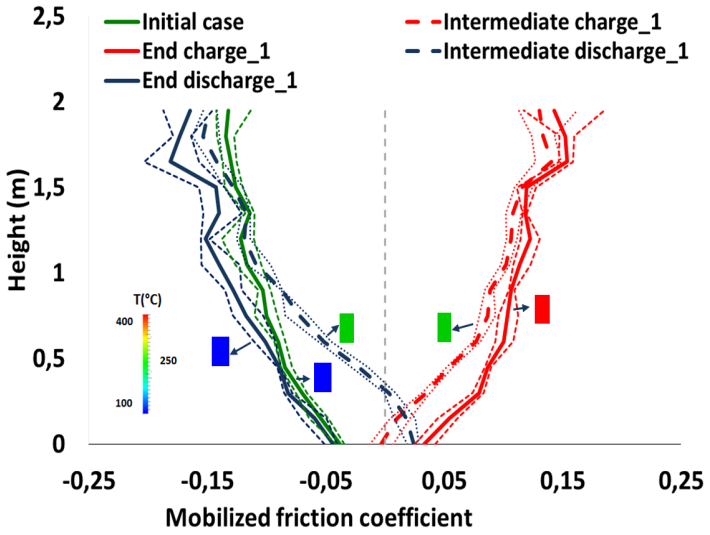

(a)

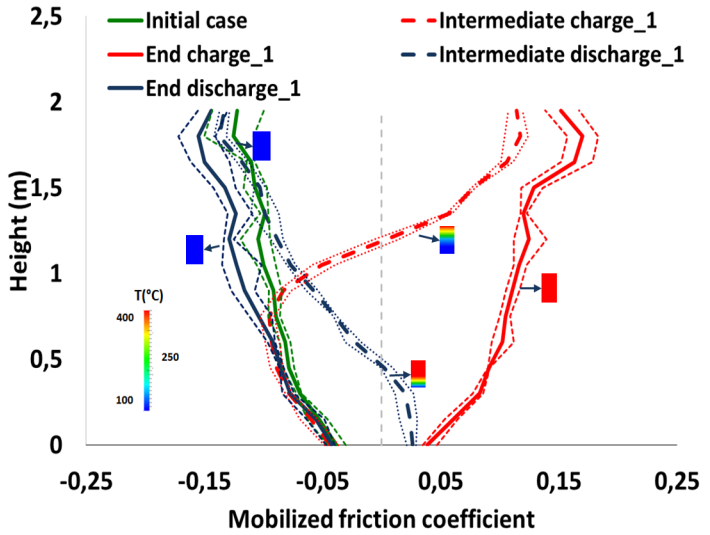

(b)

FIGURE 4.9: Evolution of the mobilized friction angle (the ratio ratio of tangential stresses σ_{rz} over normal stresses σ_{rr}) along the tank's height within one cycle: (a) homogeneous cycling, (b) MTG cycling

obvious: the normal stresses increase during both the charging and the discharging stages. Compared to the initial values, an increase in the radial stresses by a factor of 3 after 108 cycles is visible. As the particles tend to remain constant (referring to Figure 4.10b), the induced normal stresses tend to converge to a constant limit. The porosity n decreases to 0.387 compared to 0.390 initially.

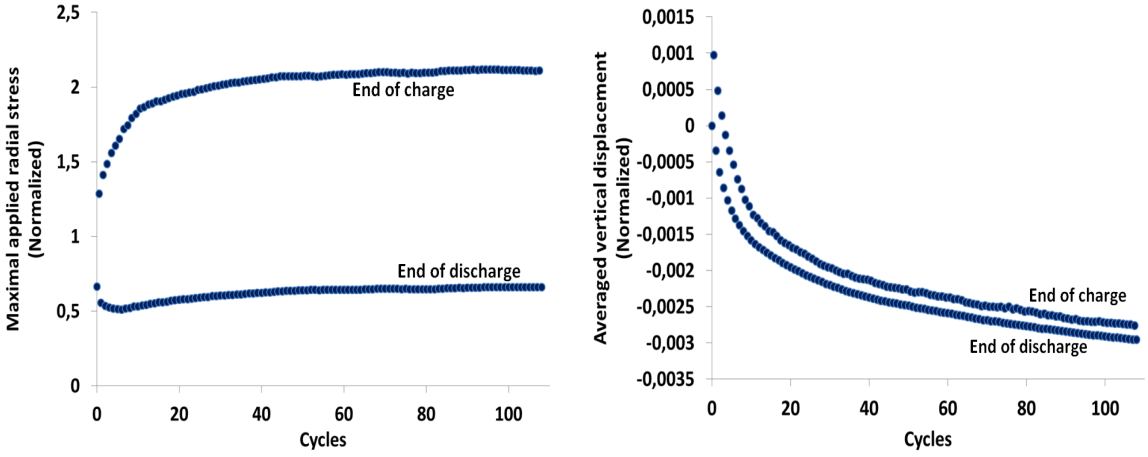

(a) (b)

FIGURE 4.10: Influence of cycling on: (a) Applied normal stresses (normalized by the hydrostatic pressure at the bottom) (b) Rearrangement of particles

4.1.4 Influence of the mechanical properties: friction angle

The influence of friction on the applied radial stresses on the tank and on the particles' displacements is investigated. Different simulations, where different values of particle/particle friction angle φ and wall/particle friction angle φ_s are considered, are also run with a MTG configuration and compared to the previously discussed case (where $\varphi = \varphi_s = 45°$). For each studied case, three samples are considered and the corresponding mean values and error bars are calculated. The evolution of applied maximal normal stresses (normalized by the hydrostatic pressure at the bottom) and the averaged vertical displacement of particles (normalized by the height of the packed bed) at the end of charging and discharging phases of 8 thermal cycles are presented in Figure 4.11. As it is depicted in Figure 4.11a, increasing the friction in the tank (whether the particle/particle φ or the particle/wall φ_s friction angles) leads to higher induced stresses. In fact, increasing the internal angle of friction between particles increases the bed shear strength and thus increases the resistance of particles to rearrangements. The increase of φ_s increases the resistance of particles to slide along the tank walls. Hence, particles inside the tank are more restricted to move and rearrange when dealing with high friction angles: as it is shown in Figure 4.11b, the averaged vertical displacement of particles is higher when low values of friction are considered. The easier the particles can move, the lower the stresses are generated. The stresses are more rapidly accumulated over the cycles of thermal loading and unloading when high friction values are considered. Note that during the unloading cycles, the induced normal stresses converge all to a lower value than the initial state independently of the friction involved in the tank.

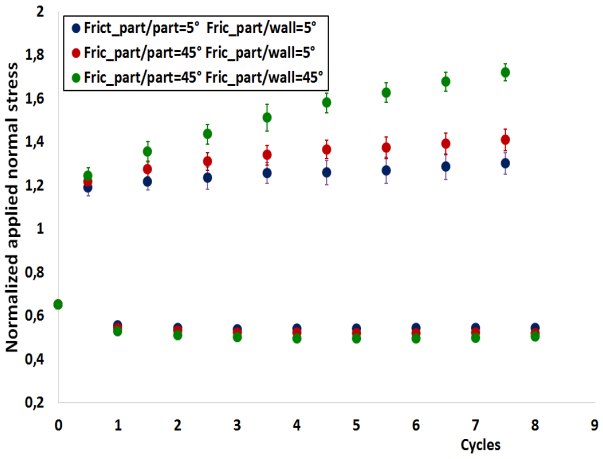

(a)

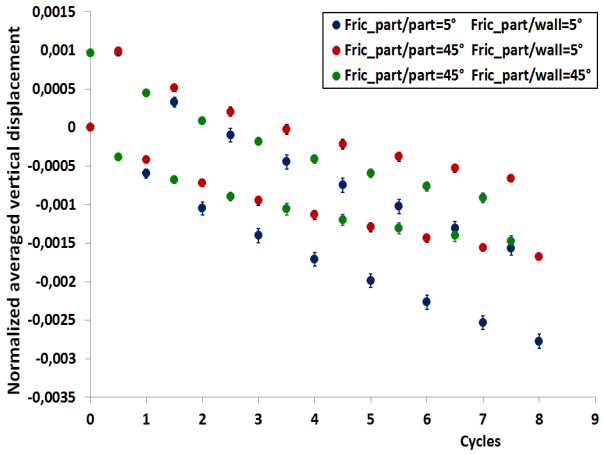

(b)

FIGURE 4.11: Influence of friction on: (a) Applied normal stresses (normalized by the hydrostatic pressure at the bottom), (b) Averaged vertical displacement of particles (normalized by the bed's height)

4.2 Deformable wall

This second part of the numerical chapter intends to present the numerical results obtained when considering tank walls capable of expanding/contracting with temperature variations. Two boundary cases are considered: the tank walls have a greater thermal expansion coefficient than the filler bed or inversely. Subsequently, these two boundary cases are modeled, considering a difference in the thermal expansion coefficient equal to $\pm 12 \times 10^{-6}/°C$ and then are compared with the rigid tank walls case. The different studied boundary cases are detailed in Table 4.3.

As before, the tank (tank's diameter D=1m, bed's height H=2m) is cycled between 100 and 400°C with different thermal configurations: the homogeneous (Figure 4.2a) and the thermal gradient (Figure 4.4) configurations. Another configuration is added to these two, where a

Cases	α_w (/°C)	α_b (/°C)	$\Delta\alpha = \alpha_w - \alpha_b$ (/°C)
Case 1 $\alpha_w > \alpha_b$	16×10^{-6}	4×10^{-6}	$+12 \times 10^{-6}$
Case 2 $\alpha_w < \alpha_b$	4×10^{-6}	16×10^{-6}	-12×10^{-6}
Case 3 Rigid boundaries	-	12×10^{-6}	-12×10^{-6}

TABLE 4.3: Different cases of boundary conditions considered in the study

"steeper" thermal gradient is applied to the tank. This configuration, which will be referred as SMTG configuration, is closer to the intended thermal configuration in a thermocline storage tank providing higher efficiency. The corresponding temperature profiles are presented in Figure 4.12. The mechanical properties for the bed particles are kept the same as in the

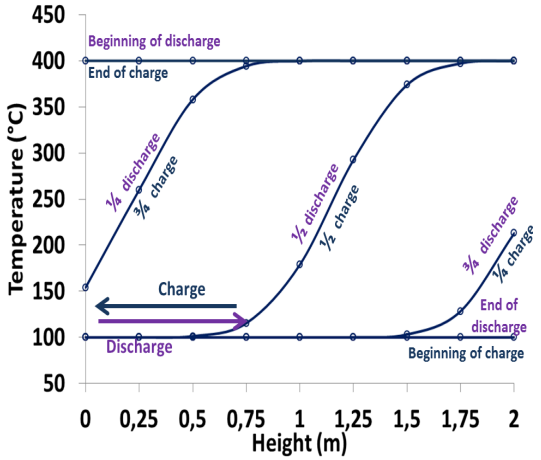

FIGURE 4.12: Steep thermal gradient configuration (STMG configuration)

TABLE 4.4: Mechanical properties for: (a) Granular bed, (b) Cylinders forming the steel membrane, see Chapter 3, Section 3.2.2.4

(a)

Mean particle radius (m)	Particle density (Kg/m^3)	K_n (N/m)	K_t (N/m)	φ (°)	φ_s (°)	damping (-)
0.029	2750	3×10^6	1.05×10^6	45	45	0.4

(b)

l_{0x} (m)	l_{0y} (m)	Cylinder radius Rc (m)	Cylinder Young's Modulus E^{Micro} (Pa)	Steel Membrane Young's Modulus E^{Macro} (Pa)	Poisson's ratio ν
0.1570	0.1354	0.01	1.811×10^{12}	210×10^9	0.33

previous part of rigid boundaries and recapitulated in Table 4.4. The mechanical properties

for the cylinder forming the membrane, listed in Table 4.4 as well, are adjusted to model a steel membrane.

4.2.1 Thermal cyclic conditions

4.2.1.1 Normal stress and tank wall deformation for the first thermal cycle

The evolution of the induced normal stresses and the radial wall deformation are presented in Figures 4.13 through 4.16 for the homogeneous and SMTG configurations. Both cases, $\alpha_w > \alpha_b$ and $\alpha_w < \alpha_b$, are compared.

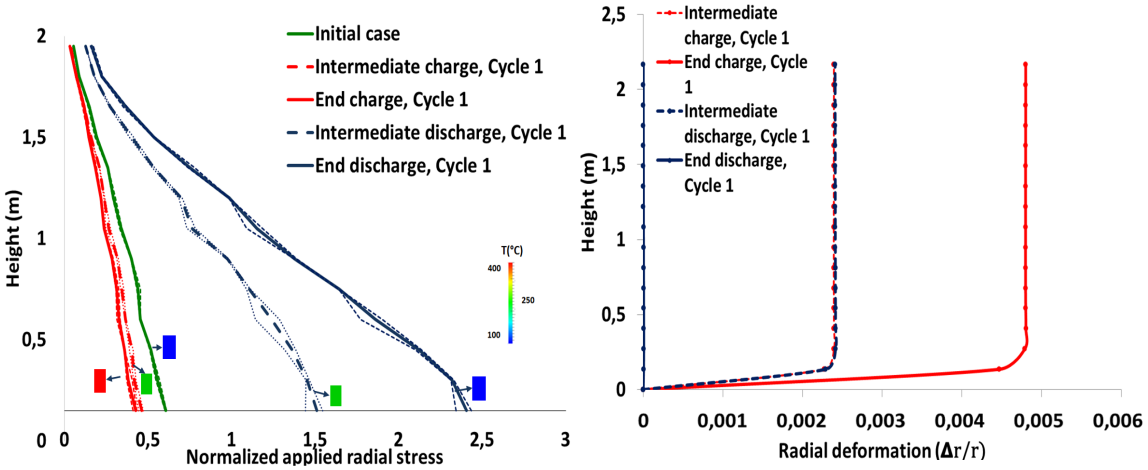

(a) (b)

FIGURE 4.13: Case 1 ($\alpha_w > \alpha_b$), first thermal cycle within an homogeneous configuration: (a) Normalized radial stresses evolution along the tank height, (b) Evolution of the tank wall deformation

The figures present the averaged values of three performed simulations. The normal stresses are normalized with the hydrostatic pressure and are plotted at different stages of the cooling/heating processes for the first thermal cycle. Each curve is bounded by the minimum and maximum values obtained within the three performed simulations. The radial deformation ($\Delta R/R$) of the tank walls is averaged over the circumference. The evolution of normal stresses and the tank walls deformation follow the evolution of temperature in the tank. For instance, Figures 4.13 and 4.14, which correspond to the homogeneous configuration, show that the normal stresses evolve homogeneously through time along the tank's height. For Case 1, $\alpha_w > \alpha_b$, the tank walls expand more than the granular particles during the charging process, relieving the stresses on the tank walls. Whilst, during the discharge cycle, the tank walls contract against the granular bed resulting in higher stresses in the wall. Inversely, in Case 2, where $\alpha_w < \alpha_b$, higher stresses are generated during the charge caused by particles expansion.

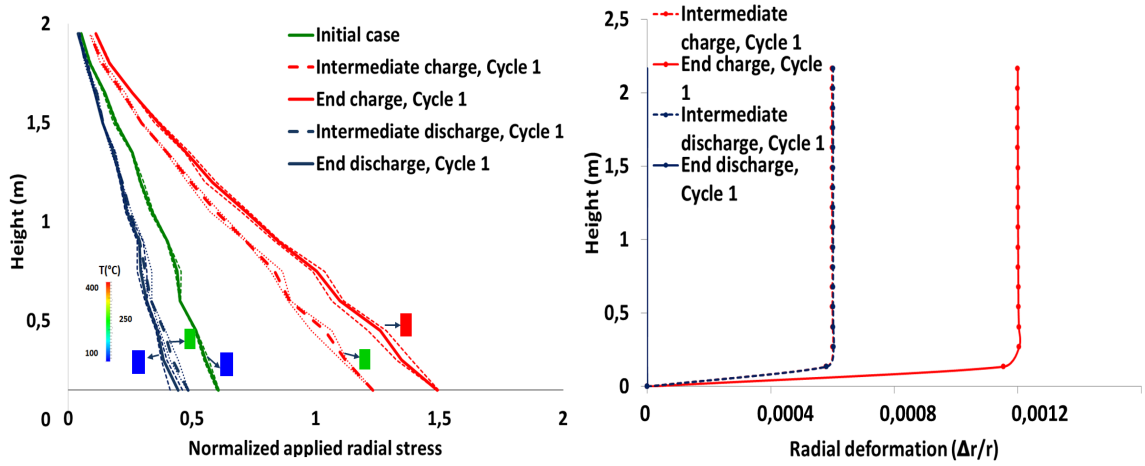

(a) (b)

FIGURE 4.14: Case 2 ($\alpha_w < \alpha_b$), first thermal cycle within an homogeneous configuration: (a) Normalized radial stresses evolution along the tank height, (b) Evolution of the tank wall deformation

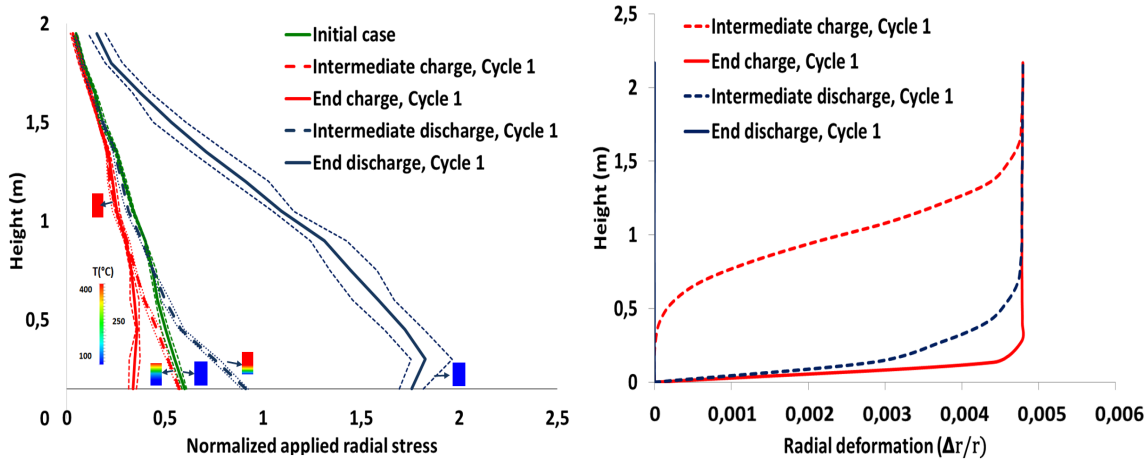

(a) (b)

FIGURE 4.15: Case 1 ($\alpha_w > \alpha_b$), first thermal cycle within a SMTG configuration: (a) Normalized radial stresses evolution along the tank height, (b) Evolution of the tank wall deformation

When a steep thermal gradient is applied, the stresses and the walls follow its evolution in the tank. Figure 4.15 shows that high thermal stresses start to generate at the bottom due to the tank's contraction at the discharge phase in Case 1 (i.e. dashed blue curve standing for the intermediate phase of the discharge). In Case 2, the thermal stresses are generated starting from the top of the tank during the charging cycle (i.e. dashed red curve, corresponding to the intermediate phase of the charging process), alongside with particles expansion, similarly to the case with rigid boundaries, discussed in Section 4.1.1.1. Note that the tank walls are blocked at the base resulting in null deformations at this level.

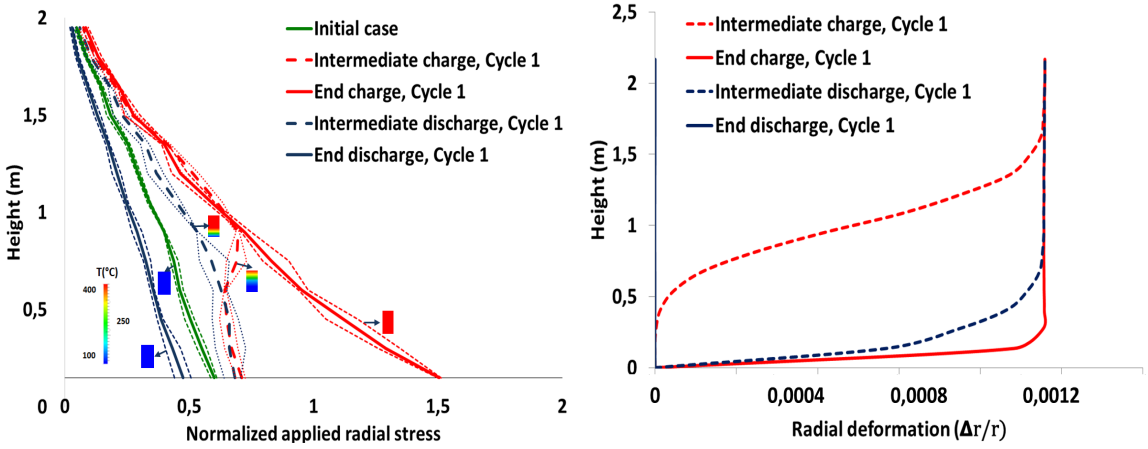

(a) (b)

FIGURE 4.16: Case 2 ($\alpha_w < \alpha_b$), first thermal cycle within a SMTG configuration: (a) Normalized radial stresses evolution along the tank height, (b) Evolution of the tank wall deformation

4.2.1.2 Influence of repeated cycles

30 thermal cycles are performed on three different samples. The influence of repeated charging/cooling cycles is investigated in both cases ($\alpha_w > \alpha_b$ and $\alpha_w < \alpha_b$) and under different thermal configurations in the subsequent sections.

4.2.1.2.1 Normal induced stresses

The maximum normalized normal stresses induced at the end of charging/discharging phases are plotted in Figure 4.17. The average values of the three simulations are presented in each

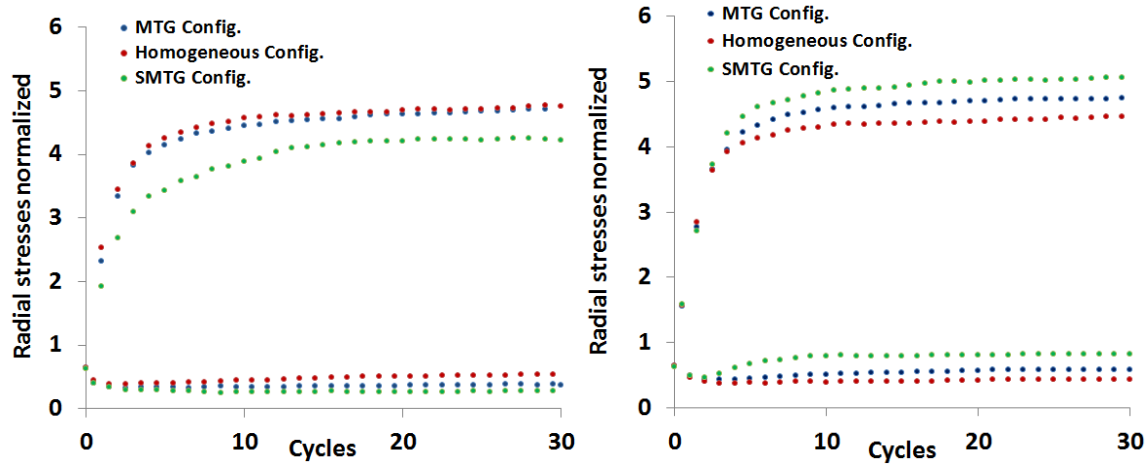

(a) (b)

FIGURE 4.17: Evolution of applied radial stresses on the tank over 30 thermal cycles, within different cyclic configurations: (a) Case 1 ($\alpha_w > \alpha_b$), (b) Case 2 ($\alpha_w < \alpha_b$)

case. The three types of thermal loadings are compared: the homogeneous, the MTG and the STMG configurations. Higher stresses are generated at the end of the discharge phases in Case 1 while at the end of the charging phase in Case 2.
Although the ability of the wall to deform with temperature variations, the induced stresses accumulate over cycles but they end by stabilizing after a certain number of performed cycles, in both cases and regardless to the applied thermal configuration. The SMTG configuration leads to the lowest level of stress in Case 1 ($\alpha_w > \alpha_b$) comparing to the MTG and homogeneous configurations. Inverted results are obtained in Case 2, where the SMTG configuration leads to the highest stresses.

4.2.1.2.2 Tank wall deformation

The evolution of the radial deformation of the wall, averaged over its circumference, is plotted in this section. The averaged values of the three simulation runs are calculated. The homogeneous and the SMTG configurations are compared in both boundary cases: $\alpha_w > \alpha_b$ and $\alpha_w < \alpha_b$. The strain accumulation occurs at the end of the discharge process in Case 1, where the walls with a higher TEC are unable to contract against the settled granulate filler. Whereas, in Case 2, the accumulation of radial strain is mainly observable at the end of each charging process. Thereafter, the accumulation of strain at the end of the discharge cycles for Case 1 and at the end of the charge process for Case 2 is shown in Figures 4.18a and 4.19a, and Figures 4.18b and 4.19b, respectively.

It is remarkable that the deformation of the wall tends to stabilize after a certain number of cycles, agreeing with the stress stabilization shown in Figures 4.17. In Case 1, the stabilization of the applied stresses/induced wall deformation seems to be faster when an homogeneous thermal configuration is applied. Figure 4.18a, referring to homogeneous configuration, shows that the radial wall deformation remains almost constant after the 10^{th} cycle, while it continues to accumulate, after 30 thermal cycles, with a SMTG configuration (Figure 4.19a). The wall deformation is slightly higher when a SMTG configurations are applied comparing to thermally homogeneous loadings (e.i. the reached value in Case 1, is approximately 1.5×10^{-5} compared to 1.3×10^{-5}, respectively). Similar observations also apply when $\alpha_w < \alpha_b$ (Figures 4.18b and 4.19b).

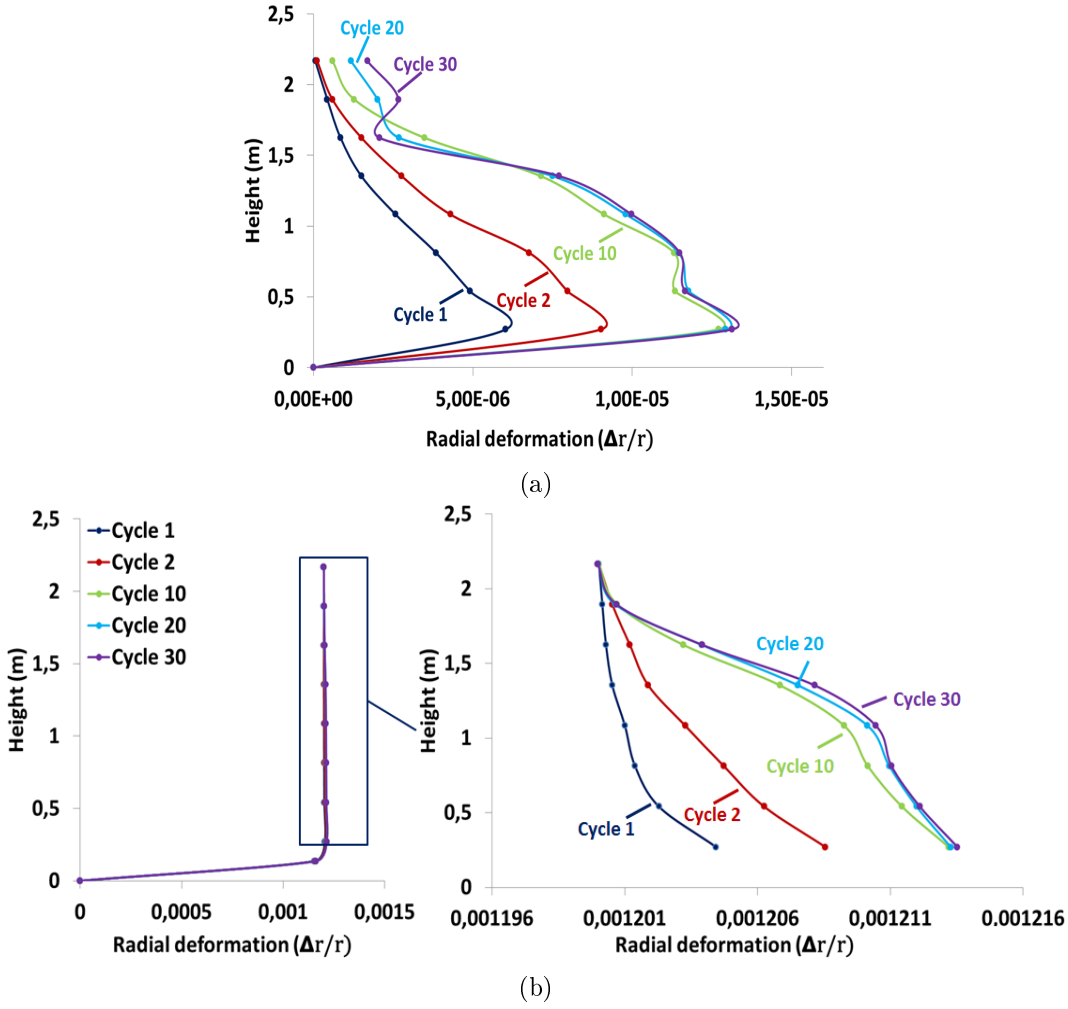

FIGURE 4.18: Accumulation of tank wall deformation over 30 thermal cycles within an homogeneous configuration: (a) Case 1 ($\alpha_w > \alpha_b$), end of discharging cycle, (b) Case 2 ($\alpha_w < \alpha_b$), end of charging cycle

4.2.1.2.3 Averaged vertical displacements

The vertical displacement in the five different layers, normalized by the bed's height, is plotted in Figures 4.20 for the homogeneous configurations and 4.21 for the SMTG configurations. Both boundary cases are considered as well :$\alpha_w > \alpha_b$ and $\alpha_w < \alpha_b$.

One can see that always the deepest particles exhibit small displacements comparing to particles close to the top free surface. Moreover, for Case 1, the tank walls expand more than the granular filler during the heating cycle, allowing the settlement of particles, revealing a downward displacement of particles at the beginning. For the subsequent heating cycles, the growth of particles (leading to upward displacements) interferes with particles settlement (leading to downward displacements) due to wall expansion. This point will be further discussed in the following section.

In the second case, where $\alpha_w < \alpha_b$, the expanded particles displace upwardly during the heating

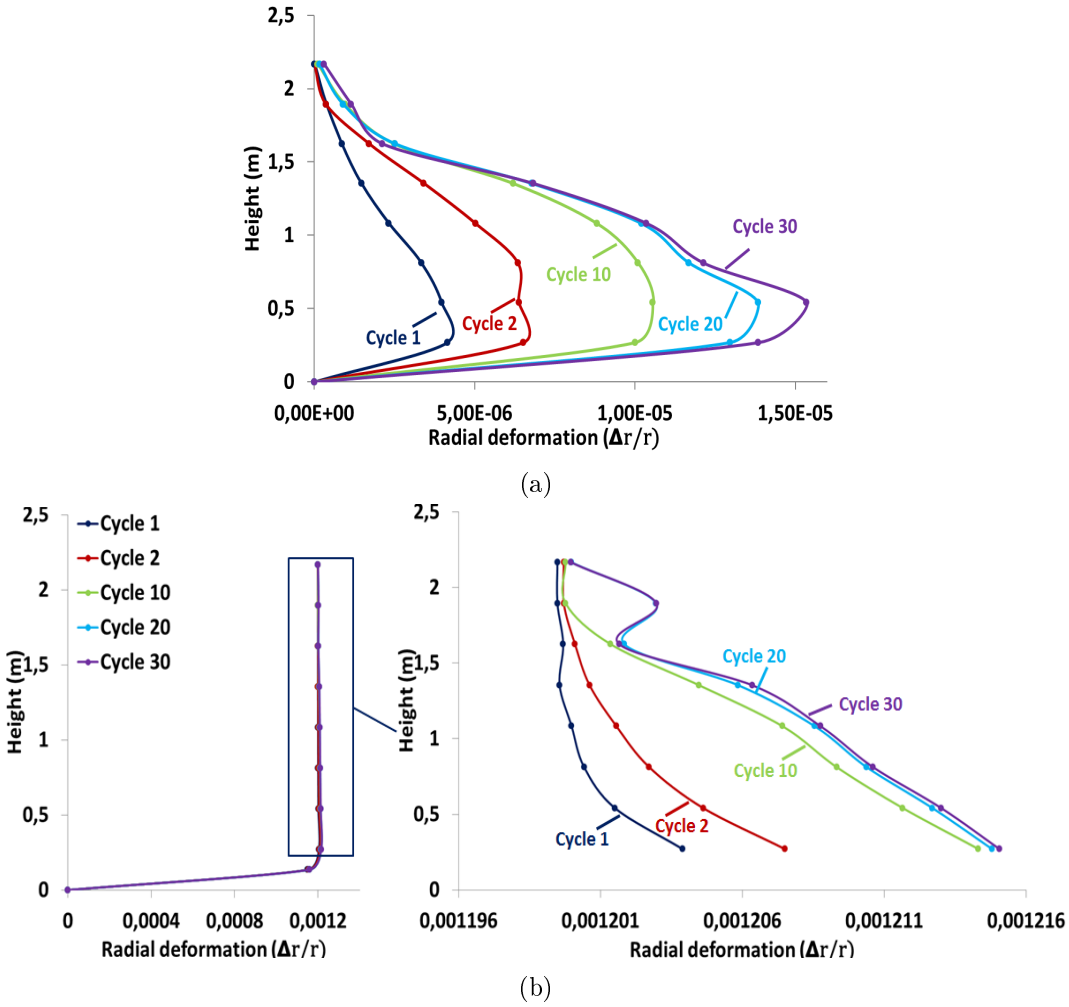

FIGURE 4.19: Accumulation of tank wall deformation over 30 thermal cycles within a SMTG configuration: (a) Case 1, end of discharging cycle, (b) Case 2, end of charging cycle

cycle and then settle down during the discharge cycle. Also, it can be seen that the average vertical displacement of the particles is slightly more significant when a thermal gradient is applied comparing to the homogeneous configuration in both boundary cases. The kinematics of the granular material inside the tank will be further investigated afterwards. The responses of the bed towards these two different thermal cyclic conditions and in both boundary case will be detailed in Section 4.2.2.1.

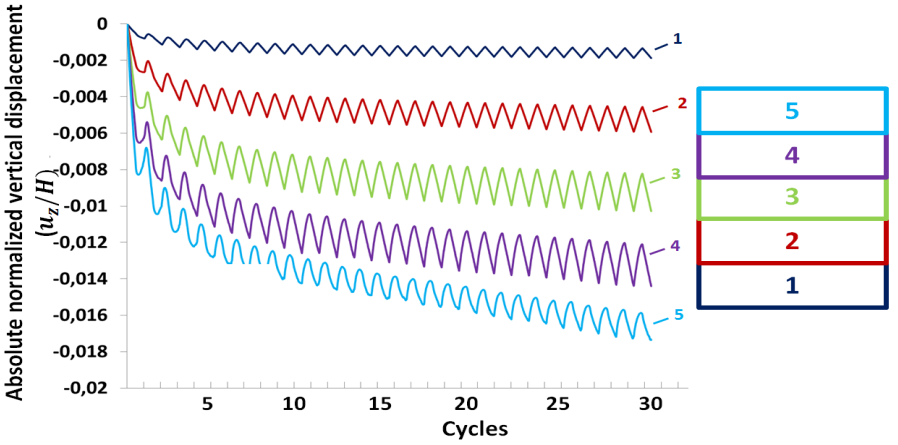

(a)

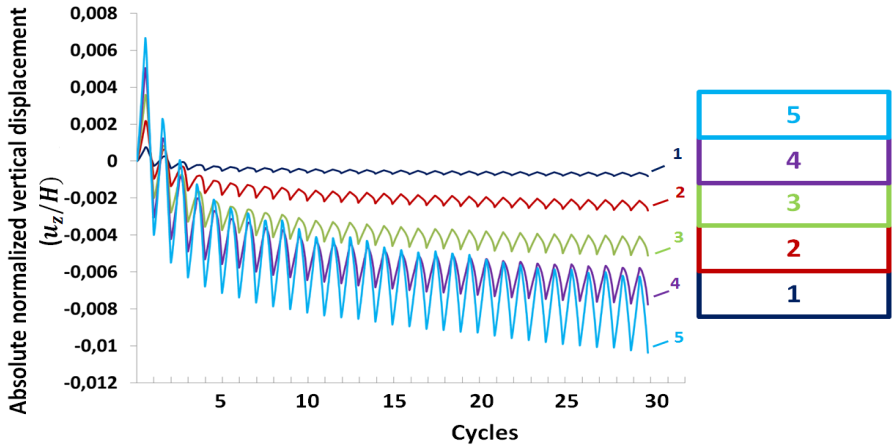

(b)

FIGURE 4.20: Vertical displacements of particles at different depths within an homogeneous configuration for: (a) Case 1 ($\alpha_w > \alpha_b$), (b) Case 2 ($\alpha_w < \alpha_b$)

4.2.2 Analysis of the numerical results

Given the complexity of the resulted kinematic responses of the granular bed inside a thermocline storage tank and their dependency on the applied thermal loads and boundary conditions, the kinematical behavior is studied in detail and then compared to the rigid boundaries cases.

4.2.2.1 Kinematical behavior of the granular bed

Globally, referring to Figures 4.20 and 4.21, the behavior of the granular bed is quite different regarding the way of heating/cooling the tank and the considered boundary conditions ($\alpha_w > \alpha_b$ or $\alpha_w < \alpha_b$). The particles motion is also dependent on their position inside the tank. It has been demonstrated (in Section 4.1.2) that the motion of the particles inside the tank

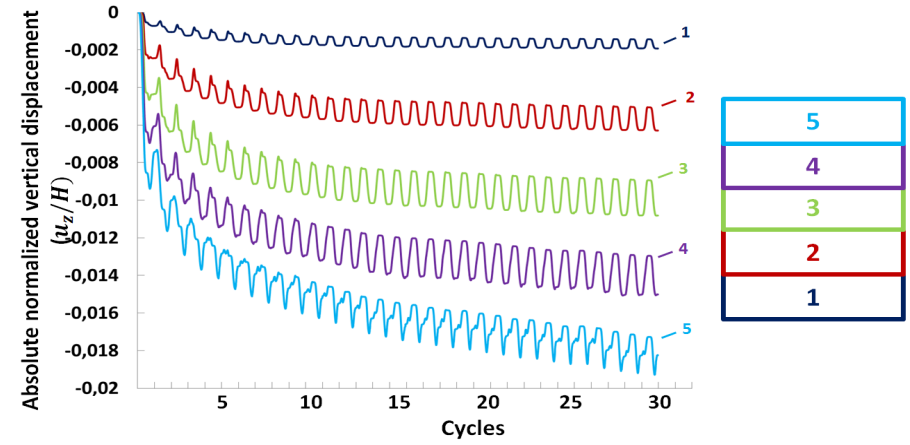

(a)

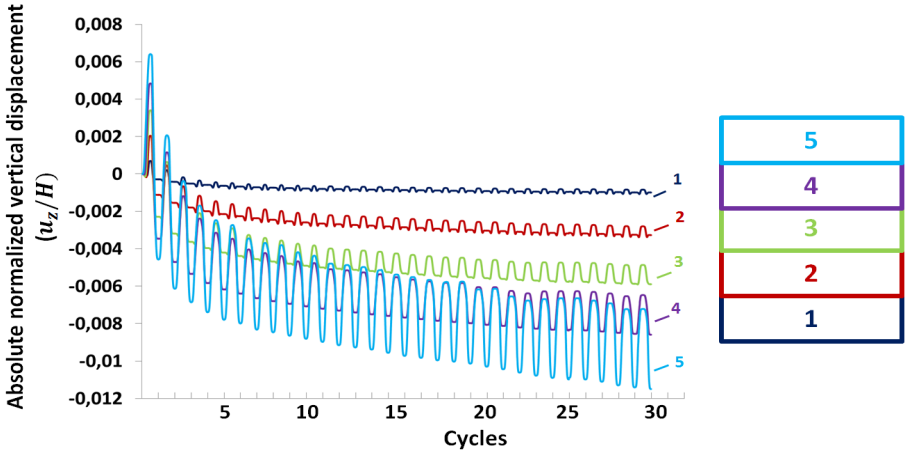

(b)

FIGURE 4.21: Vertical displacements of particles at different depths within a SMTG configuration for: (a) Case 1 ($\alpha_w > \alpha_b$), (b) Case 2 ($\alpha_w < \alpha_b$)

strongly impact the resulted stresses/strain on the tank walls, especially the response of the deepest layers. In fact, thermal stresses appear when heated particles are trapped at the bottom of the tank and cannot rearrange.

Each case will be studied separately. Moreover, the averaged displacement of each layer is considered here alone, instead of accumulating it over the bed's height, aiming at understanding the behavior of each layer apart, as mentioned in Equation 4.1.

$$\frac{\Delta u_z^n}{H^n} = \frac{u_z^n - u_z^{n-1}}{H^n} \tag{4.1}$$

Where u_z^n refers to the averaged vertical displacement of the layer n itself, u_z^{n-1} is the averaged vertical displacement of the layer just below the corresponding layer n and H_n is the height of the layer n. The quantity $\Delta u^n / H^n$ will be referred to as "relative" displacement. However it relates to the relative change in the height of a layer and is therefore similar to the vertical

component of strain. $\Delta u^n/H^n$ was used instead of the properly-defined vertical strain for convenience since it is much easier to calculate.

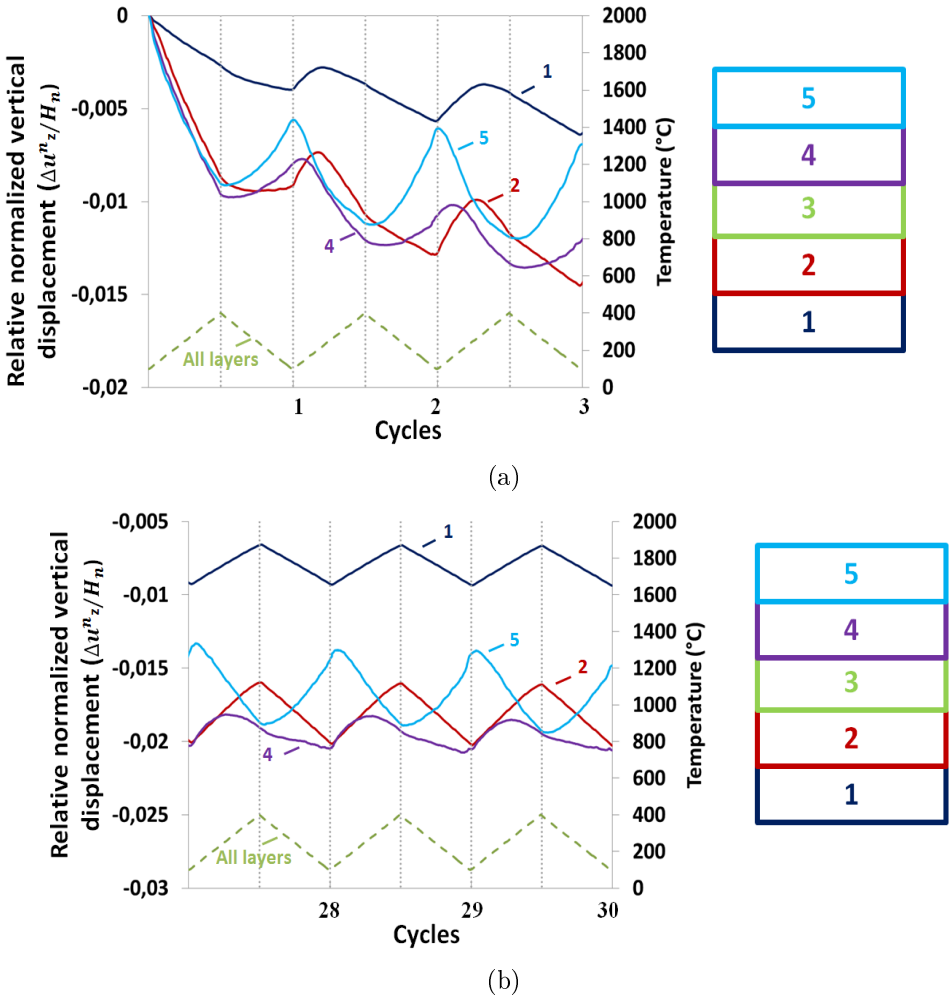

FIGURE 4.22: Case 1 ($\alpha_w > \alpha_b$): Evolution of the kinematic response of particles at deep within an homogeneous configuration for: (a) first three performed cycles, (b) last three performed cycles (the 28^{th}, 29^{th} and 30^{th} cycles), dashed lines correspond to the temperature evolution for all layers

Case 1, $\alpha_w > \alpha_b$:

- **Homogeneous configuration:** Figure 4.22 shows the evolution of particles motions at the different considered layers, where only the first and the last three thermal cycles are plotted. The middle layer (0.8-1.2 m) is deleted not to overload the figure, but its motion trends can be deduced from the motion of the layers bounding it. Also, dashed lines are plotted, separating successively the charging and the discharging processes. The temperature evolution, identical for all the layers, is added in dashed green line too.

As a starting point, it is remarkable that in Figure 4.22b, layers 1 and 2 (bottom) follow the temperature variations while layer 5 (top) behaves in an opposite manner (shrinking upon heating and expanding upon cooling). Recalling that Figure 4.22b is related to the stabilized configuration after 27 cycles, this behavior can be understood in the following way.

Layer 5, located at the top, behaves like an unrestrained layer: upon heating, the tank expands more than the filler, and the filler settles down (shrinkage in the vertical direction associated to expansion in the horizontal directions). Upon cooling, the wall shrinks, causing shrinkage of the filler in the horizontal directions and expansion in the vertical direction. Layer 1 behaves like a totally constrained layer: After many cycles, the filler settles down, and because of the layers above, cannot recover. Contrarily to Layer 5, the particles in Layer 1 are prevented to rearrange during cycles in the stabilized regime. Therefore, at the discharged state the tank applies a great pressure on the filler but its diameter cannot decrease much below the diameter imposed by the cold filler's particles. In such a case, the deformation of Layer 1 is dictated mainly by thermal expansion of the particles, and therefore follow the temperature profile. Layers 3 (not shown) and 4 behave in-between. In particular, Layer 4 starts expanding vertically during charging (due to thermal expansion of the particles) and then starts to shrink before the end of the discharge phase. The filler is expanding while the stress applied by the tank is released with the increase in temperature. At some point, the stress is released and the tank expands (its diameter increases) liberating the particles which start rearranging and settling down like in Layer 5.

Once this process is understood, the behavior in the first cycles shown in Figure 4.22a can be better understood by considering that the same mechanisms are at stake. However, there is also a global densification of the medium due to thermally-induced rearrangement, adding a decreasing trend to all the curves of Figure 4.22a compared to Figure 4.22b. In particular, the expansion of Layer 1 during first charge is made totally invisible during the first charge. However, it starts appearing in the second charge and it is even more visible in the third charge.

- **SMTG configuration:** The vertical relative displacement, appropriate for each layer, is plotted at the first and the last 3 cycles (Figure 4.23). The temperature evolution, in dashed color lines, is added too. Light gray lines separate the charging and discharging cycles.

  At the first charging cycle, all layers show a vertical shrinkage, linked to the wall expansion with heat. Then, during the first discharge cycle, the particles at bottom are the first to shrink, thus they move down. The particles of the layers above start by shrinking vertically upon cooling before exhibiting a vertical expansion when the tank starts to shrink.

  During the second charging cycle, the layers at top settle down as the wall expands. The

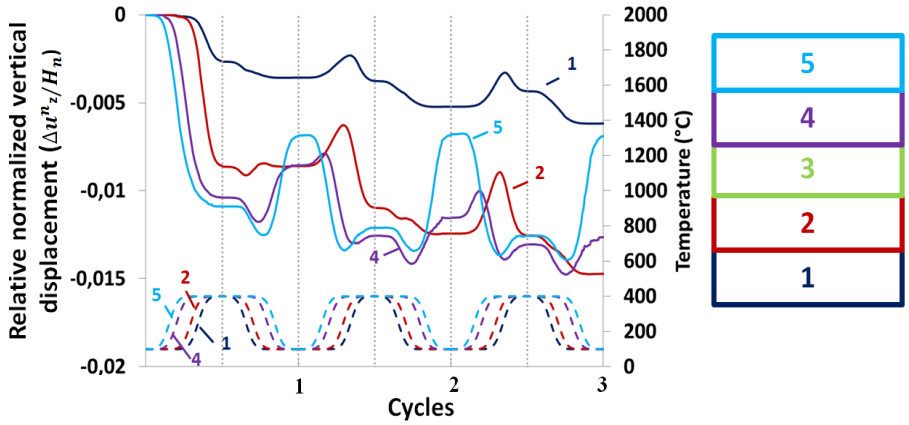

(a)

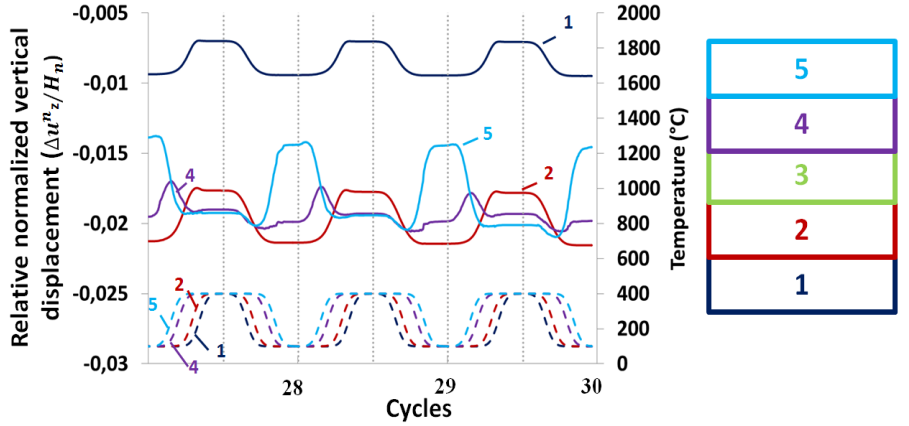

(b)

FIGURE 4.23: Case 1 ($\alpha_w > \alpha_b$): Evolution of the kinematic response of particles at deep within a SMTG configuration for: (a) First three performed cycles, (b) Last three performed cycles (the 28^{th}, 29^{th} and 30^{th} cycles), dashed lines correspond to the temperature evolution for each layer

layers below start to expand vertically, even before the hot fluid reaches their level in the tank. This vertical expansion of the deepest layers is with perfect synchronization with the vertical shrinkage of the top layers. In fact, during the charging cycle, the settlement of the top layers (i.e. vertical shrinkage of the top layers) results in a release of the deepest layers leads to a vertical expansion of the deepest layers (see Figure 4.24a). Then, when the hot fluid reaches these deep layers, the particles grow (showing an additional vertical expansion) before settling down with the tank expansion. During the next discharge cycle, the particles at the bottom are the first to shrink, going along with a vertical shrinkage of the deepest layers. This vertical shrinkage is also visible in the top layers (Layers 4 and 5) although the fluid has not reached their levels yet. This behavior of the layers at top at this period of the cooling cycle remains incomprehensible for us. Then, by the end of the cooling cycle, the layers at bottom continue to settle

down (i.e. vertical shrinkage of the corresponding layers) while the unrestrained layers at top exhibit a vertical expansion due to the wall contraction.

As it was shown in the homogeneous configuration, the relative displacement of the deepest layers, converges to a vertical expansion during the charging cycle and a vertical shrinkage during the cooling cycle, the particles being unaffected by wall deformation (that ends by stabilizing over the thermal cycles). In fact, Figure 4.23b shows that all the layers converge towards theses motion trends that occur firstly at the deepest layer and lately at the top surface layer. This behavior would be reached when the tank reaches its final equilibrium state: the stresses and the tank deformation stabilize as well as the internal movements of the granular filler.

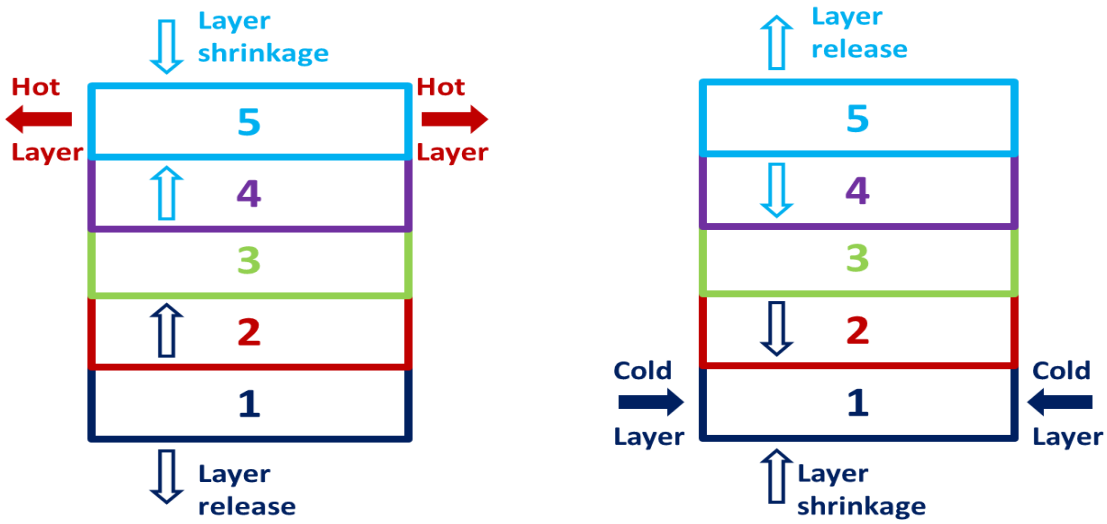

FIGURE 4.24: Schematic diagram explaining the opposite behaviors of bottom and top layers: (a) During the charging cycle , (b) During the discharge cycle

The maximum stresses generated at the tank are affected by the motion of the particles at the deepest layers. Thus, Figure 4.25 shows the evolution of the displacement of the particles at deep over the 30 thermal cycles. The convergence of the motion of this layer to an upward displacement during the charge and a downward displacement during the discharge is faster when dealing with a homogeneous configuration. This means that within this configuration, the particles are rapidly unaffected by the wall movements (that can be shown with the rapid strain stabilization in Figure 4.18a comparing to a SMTG configuration, Figure 4.19a). This might explain the higher stresses obtained with thermally homogeneous loadings.

Case 2, $\alpha_w < \alpha_b$**:**

- **Homogeneous configuration:** Figure 4.26 shows the evolution of the vertical relative displacements of the different layers by comparing their behavior at the first to the

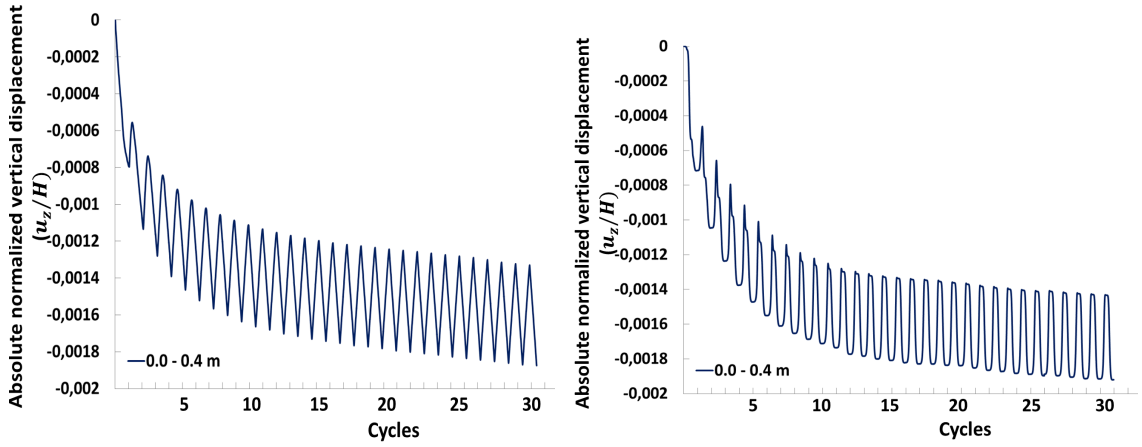

FIGURE 4.25: Case 1 ($\alpha_w > \alpha_b$): Evolution of the kinematic response of particles at deep for: (a) homogeneous configuration, (b) SMTG configuration

last three cycles. In this case, all layers show similar behaviors regardless the number of performed cycles: a vertical expansion during the charging cycle (coming with the particles growth) followed by a vertical shrinkage during the discharge cycle as the particles shrink. Note that, referring to Figure 4.26a, the vertical shrinkage of the deepest layers (Layer 1 and 2) is gradually appearing upon the first cooling cycles, while it is more brutal (going along with the temperature decrease) in Layers 4 and 5 (at top). Then, after performing 30 thermal cycles, the gradual vertical shrinkage appears in the layers at top (Layer 4) at the beginning of the cooling phases, while the deepest layers shrink vertically following the temperature variations (see Figure 4.26b). This might be linked to the gradual stabilization of the thermolcine tank, starting from the bottom layers and ending by the top ones.

- **SMTG configuration:** Within a SMTG configuration, the temperature profiles are added to the particles relative displacement aiming at simplifying the understanding of the complex behavior of the granular bed. The kinematical behavior of the bed in this case ($\alpha_w < \alpha_b$) is very similar to the case of rigid boundaries, detailed in Section 4.1.2. After performing a certain number of cycles, the bed becomes denser and the particles at the deepest layer restore a part of the downward displacement during the discharge cycle (i.e. the vertical expansion shown during the cooling cycles for Layer 1 in Figure 4.27b). This mechanism of elastic compression that occurs when dealing with a progressive thermal gradient configurations, allows for a faster settlement of the particles at bottom, compared to the homogeneous configuration (see Figure 4.28). Moreover, it is important to note that an inverted behavior is shown when comparing the behaviors of the top and bottom layers during the discharging process. Referring to Figure 4.27b, the negative peak (concave peak) of the deepest layers synchronizes with the positive peak (convex peak) of the surface layers. When the deepest layers shrink

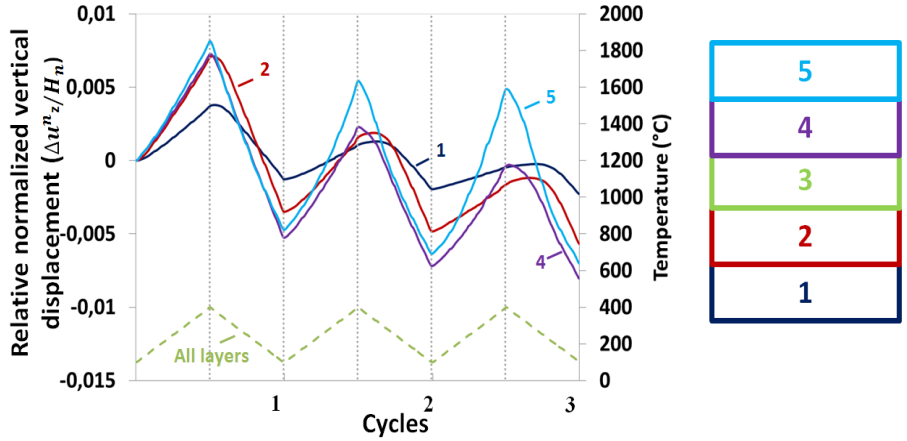

(a)

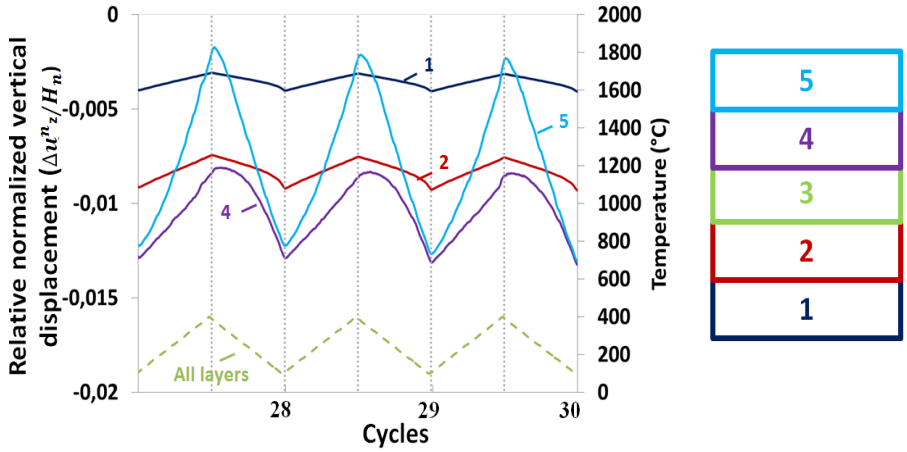

(b)

FIGURE 4.26: Case 2 ($\alpha_w < \alpha_b$): Evolution of the kinematic response of particles at deep within an homogeneous configuration for: (a) first three performed cycles, (b) last three performed cycles (the 28^{th}, 29^{th} and 30^{th} cycles), dashed lines correspond to the temperature evolution for all layers

due to cooling, they liberate the top layers leading to their vertical expansion and vice versa (Figure 4.24).

Comparing the induced stresses within Case 2 for both thermal configurations, higher stresses are obtained when a SMTG configuration is applied. The reason behind is most likely linked to the kinematical behavior of the particles at deepest layers, as it was detailed in the rigid boundary Case (Section 4.1.2).

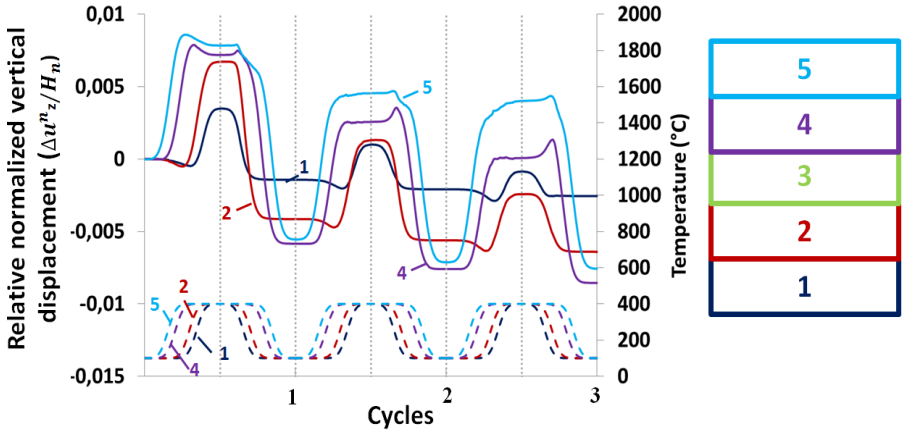

(a)

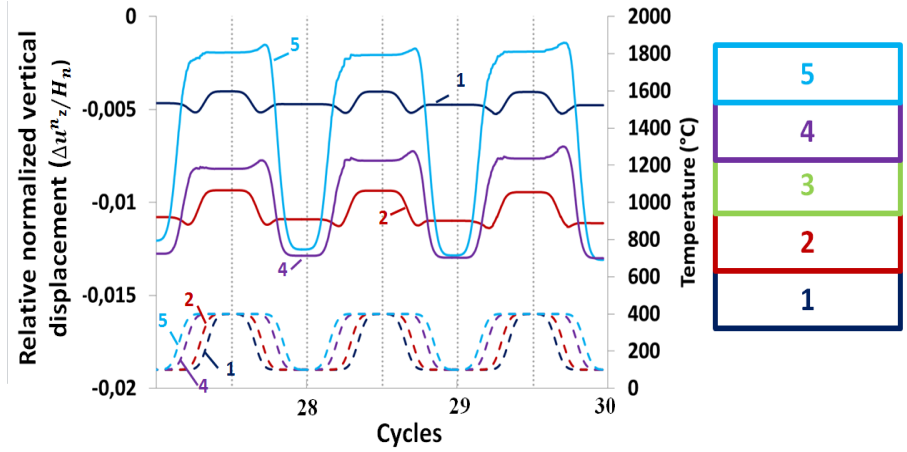

(b)

FIGURE 4.27: Case 2 ($\alpha_w < \alpha_b$): Evolution of the kinematic response of particles at deep within a SMTG configuration for: (a) First three performed cycles, (b) Last three performed cycles (the 28^{th}, 29^{th} and 30^{th} cycles), dashed lines correspond to the temperature evolution for each layer

4.2.2.2 Comparison with rigid boundaries Case

The previously presented results has shown that the behavior of the bed towards different thermally studied configurations in Case 2 is very similar to the rigid boundaries Cases. Besides, and in order to better compare, and in a more quantitative way, the results obtained with deformable walls to the rigid case, new simulations with rigid boundaries are run considering a $|\Delta\alpha| = 12 \times 10^{-6}/°C$. Only the MTG configuration is considered in this case aiming at reducing the calculation time. In Figure 4.29, the evolution of normal stresses over the 30 cycles with a MTG configuration obtained within the three different boundary Cases are compared. The higher stresses are obtained when dealing with rigid boundaries. In this case, the "non-deformable" walls prohibits the release of the thermal stresses into wall deformation and leads to higher stresses generation.

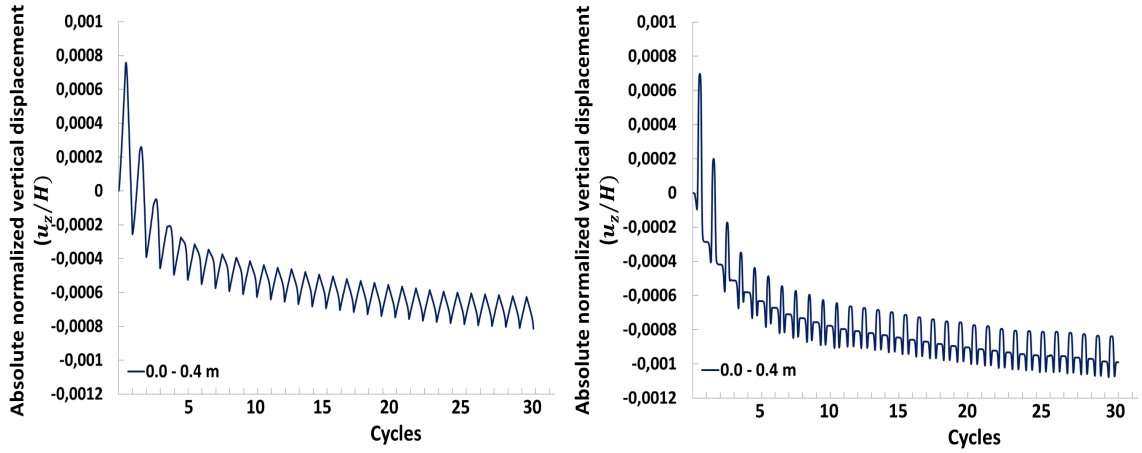

FIGURE 4.28: Case 2 ($\alpha_w < \alpha_b$): Evolution of the kinematic response of particles at deep for: (a) homogeneous configuration, (b) SMTG configuration

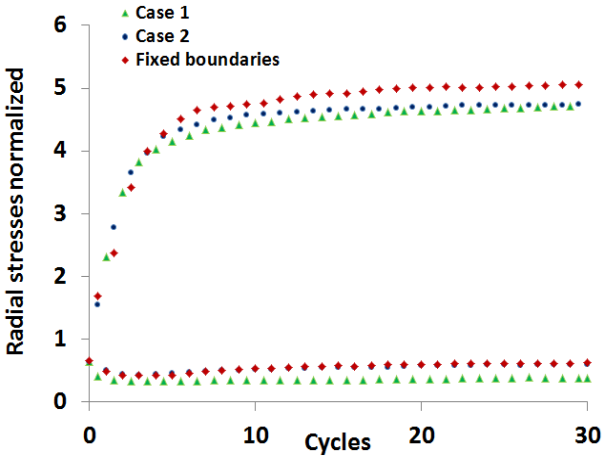

FIGURE 4.29: Radial stresses evolution: Comparison with rigid boundary Case

4.2.3 Influence of the differential of TEC between filler/walls

The influence of the differential of thermal expansion coefficients between the wall and the filler is investigated here. Since not much differences in terms of normal stresses are obtained among all the different studied cases, only Case 1 (where $\alpha_w > \alpha_b$) with an homogeneous thermal configuration is considered in this Section. Different values of $|\Delta\alpha| = |\alpha_w - \alpha_b|$ are considered (4, 8 and 12 $\times 10^{-6}/°C$), the α_b is fixed to $4 \times 10^{-6}/°C$ (see Figure 4.30).
Figure 4.30(right) shows that the maximum induced stresses are linearly proportional to the $|\Delta\alpha|$. For instance, a $|\Delta\alpha|$ twice or three times higher leads to 2 or 3 times greater stresses generated on the tank walls, respectively.

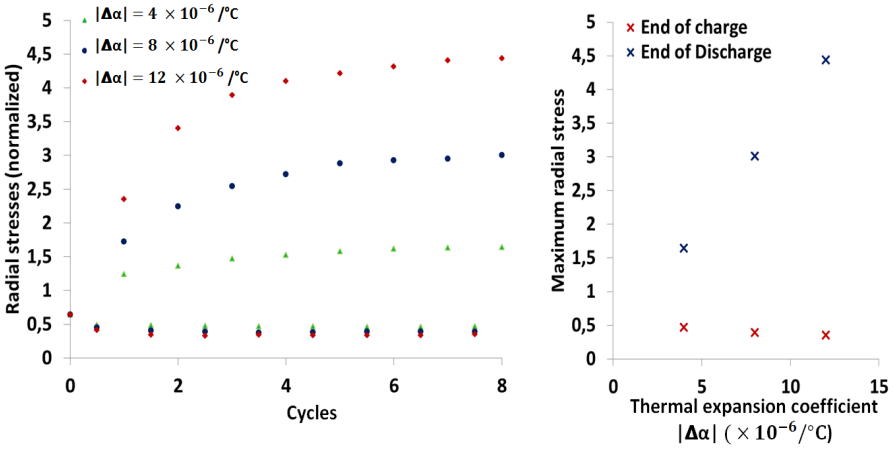

FIGURE 4.30: Influence of the thermal differential coefficient $|\Delta\alpha|$ on the induced stresses

4.2.4 Pluri-disperse particle size distribution

So far, all the presented results were based on a mono-disperse size distribution of particles inside the tank. In this section, the influence of pluri-dispersity of particle sizes is investigated. To do this, three samples are created, within 32 000 particles of different diameters. The maximum particle's radius is fixed to 0.029 m, maintaining the same problem's discretization as in previous calculations. The ratio $\frac{r_{0max}}{r_{0min}} = 10$, where r_{0max} and r_{0min} correspond to the maximum and minimum particle's radius respectively. The initial obtained porosity is 0.37 in this case.
These three samples are submitted to thermal cyclic loadings and the results are averaged. The obtained results are presented in Figures 4.32. A pluri-disperse distribution induces slightly higher stresses on the tank walls. The applied stresses are 1.1 times higher than the ones induced with a monodisperse-like size distribution. Eventually, with a $|\Delta\alpha\Delta T| = 12 \times 300 \times 10^{-6}$, the applied stresses are about 10 times greater than the initial stress values, preceding any thermal cyclic loadings.

Besides the study of different thermal configurations and boundary conditions (Rigid boundary Case, Case 1 ($\alpha_w > \alpha_b$) and Case 2 ($\alpha_w < \alpha_b$)), a different potential tank's geometry (i.e. truncated conical tank) and membrane's properties (i.e. Aluminum tank wall) are studied and presented in Appendix A.

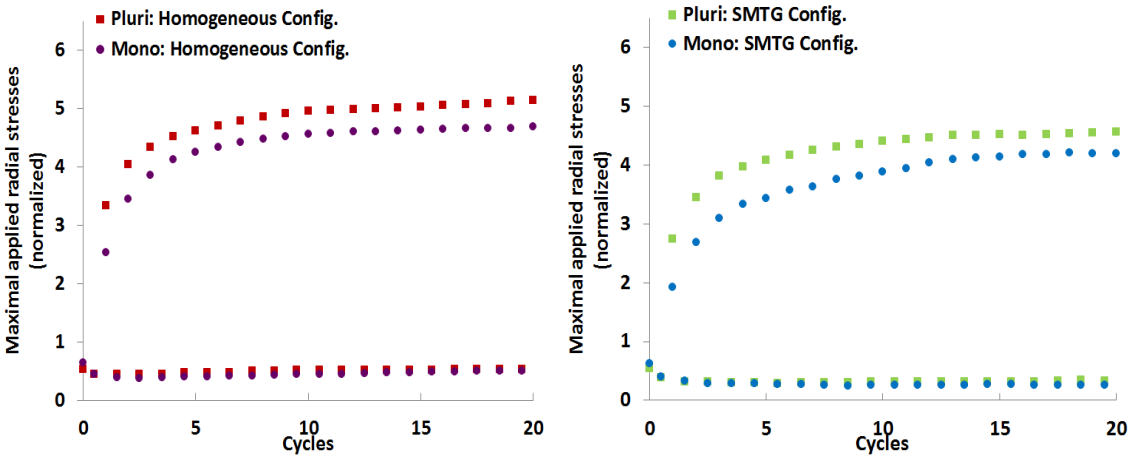

(a) (b)

FIGURE 4.31: Influence of the pluri-disperse particle size distribution: radial stress evolution in Case 1 ($\alpha_w > \alpha_b$): (a) Homogeneous configuration, (b) SMTG configuration

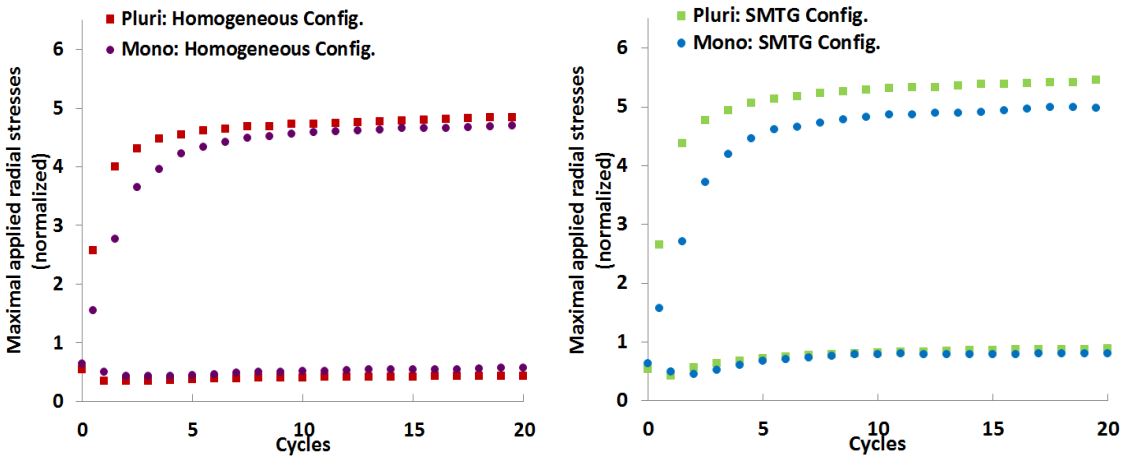

(a) (b)

FIGURE 4.32: Influence of the pluri-disperse particle size distribution: radial stress evolution in Case 2 ($\alpha_w < \alpha_b$): (a) Homogeneous configuration, (b) SMTG configuration

4.3 Conclusion

The study of induced thermal stresses of a thermocline-like storage tank structure has been presented using the discrete element method (All simulations were performed using the open-source code YADE). Based on the assumption of rigid walls, the induced stresses increase due to the thermal expansion of the particles during the loading phases, and decrease during unloading phases. Two other boundary condition cases are studied: (i) Case 1: the thermal expansion coefficient of the tank walls is higher than the granular bed and (ii) Case 2: the granular bed has the highest thermal expansion coefficient. Similarly to the rigid boundary case, higher stresses are induced during the charging cycle when dealing with Case 1. Inverted results (i.e. higher stresses at the end of the discharge cycle) are obtained when the tank walls dilate more than the granular bed during the charge. Furthermore, in all cases, thermal stresses increase with increasing bed depth, since the motion of the deepest elements is restricted generating higher thermal stresses in the tank.
Different cycling configurations were compared: homogeneous vs. gradient thermal loadings and unloadings. Moreover, two different temperature profiles reproducing the evolution of a moving thermal gradient inside the tank but one with steeper conditions than the second are considered too. The effects of the thermally induced loadings depends on the boundary condition Cases. The results show that the stress values developing in the case of the thermal gradient are higher than in the case of the thermally homogeneous loadings for both Case 2 and rigid boundary Case. Whilst in Case 1, the steep moving thermal gradient configuration is less critical in terms of induced stresses than the homogeneous configuration. All these stresses results are largely dependent on the kinematical behavior of the bed, especially at deep.
Then, the motion of the particles is dependent on the way the charging/discharging cycles are applied to the packed bed. The displacement of the deepest particles is dependent on the position of the moving thermal gradient inside the tank. This leads to a higher densification of the medium when dealing with a moving thermal gradient configuration comparing to the homogeneous one, thus to a faster rearrangement of particles in Case 2 and rigid walls. However, a faster stabilization is shown when the bed is cycled homogeneously in Case 1.
Globally, the macroscopic behavior of the tank in terms of stress levels generated on the wall or kinematical response of the bed, is not so different from one case to another (boundary cases whether $\alpha_w > \alpha_b$ or $\alpha_w < \alpha_b$ and thermal configurations). The stress accumulation tends to stabilize with large number of performed thermal cycles. A factor of about 9 is observed between the attained radial stresses values and the initial ones after performing 30 cycles (considering $|\Delta\alpha\Delta T| = 12 \times 300 \times 10^{-6}$). The stress accumulation is thus related, at the first order, to the bed's settlement due to an imposed $|\Delta\alpha\Delta T|$, regardless the behavior of the tank walls towards temperature variations. In addition to this, the resulted stresses are directly proportional to the $|\Delta\alpha\Delta T|$ factor.
Pluri-disperse size distribution can cause additional stresses on the tank walls.

Furthermore, the friction between particles themselves or at their contact with tank walls has a great influence on the induced stresses on the walls. A high particle/particle friction angle increase the shear strength of the granular medium and particles are more restricted to move or displace. When particles are unable to rearrange, higher levels of induced thermal stresses acting on the tank walls are generated.
The influence of the slenderness ratio is investigated as well. The induced thermal stresses increase with an increasing slenderness ratio until they saturate for large slenderness ratios. This dependency could be caused by the fact that increasing the slenderness ratio increases the influence of the tank wall friction. Janssen's effect is induced between the granular medium and the container promoting the formation of arches inside the tank.
Finally, the evolution of forces due to thermal expansion of the particles as well as the decrease step of the forces due to shrinking particles and the densification effects can be reproduced with the present model.
All studied cases are recapitulated in Table 4.5.
To sum up, the consequences of bed's settlement inside a thermocline storage tank (i.e. stresses accumulation and tank walls deformation) can be minimized with optimizing the mechanical/thermal properties of the involved materials. A steep thermal gradient moving through a non-frictional mono-disperse granular filler inside the tank can be the optimized solution for limiting the potential effects of thermal ratcheting. One more condition has to be verified too: the tank wall has to have a higher TEC than the granular bed.
Overall, a larger number of cycles should be now performed to better understand the evolution of stresses as well as the response of the packed bed in all cases. All the afore-mentioned trends can be further verified. Moreover, it would also be suitable to implement a thermo-elasto-plastic model for the tank wall to investigate the potential plastic strain accumulation over the thermal cycles, which may affect the afore-presented results.

TABLE 4.5: Summary of all studied cases, numerically

Sim.	Boundary conditions			Thermal configuration			Bed size distribution		Friction angles		$\lvert\Delta\alpha\Delta T\rvert$	Conclusions
	rigid Boundary	($\alpha_w > \alpha_b$)	($\alpha_w < \alpha_b$)	Homog -eneous	MTG	SMTG	$\frac{r_{0max}}{r_{0min}} = 1.1$	$\frac{r_{0max}}{r_{0min}} = 10$	φ (°)	φ_s (°)	$\times 10^{-6}$	
1	x			x			x		45	45	4 x 300	- Higher stresses are obtained when dealing with MTG than homogeneous config. - $\sigma_{rrmax}/\sigma_{rrini} \approx 3$ - Detailed in Section 4.1.1
2	x				x		x		45	45	4 x 300	
3		x		x			x		45	45	12 x 300	- The highest stresses are obtained within homogeneous config. - The knimetaical behavior is dependent on the position of the moving thermal gradient inside the tank - Faster stabilization of the system (granular bed + tank wall) is shown within the homogeneous config. - $\sigma_{rrmax}/\sigma_{rrini} \approx 8-9$ - Detailed in Section 4.2.1
4		x			x		x		45	45	12 x 300	
5		x				x	x		45	45	12 x 300	
6			x	x			x		45	45	12 x 300	- The highest stresses are obtained within SMTG config. - The kinematical behavior is dependent on the position of the moving thermal gradient inside the tank - Faster stabilization of the system (granular bed + tank wall) is shown within the SMTG config. - The thermocline's behavior in the case of is similar to the case of rigid boundaries (Sim. 1 and 2) - $\sigma_{rrmax}/\sigma_{rrini} \approx 8-9$ - Detailed in Section 4.2.1
7			x		x		x		45	45	12 x 300	
8			x			x	x		45	45	12 x 300	
9	x				x		x		45	45	12 x 300	- Comparing with Sim. 4 and 7, the highest stresses are obtained when dealing with rigid boundary due to the "non-deformable" walls - Detailed in Section4.2.2.2
10	x				x		x		5	5	4 x 300	- Referring to Sim. 2, 10 and 11, increasing the friction in the tank (whether the particle/particle φ or the particle/wall φ_s friction angles) leads to higher induced stresses. - Detailed in Section 4.1.4
11	x				x		x		45	5	4 x 300	
12		x		x			x		45	45	4 x 300	- Referring to the Sim. 3, 12 and 13, the maximum induced stresses are linearly proportional to the $\lvert\Delta\alpha\Delta T\rvert$ - Detailed in Section 4.2.3
13		x		x			x		45	45	8 x 300	
14		x		x				x	45	45	12 x 300	- The applied stresses are 1.1 times higher than the ones induced with a monodisperse-like size distribution - Detailed in Section 4.2.4
15		x				x		x	45	45	12 x 300	
16			x	x				x	45	45	12 x 300	
17			x			x		x	45	45	12 x 300	

Chapter 5

Experimental setup aiming at studying the thermal ratcheting

This chapter presents the experimental setup ESPERA, mounted in the CEA laboratory, Grenoble. The laboratory-scale installation aims at studying the thermal ratcheting phenomenon in packed-bed storage tanks by measuring the induced stresses applied on its container walls. The measurements are realized using home-made force sensors fixed on the container wall at different locations. Section 5.1 recapitulates all the steps that led to a functional installation, starting from detailing its concept and its objectives, passing by presenting the development of the force measurement devices and ending by showing all the tests preceding its start-up (i.e. calibration tests at ambient and high temperatures).
Section 5.3 is dedicated to show the experimental results that were obtained on ESPERA, after passing the validation tests of the force measurement devices on an another setup, called P'tit-Pousse detailed Section 5.2. Both experimental results obtained on P'tit-Pousse and ESPERA are compared with the numerical simulations. However, the comparison between the numerical results and the measured ones obtained on ESPERA remains somehow preliminary due to the difference between the input data used in each approach. Unfortunately, the run of new compatible simulations with the experimental ones has been prevented due to the lack of time.

5.1 Experimental setup development

5.1.1 Objectives

As it was detailed in previous chapters of this manuscript, the literature review shows a lack of trustful experimental data limiting the understanding of the thermo-mechanical behavior

of a granular material inside a packed-bed thermocline storage tank. The sizing of tanks by engineers is still the subject of strong assumptions; their durability over time is thus uncertain. The problematic of the thermal ratcheting needs more research efforts in the aim of reaching a predictive law defining the behavior of the granular bed inside the storage tank.

To this aim, a representative simple configuration of a packed-bed heat storage tank was built in the CEA laboratory in Grenoble, France. The experimental setup will be referred to "ESPERA" in the following. The objectives behind its construction are to reproduce the thermal ratcheting phenomenon, to measure the applied radial stresses on the tank's membrane and evaluate their dependence on different parameters and operational conditions and finally to validate the previously developed numerical model with real and significant data. Eventually, the thermal ratcheting risks can be evaluated in real.

5.1.2 Description of the setup

The experimental setup consists of a cylindrical tank containing the granular medium in order to characterize its thermo-mechanical behavior. The tank is subjected to cycles of heating and cooling using air as the heat transfer fluid, minimizing the technological difficulties confronted when using liquids as heat transfer fluid and getting advantage of an existent air heating loop "CLAIRETTE" at the CEA (Grenoble), schematically presented in Figure 5.1. CLAIRETTE loop has been modified to fulfill ESPERA's objectives, automation and monitoring. The flow rate of the compressed environmental air is regulated (by the regulation valves VRM1 and VRM2 in Figure 5.1), then it is heated before passing through the tank. The tank is cycled between ambient temperature and 185°C. The loading and unloading phases of a heat storage tank are reproduced here: four valves (VAP 1 through 4 in Figure 5.1) permit the reversion of loading/unloading flow directions. Thus, the heated air enters the tank from the top during the charging process (VAP 1 and VAP 4 are open) while the cold air is injected from the bottom during the discharging process (VAP 2 and VAP 3 are open and the heater is switched off). In addition to this, the automation of the CLAIRETTE loop permits the realization of several thermal cycles by switching the corresponding valves to reverse the flow directions. The idea then is to be able to measure the induced stresses applied by the granular bed on the cylindrical tank walls.

To do so, different configurations have been thought out at the beginning, such as considering a very thin thickness for the container walls. Thus, their deformation will be relatively high and can be measured through different techniques as image correlation or inductive capacitor sensors. However, the difficulties of such configuration are crucial: it is difficult to determine a container thickness ensuring that it is, at the same time, sufficiently strong to resist the applied stresses and sufficiently deformable so that its deformation is large enough to allow for an accurate measurement, noting that the main purpose of this setup is to measure the

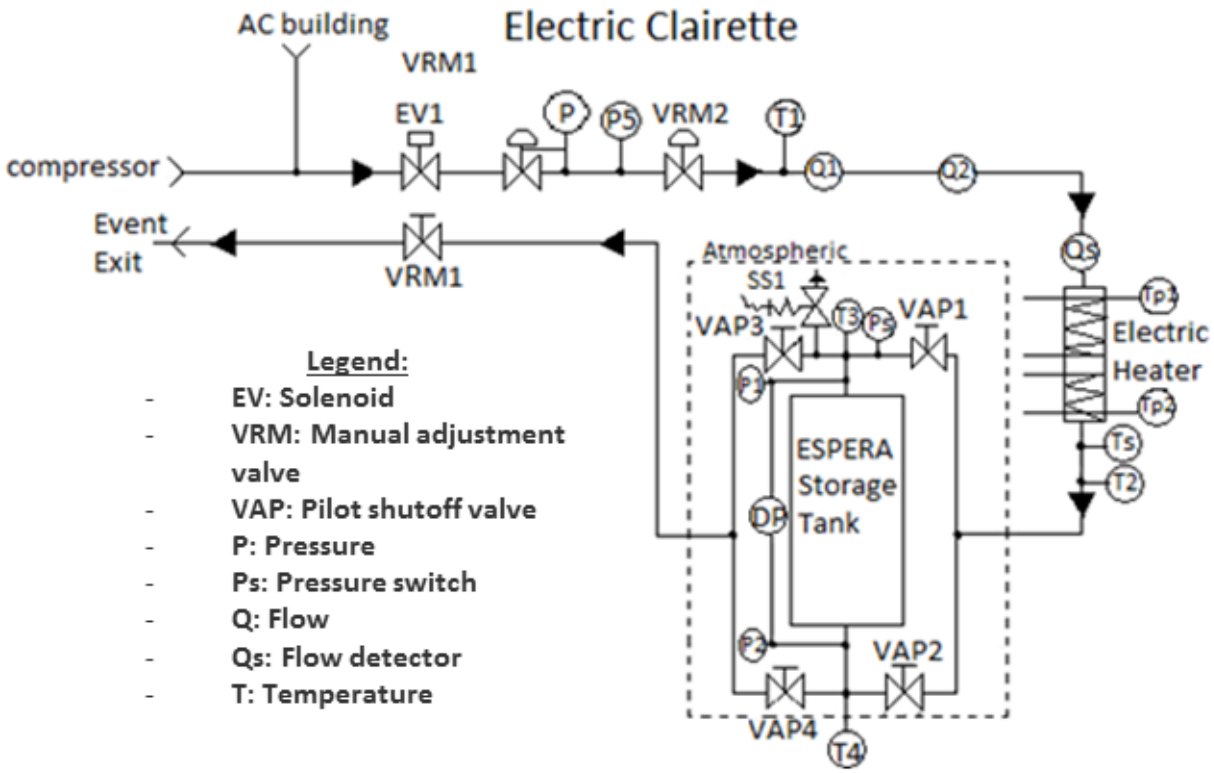

FIGURE 5.1: Schematic of the CLAIRETTE installation, ESPERA included

unknown efforts applied on the container walls. At the end, this configuration appeared to be risky and expensive to implement and the final decision went towards a new configuration: a thick cylinder fed by several force measurement devices placed at different locations on the container wall enabling the measurement of local efforts.

The thermal storage facility consists in a 5 mm-thick cylindrical aluminum tank with a diameter of 200 mm. The aluminum material is chosen for the container as it provides a high thermal expansion coefficient ($\alpha_{alum} = 23 \times 10^{-6}/°\text{C}$) allowing the amplification of the differential thermal expansion between the tank's shell and the filler. Figures 5.2 and 5.3 present a 3D view of ESPERA, showing all its constituting elements. An air channel is assured between the main cylinder (interior tank) and the cover (exterior tank) enabling the heating/cooling of the main tank's shell. Moreover, a "diaphragm" system is used for fluid flow regulation at the tank level: it equilibrates the air flow passing inside the tank (through the granular material) and outside the shell (between the main cylinder and the cover). The annular gap with the diaphragm system assures that the temperature of the tank shell evolves in the same way as inside limiting the thermal losses with the external environment. Figure 5.4a shows a photograph of ESPERA setup where the outer aluminum cylinder is removed to let the internal cylinder appear, and Figure 5.4b shows the setup insulated for the sake of limiting the environmental thermal losses.

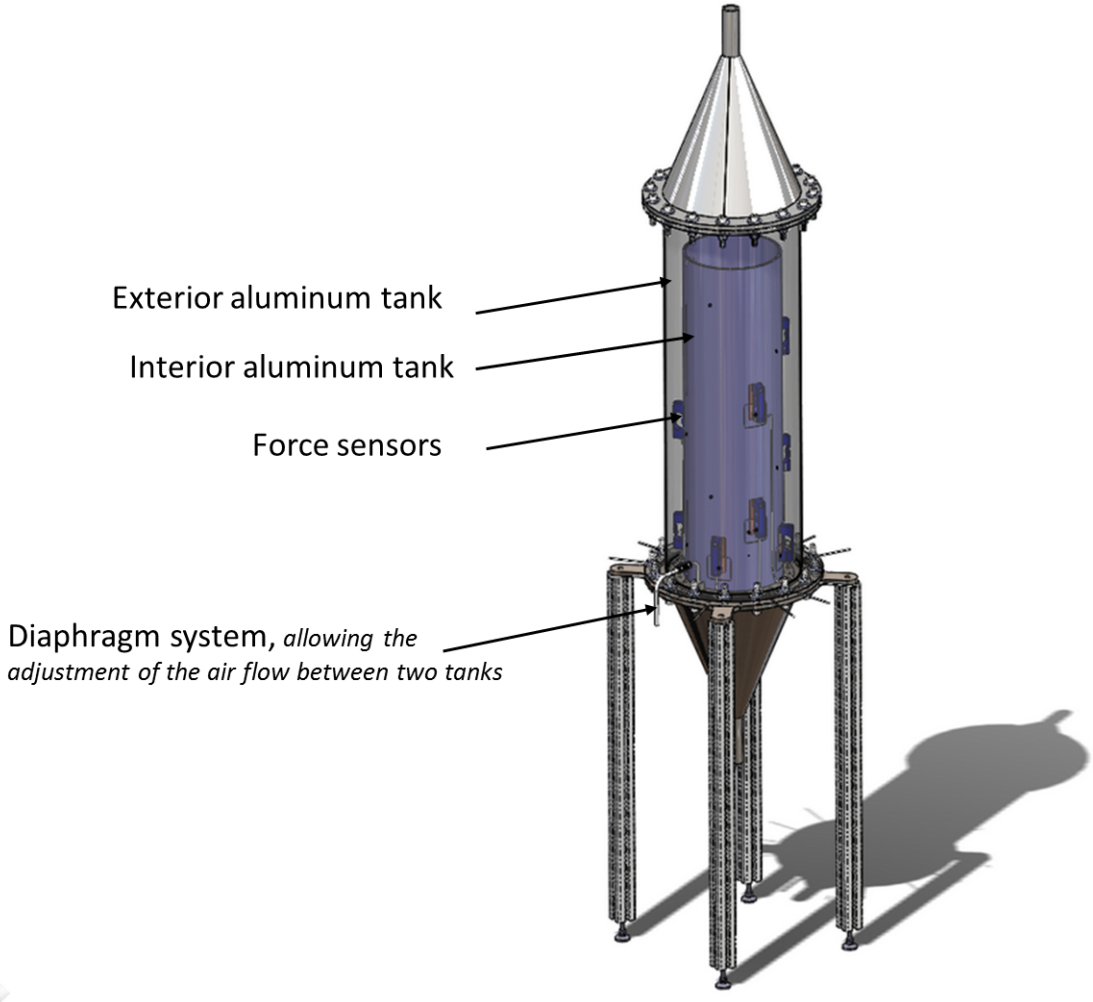

FIGURE 5.2: ESPERA setup with all its constituting elements

Firstly, the tank is filled with spherical glass beads representing the granular medium. A mono-disperse distribution with 4 mm-diameter beads is used. Also, a bi-disperse size distribution with beads of 1.5 mm and 4 mm of diameter as well as a granular medium are envisaged to be used in the future work . At the tank's base, a grid is used allowing air circulation but retaining the beads. Table 5.1 lists the material properties of the tank and the glass beads.

The main cylinder is equipped with force measurement devices placed at different levels of the tank (Figure 5.2). Moreover, the tank can be filled to different height levels (up to 600 mm), allowing the study of slenderness ratio influence (recalling that the slenderness ratio S_r is the bed's height over the tank's diameter).

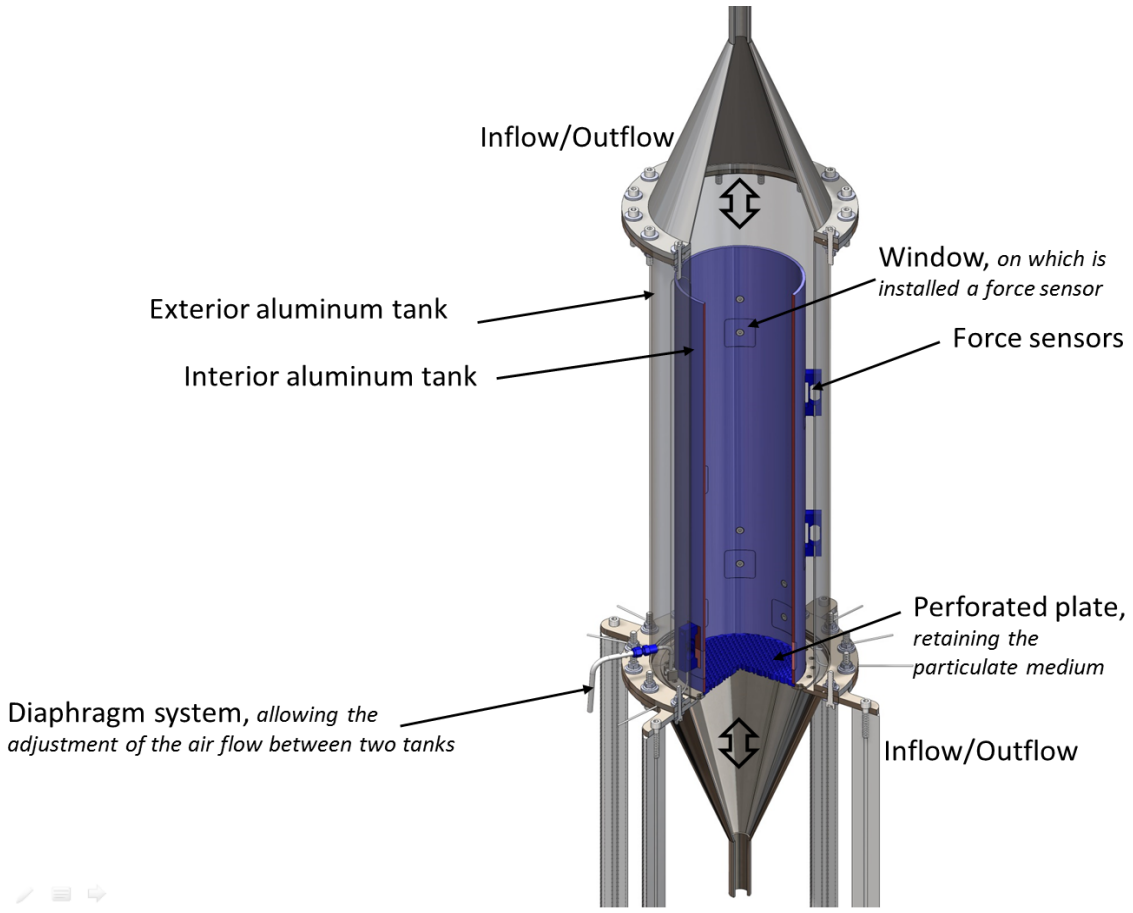

FIGURE 5.3: ESPERA setup with all its constituting elements

5.1.3 Force measurement device

The mechanical instrumentation of the tank remains an important part: windows are created in the tank's shell (interior tank) and the applied forces on these windows are then measured through force sensors. They were developed at the CEA due to the scarcity of force measurement devices that can operate at the desired temperature and effort ranges besides their high cost. They are developed based on the principle of deformable parallelogram sensors. The schematic diagram is given in Figure 5.5. The granular medium exerts stresses on the movable window causing bending in the force measurement device, since its upper side is attached to the fixed part of the shell. The deformable parallelogram system ensures that the motion of the movable part is a pure translation. Four strain gauges are placed at the thinner zones of the deformable parallelogram sensor in order to measure the maximal induced deformations. The strain gauges are mounted in a full Wheatstone bridge configuration (Figure 5.6). Besides increasing the sensitivity and the accuracy of the device, the full bridge configuration allows for temperature and cable length compensations (Hoffmann (1974)). The strain gauges installation on the devices was the responsibility of the HBM company, professionals in the field of strain gage measurements in France. Moreover, a temperature sensor is also glued at

(a) (b)

FIGURE 5.4: (a) ESPERA setup; the external cover is removed, (b) ESPERA with the external heat insulator

Tank's properties	
Material	Aluminum, serie 7000
Height (m)	0.7
Diameter (m)	0.2
Thickness (mm)	5
TEC ($\times 10^{-6}$/°C)	23
Spherical particles	
Material	glass beads
Diameter	Mono-disperse: 4 mm Bi-disperse : 1 and 4 mm
Density (kg/m^3)	2500
TEC ($\times 10^{-6}$/°C)	9

TABLE 5.1: Different numerical studied cases: the corresponding microscopic friction angles and the calculated porosity of the samples

one unconstrained side of each device. This temperature sensor allows to detect the thermal stabilization of the system at the end of charging/discharging phases.

The dimensioning of the sensor is carried out according to different criteria: ensuring the greatest possible elastic deformation at the hinges of the deformable parallelogram while minimizing the intrusion of the sensor into the phenomenon to be measured, by limiting the displacement of the deformable parallelogram. Numerical simulations on SolidWorks were run

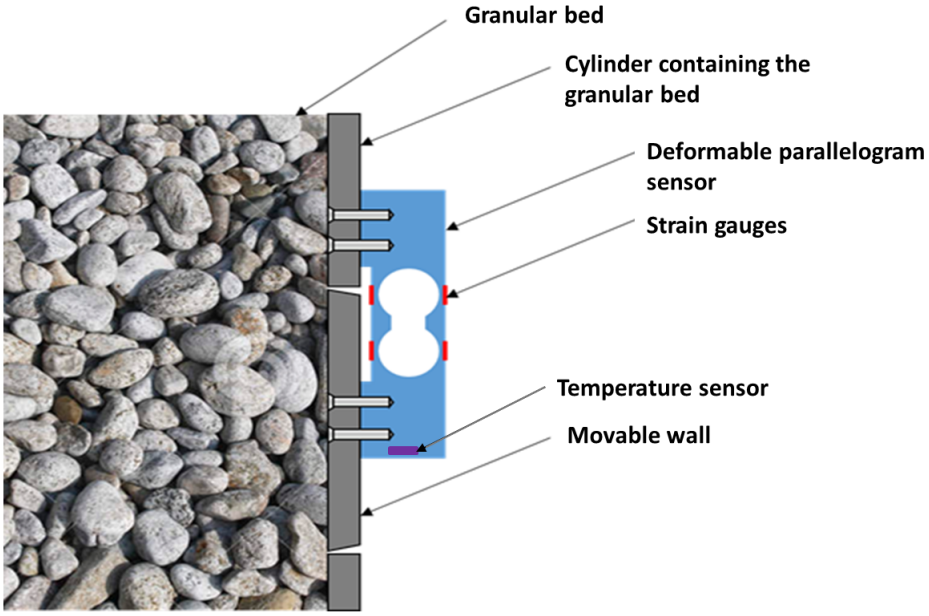

FIGURE 5.5: Concept of the force measurement device placed on the tank's wall

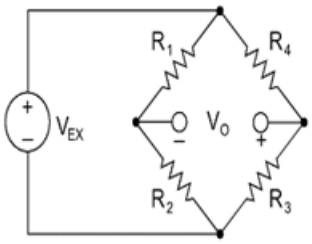

FIGURE 5.6: Full bridge configuration

in order to test different holes radii. A compromise is assured by fixing the two holes' radii to 18 mm. The adopted dimensions for the sensor are provided in Figure 5.7.

A data acquisition system with 8 channels for strain measurements is disposable at the CEA Laboratory (QuantumX MX840B from HBM company). Therefore, 8 force sensors are produced and can be used at a time for effort measurements at different positions of the tank. The positions of the force sensors depends on the bed filling levels. In total, 11 windows are created in the tank's shell distributed at different heights and orientations. The windows at top are not exploited when dealing with low slenderness ratio.

Figure 5.8 shows the positions of the windows along the tank's height including a section at each level (all dimensions are in millimiters). These sections permit to identify the different orientations of the windows besides their number at each level. The windows are distributed along 7 different height levels along the tank's shell where 4 windows exist at the first bottom level (i.e. at a height of 25 mm), 2 windows at the second level and one window at

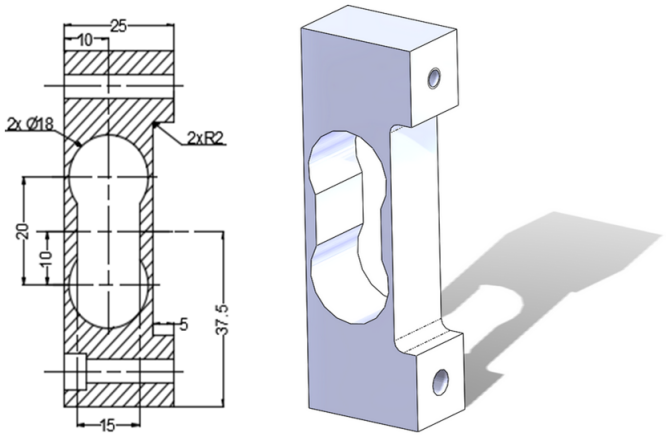

FIGURE 5.7: Dimensions of the force measurement device

each remaining upper level. In addition, 14 thermocouples are integrated inside the principal cylinder and between both the principal and the outer cylinders in order to follow the evolution of the temperature of the granular bed and the tank's shell. The positions of the thermocouples, presented by a red circles, are shown in Figure 5.9. Figure 5.10 shows a top view of the principal cylinder equipped with thermocouples distributed among the spherical glass beads. More plans and sections either for ESPERA setup or for the force measurement devices are presented in Appendix B.

5.1.4 Force sensor calibration

5.1.4.1 Calibration process

The calibration of the force measurement devices is realized at ambient and high temperatures. The objective behind is to identify the relationship between the imposed weight (corresponding force) and the measured tension at different temperature ranges. With eight sensors devices, the calibration process consists of using two assemblies of four sensor devices, as shown in Figure 5.11a in order to hasten the process. This way, the imposed weight at the top is transmitted from one device to another.
The calibration at high temperature is done inside an oven. The used oven, available at the CEA laboratory, is characterized by a hole at its upper side, allowing the weight transmission to the assembly through a vertical rod (Figure 5.11b).

At the beginning, 2 cycles of heating and cooling at extremum temperatures (20 and 200°C) are imposed to the assembly before any measurements without imposing any weights. These cycles aim at eliminating any residual deformation in the devices. Then, the devices are heated by intervals of increasing temperature. Once the desired temperature of all devices is

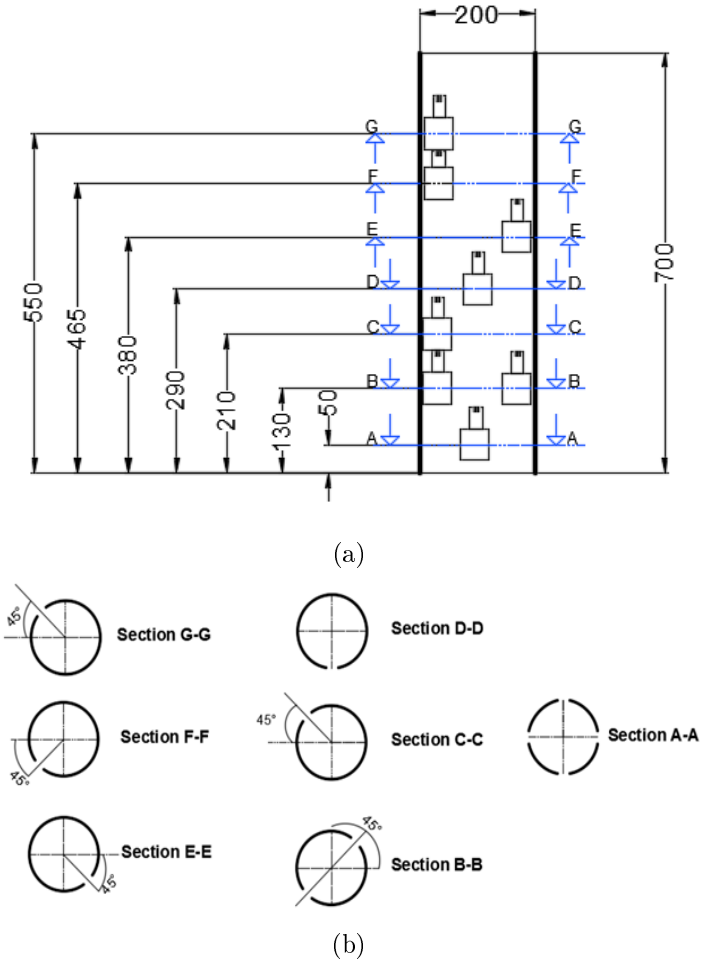

FIGURE 5.8: (a) Positions of windows along the tank's height, including a section at each level (all dimensions are in mm), (b) Different sections through the tank, showing the orientation and number of the existing windows

reached and stabilized (measured by the temperature sensor installed on each force sensor), the weights are imposed and the obtained voltage is noted for each applied weight.

5.1.4.2 Calibration results

Figure 5.12 presents the calibration results of one assembly of four force measurement devices at ambient and high temperatures. A linear behavior is obtained between the subjected force and the measured tension. Moreover, the behavior of the force sensors is independent of the temperature variations, due to the full bridge configuration and the use of strain gauges having compatible TECs with the force measurement device material (see Figure 5.13, showing the response of one sensor towards different temperatures). The behavior of all the other devices is very similar to the presented one and are provided in Figure 5.14.

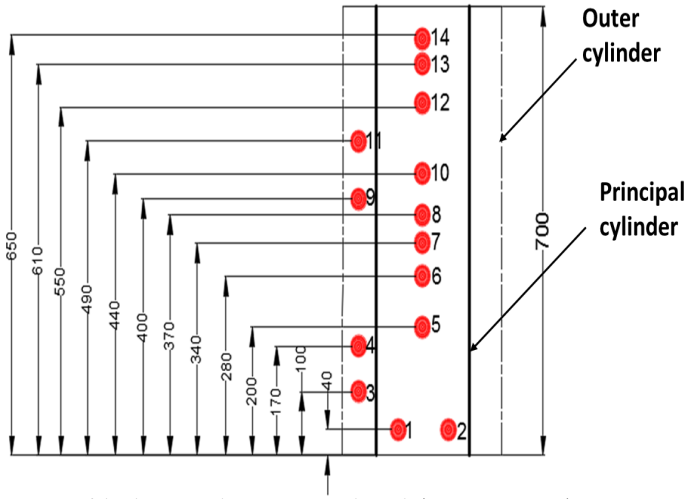

FIGURE 5.9: Positions of the thermocouples in or outside the tank (dimensions in mm)

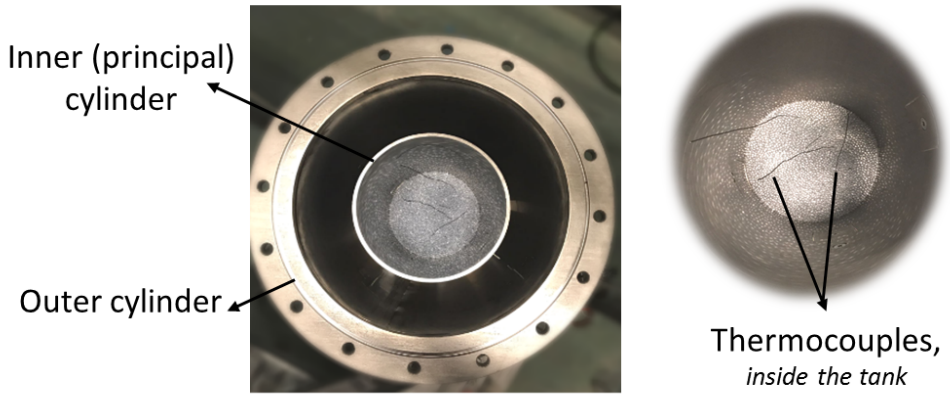

FIGURE 5.10: Top view of both cylinders showing the thermocouples inside the tank)

5.2 Numerical and experimental validation of force measurement device through P'tit-Pousse setup

5.2.1 P'tit-Pousse setup

In order to guarantee the sensitivity and the efficiency of the designed force measurement devices towards the desired force ranges, another setup is installed, called "P'tit-Pousse". Figures 5.15 and 5.16 show the installation in question. It consists of a rectangular container ($0.1 \times 0.1 \times 0.2$ m^3) filled with the same glass beads used in ESPERA. One side of the container walls is fixed while the other 3 sides can move altogether, being connected to a motorized micrometric table. A linear motion is thus provided in both positive (in the direction of pushing the beads or charging direction) and negative (in the direction of release or discharging

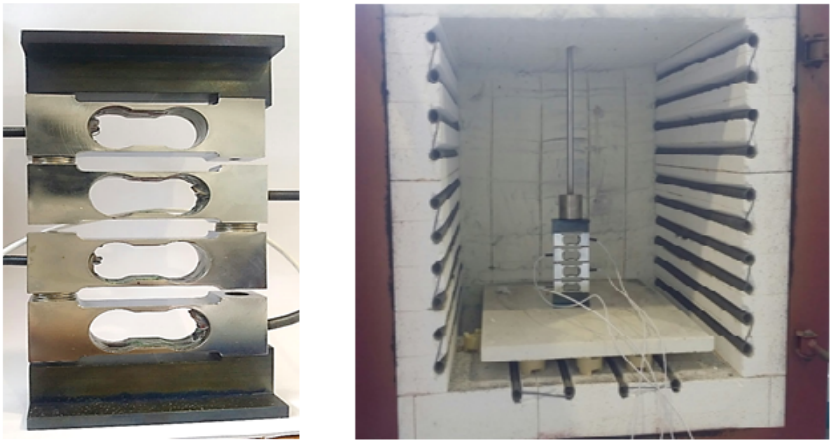

(a) (b)

FIGURE 5.11: (a) The assembly of 4 sensors, (b) The assembly in the oven used for the calibration process at high temperature

direction) directions. The walls being displaced in the positive direction, the beads apply higher stresses on the fixed side of the container comparing to the discharging direction. Therefore, the resulted stresses are measured by the force measurement device installed on the fixed side through the "window-principle" used in ESPERA setup (see Figure 5.17). Thus, this setup provides a configuration close to the actual use of the force sensors in ESPERA enabling their validation. A 5×5 cm^2 window is created at the height of 5 cm. Besides the validation of the force sensors sizing and functionality, P'tit-Pousse permits the calibration of the numerical model parameters (i.e. the adequate friction angles for glass beads contacts and beads/walls contacts). These calibration results can be used for a later numerical validation of the developed model, based on the experimental results obtained on ESPERA.

5.2.2 Experimental results on P'tit-Pousse

The container is filled to a height of 15 cm with 4 mm-diameter spherical glass beads. Different displacements are imposed ($\pm$3 mm and $\pm$10 mm), each time with 2 performed cycles of charging/discharging. In order to be more accurate, the filling is repeated 8 times for each displacement after emptying and refilling the container. The porosity of the medium is measured and equal to 0.37. Using the calibration force/tension curve of the installed force measurement device obtained at ambient temperature, a pressure/time curve is thus established. Figure 5.18 presents the measured stresses time-variation for a 3 mm displacement with a velocity of 0.0166 mm/s for the linear motion. The results of the 8 performed fillings within the 2 cycles of charging/discharging are presented in dashed lines and their average is plotted in a continuous line.

The response of the force sensor is precise: the sensor is capable of detecting the applied

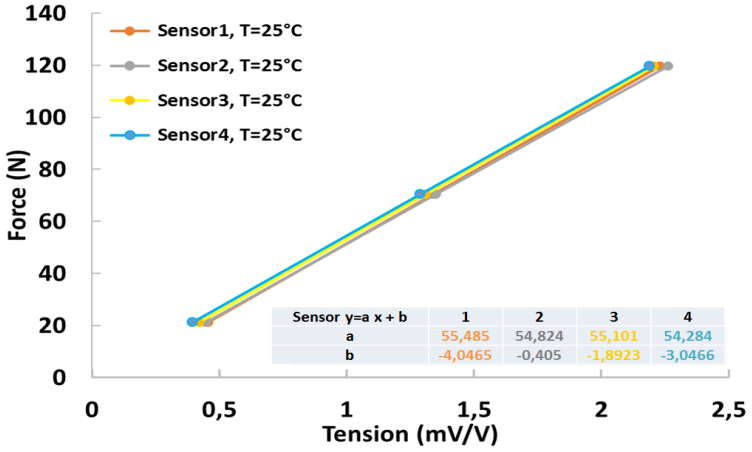

(a)

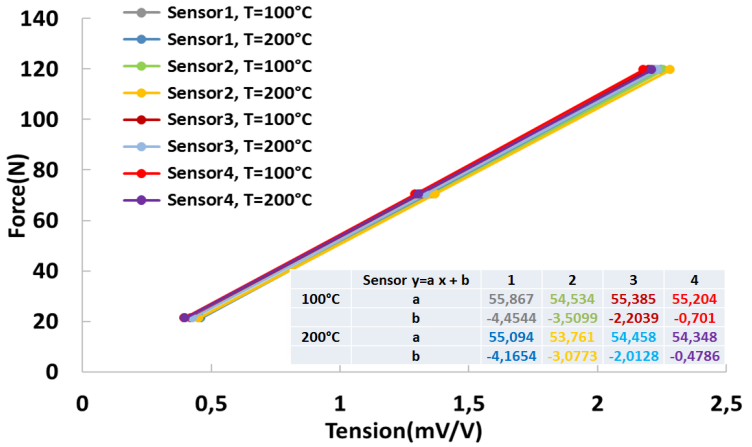

(b)

FIGURE 5.12: Calibration results for the first assembly: Force/Tension curves: (a) At ambient temperature, (b) At high temperatures (100 and 200° C)

stresses which validates its dimensions. As predicted, the stresses applied on the walls increase during the charge and decrease during the discharge.

Then, stress/displacement curves representing the average of the 8 fillings are plotted within the 2 performed cycles. Figure 5.19 shows the variation of the applied stresses with respect to the imposed displacement for the 3 mm and 10 mm cases. Figure 5.20 shows both responses, superposed, obtained within 3 and 10 mm of displacements.

5.2.3 Numerical validation

The experiment is reproduced numerically on Yade. The rectangular container is filled by pluviation by around 9000 particles to a height of 15 cm. A mono-disperse distribution of spherical particles with a radius of 2.9 mm is considered, reducing the total number of particles (thus the calculation time needed) but assuring a sufficient discretization of the sample. The

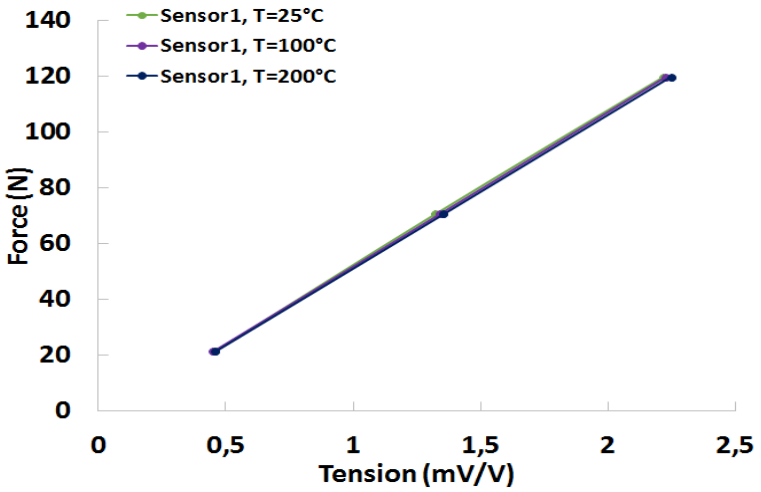

FIGURE 5.13: Calibration results for the first sensor: Force/Tension curves for sensor 1 at ambient and high temperatures

same mechanical properties of the particles are used as in previous calculations and summarized in Table 5.2. Once the stabilization of the sample under gravitational loads is reached, cycles of charging and discharging are performed by a linear motion of the movable walls of the container. A velocity of 0.0166 mm/s and a maximum displacement of 3 mm are imposed. The stabilization is assured progressively during the cycling and the applied stresses on the walls are calculated. It is important to note that each cycle of charging/discharging lasts approximately three weeks.

Different values of microscopic internal friction angles are considered numerically for the purpose of having a macroscopic behavior similar to the experimental results obtained in P'tit-Pousse for the 3 mm displacement (Section 5.2.2). In this context, three cases, where the internal friction angle between particles and the friction angle at the contact with the wall, are varied either at the sample generation or before the cycling. Note that the internal friction angles chosen at the sample generation (by pluviation) greatly influences the properties of the sample, affecting its initial porosity n. For instance, low values of microscopic friction angles chosen at the sample generation lead to a denser medium after the stabilization under gravitational loads, comparing to an another sample generated with higher values of microscopic friction angles. All studied cases are presented hereafter:

- **Simulation 1:** The internal friction angle between particles φ and static friction angle at the contact with the wall φ_s are both set to 5° at the sample generation and during cycling.
- **Simulation 2:** Both friction angles φ and φ_s are set to 5° at the sample generation then, once the stabilization of the sample is attained, they are both changed to 45° before starting the cycling.

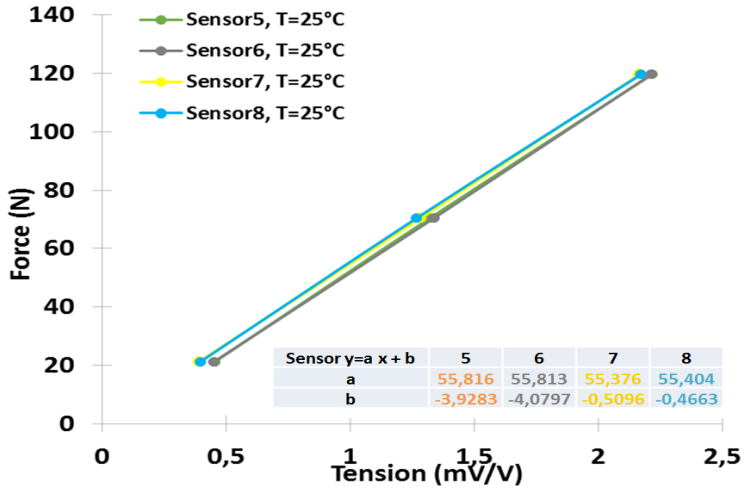

(a)

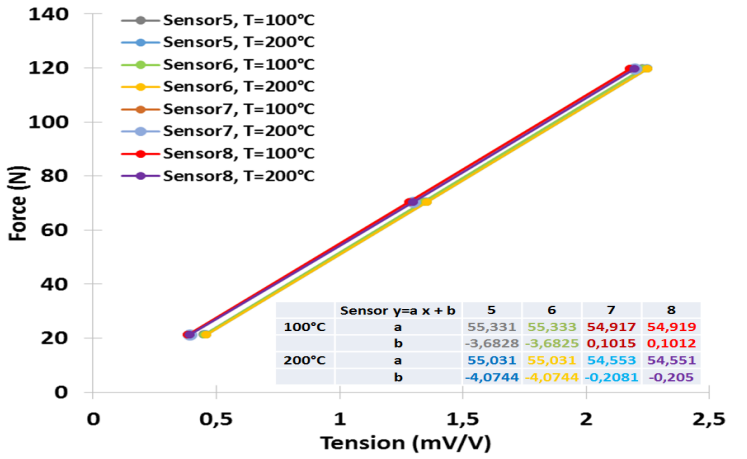

(b)

FIGURE 5.14: Calibration results for the second assembly: Force/Tension curves: (a) At ambient temperature, (b) At high temperatures (100 and 200°)

- **Simulation 3:** Friction angles φ and φ_s of 45° are considered during the sample generation and the cycling.

Table 5.2 recapitulates all three cases, presenting the porosity of the samples at the initial state (after the stabilization of the sample under gravitational loads) and at the final state (at the end of the cycling process). Two cycles of charging/discharging are performed for each case and then compared to the results obtained experimentally on P'tit-Pousse. The numerical results are presented in Figures 5.21 through 5.23.

Referring to Figure 5.22, it is clear that results obtained with Simulation 2 (at the sample generation: $\varphi = \varphi_s = 5°$, then before cycling: $\varphi = \varphi_s = 45°$) do not fit with the experimental results. Thus, only one cycle is performed in this case.
Regarding Simulations 1 and 3 (Figures 5.21 and 5.23), one can see that the numerical results

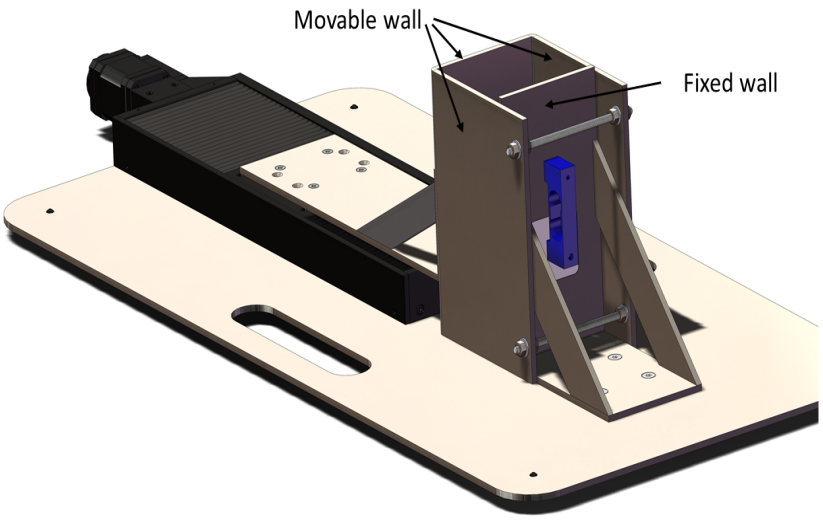

FIGURE 5.15: Schematic view of P'tit-Pousse installation

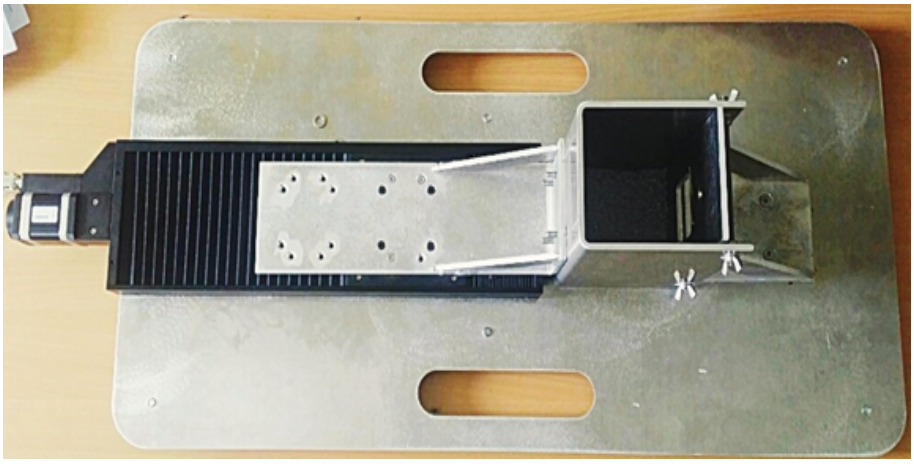

FIGURE 5.16: P'tit-Pousse installation

are in the same order of magnitude of the experimental ones. Same behavior is observed where the applied stresses on the walls increase during charging and decrease during discharging. Simulation 1 ($\varphi = \varphi_s = 5°$ throughout the whole process) seems to be closer to the experimental results.

It is remarkable that the stresses increase from cycle to cycle in the numerical results, due to bed's densification after cycling, while it is not the case for the experimental ones. Moreover, the difference between the last two cases, Simulations 2 and 3, is the initial porosity of the medium. In fact, starting from a dense medium and high internal friction angles greatly increases the macroscopic friction angles of the sample.

Comparing both numerical and experimental results, one can see that the decrease of the applied stresses on the wall during the discharge cycle is more brutal within numerical results than the experimental ones. This might be due to the elastic stiffness of the "force measurement/window" system, enabling the gradual decrease of the applied stresses. Additional

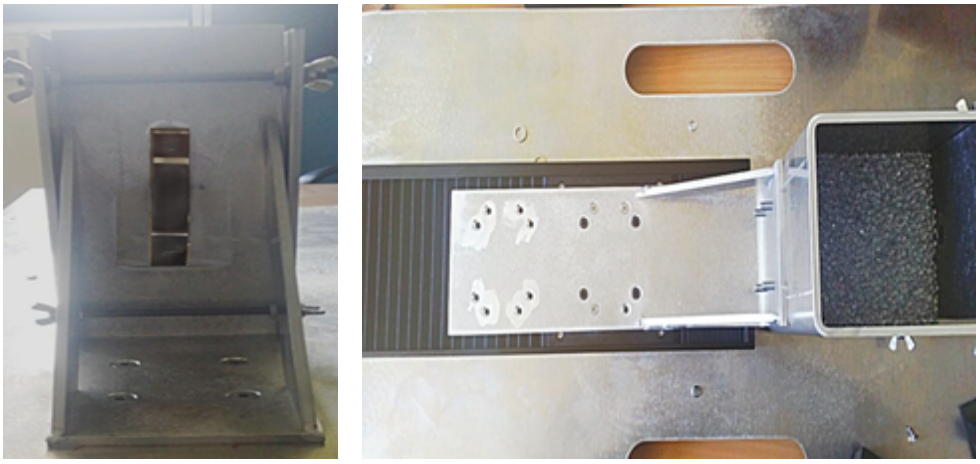

(a) (b)

FIGURE 5.17: (a) Force measurement device installed on the fixed wall of P'tit-Pousse, (b) P'tit-Pousse filled with glass beads

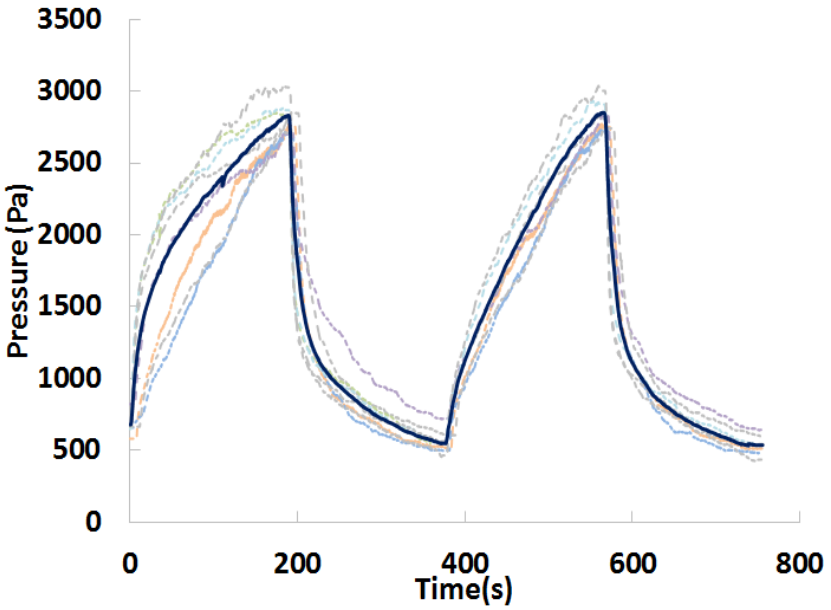

FIGURE 5.18: Stress variation over 2 cycles of charging/discharging (±3 mm of displacement), responses of 8 experimental tests (dashed lines) and their average (continuous line)

numerical simulations have to be performed in order to better fit the experimental obtained results. Setting φ and φ_s to 10° might give better results. Unfortunately, this case could not be tested due to the lack of time. Eventually, the comparison of these numerical results with the experimental ones obtained on P'tit-Pousse can validate the choice of the numerical values of the mechanical parameters, that will be subsequently used for a validation of the developed numerical model based on the experimental results on ESPERA.

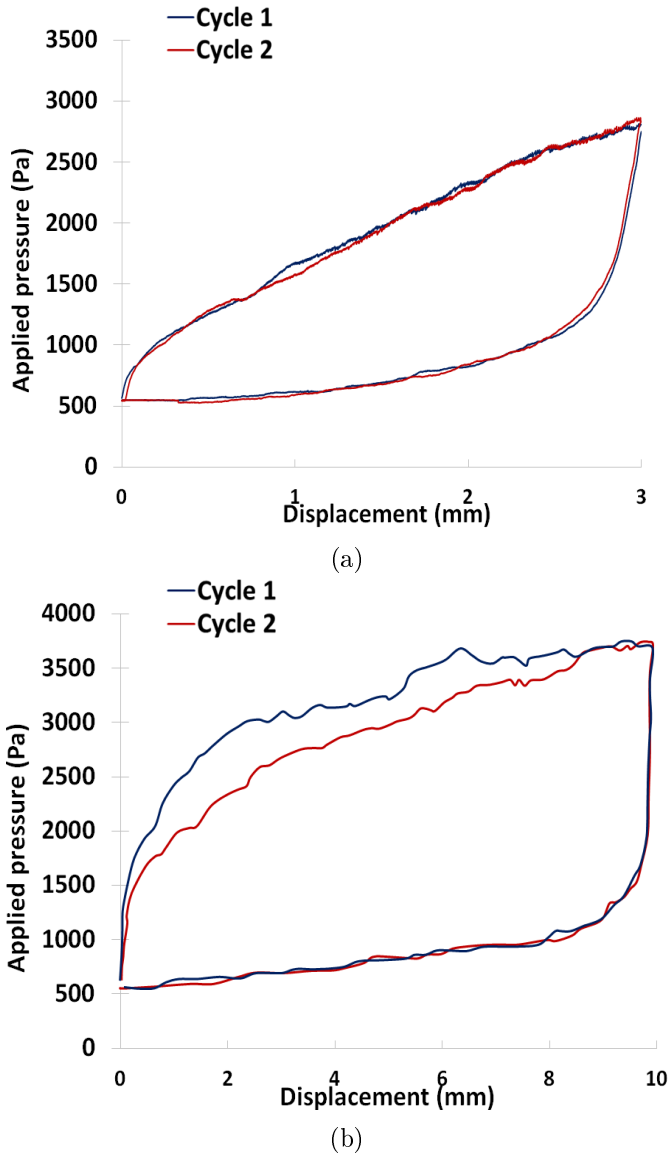

FIGURE 5.19: Stress vs. imposed displacement curves for: (a) ±3 mm of displacement, (b) ±10 mm of displacement

5.3 Preliminary results on ESPERA

5.3.1 Temperature evolution in ESPERA

Some preliminary tests of cycling have been carried out. The cylindrical tank is filled with the 4-mm glass beads to a height of 400 mm (S_r=2) and cycled between 25°C and 185°C as minimum and maximum cycling temperatures respectively. The maximum inlet temperature was set to 240°C so as to have a temperature of 185°C inside the tank during the charging process. The flow rate was set to 14.6 m^3/h in order not to exceed the maximum pressure equal to 1.5 bara.

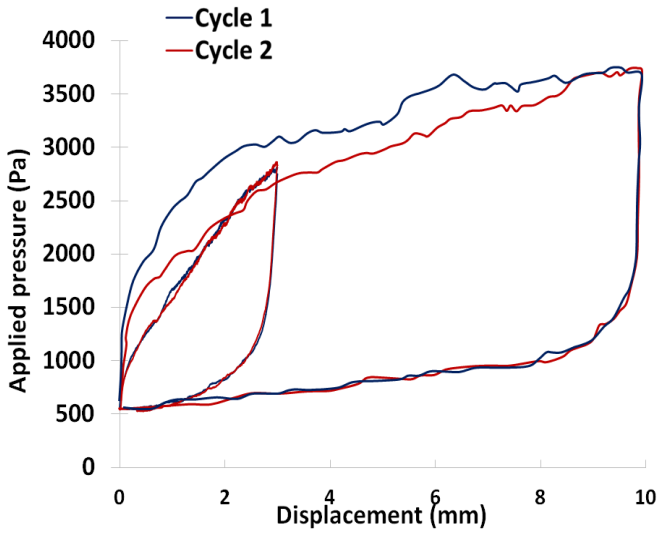

FIGURE 5.20: Stress variation over 2 cycles of charging/discharging for both ±3 mm and ±10 mm displacements

Simulations	At the sample generation		Just before the cycling		Porosity n	
	φ (°)	φ_s (°)	φ (°)	φ_s (°)	Initial state (before the cycling)	Final state (after the cycling)
Simulation 1	5	5	5	5	0.40	0.38
Simulation 2	5	5	45	45	0.40	0.38
Simulation 3	45	45	45	45	0.44	0.41

TABLE 5.2: Different numerical studied cases: the corresponding microscopic friction angles and the calculated porosity of the samples, φ is the internal friction angle between particles and φ_s is the static friction angle at the contact with the wall

The thermocouples give the evolution of temperatures in the granular medium and on the tank's shell. The charging time is fixed based on the stabilization of the temperature provided by the thermocouples 1 and 2 located at the bottom of the tank (see Figure 5.9) in order to ensure the thermal stabilization of the whole tank, since the fluid is injected by the top during the charging process. The discharging time is fixed referring to the thermocouple 8 located at the top surface of the glass beads remembering that the cold fluid enters the tank from the bottom during discharging phase. Figure 5.24 shows the temperature evolution for the average of the bottom thermocouples 1,2 and for the thermocouple 8 over one cycle of charging/discharging. It can be seen that approximately 9 hours and a half are required for the temperature stabilization during charging and discharging.

Unfortunately, the 9 hours and a half needed to ensure the thermal stabilization could not been assured because of the low-cost timer used for valves monitoring. This timer is able to reproduce a number of cycles but it re-initializes every 24 hours and cannot exceed a total of 10 hours for each performed charging or discharging cycle. Thus, the time of each of charging and discharging processes is fixed to 6 hours (divisor number of 24 hours) and the minimum

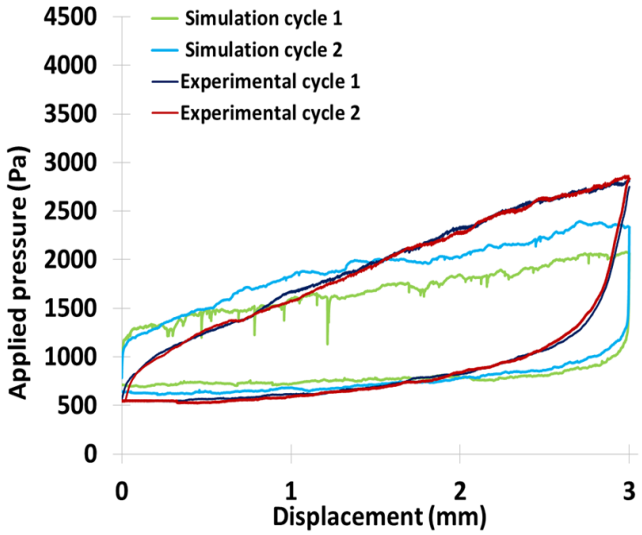

FIGURE 5.21: Simulation 1: Stress/displacement numerical curves over 2 cycles of charging/discharging compared to the experimental curves, with $\varphi = \varphi_s = 5°$ throughout the whole process

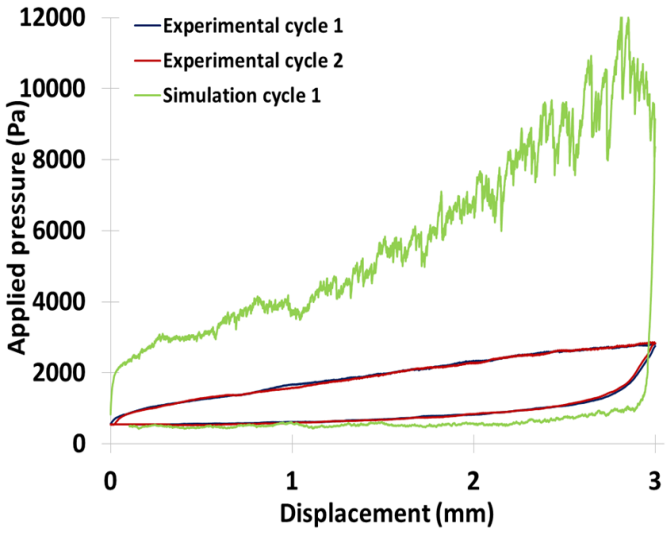

FIGURE 5.22: Simulation 2: Stress/displacement numerical curves over 2 cycles of charging/discharging compared to the experimental curves, at the sample generation: $\varphi = \varphi_s = 5°$, then before cycling: $\varphi = \varphi_s = 45°$

cycling temperature is increased to 50°C reducing the time needed for the stabilization. The corresponding temperature evolution for one charging/discharging cycle of the averaged of the two bottom thermocouples 1 and 2 and the top thermocouple 8 is given in Figure 5.25.

5.3.2 Resulted stresses on ESPERA

Three different fillings are realized on ESPERA and each time, 7 thermal cycles are performed. The initial porosity n is measured and is equal to 0.37. The mean stress values obtained in

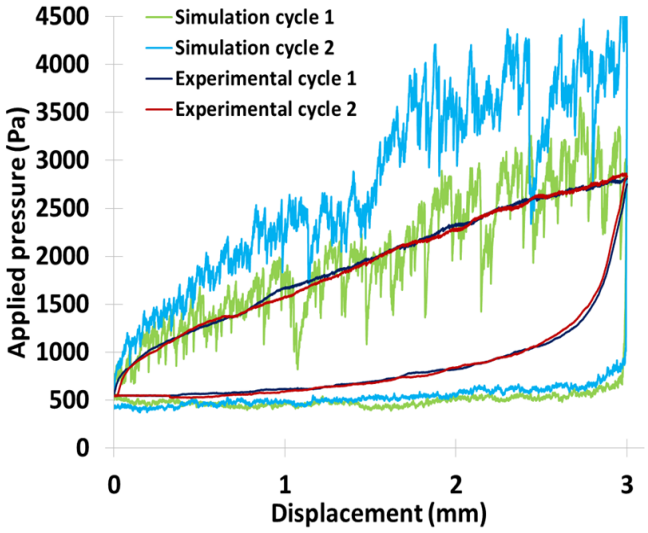

FIGURE 5.23: Simulation 3: Stress/displacement numerical curves over 2 cycles of charging/discharging compared to the experimental curves, with $\varphi = \varphi_s = 45°$ throughout the whole process

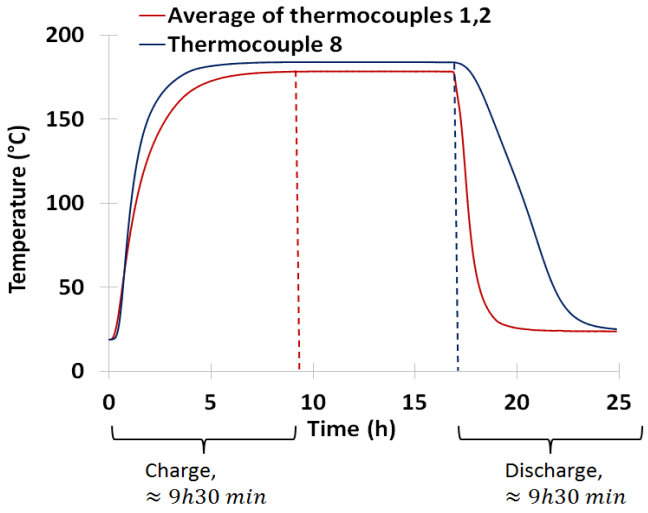

FIGURE 5.24: Temperature evolution over one thermal cycle for the average of thermocouple 1,2 (at bottom) and for thermocouple 8 (at top), cycling between ambient temperature and 185°C

the 3 fillings and their corresponding error bars are plotted in Figure 5.26 for the four different layers. The values of the force measurement devices, belonging to a same layer are averaged and the results are plotted only at the end of the charging or discharging processes. The resulted stresses are also normalized by the hydrostatic pressure at the bottom of the tank. As predicted, the experimental resulted stresses release during the charging cycle and increase during the discharge cycle, dealing with a case where $\alpha_w > \alpha_b$. A factor of 4 is obtained between the maximum resulting stresses at the end of the cooling period and the initial state.

The comparison of the obtained experimental results with the numerical ones is quite difficult.

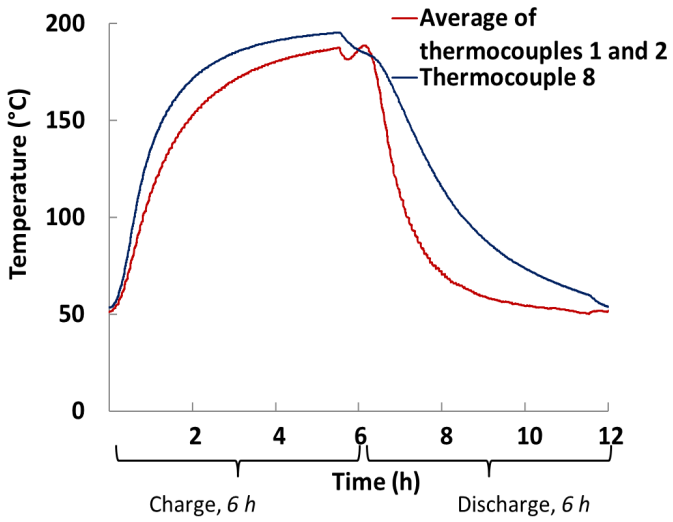

FIGURE 5.25: Temperature evolution over one thermal cycle for the average of thermocouple 1,2 (at bottom) and for thermocouple 8 (at top), cycling between 50 and 185°C

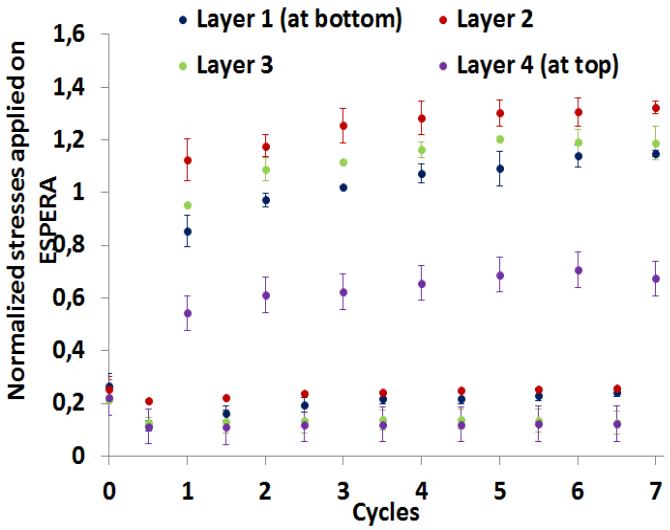

FIGURE 5.26: Applied stresses on ESPERA within 7 performed thermal cycles, normalized with the hydrostatic pressure at the bottom of the tank

In fact, the input data (as TECs of the used materials, the differential of temperature, the friction angles ...) in the numerical simulations do not correspond to the experimental ones. The experimental setup arrives lately during this work, limiting the time of its exploitation and making the numerical validation difficult, considering that the calculation time needed are very long.

Although the incompatibility of the numerical and the experimental input data, the comparison is done by referring to the numerical results obtained in Chapter 4- Figure 4.30 where the maximum stresses are demonstrated to vary linearly with the differential of TECs. Based on this, the numerical results presented in Figure 4.30 (the ones with the lowest $\Delta\alpha$) are used to compare with the experimental measurements on ESPERA. Recalling that these numerical

	Experimental properties	Numerical properties
TEC particle, α_b (/°C)	9×10^{-6}	4×10^{-6}
TEC wall, α_w (/°C)	23×10^{-6}	8×10^{-6}
Boundary condition case	$\alpha_w > \alpha_b$	$\alpha_w > \alpha_b$
Temperature profiles	Referring to Figure 5.25	Referring to Figure 4.4
ΔT (°C)	135	300
$\Delta\alpha\Delta T$	0.00189	0.0012
Friction angle (°)	Low levels of friction	$\varphi = \varphi_s = 45°$
Initial porosity n	0.37	0.39

TABLE 5.3: Input data: Experimental and numerical material properties and thermal conditions

results deal with an homogeneous thermal configuration and an higher thermal expansion coefficient devoted for the tank wall (Case 1: $\alpha_w > \alpha_b$). High friction angles between the particles themselves ($\varphi = 45°$) and at the contact with the wall ($\varphi_s = 45°$) are used here too. A comparison table between the numerical and experimental input data is presented in Table 5.3. Given that a higher $\Delta\alpha\Delta T$ is considered experimentally (with a factor of $f = \frac{(\Delta\alpha\Delta T)_{exp}}{(\Delta\alpha\Delta T)_{num}} = 1.575$), only the maximum numerical values (obtained at the end of the discharging cycle) are multiplied by the same factor f (based on the linear proportionality between the maximum stresses and the imposed $\Delta\alpha\ \Delta T$). The numerical initial stress and the stress obtained at the end of the charging cycle are kept unchanged. Both experimental and numerical results are presented in Figure 5.27. The numerical results are higher than the experimental ones. The difference between them is mainly caused by the different initial stress values, as if the numerical results are shifted from the experimental ones. This initial stress difference between both numerical and experimental calculations was also shown in P'tit-Pousse results (Figure 5.21). Moreover, the tests realized on P'tit-Pousse has shown that the numerical results obtained with low friction angles ($\varphi = \varphi_s = 5°$) were the closest to the experimental ones and able to better reproduce the glass beads medium than higher values of friction angles. Referring to Figure 4.11a, high friction coefficients lead to higher stresses and a faster stress accumulation over thermal cycles comparing to the low values. Thus, the numerical results performed with low friction values might be even lower than the presented ones in Figure 5.27, approaching the experimental measured stresses.

After all, the aforementioned numerical and experimental comparison remains a preliminary one. New numerical simulations, respecting the mechanical and thermal properties of the used material as well as the thermal imposed conditions of the experiment, should be performed. A better comparison, thus a better understanding can be then assured.

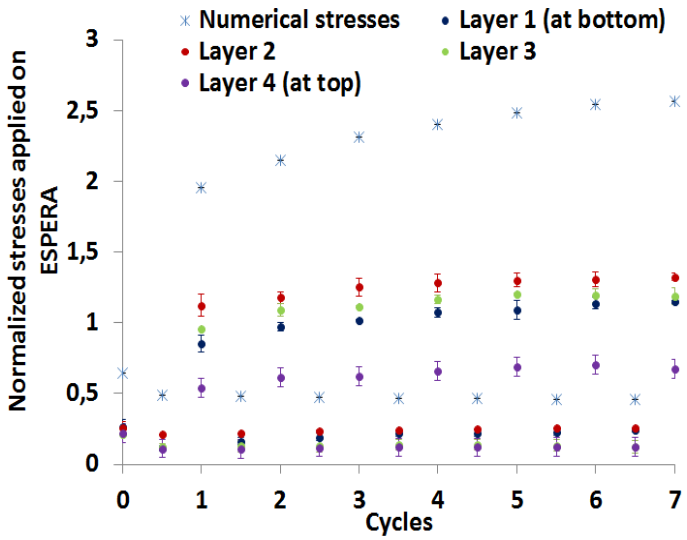

FIGURE 5.27: Applied stresses on the ESPERA within 7 performed thermal cycles and compared with the numerical results, referring to Table 5.3

5.4 Conclusion

An experimental setup ESPERA, aiming at the study of thermal ratcheting phenomenon was designed and constructed at the CEA laboratory, France. It is a dual-media thermocline prototype with air as thermal fluid, equipped with force measurement devices installed at different positions of the tank. The stresses applied by the particulate filler on the wall can be thus measured over the thermal cycles.

The force measurement devices, on which 4 strain gauges were glued, were calibrated at ambient and high temperature. A linear relationship was obtained between the imposed load and the measured voltage. The temperature was also compensated by means of a full bridge configuration. A different setup, named P'tit-Pousse, was designed to calibrate the friction coefficient between the particles of the filler and to verify the accuracy of the homemade force sensors in the range of the forces encountered. P'tit-Pousse consists in a rectangular container filled with spherical glass beads. Three walls of the container are movable and permit a cyclic linear displacement either in the direction of pushing the beads onto the fixed remaining wall or in the reverse direction. Then, the stresses applied by the beads on the wall were measured through a force measurement device installed on the fixed wall of P'tit-Pousse. The results showed that the force measurement device was capable of detecting and very precisely the applied stresses, validating its sensitivity. Moreover, numerical simulations reproducing P'tit-Pousse were also run to compare the experimental results. The comparison between both numerical and experimental approaches allows for the calibration of the numerical model by precising the suitable friction angles that are able to better reproduce the experimental behavior.

In addition to this, thermal cycles were performed on ESPERA. The stresses applied by the

spherical beads on the tank wall were measured at the end of the charging and discharging processes. The stresses were released during the charging cycle, due to the wall expansion (since the TEC of the wall is greater than the filler), while during the discharging cycle, higher stresses were applied. The comparison with the numerical results was also realized. Although the input data (temperature profiles, TECs of the materials...) used for each approach are not fully compatible, the comparison is assured based on previously obtained numerical results, allowing for an extrapolation/approximation of the numerical results obtained on ESPERA. The global behavior of the particulate filler (i.e. release of stresses during the charging cycle followed by an increase of stresses during the discharging cycle) is validated numerically and experimentally. However, the numerical results seemed to be shifted from the experimental ones. This may be due to the difference of the initial states. All in all, appropriate numerical simulations with compatible input data have to be run for a better comparison with the experimental data. Unfortunately, the lack of time prevented the realization of additional long lasting numerical simulations.

Chapter 6

Conclusions and perspectives

This research was devoted to study the thermo-mechanical behavior of a thermocline storage tank and the interaction of the granular bed with the wall. The importance of this work lies in its application for the safety and durability of thermocline structures over thermal cycles. The objectives of this study was to understand the mechanical behavior of the granular bed inside the packed-bed storage facility, and what comes with this behavior such as bed's densification and stress accumulation on the wall. To achieve it, we have followed an approach which consisted of the following steps:

- Definition of a DEM model to reproduce the thermocline storage tank consisting of a granular assembly inside a cylindrical tank and submitted to temperature variations;
- First investigations of the bed's behavior based on the assumption of rigid boundaries (i.e. without taking into account the tank's deformation with thermal variations);
- Implementation of deformable tank wall (i.e. affected by the imposed temperature variations) allowing the study of the granular bed/wall interactions;
- Designing an experimental setup equipped with home-made force measurement devices able to measure the applied stresses on the wall;
- Performing experimental tests using a simplified setup, assuring from the sensitivity and the functionality of the force measurement devices, before performing tests using the newly developed thermocline prototype;

The major contributions and conclusions obtained from this study are summarized in this chapter. Moreover, perspectives and recommendations for future research work are also presented.

Major contributions

On the numerical approach basis

A discrete numerical model was defined to study the thermo-mechanical behavior of a particulate filler inside a thermocline storage tank, using spherical particles based on linear contact laws between particles. All simulations were performed using the open-source code YADE.
As a first approximation, rigid boundaries were considered: only the granular filler is subjected to thermal variations by imposing a growth/shrinkage of each particle's volume (i.e. radius). Then, a more sophisticated model was developed, allowing the deformation of the thermocline wall with temperature variations and applied stresses by the granular media. The tank wall, behaving as a truss structure, is modeled using discrete elements as well. Using the deformable boundaries, two cases were also studied: the case where the thermal expansion coefficient (TEC) of the wall is higher than the filler one and inversely. Besides the different boundary condition cases, different thermal configurations were studied as well: the homogeneous, the moving thermal gradient and the steep moving thermal gradient configurations. Recalling that the heating process is always started form the top of the tank and the cooling process from the bottom. In all cases, the numerical results showed an accumulation of stresses over the thermal cycles, due to granular bed densification that tends to stabilize after a certain number of performed cycles.
It was remarkable that the generated stresses and the motion of the particles are dependent on the way the charging/discharging cycles are applied to the packed bed, on their positions inside the storage tank and on the applied boundary condition case. The numerical results show that the stress values developing in the case of moving thermal gradient are higher than in the case of the thermally homogeneous loadings for these both cases: the case dealing with higher thermal expansion coefficient (TEC) for the bed than the wall and the rigid boundary case. Whilst in the case where the TEC of the bed is lower than the wall's TEC, the steep moving thermal gradient configuration is less critical in terms of induced stresses than the homogeneous configuration. All these stresses results are largely dependent on the kinematical behavior of the bed inside the tank, especially at deep.
The displacement of the deepest particles is dependent on the position of the moving thermal gradient inside the tank and leads to a faster rearrangement of particles in the case where the TEC of the bed is greater than the wall's TEC and rigid wall case, comparing to an homogeneous thermal configuration. However, a faster stabilization is shown when the bed is cycled homogeneously in the case where the TEC of the wall is higher than the bed's TEC.
Globally, the macroscopic behavior of the tank in terms of stress levels generated on the wall or kinematical response of the bed, is not so different from one case to another (boundary condition cases and thermal configurations). The stress accumulation tends to stabilize with large number of performed thermal cycle and is related, at the first order, to the bed's settlement due to an imposed thermal conditions ($|\Delta\alpha\Delta T|$), regardless the behavior of the tank

walls towards temperature variations (i.e. different boundary conditions). In addition to this, the resulted stresses are directly proportional to this $|\Delta\alpha\Delta T|$ factor.

On the experimental approach basis

An experimental setup ESPERA, aiming at studying the thermal ratcheting phenomenon was designed and built up at the CEA laboratory. The thermocline prototype ESPERA is a cylindrical tank, cycled with air as heat transfer fluid, equipped with force measurement devices installed at different positions of the tank. The force measurement devices permit the measurement of the stresses applied by the particulate filler on the wall over the performed thermal cycles.
The force measurement devices, on which 4 strain gauges were glued, were calibrated at ambient and high temperature. The temperature compensation was assured through the full bridge configuration and a linear relationship was obtained between the imposed weight and the measured voltage. Then, their sensitivity and their functionality were tested on a different installed setup, called P'tit-Pousse. P'tit-Pousse consists in a rectangular container that was filled with spherical glass beads. Three walls of the container are related to a motorized micrometric table allowing for a linear motion either in the direction of pushing the beads onto the fixed remaining wall or in the direction of releasing of the beads. Then, the stresses applied by the beads on the wall were measured through a force measurement device installed on the fixed wall of P'tit-Pousse. The results showed that the force measurement device is able to detect the applied stresses, validating its sensitivity and its design dimensions. Moreover, P'tit-Pousse was reproduced numerically enabling a comparison with the experimental results. Besides the validation of the developed model, the comparison between both approaches allows also for the calibration of the numerical model by precising the suitable friction angles used numerically at the contact that are able to better reproduce the experimental behavior of the glass beads.
In addition to this, thermal cycles were performed on ESPERA. The stresses applied by the spherical beads on the tank wall were measured at the end of the charging and discharging processes. The global behavior of the thermocline agrees well with the numerical results: a release of stresses is observable during the charging cycle (since the TEC of the wall is greater than the filler) and an increase of stresses is obtained during the discharging cycle. The quantitative comparison with the numerical results was also realized. Although the difference nature of the input data (temperature profiles, TECs of the materials...) used for each approach, the trend comparison is assured based on previously obtained numerical results, allowing for an extrapolation/approximation of the numerical results obtained on ESPERA. The numerical results seemed to be shifted from the experimental ones, due to the difference of the initial states. In both numerical and experimental results, an increase in the

radial stresses by a factor of 3-4 is visible when dealing with a $|\Delta\alpha\Delta T| = 1890\mu m/m$ (approx 2000 $\mu m/m$).

Perspectives and recommendations

This study has opened new research paths that can be interesting. In what follows, recommendations for future research work are presented which concerns both numerical and experimental approaches.

Perspectives for improving the numerical model

- The developed numerical model is based on elastic laws for the tank wall. It would also be suitable to implement a thermo-elasto-plastic model for the tank wall to investigate the potential plastic strain accumulation over the thermal cycles, which may affect the previously presented results in Chapter 4.
- A larger number of cycles has to be performed in order to verify the obtained trends results, regarding the stress/wall deformation and the bed's densification stabilization. A better comparison between the different thermal configurations and the different boundary cases can be assured as well.
- A bi-disperse particle size distribution can be numerically performed in order to better represent the solid filler mixture used in thermocline tanks (rocks and sand mixture).
- The proposed model can be improved by using clumps instead of spherical particles. The clumps, consisted of an assembly of overlapped spheres, can simulate particles with irregular shapes. Besides, they allow to predict if the fracture of particles might happen inside the tank over the thermal cycles. This can be done by tracking the breakage of bonds of the particles consisting the clump.

Perspectives for improving the experimental approach

- ESPERA can be exploited by conducting different tests that could not been investigated during this work due to the lack of time:
  - Larger number of realizations (emptying and filling) have to be performed aiming for more precise results.
  - Larger number of thermal cycles have to be performed aiming at studying the influence of repeated cycles.

  - Different particle size distributions can be tested: the bi-disperse configuration (mixture of 1.5 and 4 mm particles diameters). Also, it would be interesting to test a real granular bed with particles shape close to the solid filler used in thermocline storage tanks.
  - The influence of slenderness ratio S_r could be also investigated by filling the tank up to different heights (up to $S_r = 3$).
  - The filling procedure might be of a great importance and it would be interesting to test its influence. In fact, the resulted stresses on the wall would differ if the filling of ESPERA is realized from a central fixed point or through a sieve that gradually moves along the tank's height. In the previously experimental results, the tank was filled from the top using a small shovel. Note that the porosity of the medium was measured throughout different realizations (filling and emptying) using the shovel and was always equal to 0.37.

- Besides the different possible tests, more precise results can be obtained by mounting a larger number of force measurement devices. It is recommended to have 4 windows (and thus to install 4 force measurement devices) at each level of the existent windows. Given the stochastic nature of a particulate bed, the results can be averaged and more accurate values can be obtained.

- The low-cost timer used in ESPERA to monitor the opening and the closing of valves could not allow for the stabilization of the thermal conditions along the tank. The replacement of the monitoring system used in ESPERA is important, allowing for the thermal stabilization of the tank and for a higher range of temperature differences between the charging and discharging (cycling between 25/185°C instead of 50/185°C)

- The validation of the numerical model is crucial by reproducing the experiments with the compatible input data. ESPERA results would provide trustful data that can be used to validate and improve the proposed numerical model.

Appendix A

Potential tank's geometries and properties

This appendix provides different potential thermocline storage tank geometries and properties. First, aluminum wall tank are considered and compared to Steel tank wall, detailed in Chapter 4. Then, a potential tank's geometry is tested under thermal cycling: a truncated conical tank, with an enlarged top radius.

A.1 Aluminum tank walls

In this Section, the mechanical properties of the cylinders composing the membrane are adjusted to model an aluminum tank membrane. The objectives is to see the influence of the membrane's stiffness. The macroscopic Young's Modulus is set to 69×10^9 Pa (corresponding to $E^{Micro} = 5.951 \times 10^{11}$ Pa). 25 thermal cycles are performed for both boundary cases ($\alpha_w > \alpha_b$ and $\alpha_w < \alpha_b$) with homogeneous and SMTG thermal configurations. The maximal normal stresses obtained at the end of each charging/discharging cycles are plotted in Figure A.2. In Case 1, only the homogeneous configuration with steel membrane is added to the plot, while the Steel/SMTG configuration is added to Figure **??**, in order to compare the results with the critical thermal configuration in each case, without overloading the figures. As it can be noticed, not much influences are seen in terms of maximal generated stresses in both cases, whether the membrane are made of Steel or Aluminum. The resulted stresses are slightly higher when dealing with steel membrane, where thermal stresses are converted into applied stresses on the wall instead of membrane deformation.
Nevertheless, the deformation of the Aluminum-membrane is about 2 or 3 times greater than the Steel-membrane, which corresponds to the ratio of their Young's modulus ($\frac{E_{steel}}{E_{Alu}} = 3$). These results are confirmed when comparing the Figures 4.18a to A.3a and 4.19b to A.3b.

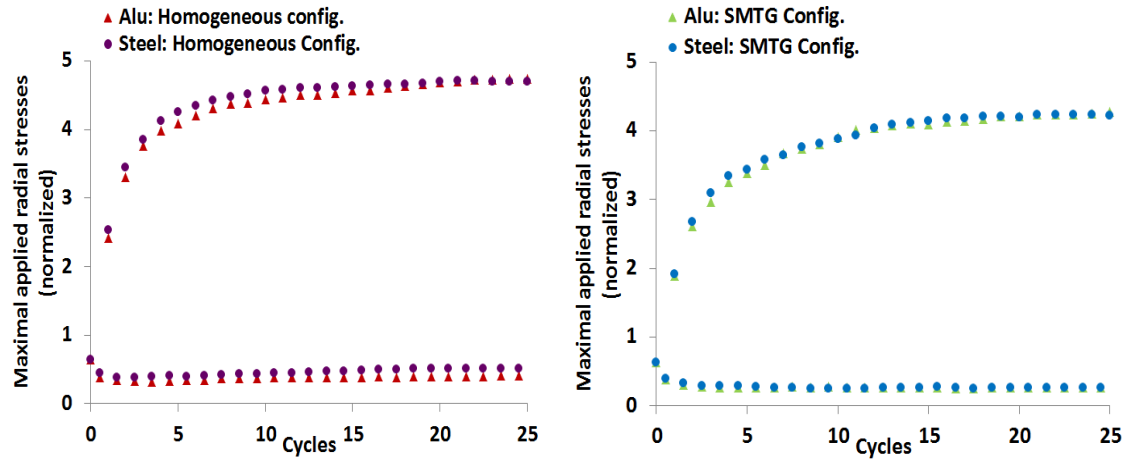

(a) (b)

FIGURE A.1: Aluminum tank walls: radial stress evolution in Case 1 ($\alpha_w > \alpha_b$): (a) Homogeneous configuration, (b) SMTG configuration

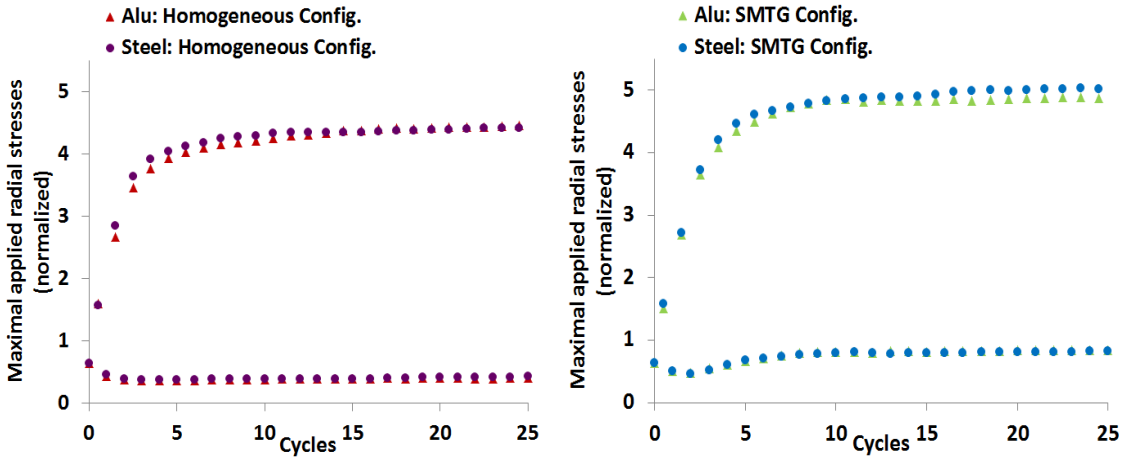

(a) (b)

FIGURE A.2: Aluminum tank walls: radial stress evolution in Case 2 ($\alpha_w < \alpha_b$): (a) Homogeneous configuration, (b) SMTG configuration

A.2 Truncated conical tank

The numerical model is used to compare the resulting thermal stresses generated during loading and unloading cycles of a thermal storage unit with truncated conical shape vs. the more commonly used cylindrical shape (shwon in Figure 4.11). From a thermal point of view, it has been shown that a conical shape can always offer a high overall thermal efficiency Zanganeh et al. (2014, 2012). In order to study the effect of such geometry on the resulting thermal normal stresses, numerical tests with rigid boundaries were realized on a 2 m high tank with an increasing radius from 0.5 m at bottom to 1.05 m at top. The wall inclination is then equal to 15° Zanganeh et al. (2014). The initial porosity of all samples is equal to 0.39. 8 cycles with a MTG configuration with an overall temperature difference of 300°C are considered.

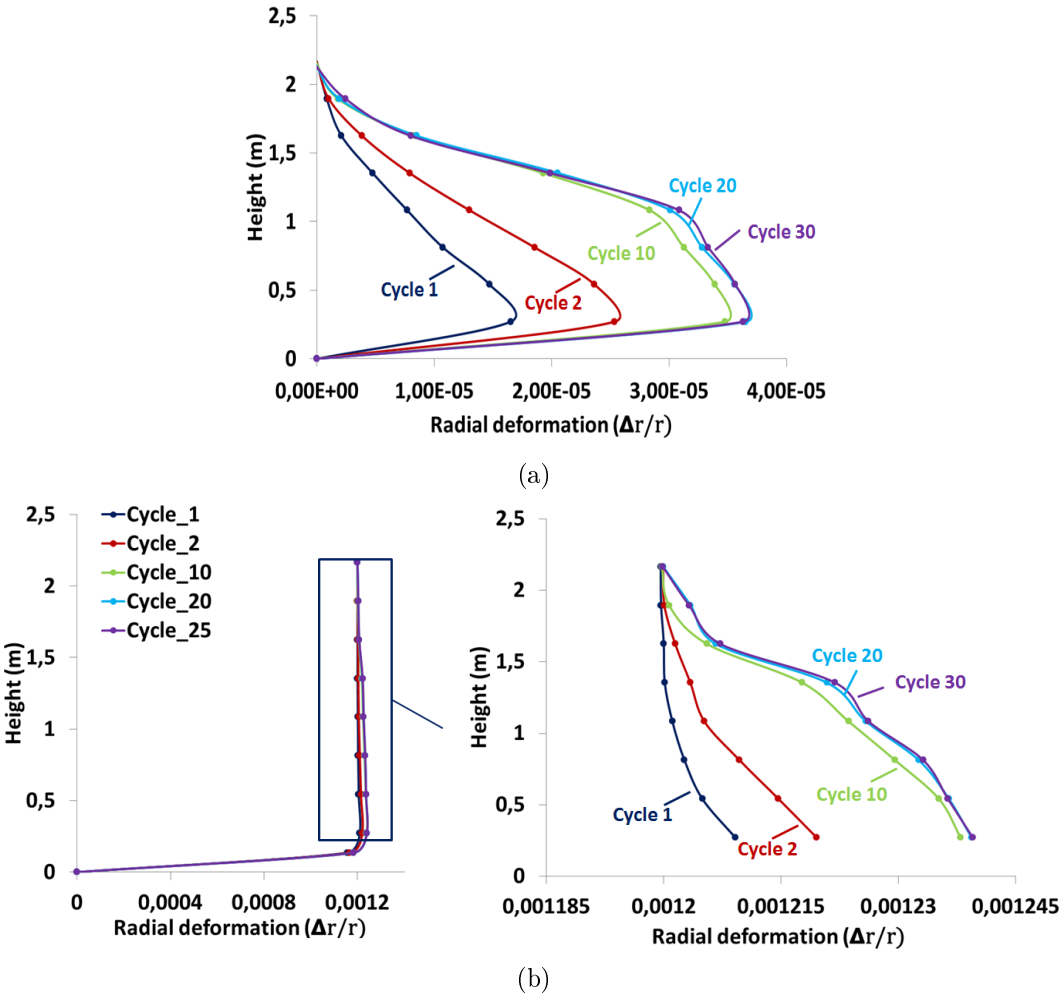

FIGURE A.3: Aluminum tank walls: evolution of tank walls deformation in: (a) Case 1 ($\alpha_w > \alpha_b$), (b) Case 2 ($\alpha_w < \alpha_b$)

Different values of particle/particle friction angle φ and wall/particle friction angle φ_s are considered as well. For each studied case, three samples are considered and the corresponding mean values and error bars are calculated. The resulted maximal normal stresses (normalized by the hydrostatic pressure at the bottom) are presented in Figure A.4. Here too, as in cylindrical tanks, increasing the friction in the tank (whether the particle/particle φ or the particle/wall φ_s friction angles) leads to higher induced stresses. The accumulation of stresses during the loading phases over the cycles is more restricted and controlled when dealing with truncated conical tanks. Figure A.4 shows that the initial applied normal stresses are lower in the case of inclined boundaries than vertical walls (compared to Figure 4.11a). The conical walls are subjected to vertical loads due to the weight of particles above resulting in further normal stresses on the wall. Then, during the loading cycles, the truncated cone shape reduces the normal forces acting on the walls during thermal expansion of the rocks by guiding them upwards due to the wall inclination comparing to cylindrical shapes. Moreover, the truncated conical shape provides a lower slenderness ratio comparing to the cylindrical shape, reducing

therefore the thermal stresses applied on the tank as it was previously seen. The conical shape allows a reduction of about 20 % of normal loads acting on the wall when high friction is considered slowing down the accumulation of stresses and then the ratcheting of the tank over the cycles.

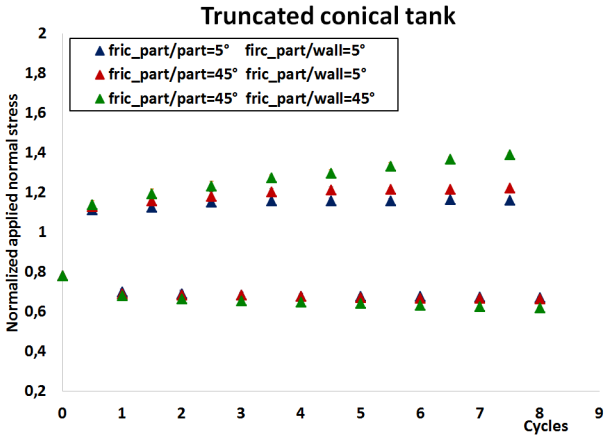

FIGURE A.4: Thermal stresses applied on truncated conical walls at different levels of friction

Appendix B

Execution plans of ESPERA

This appendix provides the execution plans of ESPERA. It presents, consecutively, an execution plan for the whole setup, cross-sectional elevations of the cylindrical tank letting appear the windows where the force sensors are placed, execution plans of the top and bottom veins, the diaphragm system and the perforated plate placed at the bottom of the tank. Also, an execution plan of the force measurement device is provided at the end.

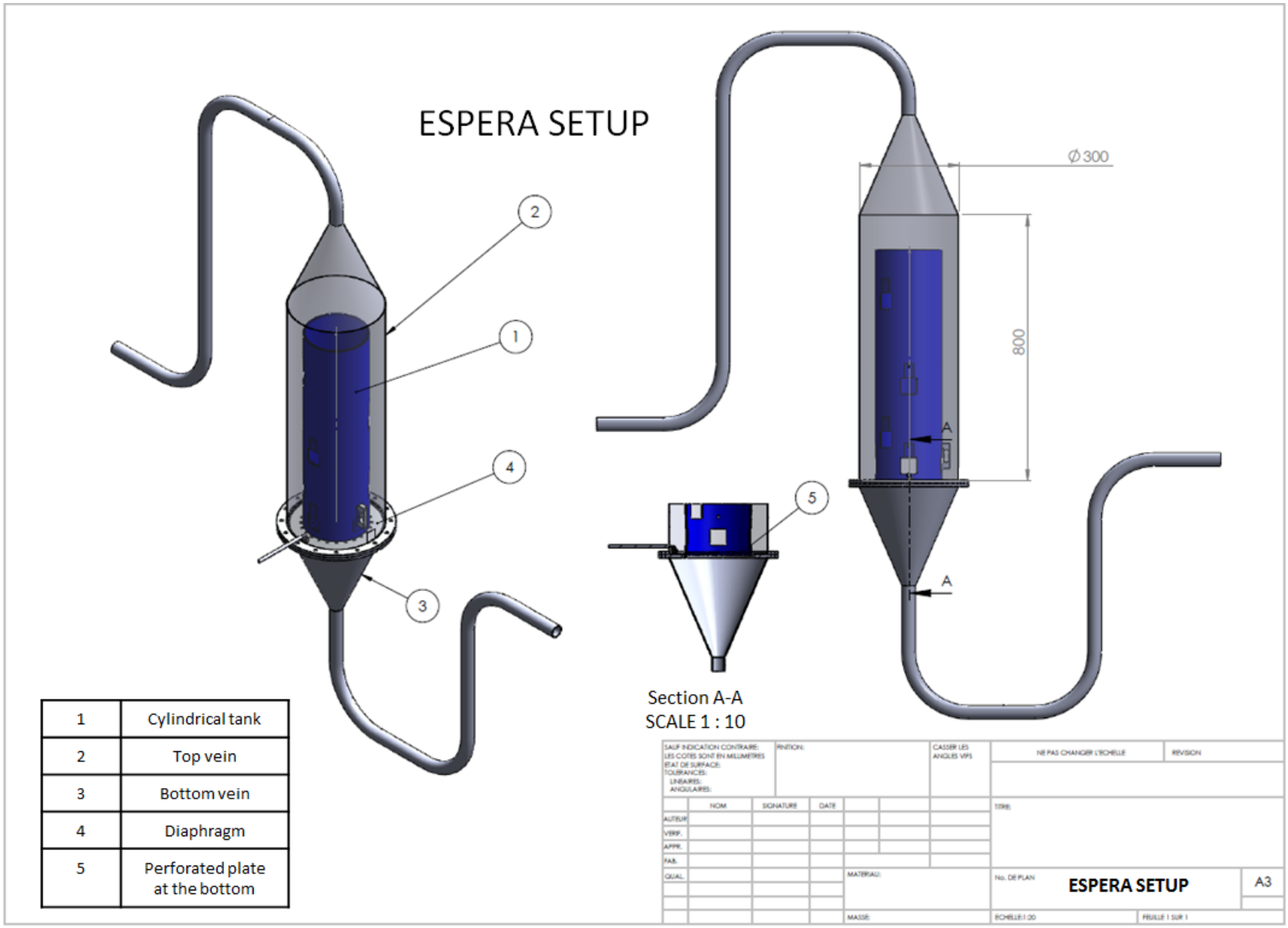

1	Cylindrical tank
2	Top vein
3	Bottom vein
4	Diaphragm
5	Perforated plate at the bottom

FIGURE B.1: Schematic plan for the whole setup

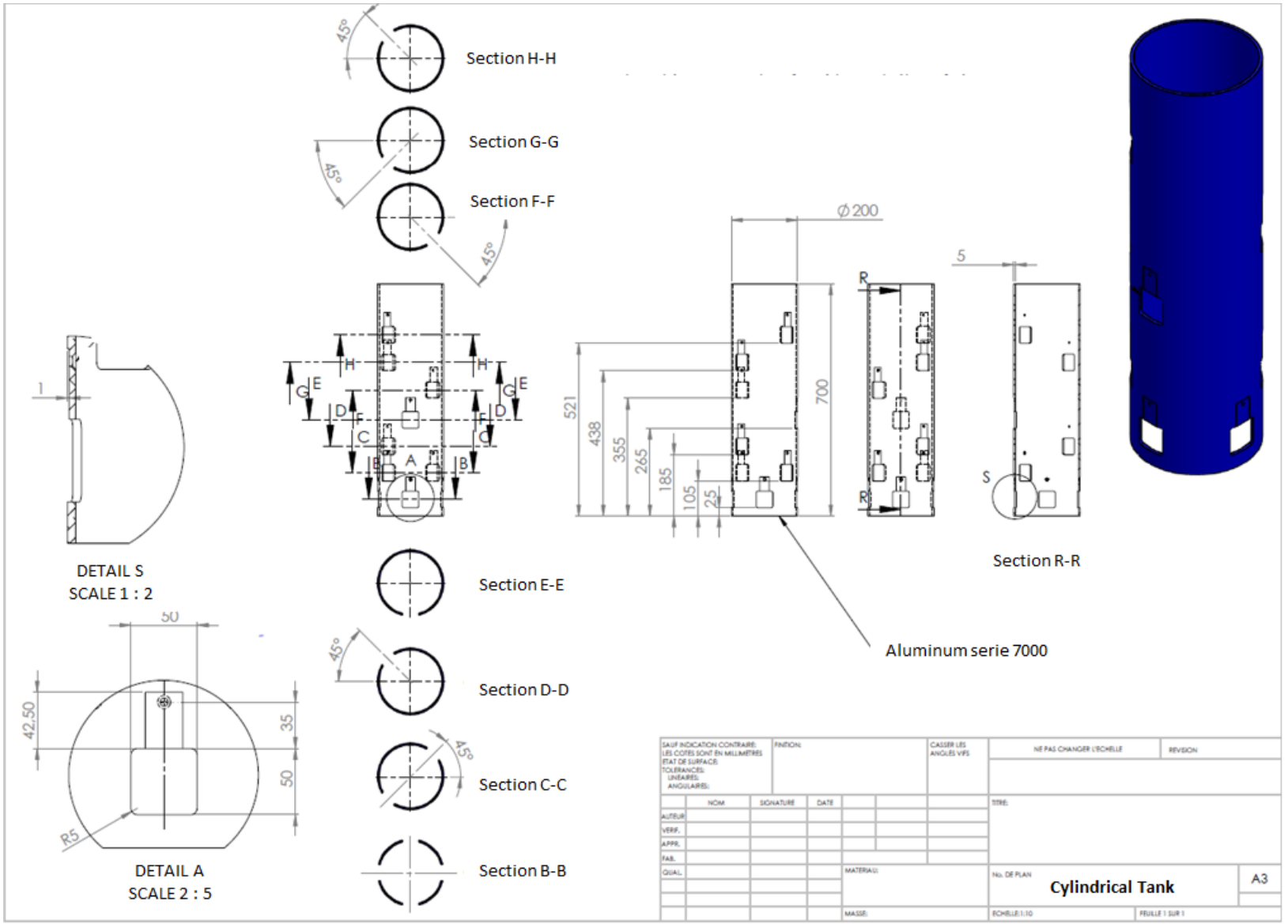

FIGURE B.2: schematic cross-sectional elevations of the cylindrical tank letting appear the windows

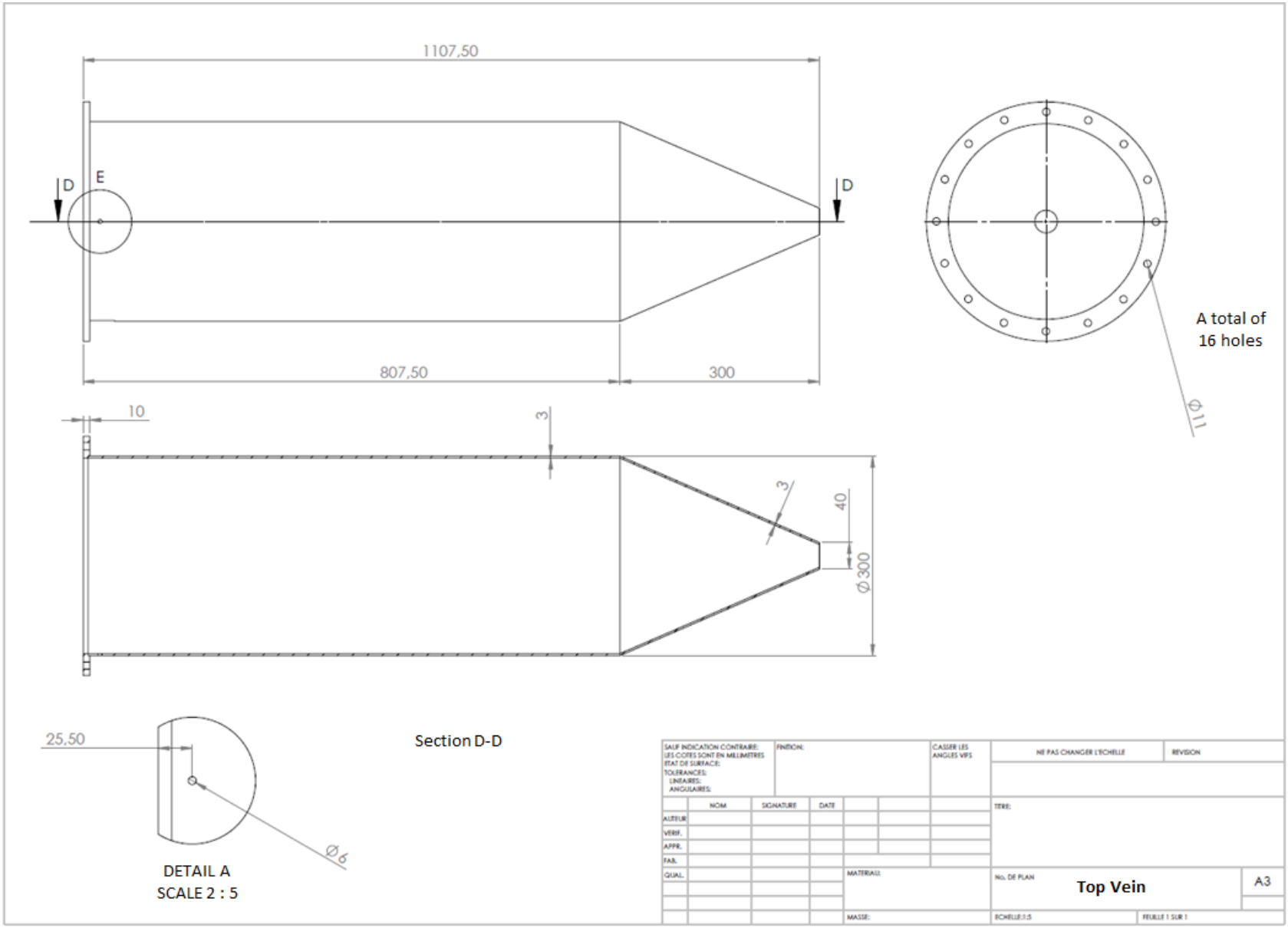

FIGURE B.3: Top vein

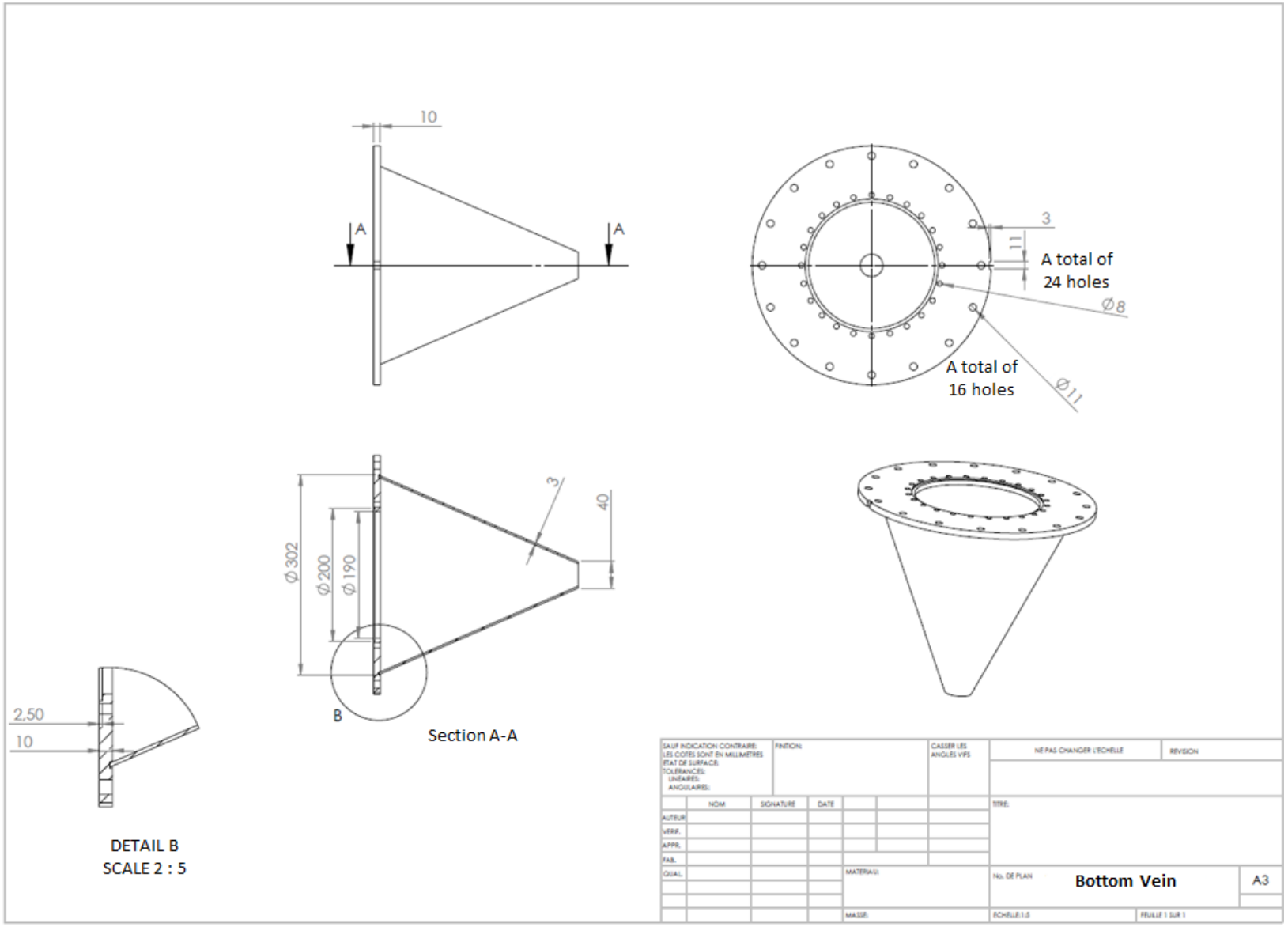

FIGURE B.4: Bottom vein

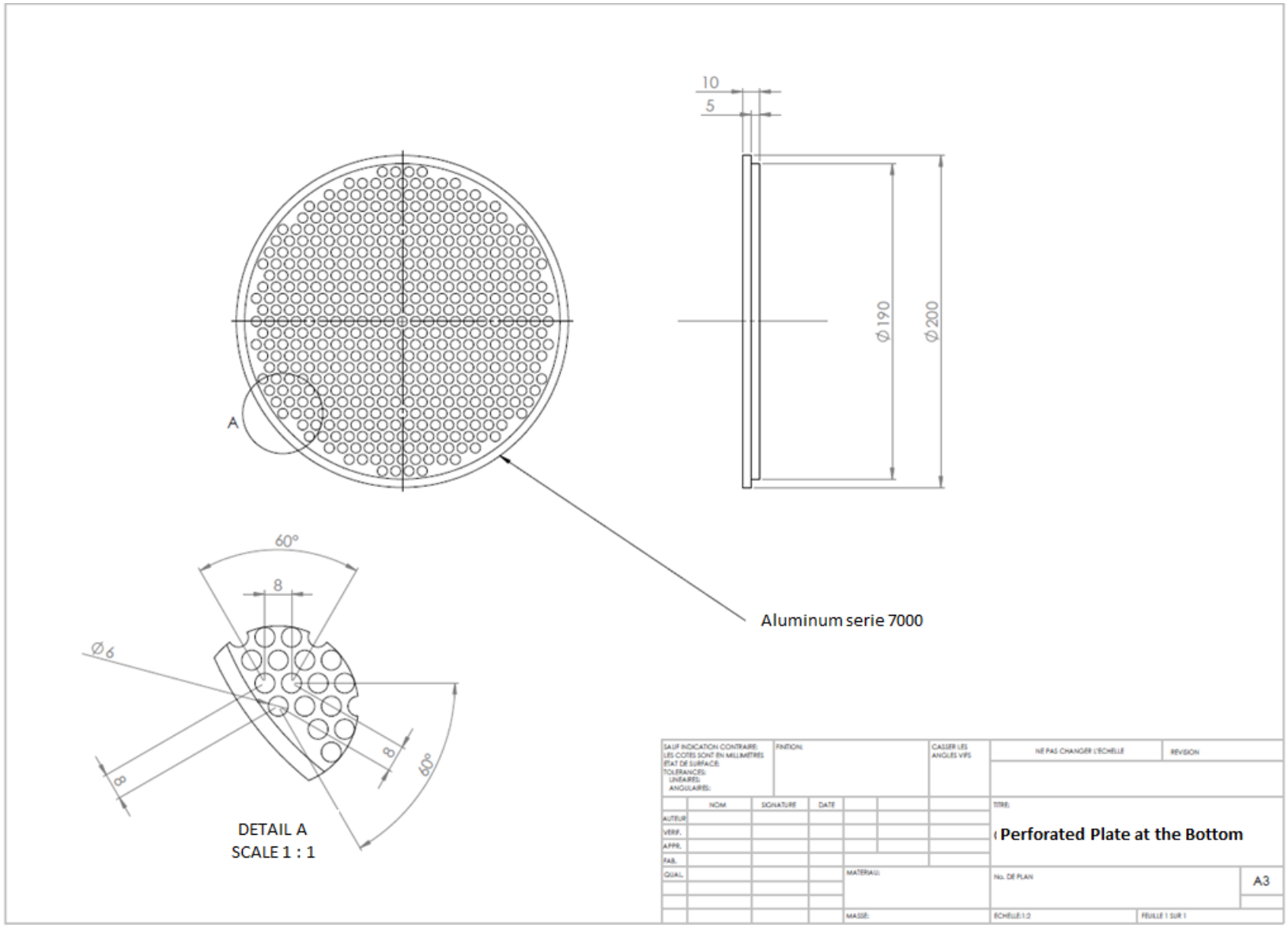

FIGURE B.5: Perforated plate at the bottom of the tank

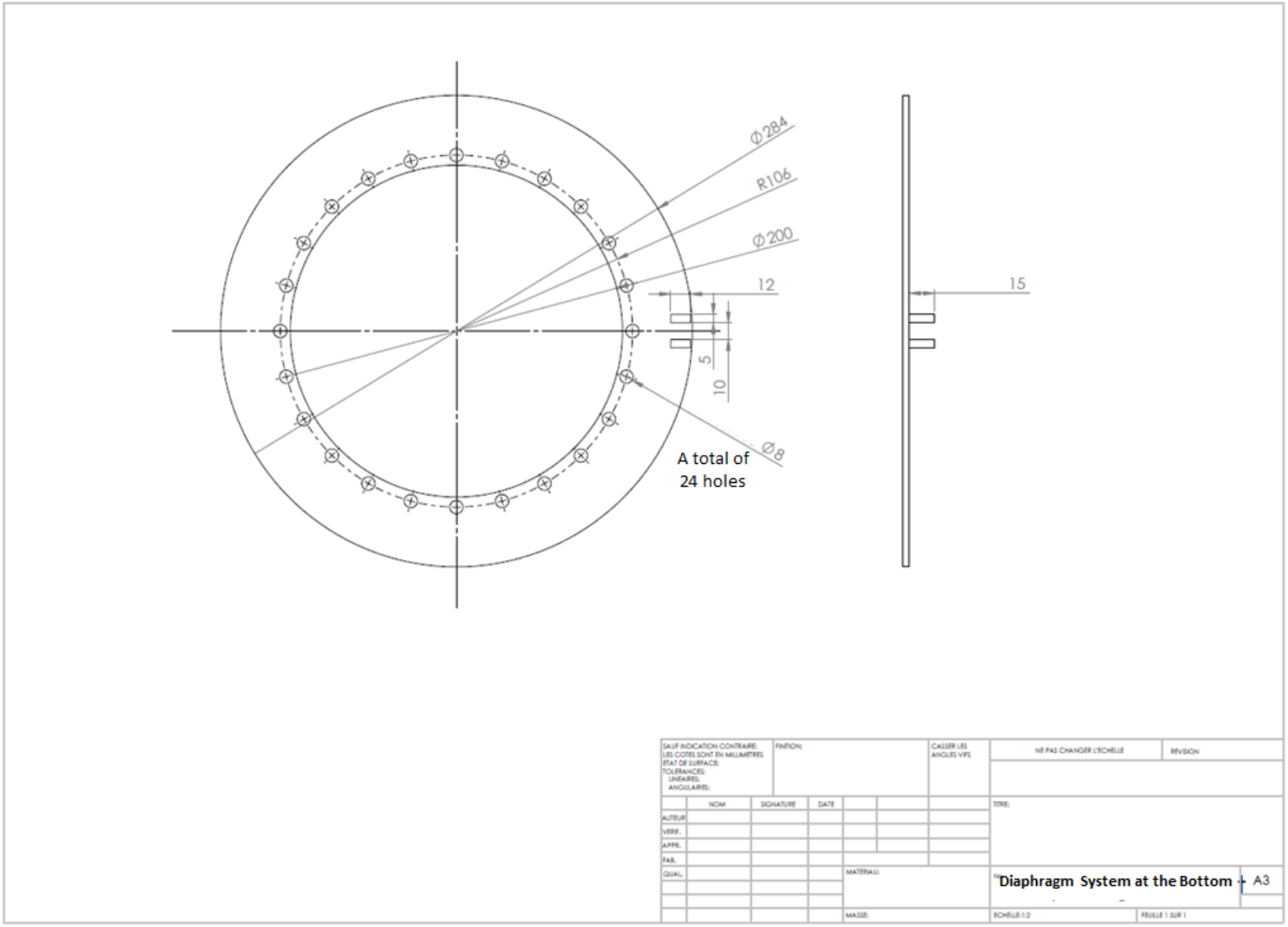

FIGURE B.6: Diaphragm system at the bottom of the tank

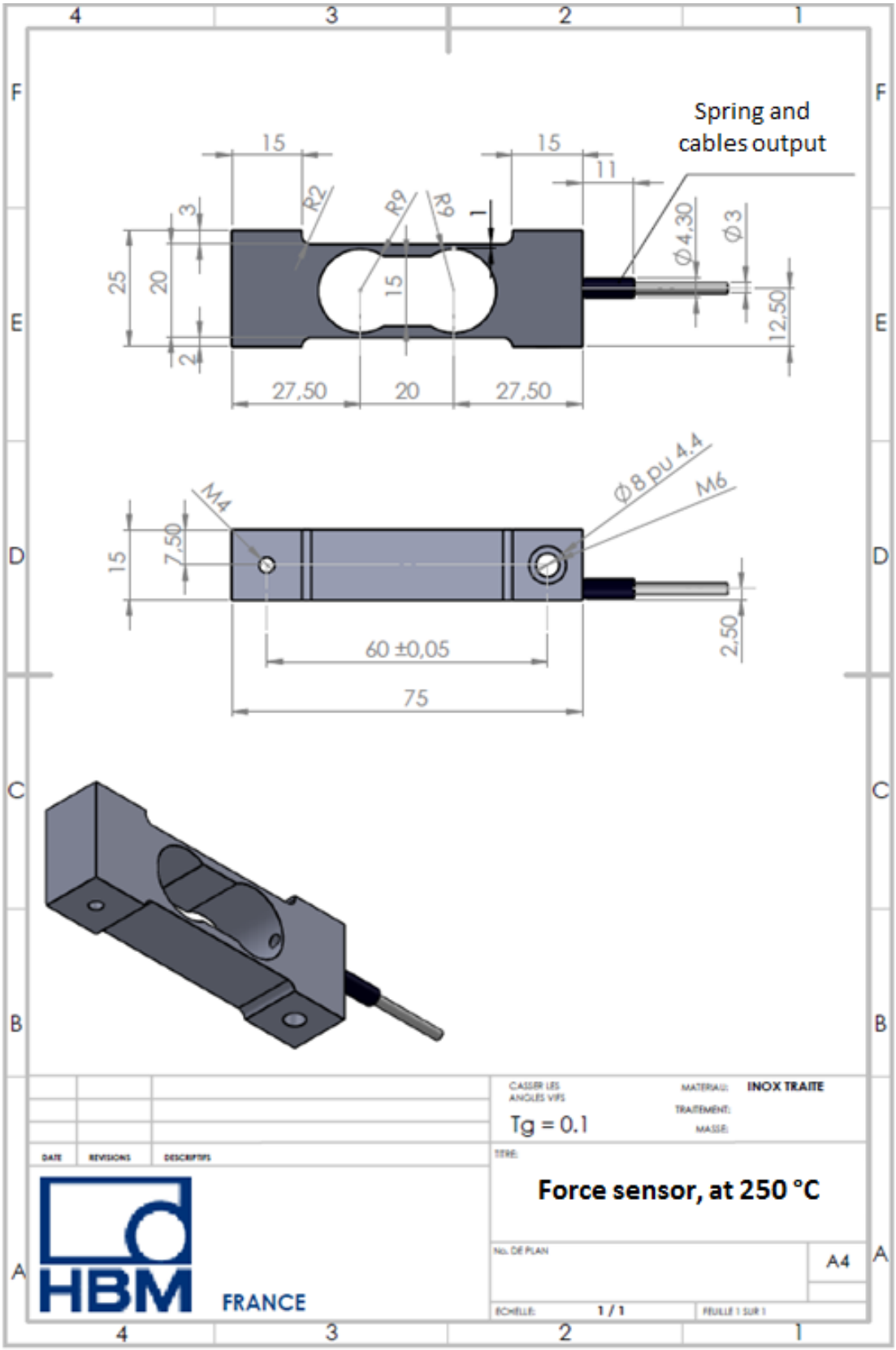

FIGURE B.7: Schematic plan of the force measurement device

Bibliography

Coastal chemical company l.l.c, hitec solar salt, http://www.coastalchem.com/pdfs/hitecsalt/hitec%20solar%20s 2011.

DO Akinyele and RK Rayudu. Review of energy storage technologies for sustainable power networks. *Sustainable Energy Technologies and Assessments*, 8:74–91, 2014.

BY Ao, SX Chen, and GQ Jiang. A study on wall stresses induced by lani 5 alloy hydrogen absorption–desorption cycles. *Journal of alloys and compounds*, 390(1):122–126, 2005.

ND Aparicio and ACF Cocks. On the representation of random packings of spheres for sintering simulations. *Acta metallurgica et materialia*, 43(10):3873–3884, 1995.

O. Gillia D. Imbault B. Charlas, P. Doremus. Numerical analysis of a metal hybrid powder bed under swelling or lateral compaction by the discrete element method.

Blight. Temperature changes effects overpressures in steel bins. *International Journal of Bulk Solids Storage in Silos*, 1985.

Nicholas Boerema, Graham Morrison, Robert Taylor, and Gary Rosengarten. High temperature solar thermal central-receiver billboard design. *Solar Energy*, 97:356–368, 2013.

ASME Boiler and Pressure Vessel Code. Section ii–materials. *Part D–Properties*, 1998.

Franck Bourrier, François Kneib, Bruno Chareyre, and Thierry Fourcaud. Discrete modeling of granular soils reinforcement by plant roots. *Ecological Engineering*, 61:646–657, 2013.

Doug Brosseau, John W Kelton, Daniel Ray, Mike Edgar, Kye Chisman, and Blaine Emms. Testing of thermocline filler materials and molten-salt heat transfer fluids for thermal energy storage systems in parabolic trough power plants. *Journal of solar energy engineering*, 127 (1):109–116, 2005.

Brad M Brown, Matt N Strasser, and R Paneer Selvam. Flueckiger2013. In *Proceedings of ASES*, volume 74, 2012.

A Bruch, JF Fourmigué, and R Couturier. Experimental and numerical investigation of a pilot-scale thermal oil packed bed thermal storage system for csp power plant. *Solar Energy*, 105:116–125, 2014.

A Bruch, S Molina, T Esence, JF Fourmigué, and R Couturier. Experimental investigation of cycling behaviour of pilot-scale thermal oil packed-bed thermal storage system. *Renewable Energy*, 103:277–285, 2017.

Nicolas Calvet, Judith C Gomez, Abdessamad Faik, Vladimir V Roddatis, Antoine Meffre, Greg C Glatzmaier, Stefania Doppiu, and Xavier Py. Compatibility of a post-industrial ceramic with nitrate molten salts for use as filler material in a thermocline storage system. *Applied energy*, 109:387–393, 2013.

John W Carson. Silo failures: Case histories and lessons learned. *Handbook of Powder Technology*, 10:153–166, 2001.

Mario Cascetta, Giorgio Cau, Pierpaolo Puddu, and Fabio Serra. Experimental investigation of a packed bed thermal energy storage system. In *Journal of Physics: Conference Series*, volume 655, page 012018. IOP Publishing, 2015.

ME Cates, JP Wittmer, J-P Bouchaud, and Ph Claudin. Jamming, force chains, and fragile matter. *Physical review letters*, 81(9):1841, 1998.

Bruno Chareyre. *Modélisation du comportement d'ouvrages composites sol-géosynthétique par éléments discrets: application aux ancrages en tranchées en tête de talus.* PhD thesis, Université Joseph-Fourier-Grenoble I, 2003.

Bruno Chareyre and Pascal Villard. Dynamic spar elements and discrete element methods in two dimensions for the modeling of soil-inclusion problems. *Journal of Engineering Mechanics*, 131(7):689–698, 2005.

B Charlas, F Kneib, O Gillia, D Imbault, and P Doremus. A tool for modelling the breathing of hydride powder in its container while cyclically absorbing and desorbing hydrogen. *International Journal of Hydrogen Energy*, 40(5):2283–2294, 2015.

K Chen, J Cole, C Conger, J Draskovic, M Lohr, K Klein, T Scheidemantel, and P Schiffer. Granular materials: Packing grains by thermal cycling. *Nature*, 442(7100):257–257, 2006.

K Chen, A Harris, J Draskovic, and P Schiffer. Granular fragility under thermal cycles. *Granular Matter*, 11(4):237–242, 2009.

Ke Chen. *Granular materials under vibration and thermal cycles.* The Pennsylvania State University, 2008.

Y-C Chen, I Ishibashi, and JT Jenkins. Dynamic shear modulus and fabric: part i, depositional and induced anisotropy. *Géotechnique*, 38(1):25–32, 1988.

Philippe Claudin and Jean-Philippe Bouchaud. Static avalanches and giant stress fluctuations in silos. *Physical review letters*, 78(2):231, 1997.

Eric Clément, Yaelle Serero, José Lanuza, Jean Rajchenbach, and Jacques Duran. Fluctuating aspects of the pressure in a granular column. *Powders & Grains*, 97:349, 1997.

DJ Close. Rock pile thermal storage for comfort air conditioning. *Mechanical and Chemical Engineering Transactions, Institution of Engineers (Australia), MC1 (1)*, pages 11–22, 1965.

Daniele Cocco and Fabio Serra. Performance comparison of two-tank direct and thermocline thermal energy storage systems for 1 mwe class concentrating solar power plants. *Energy*, 81:526–536, 2015.

Gaël Combe. *Origines géométriques du comportement quasi-statique des assemblages granulaires denses: étude par simulations numériques*. PhD thesis, Ecole Nationale des Ponts et Chaussées, 2001.

Peter A Cundall and Otto DL Strack. A discrete numerical model for granular assemblies. *geotechnique*, 29(1):47–65, 1979.

Thibaut Divoux, Hervé Gayvallet, and Jean-Christophe Géminard. Creep motion of a granular pile induced by thermal cycling. *Physical review letters*, 101(14):148303, 2008.

Adem Dogangun, Zeki Karaca, Ahmet Durmus, and Halil Sezen. Cause of damage and failures in silo structures. *Journal of performance of constructed facilities*, 23(2):65–71, 2009.

Frédéric V Donzé, Vincent Richefeu, and Sophie-Adélaïde Magnier. Advances in discrete element method applied to soil, rock and concrete mechanics. *Electronic Journal of Geotechnical Engineering*, 8(1):44, 2009.

Volker Dreißigacker, Hans Müller-Steinhagen, and Stefan Zunft. Thermo-mechanical analysis of packed beds for large-scale storage of high temperature heat. *Heat and mass transfer*, 46 (10):1199–1207, 2010.

Volker Dreißigacker, Stefan Zunft, and Hans Müller-Steinhagen. A thermo-mechanical model of packed-bed storage and experimental validation. *Applied energy*, 111:1120–1125, 2013.

Meenakshi Dutt, Bruno Hancock, Craig Bentham, and James Elliott. An implementation of granular dynamics for simulating frictional elastic particles based on the dl_poly code. *Computer Physics Communications*, 166(1):26–44, 2005.

Anna Effeindzourou, Bruno Chareyre, Klaus Thoeni, Anna Giacomini, and François Kneib. Modelling of deformable structures in the general framework of the discrete element method. *Geotextiles and Geomembranes*, 44(2):143–156, 2016.

Usama El Shamy, Osman De Leon, and Ryan Wells. Discrete element method study on effect of shear-induced anisotropy on thermal conductivity of granular soils. *International Journal of Geomechanics*, 13(1):57–64, 2011.

Thibaut Esence. *Etude et optimisation de systèmes de stockage thermique de type régénératif solide/fluid*. PhD thesis, UGA, 2017.

Thibaut Esence, Rocío Bayón, Arnaud Bruch, and Esther Rojas. Study of thermocline development inside a dual-media storage tank at the beginning of dynamic processes. In *AIP Conference Proceedings*, volume 1850, page 080009. AIP Publishing, 2017a.

Thibaut Esence, Arnaud Bruch, Sophie Molina, Benoit Stutz, and Jean-François Fourmigué. A review on experience feedback and numerical modeling of packed-bed thermal energy storage systems. *Solar Energy*, 153:628–654, 2017b.

S.E. Faas. *10-MWe solar-thermal central-receiver pilot plant: thermal-storage-subsystem evaluation - subsystem activation and controls testing phase*. Jul 1983a.

SE Faas. 10-mwe solar-thermal central-receiver pilot plant: thermal-storage-subsystem evaluation-subsystem activation and controls testing phase. Technical report, Sandia National Labs., Livermore, CA (USA), 1983b.

SE Faas. 10 mwe solar thermal central receiver pilot plant: Thermal storage subsystem evaluation - final report. Technical report, Sandia National Labs., Livermore, CA (USA), 1986.

Scott Flueckiger, Zhen Yang, and Suresh V Garimella. Thermocline energy storage in the solar one power plant: An experimentally validated thermomechanical investigation. *Energy Sustainability, Washington, DC, Aug*, pages 7–10, 2011.

Scott M Flueckiger, Zhen Yang, and Suresh V Garimella. Review of molten-salt thermocline tank modeling for solar thermal energy storage. *Heat Transfer Engineering*, 34(10):787–800, 2013.

ANSYS FLUENT. 12.0/12.1 documentation, ansys inc.

Q. Falcoz G. Papakokkinos and X. Py. Structured bed thermocline thermal energy storage system using recycled industrial wastes as filler materiams. *proceedings of SOLARPACES*, 2012.

Antonio García-Olivares, Joaquim Ballabrera-Poy, Emili García-Ladona, and Antonio Turiel. A global renewable mix with proven technologies and common materials. *Energy Policy*, 41:561–574, 2012.

Antoni Gil, Marc Medrano, Ingrid Martorell, Ana Lázaro, Pablo Dolado, Belén Zalba, and Luisa F Cabeza. State of the art on high temperature thermal energy storage for power generation. part 1—concepts, materials and modellization. *Renewable and Sustainable Energy Reviews*, 14(1):31–55, 2010.

I González, O Lehmkuhl, CD Pérez-Segarra, and A Oliva. Dynamic thermoelastic analysis of thermocline-like storage tanks. *Energy Procedia*, 69:850–859, 2015.

Michel Y Haller, Cynthia A Cruickshank, Wolfgang Streicher, Stephen J Harrison, Elsa Andersen, and Simon Furbo. Methods to determine stratification efficiency of thermal energy storage processes–review and theoretical comparison. *Solar Energy*, 83(10):1847–1860, 2009.

Raymon W Hallet Jr and Robert L Gervais. Central receiver solar thermal power system, phase 1. cdrl item 2. pilot plant preliminary design report. volume v. thermal storage subsystem.[sensible heat storage using caloria ht43 and mixture of gravel and sand]. Technical report, McDonnell Douglas Astronautics Co., Huntington Beach, CA (USA), 1977.

Ulf Herrmann, David W Kearney, et al. Survey of thermal energy storage for parabolic trough power plants. *TRANSACTIONS-AMERICAN SOCIETY OF MECHANICAL ENGINEERS JOURNAL OF SOLAR ENERGY ENGINEERING*, 124(2):145–152, 2002.

Karl Hoffmann. *Applying the wheatstone bridge circuit*. HBM Germany, 1974.

Olav H Hohmeyer and Sönke Bohm. Trends toward 100% renewable electricity supply in germany and europe: a paradigm shift in energy policies. *Wiley Interdisciplinary Reviews: Energy and Environment*, 4(1):74–97, 2015.

KGT Hollands and HF Sullivan. Pressure drops across rock bed thermal storage systems. *Solar Energy*, 33(2):221–225, 1984.

Taija Huotari and I Kukkonen. Thermal expansion properties of rocks: Literature survey and estimation of thermal expansion coefficient for olkiluoto mica gneiss. *Posiva Oy, Olkiluoto, Working Report*, 4:62, 2004.

HA Janssen. Versuche uber getreidedruck in silozellen. *Z. ver. deut. Ing.*, 39:1045, 1895.

Jean-François Jerier, Vincent Richefeu, Didier Imbault, and Fréderic-Victor Donzé. Packing spherical discrete elements for large scale simulations. *Computer Methods in Applied Mechanics and Engineering*, 199(25-28):1668–1676, 2010.

Melissa Jerkins, Matthias Schröter, Harry L Swinney, Tim J Senden, Mohammad Saadatfar, and Tomaso Aste. Onset of mechanical stability in random packings of frictional spheres. *Physical review letters*, 101(1):018301, 2008.

WS Jodrey and EM Tory. Computer simulation of close random packing of equal spheres. *Physical review A*, 32(4):2347, 1985.

Emerson E John, W Micah Hale, R Panneer Selvam, and Bradley Brown. Development and performance evaluation of high temperature concrete for thermal energy storage for solar power generation. In *ASME 2011 International Mechanical Engineering Congress and Exposition*, pages 1207–1213. American Society of Mechanical Engineers, 2011.

HV Kebeli, RA Bucklin, DS Ellifritt, and KV Chau. Moisture-induced pressures and loads in grain bins. *Transactions of the ASAE*, 43(5):1211, 2000.

Philipp Knödler, Volker Dreißigacker, and Stefan Zunft. Packed bed heat storage: Continuum mechanics model and validation. In *AIP Conference Proceedings*, volume 1734, page 050024. AIP Publishing, 2016.

Gregory J Kolb, Gary Lee, Panto Mijatovic, and Emanuil Valmianski. Thermal ratcheting analysis of advanced thermocline energy storage tanks. Technical report, Sandia National Laboratories (SNL-NM), Albuquerque, NM (United States), 2011.

Detlev Gustav Kröger. Packed rock bed thermal energy storage facility, March 18 2014. US Patent App. 14/786,717.

D Kunhappan, B Harthong, Bruno Chareyre, Guillaume Balarac, and PJJ Dumont. Numerical modeling of high aspect ratio flexible fibers in inertial flows. *Physics of Fluids*, 29(9): 093302, 2017.

Hans Juergen Lang, Jachen Huder, and Peter Amann. *Bodenmechanik und grundbau*, volume 4. Springer, 1990.

A Lapko and JA Prusiel. Analysis of thermal effects in grouped silos of grain elevators. *International agrophysics*, 20(4):301–307, 2006.

M Latroche. Structural and thermodynamic properties of metallic hydrides used for energy storage. *Journal of physics and chemistry of solids*, 65(2):517–522, 2004.

Edward W Law, Abhnil A Prasad, Merlinde Kay, and Robert A Taylor. Direct normal irradiance forecasting and its application to concentrated solar thermal output forecasting–a review. *Solar Energy*, 108:287–307, 2014.

Edward W Law, Merlinde Kay, and Robert A Taylor. Calculating the financial value of a concentrated solar thermal plant operated using direct normal irradiance forecasts. *Solar Energy*, 125:267–281, 2016.

C Libby. Solar thermocline storage systems: preliminary design study. *Electric Power Research Institute, Palo Alto, CA*, 2010.

C Libby, L Cerezo, R Bedilion, J Pietruszkiewicz, M Lamar, and R Hollenbach. Design of high temperature solar thermocline storage systems. In *SolarPACES Conference, Perpignan*, 2010.

Chih-Kuang Lin and Yen-Chun Chen. Effects of cyclic hydriding–dehydriding reactions of lani 5 on the thin-wall deformation of metal hydride storage vessels with various configurations. *Renewable energy*, 48:404–410, 2012.

James A Lindley, James H Whitaker, et al. *Agricultural buildings and structures.* American Society of Agricultural Engineers (ASAE), 1996.

Chu-Heng Liu and Sidney R Nagel. Sound and vibration in granular materials. *Journal of Physics: Condensed Matter*, 6(23A):A433, 1994.

HG Matuttis, S Luding, and HJ Herrmann. Discrete element simulations of dense packings and heaps made of spherical and non-spherical particles. *Powder technology*, 109(1):278–292, 2000.

ST McKillip, CE Bannister, and EA Clark. Stress analysis of hydride bed vessels used for tritium storage. *Fusion Science and Technology*, 21(2P2):1011–1016, 1992.

A Meffre, X Py, R Olives, S Guillot, A Faik, C Bessada, P Echegut, and U Michon. High temperature thermal energy storage material from vitrified fly-ashes. *proceedings of SOLARPACES*, 2011.

Maria M Melanson and Anthony G Dixon. Solid conduction in low dt/dp beds of spheres, pellets and rings. *International journal of heat and mass transfer*, 28(2):383–394, 1985.

Nicolas Mertens, Falah Alobaid, Lorenz Frigge, and Bernd Epple. Dynamic simulation of integrated rock-bed thermocline storage for concentrated solar power. *Solar Energy*, 110: 830–842, 2014.

F Motte, SL Bugler-Lamb, Q Falcoz, and X Py. Numerical study of a structured thermocline storage tank using vitrified waste as filler material. *Energy Procedia*, 49:935–944, 2014.

Gary E Mueller. Numerically packing spheres in cylinders. *Powder technology*, 159(2):105–110, 2005.

K Nasako, Y Ito, N Hiro, and M Osumi. Stress on a reaction vessel by the swelling of a hydrogen absorbing alloy. *Journal of Alloys and Compounds*, 264(1):271–276, 1998.

Masahiko Okumura, Koki Terui, Ayaka Ikado, Yasuhiro Saito, Masakazu Shoji, Yohsuke Matsushita, Hideyuki Aoki, Takatoshi Miura, and Yoshiaki Kawakami. Investigation of wall stress development and packing ratio distribution in the metal hydride reactor. *International Journal of Hydrogen Energy*, 37(8):6686–6693, 2012.

Iñigo Ortega-Fernández, Iñaki Loroño, Abdessamad Faik, Irantzu Uriz, Javier Rodriguez-Aseguinolaza, and Bruno D'Aguanno. Parametric and optimization analysis of a packed bed thermal energy storage system. In *22nd SolarPACES Conference, Abu Dhabi (United Arab Emirates)*, 2016.

James E Pacheco, Steven K Showalter, and William J Kolb. Development of a molten-salt thermocline thermal storage system for parabolic trough plants. *Journal of solar energy engineering*, 124(2):153–159, 2002.

Pedro Pardo, Alexandre Deydier, Zoé Anxionnaz-Minvielle, Sylvie Rougé, Michel Cabassud, and Patrick Cognet. A review on high temperature thermochemical heat energy storage. *Renewable and Sustainable Energy Reviews*, 32:591–610, 2014.

Cédric Philibert. *Solar energy perspectives*. OECD, 2011.

Cédric Philibert, Paolo Frankl, Cecilia Tam, Yasmina Abdelilah, Heymi Bahar, Quentin Marchais, Simon Mueller, Uwe Remme, Micheal Waldron, and Hoel Wiesner. Technology roadmap: solar photovoltaic energy. *International Energy Agency: Paris, France*, 2014.

Walter D Pilkey and Deborah F Pilkey. *Peterson's stress concentration factors*. John Wiley & Sons, 2008.

Concentrating Solar Power. Integrated solar thermochemical reaction system.

Danny Pudjianto, Marko Aunedi, Predrag Djapic, and Goran Strbac. Whole-systems assessment of the value of energy storage in low-carbon electricity systems. *IEEE Transactions on Smart Grid*, 5(2):1098–1109, 2014.

VM Puri, Q Zhang, and HB Manbeck. Influence of granular material properties on thermally induced bin loads. *Int. J. Bulk Solids Storage in Silos*, 2(3):1–7, 1986.

Xavier Py, Nicolas Calvet, Regis Olives, Patrick Echegut, Catherine Bessada, and Frederic Jay. Low-cost recycled material for thermal storage applied to solar power plants. *SolarPACES 2009*, 2009.

Xavier Py, Nicolas Calvet, Régis Olives, Antoine Meffre, Patrick Echegut, Catherine Bessada, Emmanuel Veron, and Sandra Ory. Recycled material for sensible heat based thermal energy storage to be used in concentrated solar thermal power plants. *Journal of Solar Energy Engineering*, 133(3):031008, 2011.

Feng Qin, Jiangping Chen, and Zhijiu Chen. The hydriding–dehydriding characteristics of la 0.6 y 0.4 ni 4.8 mn 0.2 and their influences in the surface strain on small-scale, thin-wall and vertical containers. *Materials & Design*, 29(10):1926–1933, 2008.

Frank GF Qin, Xiaoping Yang, Zhan Ding, Yuanzhi Zuo, Youyan Shao, Runhua Jiang, and Xiaoxi Yang. Thermocline stability criterions in single-tanks of molten salt thermal energy storage. *Applied energy*, 97:816–821, 2012.

Farhang Radjaï and Stéphane Roux. Contact dynamics study of 2d granular media: critical states and relevant internal variables. *The physics of granular media*, pages 165–187, 2003.

Jörg Reimann, E Arbogast, M Behnke, S Müller, and K Thomauske. Thermomechanical behaviour of ceramic breeder and beryllium pebble beds. *Fusion Engineering and Design*, 49:643–649, 2000.

S Rodat, A Bruch, N Dupassieux, and N El Mourchid. Unique fresnel demonstrator including orc and thermocline direct thermal storage: operating experience. *Energy Procedia*, 69: 1667–1675, 2015.

Jean-Noël Roux and Gaël Combe. Quasistatic rheology and the origins of strain. *Comptes Rendus Physique*, 3(2):131–140, 2002.

Siraj Sabihuddin, Aristides E Kiprakis, and Markus Mueller. A numerical and graphical review of energy storage technologies. *Energies*, 8(1):172–216, 2014.

Dietmar Schulze. Stresses in silos, 2005.

Joel E Skinner, Matthew N Strasser, Brad M Brown, and R Panneer Selvam. Testing of high-performance concrete as a thermal energy storage medium at high temperatures. *Journal of solar energy Engineering*, 136(2):021004, 2014.

J Szekely and JJ Poveromo. Flow maldistribution in packed beds: a comparison of measurements with predictions. *AIChE Journal*, 21(4):769–775, 1975.

Yuan Tian and Chang-Ying Zhao. A review of solar collectors and thermal energy storage in solar thermal applications. *Applied energy*, 104:538–553, 2013.

Jon T Van Lew, Peiwen Li, Cho Lik Chan, Wafaa Karaki, and Jake Stephens. Analysis of heat storage and delivery of a thermocline tank having solid filler material. *Journal of solar energy engineering*, 133(2):021003, 2011.

Nicolas Vandewalle, Geoffroy Lumay, O Gerasimov, and François Ludewig. The influence of grain shape, friction and cohesion on granular compaction dynamics. *The European Physical Journal E: Soft Matter And Biological Physics*, 22(3):241–248, 2007.

Watson L Vargas and JJ McCarthy. Thermal expansion effects and heat conduction in granular materials. *Physical Review E*, 76(4):041301, 2007.

Matthew L Wald. New solar process gets more out of natural gas. *The New York Times*, 2013.

Qi-Dong Wang, Jing Wu, Chang-Ping Chen, and Zhou-Peng Li. An investigation of the mechanical behaviour of hydrogen storage metal beds on hydriding and dehydriding and several methods of preventing the damage of hydride containers caused by the expansion of hydrogen storage metals. *Journal of the Less Common Metals*, 131(1-2):399–407, 1987.

Ben Xu, Peiwen Li, and Cholik Chan. Application of phase change materials for thermal energy storage in concentrated solar thermal power plants: a review to recent developments. *Applied Energy*, 160:286–307, 2015.

Chao Xu, Zhifeng Wang, Yaling He, Xin Li, and Fengwu Bai. Sensitivity analysis of the numerical study on the thermal performance of a packed-bed molten salt thermocline thermal storage system. *Applied Energy*, 92:65–75, 2012.

Zhen Yang and Suresh V Garimella. Thermal analysis of solar thermal energy storage in a molten-salt thermocline. *Solar energy*, 84(6):974–985, 2010.

Alice Y Ying, Zi Lu, and Mohamed A Abdou. Mechanical behavior and design database of packed beds for blanket designs. *Fusion engineering and design*, 39:759–764, 1998.

Giw Zanganeh, Andrea Pedretti, Simone Zavattoni, Maurizio Barbato, and Aldo Steinfeld. Packed-bed thermal storage for concentrated solar power–pilot-scale demonstration and industrial-scale design. *Solar Energy*, 86(10):3084–3098, 2012.

Giw Zanganeh, Andrea Pedretti, SA Zavattoni, MC Barbato, Andreas Haselbacher, and Aldo Steinfeld. Design of a 100 mwhth packed-bed thermal energy storage. *Energy Procedia*, 49: 1071–1077, 2014.

SA Zavattoni, Maurizio C Barbato, Andrea Pedretti, Giw Zanganeh, and Aldo Steinfeld. High temperature rock-bed tes system suitable for industrial-scale csp plant–cfd analysis under charge/discharge cyclic conditions. *Energy Procedia*, 46:124–133, 2014.

Q Zhang, VM Puri, HB Manbeck, and MC Wang. Finite element model for predicting static and thermally induced bin wall pressures. *Transactions of the ASAE*, 30(6):1797–1806, 1987.

Q Zhang, MG Britton, and JM Leitgeb. Thermally induced pressures in an on-farm grain storage bin. *Canadian Agricultural Engineering*, 35(1):51–56, 1993.

Olek C Zienkiewicz and Robert L Taylor. *The finite element method for solid and structural mechanics*. Elsevier, 2005.